Wind, Water, and the Sands of Mars

by Briony Heather Noelle Horgan

This thesis/dissertation document has been electronically approved by the following individuals:

Bell,James F (Chairperson)

Campbell,Donald Bruce (Minor Member)

Pritchard,Matthew (Minor Member)

Thomas,Peter Chew (Additional Member)

Herter,Terry Lee (Additional Member)

WIND, WATER, AND THE SANDS OF MARS

A Dissertation

Presented to the Faculty of the Graduate School

of Cornell University

In Partial Fulfillment of the Requirements for the Degree of

Doctor of Philosophy

by

Briony Heather Noelle Horgan

August 2010

© 2010 Briony Heather Noelle Horgan

WIND, WATER, AND THE SANDS OF MARS

Briony Heather Noelle Horgan, Ph. D.

Cornell University 2010

The north polar region of Mars is dominated by massive ice deposits and sand seas, and has been thought to be the product of the arid processes typical of the current martian geologic epoch, the Amazonian. However, new results from near-infrared spectroscopy and high-resolution images indicate that liquid water, in addition to ice, has played a major role in producing the unique compositions and morphologies of sediments in this region, and potentially elsewhere on Mars, during the Amazonian.

This first major goal of this work is to investigate the composition of north polar deposits by developing new methods to map the distribution of hydrated minerals, weathering rinds, and ferrous minerals using near-infrared spectra from the Mars Express OMEGA imaging spectrometer. The distribution of these minerals and phases places constraints on both the transport and aqueous history of sediments in the north polar region. While previous detections of aqueous alteration products in this region were limited to the sand sea of Olympia Undae, results presented in Chapter 2 indicate that hydrated minerals are ubiquitous throughout the north polar sand sea and are present within the stratigraphic record of Planum Boreum, the north polar plateau. Furthermore, Chapter 4 identifies a new class of aqueous alteration products on Mars, leached iron-bearing glass deposits, which are interpreted as having formed due to acidification of melt water from regional snowpacks or ice sheets. The leached deposits are the dominant composition in significant portions of the north polar sand sea, in the cavi unit of Planum Boreum, and in the extensive low albedo region of

Acidalia Planitia, suggesting that large regions of Mars have been pervasively altered by the action of ice and water during the Amazonian.

The second major goal of this work is to investigate the effects of ice and water on the morphology and activity of dunes in the north polar sand sea, by mapping the distribution of decameter-scale features on the dunes. Although the dunes in this region appear to be active based on their lack of dust, sharp crestlines, and the observations of recent grain flow described in Chapter 3, remote sensing data sets and morphologic features suggest that the presence of ice and sulfates within the dunes may have slowed the rate of migration below what we have been able to observe. Additionally, a strong correlation between surface cracks and gypsum abundance in Olympia Undae suggests that the dunes are chemically cemented by the sulfates, most likely by gypsum deposited near the surface of the dunes by capillary wicking of brines. As the dunes have most likely been active recently, these brines must also be active and stable under current climatic conditions.

This work presents a collection of new and unique observations of the effects of water and ice on the composition and morphology of martian north polar sediments. These observations suggest that although the Amazonian has typically been thought of as an arid period dominated by physical weathering, the northern plains have been, and likely continue to be, a dynamic cryo-sedimentary system where both physical and chemical weathering processes have been recently active.

BIOGRAPHICAL SKETCH

Briony Horgan was born in Klamath Falls, OR in 1983 during a December blizzard to Gerard and Jauvie Horgan, and the smell of cedars and the sight of big open skies still remind her of home. Briony was transplanted from the sagebrush of Klamath to the suburbs of Portland, OR in 1989, where she graduated from Southridge High School in 2001. After heading off to Oregon State University in 2001 to pursue a degree in physics, Briony participated in research internships in the swamp at the Laser Interferometer Gravitational-wave Observatory (LIGO) in Livingstone, LA and on the beach at the University of California – Santa Barbara. Briony received her B.S. in Physics from Oregon State University (Corvallis, OR) in 2005. After being inspired by the likes of Carl Sagan and Kim Stanley Robinson to explore the universe through planetary science, Briony enrolled as a graduate student in Astronomy at Cornell University in Ithaca, NY in 2005, earning her M.S. in 2008 and her Ph.D. in 2010.

I would like to dedicate this dissertation to my father, Gerard for all his wonderful support during the past five years, and to my mother, Jauvie, who I miss dearly and who I know would have been thrilled to call me "doctor".

ACKNOWLEDGMENTS

I would like to thank:

Ken Tanaka, Mary Bourke, and Rob Sullivan, for immeasurable help in expanding my knowledge of stratigraphy and aeolian processes,

Ryan Anderson, Eldar Noe Dobrea, Karrie Kressler, and Jonathan Joseph, for help in developing the OMEGA calibration and mapping pipeline,

Mary Mulvanerton, for making sure that I was always taken care of,

Ed Cloutis, his sweathogs, and his hammers, for all the spectral lab work, all the fabulous field opportunities, and teaching me the meaning of "booter", and

Rick, for his unwavering support, for putting up with the pre-conference all-nighters, and for accepting that I now would much rather talk about rocks than physics.

Finally, I would like to thank my fabulous advisor Jim Bell, for teaching me how to make science work for me, and not the other way around (although he still hasn't shown me the secret handshake).

This work was supported by the NASA Harriet G. Jenkins Predoctoral Fellowship as well as by grants from the Mars Data Analysis Program under contracts from NASA, the Mars Odyssey Participating Scientist program under contracts from the Jet Propulsion Laboratory, and the Canadian Space Agency.

TABLE OF CONTENTS

LIST OF FIGURES

Chapter 4:

LIST OF TABLES

PREFACE

The Sands of Mars is a novel by Arthur C. Clarke from 1951. In this book, an intrepid traveler reaches Mars to discover that it is populated by kangaroo-like aliens and that the low albedo regions are vast fields of rubbery plants. While the investigations of the geologic history of sediments in the north polar region of Mars presented in this dissertation may not be quite as exotic as the Mars of Arthur C. Clarke, they do reveal that there is still a fascinating and real story waiting to be told about the sands of Mars.

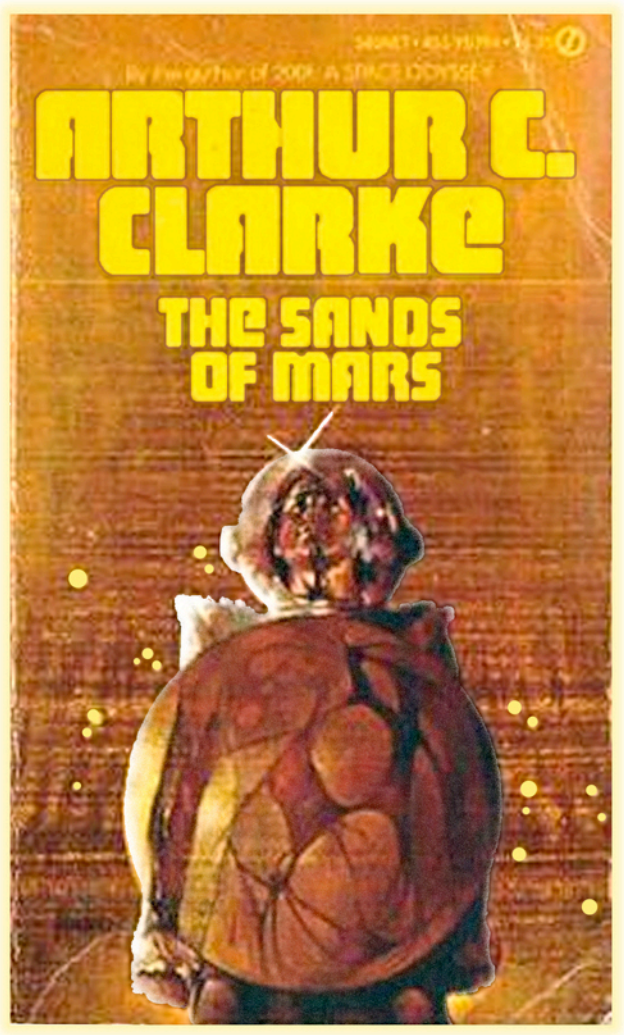

CHAPTER 1

THE NORTH POLAR REGION OF MARS

The north polar region of Mars lies near the lowest elevations of the basin that encompasses much of the northern hemisphere of Mars, and has likely been the site of ongoing accumulation of ice and sediments throughout most of martian history. The sheer volume of sediments and the action of polar processes over timescales orders of magnitude longer than observed in terrestrial geologic systems has made the north polar region of Mars a unique geologic province within the solar system. While deposits in this region potentially record billions of years of martian climatic and geologic history, the region also serves as a natural laboratory for studying processes on modern Mars that may have modified much of the surface.

While satellite observations of the north polar region have allowed extensive investigations of the morphology and stratigraphy of both the north polar layered deposits and the north polar sand sea, much less work has been done on the composition of these deposits, and no major studies have been completed on how the morphology and composition of the deposits are related. Therefore, the primary goal of my work has been to place constraints on the overall composition of north polar deposits and thus on their primary mineralogy, their sources, and the history of aqueous alteration processes in the region. By applying the results of this investigation into composition and processes to high-resolution morphologic studies, my work has shown that north polar landforms and materials are the result of modification due to periglacial, aeolian, and aqueous processes, many of which could have occurred or are still occurring under current martian climatic conditions.

To set the stage for the following detailed studies on the composition and morphology of martian north polar deposits, this chapter provides an overview of the

current state of knowledge of the landforms, composition, and geologic history of the north polar region of Mars.

1. Context: The northern lowlands

The surface of Mars is dominated by a north-south dichotomy in both topography and surface morphology (Figure 1.1). Much of the northern hemisphere lies within several extensive basins with elevations decreasing toward the north pole, to a minimum of ~5.2 km below the global mean elevation (Figure 1.2; Zuber *et al*., 1998). The northern lowlands are also characterized by much smoother surfaces and lower crater densities compared to the southern highlands. This difference in surface texture was observed as early as Mariner 9 in 1971, and has been consistently interpreted as resulting from resurfacing of the northern plains (*e.g.*, Scott and Carr, 1978). However, clear identification of the processes that did the resurfacing and constraints on the timing of the resurfacing have both become apparent only in more recent mapping efforts (*e.g.* Tanaka *et al*., 2003).

Without access to sample-based laboratory isotope dating methods, estimates of the ages of planetary surfaces are determined by comparing the size distribution and density of impact craters on the surface to expected impactor production functions (*e.g.,* Hartmann and Neukum, 2001). While this process is plagued with uncertainties, large differences in crater densities probably do reflect large differences in surface exposure ages. For example, the southern highlands of Mars are heavily cratered and exhibit crater densities for the largest craters (D > 65 km) similar to the ancient lunar highlands, whereas craters of this size are virtually non-existent on the smoothest martian surfaces (*e.g.*, Tanaka, 1986; Hartmann and Neukem, 2001). Thus, on Mars, most surfaces have been assigned to one of three geologic epochs based on their crater

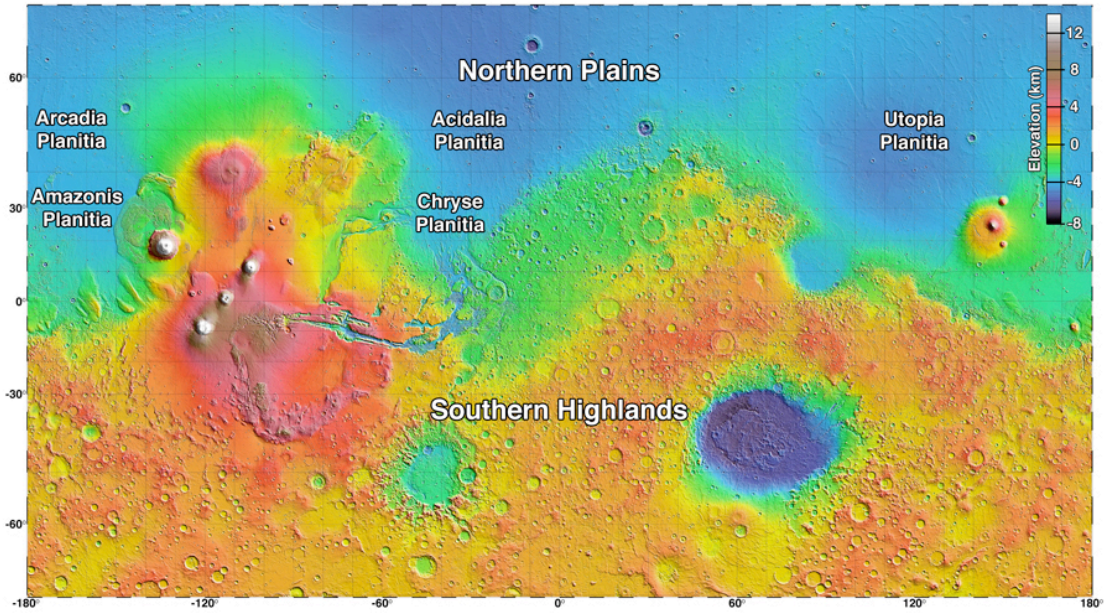

Figure 1.1: Global topography of Mars from MOLA overlain on MOLA shaded relief. Equatorial Mercator projection to +/- 70°N (Smith *et al*., 2001).

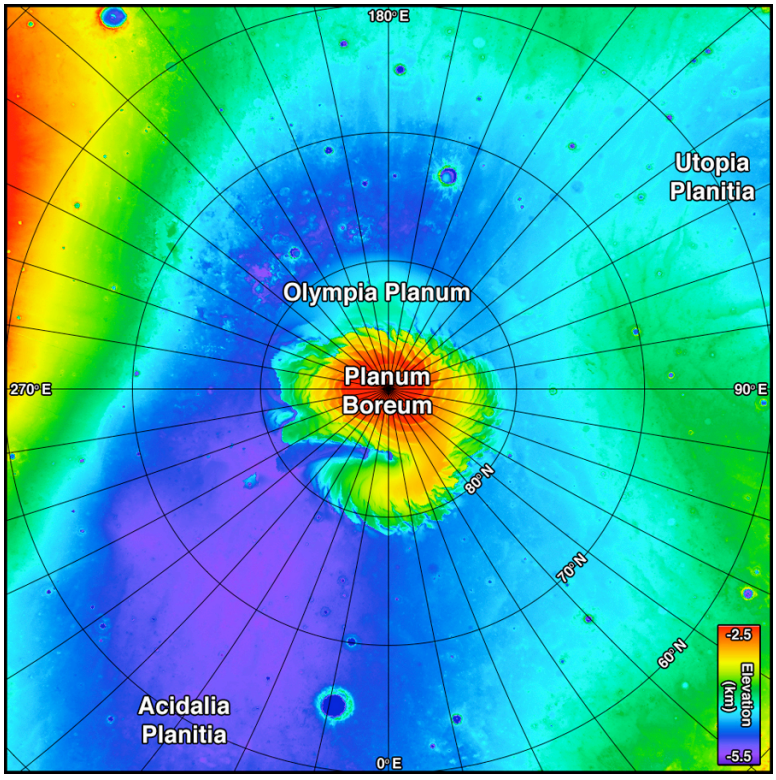

Figure 1.2: Topography of the northern basin from MOLA. North polar simple cylindrical projection, produced in JMars (Gorelick *et al*., 2003).

densities (Tanaka, 1986): the Noachian (before ~3.5 Gyr), the Hesperian (~3.5 to 3.0-2.0 Gyr), and the Amazonian (after 3.0-2.0 Gyr).

The northern plains represent the youngest major surface region on Mars, and are thought to have been resurfaced in multiple events, starting in the Early Hesperian and continuing into the Early Amazonian (*e.g.,* Tanaka *et al*., 2003). Many processes probably contributed to the resurfacing, including large influxes of fluids and sediments from outflow channels originating in the southern highlands, especially those flowing from the Chryse Planitia outflow channels into Acidalia Planitia, and local volcanic flows, such as in Amazonis and Utopia Planitia (*e.g.,* Tanaka *et al*., 2003; Tanaka, 2005).

Since at least the Early Amazonian, the northern plains appear to have been reworked extensively by periglacial processes (*e.g.*, Tanaka, 2003), and these processes appear to be ongoing under current climatic conditions (*e.g.*, Mellon *et al*., 2008; Smith *et al*., 2009; Kreslavsky *et al*., 2010). The northern plains contain a variety of periglacial and glacial landforms, including polygonal terrain, putative mud volcanoes, ice-rich crater ejecta, ice-rich glacial remnants and surface mantles potentially derived from sublimation (*e.g.*, Mustard *et al*., 2001; Tanaka *et al*., 2003, 2008; Mellon *et al*., 2008; Kadish *et al*., 2009; Morgan *et al*., 2009; Plaut *et al*., 2009; Oehler and Allen, 2010). Indeed, models predict ground ice within meters of the surface down to 45°N under current climatic conditions, and suggest that the ice may have extended much farther in the past (*e.g.,* Paige, 1992; Mellon and Jakosky, 1995; Mischna *et al*., 2003). These predictions have been confirmed by the hydrogen detections of the Mars Odyssey (ODY) Neutron Spectrometer that are interpreted as evidence for ground ice (Boynton *et al*., 2002), by direct Phoenix lander observations of ground ice (Smith *et al*., 2009), as well as by direct observations of ice exposed at the bottom of fresh impact craters (Byrne *et al*., 2009).

2. The north polar layered deposits

The north polar region of Mars is dominated by two major geologic features: Planum Boreum (the north polar cap of Mars) and the north polar sand sea, which encircles the polar cap (Figure 1.3). The internal structure of Planum Boreum is herein referred to as the north polar layered deposits (NPLD), and some layers within the NPLD appear to provide a source of sand for the north polar sand sea. The NPLD is composed of ~3 km of sand, dust, and water ice, capped by a residual pure water ice layer (*e.g.*, Tanaka *et al*., 2008; Figure 1.4). For reference, Planum Boreum has about twice the average thickness (~3 km vs. ~1.6 km) and about half the average diameter (~1180 km vs. ~2360 km) of the Antarctic ice cap (*The World Factbook 2009*. Washington, DC: Central Intelligence Agency, 2009). Stratigraphic mapping and sub-surface radar sounding investigations have revealed that Planum Boreum has a complex internal structure, probably resulting from many episodes of deposition and erosion (*e.g.*, Rodriguez *et al*., 2007; Tanaka *et al*., 2008; Putzig *et al*., 2009; Smith and Holt, 2010). The internal structure is exposed in spiral troughs ("cavi" or "chasma") that cut into Planum Boreum (Figure 1.2). As shown in Figure 1.3, the largest trough, Chasma Boreale, divides the polar cap into the main body and a more southerly lobe (Gemina Lingula). These troughs are apparently lengthened in the east-west direction by katabatic winds flowing over steep scarps at the head of the chasma (*e.g.*, Warner and Farmer, 2008) and modified in the north-south direction by sublimation of ice-rich materials on the equator facing slope and aeolian transport and deposition onto the pole facing slope (*e.g.* Howard, 1978; Smith and Holt, 2010). The lowest units of the NPLD include the Rupes Tenuis unit and the Cavi unit (Figure 1.4). The Rupes Tenuis unit is interpreted to be composed of reworked sediments derived from surrounding plains materials and is up to 1.4 km thick. This unit is observed outcropping at the mouth of Chasma Boreale, at deep chasma head scarps,

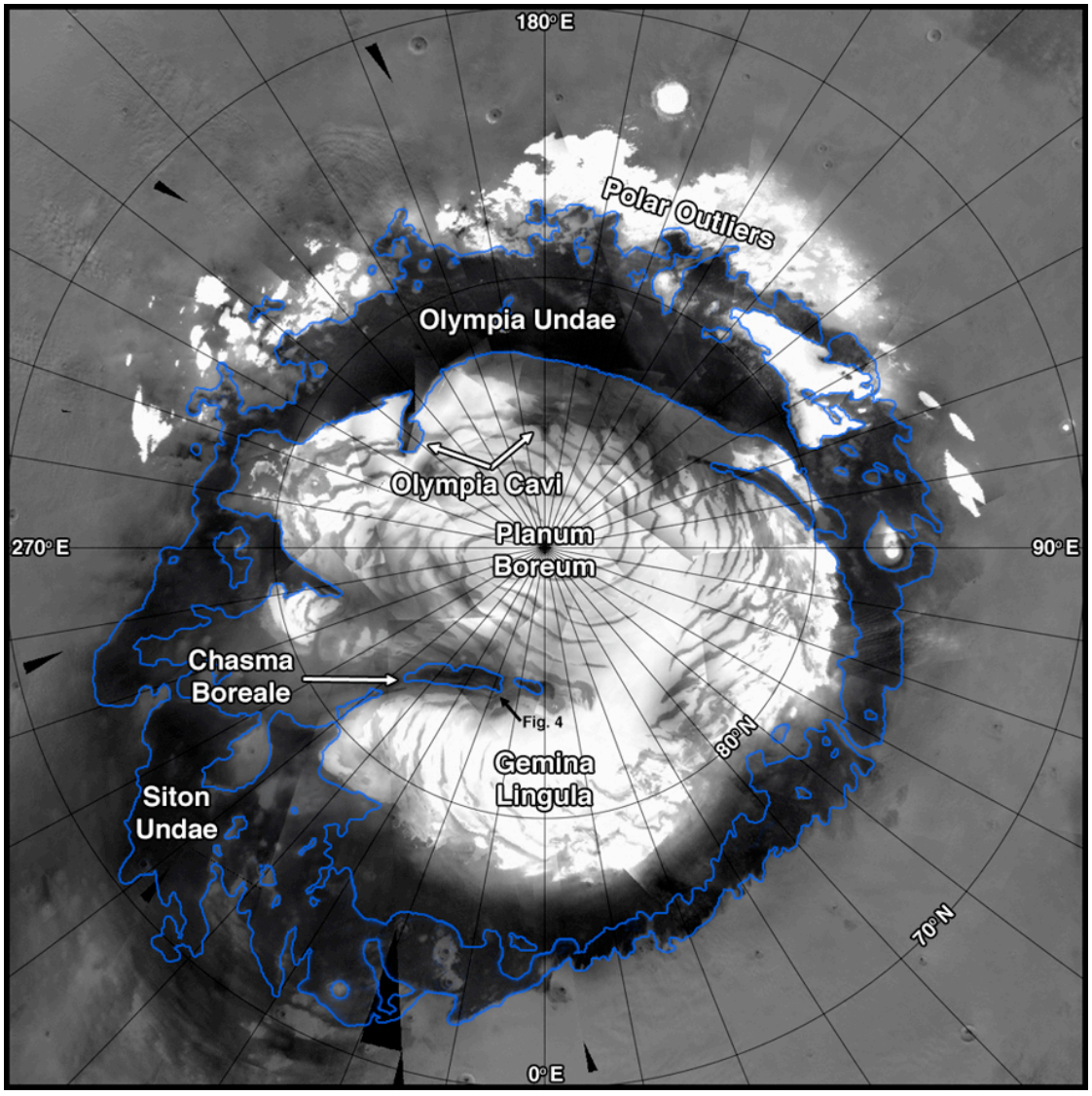

Figure 1.3: Major features in the north polar region of Mars. MGS/MOC wide-angle mosaic, north polar simple cylindrical projection. Blue outlines indicate dune fields as mapped by Hayward *et al*. (2010). On Mars, 1° of latitude represents ~60 km.

and as the capping unit on pedestal craters in the northern plains (Fishbaugh and Head, 2005; Tanaka *et al*., 2008). The Cavi unit is heterogeneously distributed within Planum Boreum, and has been interpreted as the remnants of a large sand sea deposited during an extended period of erosion sometime during the Middle Amazonian (from ~1 Gyr until recently; Tanaka *et al.*, 2008; Kocurek and Ewing, 2010). The Cavi unit has been postulated to be the primary modern source of sand for the north polar sand sea, as it contains many sand-rich layers (Figure 1.4), and sand dunes are observed emanating from outcrops of the Cavi unit (Tanaka *et al*., 2008).

The upper units of Planum Boreum make up what has classically been called the polar layered deposits (PLD; *e.g.*, Blasius and Cutts, 1982), because of their characteristic thin layers of varying albedo (Figure 1.4). However, as high-resolution imagery has allowed more detailed stratigraphic mapping, it has become apparent that the term "PLD" is now overly vague except for in the most general discussions of north polar geology (Tanaka *et al*., 2008). As such, here we only use "NPLD" to refer to the entire interior structure of Planum Boreum, and refer to the individual units by the names proposed by Tanaka *et al*. (2008). Of the major upper Planum Boreum units, the lowest is the Planum Boreum 1 unit (PB1; classically the "lower PLD"). This unit is 1.5 km thick or more, as compared to the similar but thinner Planum Boreum 3 unit (PB3; classically the "upper PLD"), which is on the order of tens of meters thick. These units are interpreted to be the result of ice and dust deposition, with the amounts of ice and dust varying with changes in insolation due to climate and obliquity cycles (Tanaka and Scott, 1987; Herkenhoff, 2003; Fishbaugh and Head, 2005; Tanaka, 2005; Tanaka *et al*., 2008).

PB1 and PB3 are separated by a well-defined unconformity that contains low-albedo materials that erode out at scarps and obscure underlying units (Rodriguez *et al*., 2007). These dark sediments are known as the Planum Boreum 2 unit (PB2), and

are interpreted to be composed of sand and dust particles with little water ice, and likely resulted from sediment accumulation following a period of erosion. PB2 appears to be the source for the thin, dark sand sheets that encircle the polar cap north of the dune fields between 300°E and 45°E (Figure 1.3; Rodriguez *et al*., 2007; Tanaka *et al*., 2008).

3. The north polar sand sea

The north polar sand sea is the largest aeolian accumulation on Mars, with a surface area of 10^5-10^6 km^2 (Lancaster and Greeley, 1990; Hayward *et al*., 2010). For scale, this is slightly larger than the state of California and 150% larger than the largest active erg (sand sea) on Earth (Rub al Khali, Saudi Arabia; Tsoar *et al*., 1979). Within the solar system, the martian north polar sand sea is only rivaled in size by the equatorial sand seas of Titan (~10^6-10^7 km^2; Lorenz and Radebaugh, 2009). Individual dune fields within the north polar sand sea include Olympia Undae, which encircles the polar cap between 110°E and 250°E, Siton Undae, which lies in the deepest part of the northern basin between 290°E and 320°E, and Hyperborea Undae, which extends out of the mouth of Chasma Boreale (Figure 1.3).

Previous workers have proposed that the current source of the dark dune material is somewhere within the lowest layers of the NPLD, previously referred to as the "basal unit" (Thomas and Weitz, 1989; Byrne and Murray, 2002; Fishbaugh and Head, 2005). However, more recent geologic mapping has specifically identified the Cavi unit as the primary source (Figure 1.4; Tanaka *et al*., 2008). Extensive sand seas have probably been present in the north polar region throughout the Amazonian, as the Cavi unit appears to be the indurated remnants of a Middle Amazonian sand sea (Tanaka *et al*., 2008; Kocurek and Ewing, 2010).

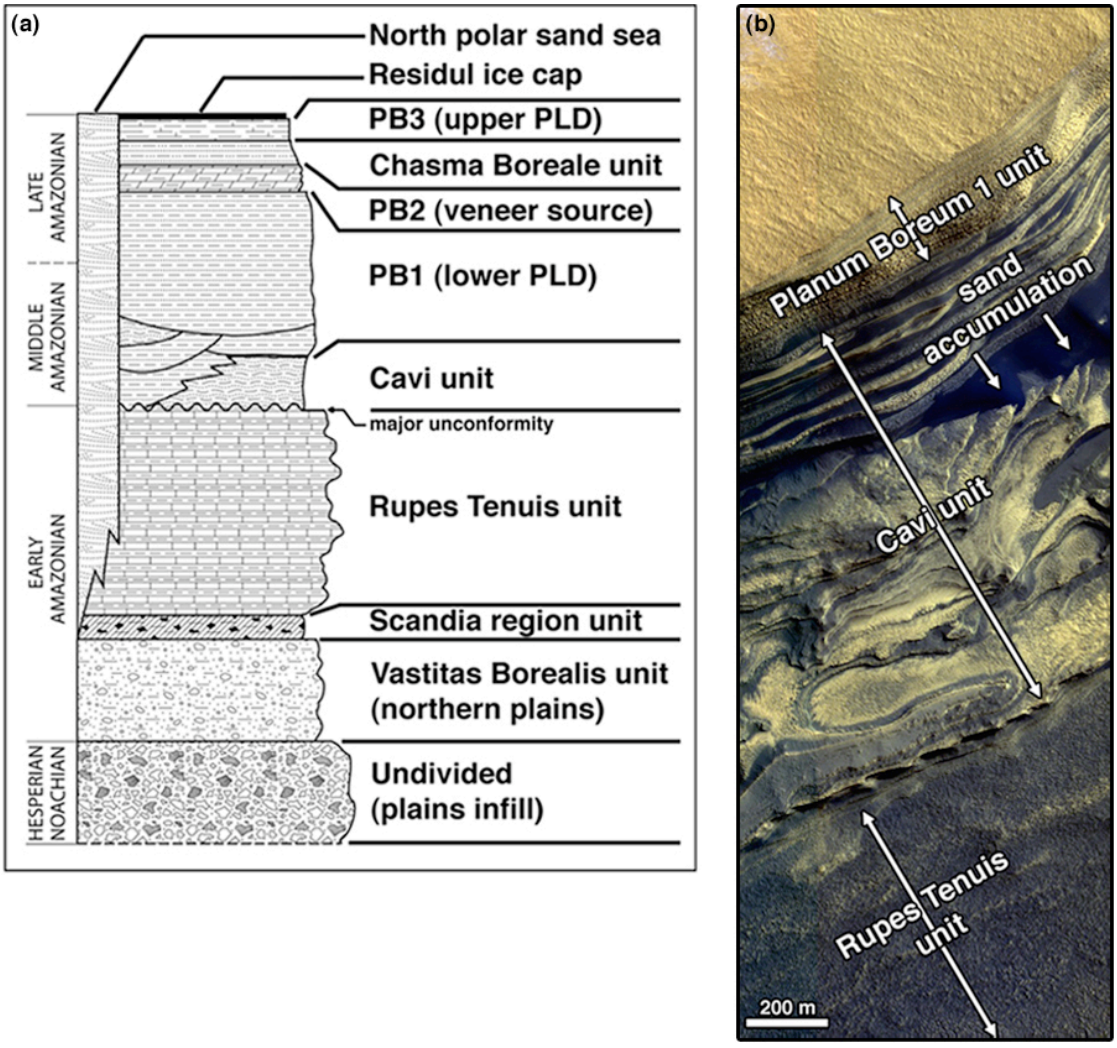

Figure 1.4: The internal stratigraphy of Planum Boreum. (a) Model stratigraphic column depicting north polar geologic units. Modified from Figure 1.3c of Tanaka *et al*. (2008). (b) False color MRO/HiRISE image PSP_001334_2645 showing the lower head scarp of Chasma Boreale with exposures of many of the units in Planum Boreum. Note the apparent sand accumulation at the break in slope of the Cavi unit. Illumination from upper right. Unit definitions from Tanaka *et al*. (2008), Figure 1.9a.

Much of the north polar erg appears relatively young and recently active, as most dunes in the sand sea appear fresh with sharp features and low albedos indicating minimal dust cover, potentially due to recent saltation. Indeed, recent searches in HiRISE images across 1640 sq. km in Olympia Undae for impact craters >5 meters in diameter have revealed only exactly one crater (Kreslavsky, 2010). Although extracting an absolute crater retention age of the surface from one crater is problematic, estimates place it on the order of 0-1000 years. Regardless, the lack of impact craters >5 meters in diameter implies that Olympia Undae, and possibly the rest of the sand sea, is very young and has been active under current climatic conditions (Kreslavsky, 2010). However, dune migration has not been observed in the north polar sand sea or anywhere else on Mars over more than 30 years of orbital imaging, at a variety of spatial and temporal scales (*e.g.* Edgett and Malin, 2000; Zimbelman, 2000; Edgett, 2002; Schatz *et al*., 2006; Bourke, 2008). The only changes in dune morphology that have been reported to date are the apparent removal by erosion of several small dome dunes in the dune fields east of Olympia Undae, near 95°E (Bourke *et al*., 2008) and the modification (probably erosion) of several small dunes in Endeavour Crater, Meridiani Planum (Chojnacki *et al*., 2010).

The dearth of observed dune movement on the planet is probably not due to a lack of wind speeds above the saltation threshold for loose sand. Saltation of individual grains and ripple migration have regularly been observed from the Mars Exploration Rovers during wind events (Sullivan *et al*., 2008), ripple migration and dune erosion have been observed in some orbital images (Bourke, 2008; Chojnacki *et al*., 2010; Silvestro *et al*., 2010), and streaks of dark sand are often observed downwind of dunes and other landforms (*e.g.*, Tanaka *et al*., 2008; Geissler *et al*., 2008). Instead, it has been hypothesized that the lack of migration is due to induration, or stabilization, of the dunes (*e.g.*, Schatz *et al*., 2006). Available *in situ* and orbital

observations suggest that induration of sediments is a common process on Mars. For example, indurated surface crusts have been observed at all mid- and low-latitude landing sites (Arvidson *et al.*, 1989, 2004; Moore *et al*., 1999; Sullivan *et al*., 2008), and indurated sandstones have been observed both from orbital (*e.g.*, Edgett and Malin, 2000; Kocurek and Ewing, 2010) and *in situ* observations (*e.g.*, Squyres *et al*., 2004; Squyres and Knoll, 2005; Grotzinger *et al*., 2005). However, it is unknown what mechanisms cause induration, what timescales these mechanisms act over, and how these mechanisms affect dune morphology and migration.

In the north polar sand sea, one factor that may influence the induration state and morphology of the dunes is the presence of water ice within the dunes. Analysis of ODY Neutron Spectrometer and thermal infrared data at a range of scales (100 m to 600 km) indicate that Olympia Undae is best modeled as an ice-cemented layer covered by a layer of non-indurated, ice-free sand, with ice burial depths on the order of 10 cm (Feldman *et al*., 2008; Bandfield and Feldman, 2008; Putzig *et al*., 2010; Titus *et al*., 2010). Based on this model, Feldman *et al.* (2008) proposed that the dune interiors are cemented by pore ice. Morphologic features on the dunes that have been cited in support of this hypothesis include: pits and chains of pits along dune crests, interpreted as collapse features resulting from denivation (sublimation and/or melting of ice); narrow sinuous depressions, interpreted as tensional surface cracks resulting from change in volatile volume below a coherent surface layer; and high albedo arcuate ridges exposed in interdune areas, interpreted as the permafrost indurated remnants of barchan dune strata (Feldman *et al*., 2008).

4. Mafic composition of north polar deposits

Aeolian bedforms on Mars are dominantly composed of dark sand grains, which are mafic (iron/magnesium rich) in composition based on remote sensing and *in*

situ observations (*e.g.,* Bell *et al.,* 2004; Bibring *et al.,* 2005; Christensen *et al.,* 2000, 2004b; Gellert *et al.,* 2004; Morris *et al.,* 2006; Rogers and Aharonson, 2008). Previous workers have classified the north polar sand sea as the lowest albedo dune field on the planet (Thomas and Weitz, 1989; Herkenhoff and Vasavada, 1999), possibly implying that the erg has undergone unique processes and has a distinct composition as compared to other martian dune fields.

Bell *et al.* (1997) identified a strong 953 nm absorption restricted to the circum-polar dark deposits in near-infrared (NIR) Hubble Space Telescope (HST) multi-spectral images of the north polar region, implying a strong mafic component to the dunes, most likely a pyroxene. Initial analysis of Mars Global Surveyor Thermal Emission Spectrometer (MGS/TES; Christensen *et al*., 2001) observations by Noe Dobrea and Bell (2001) also suggested a strong pyroxene component to the dunes. OMEGA observations have suggested minor amounts of pyroxene in Olympia Undae (Fishbaugh *et al.*, 2007); however, these detections are largely confined to localized areas outside the main dune field.

5. Alteration history of north polar deposits

As shown in Figure 1.5, the dunes of Olympia Undae exhibit the strongest and most areally-extensive hydrated sulfate signature yet seen on Mars (Poulet *et al*., 2007), based on the presence of a deep H_2O absorption at 1.9 μm attributed to water within the structure of a polyhydrated sulfate mineral (Langevin *et al*., 2005a). The sulfate signature was first identified by the Mars Express spacecraft's OMEGA NIR imaging spectrometer investigation (Bibring *et al.*, 2004), and has since been confirmed by the MRO Compact Reconnaissance Imaging Spectrometer for Mars (CRISM; Murchie e*t al*., 2009). Additional absorptions in the 1-2.5 μm range indicate that the hydrated sulfate is most likely gypsum ($CaSO_4$•2(H_2O); Langevin *et al*.,

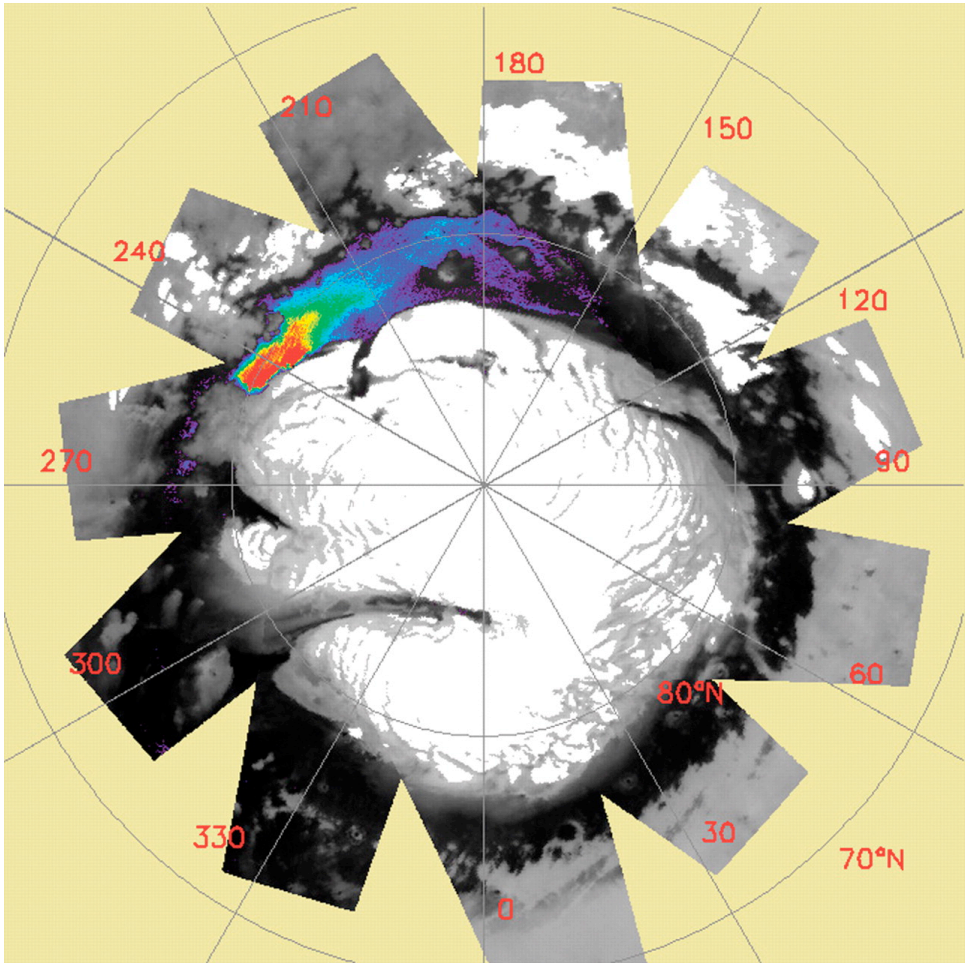

Figure 1.5: OMEGA 1.9 μm band depth (purple: 6%, red: 25%) over 1.085 μm albedo. This parameter has been postulated to represent the abundance of gypsum in the north polar region. Figure 1.1 of Langevin *et al*. (2005a).

2005a). As gypsum only forms as a precipitate or evaporite from water, the presence of gypsum in Olympia Undae may imply an important role for surface or near-surface water in the alteration of the dune materials (Langevin *et al*., 2005a; Fishbaugh *et al*., 2007).

Gypsum can be formed in a variety of environments, but in general, gypsum formation requires a source of sulfur and H_2O (in the liquid or gas phase) interacting with Ca-bearing minerals. Most previous authors have assumed that the alteration to produce the gypsum has occurred recently, likely within the modern dune field (Langevin *et al*., 2005a; Fishbaugh *et al*., 2007). In this model, the only apparent source of water in the region is meltwater from the polar cap, produced via local geothermal heating, basal melt, or an impact. However, Tanaka *et al*. (2008) argued that there is no clear geologic evidence for polar outflows during the Amazonian and that the topography of the region would generally cause any fluids to flow toward the lowest point of the basin, south of Chasma Boreale, where no gypsum has yet been identified.

The north polar sand sea and the low albedo deposits of Acidalia Planitia have also been identified as the type localities for the TES surface type 2 (ST2) composition (Wyatt *et al*., 2004; Ruff and Christensen, 2007), which was initially identified by Bandfield *et al* (2000). Model-derived compositions of ST2 differ from the more widespread olivine-basaltic composition of Surface Type 1 by including an additional amorphous or poorly crystalline high-silica phase (Michalski *et al*., 2005). However, the nature of this phase is not well constrained. Possible high-silica phases include both primary volcanics (*e.g.,* obsidian glass, alkali glass) and secondary alteration products (*e.g.,* zeolites, opal, amorphous silica coatings; Bandfield *et al*., 2000; Wyatt and McSween, 2002; Michalski *et al*., 2005; Rogers *et al*., 2007; Ruff and Christensen, 2007). These possibilities have significantly different implications for

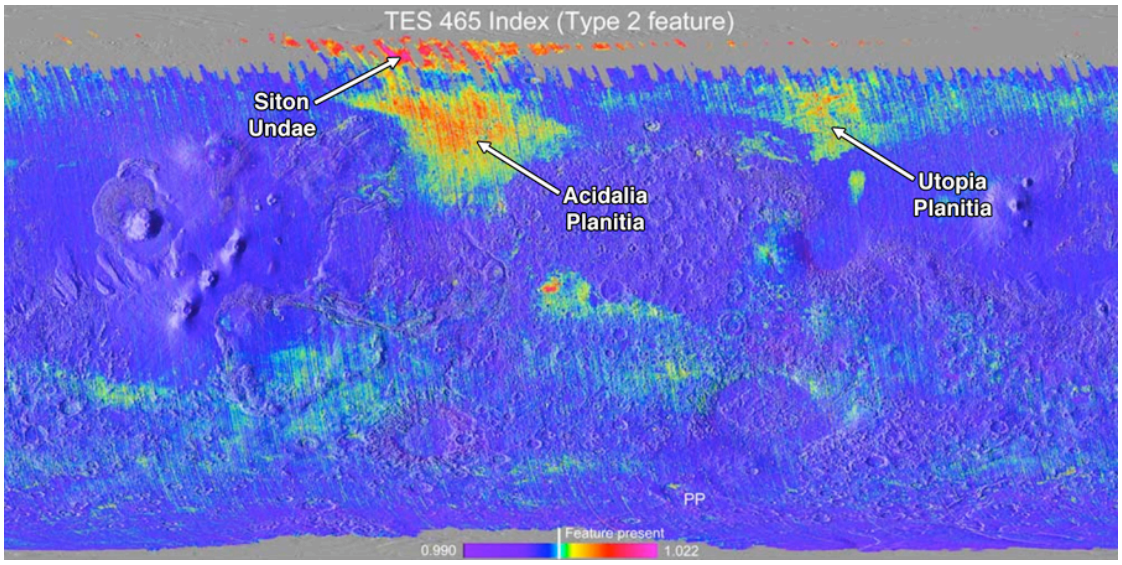

Figure 1.6: A global TES parameter map indicating the presence of an absorption band at 465 cm^{-1}, which is characteristic of ST2. Note the increase in the parameter within the low albedo deposits of the northern basin (Acidalia and Utopia Planita, Siton Undae). Modified from Figure 2 of Ruff and Christensen (2007).

martian history. For example, if ST2 is derived from a more andesitic magma, then it implies substantial compositional evolution from typical martian basaltic magma; if ST2 contains a silica-rich aqueous alteration product, however, then it could instead imply widespread leaching or dissolution of basalt. Studies of Acidalia in the NIR have not resolved this ambiguity. Acidalia is unique among martian low albedo regions because it is nearly spectrally featureless in the NIR, suggesting that spectrally-obscuring coatings or spectrally-featureless glasses might dominate the region (Mustard *et al*., 2005; Poulet *et al*., 2007).

6. Outstanding questions

This dissertation aims to resolve several outstanding questions regarding martian north polar processes and landforms, with a particular focus on processes

involving potential interactions between sediments and ice/water. The three primary questions that I address are as follows:

(1) What is the distribution and source of the north polar sulfates and what constraints does these place on how/when they were formed?

(2) What process could be responsible for the apparent induration of dunes in the north polar sand sea?

(3) What is the bulk composition of the north polar sand sea and how does it relate to TES ST2?

7. Outline of following chapters

Chapter 2 addresses the distribution of hydrated minerals in the north polar sand sea and within the NPLD. The primary result of this study is that hydrated minerals, most likely sulfates, are present in nearly all dune seas in the region, as well as within certain layers of the NPLD. This result implies a complex cycle of sediment exchange between Olympia Undae and the other polar units, an earlier origin for the hydrated minerals than originally postulated, and the occurrence of significant water activity in this region during the Amazonian. Chapter 2 was peer reviewed and published in full in the January 2009 issue of the *Journal of Geophysical Research – Planets* (Horgan *et al*., 2009).

Chapter 3 investigates the causes of putative dune induration on Mars by examining the morphology and distribution of decameter-scale features on dunes in the north polar sand sea. Results from this study indicate that both ice and sulfate induration are ongoing processes in the north polar sand sea and that sulfate brines appear to have been present in the dunes recently, under current climatic conditions. The results from Chapter 3 were presented at the Second International Planetary

Dunes Workshop (Horgan *et al*., 2010), and are currently in preparation for submission to *Icarus* (Horgan *et al*., in prep).

Chapter 4 provides a detailed analysis of the ferrous and silicate composition of the north polar sand sea, based on analysis of laboratory spectra of a suite of ferrous minerals. Results from this study indicate that the primary ferrous phases in the sand sea are likely high calcium pyroxene and iron-bearing glass, contrary to previous findings. Furthermore, the high-silica phase of TES ST2 may thus be a silica-enriched leached glass rind on the iron-bearing glass, produced during acidic alteration of mafic sand. These deposits potentially represent a new type of alteration byproduct on Mars, and their extent over millions of square km in the northern lowlands likely implies that the source of the acidic fluids was melt from regional ice sheets or snow packs. The major results presented in Chapter 4 are currently under consideration by *Nature Geoscience* (Horgan and Bell, submitted).

Chapter 5 synthesizes these results, discusses their implications for the geologic history of the north polar region and Mars in general, and provides a discussion of future applications of the techniques developed in this work.

CHAPTER 2

THE DISTRIBUTION OF HYDRATED MINERALS IN THE NORTH POLAR REGION OF MARS[1]

0. Abstract

The previous discovery of extensive deposits of hydrated minerals in Olympia Planum in the north polar region of Mars by the Mars Express OMEGA instrument raises important questions about the origin and subsequent redistribution of these hydrated minerals. Here we present a new map of the distribution of hydrated minerals within the north polar region of Mars, by applying both standard and new spectral analysis techniques to near-infrared spectral data from OMEGA. Our results are in agreement with the previous OMEGA observations, but also show more extensive detections of hydrated minerals throughout the circum-polar plains, as well as new detections of hydrated minerals on the surface of Planum Boreum and within the polar troughs. We find that while the circum-polar plains hydration signatures appear to be correlated with the dark dunes of the north polar erg, hydration signatures in Planum Boreum instead appear to be correlated with the north polar veneers and their sources within the polar layered deposits. By applying laboratory-derived empirical models of the dependence of gypsum spectra on grain size and abundance, we provide approximate abundance estimates for the hydrated minerals we have identified in OMEGA and CRISM data. We find that the presence of hydrated minerals throughout the north polar region suggests: (1) a complex cycle of sediment exchange between the Olympia Planum dunes and the other polar units; (2) an earlier

[1] Reproduced by permission of the American Geophysical Union. Full citation: Horgan, B.H., J.F. Bell III, E.Z. Noe Dobrea, E.A. Cloutis, D.T. Bailey, M.A. Craig, L.H. Roach, J.F. Mustard. Distribution of hydrated minerals in the north polar region of Mars. *J. Geophys. Res., 114*, doi:10.1029/2008JE003187, 2009. Copyright 2009, American Geophysical Union.

origin for the hydrated minerals than originally postulated; and (3) the occurrence of significant water activity in this region during the Amazonian.

1. Introduction

The north polar region of Mars is situated at the lowest elevation within a basin that encompasses much of the northern hemisphere, making it an ideal place for the potential deposition of outflow channel fluids and sediments (Fishbaugh and Head, 2000; Tanaka, 2005; Tanaka *et al.*, 2008). Today, dark-toned sedimentary structures dominate the non-ice regional geology. Dark-toned sediments make up the large, aeolian dune fields and sand sheets in the circumpolar plains (the north polar ergs) between about 75°N and 85°N (Figure 1.1; Tsoar *et al.*, 1979; Thomas and Weitz, 1989; Lancaster and Greeley, 1990), while on Planum Boreum, dark-toned sediments are present within the polar layered deposits and on the surface as water-ice free, low albedo surfaces, classified as the north polar veneers (*e.g.* Rodriguez *et al*., 2007; Tanaka, 2005; Malin and Edgett, 2001). Evidence in the region for large, aqueous outflows from the ice cap (Fishbaugh and Head, 2002), volatile-driven resurfacing (Tanaka *et al.,* 2003; Wyatt *et al.*, 2004), and water-equivalent hydrogen contents of the subsurface in excess of 30% by mass (Feldman *et al.*, 2004) suggest that, in addition to aeolian processes, surface or ground water may have played a role in the formation and modification of these deposits. Consequently, the composition, morphology, and current physical state of the dark-toned sedimentary deposits may give insight into surface deposition and modification processes in the north polar region, throughout, or even prior to, the Amazonian.

Results from the Mars Express spacecraft's Observatoire pour la Minéralogie, l'Eau, les Glaces et l'Activité (MEx/OMEGA) near-IR imaging spectrometer investigation (Bibring *et al.*, 2004) have indicated the presence of extended deposits of

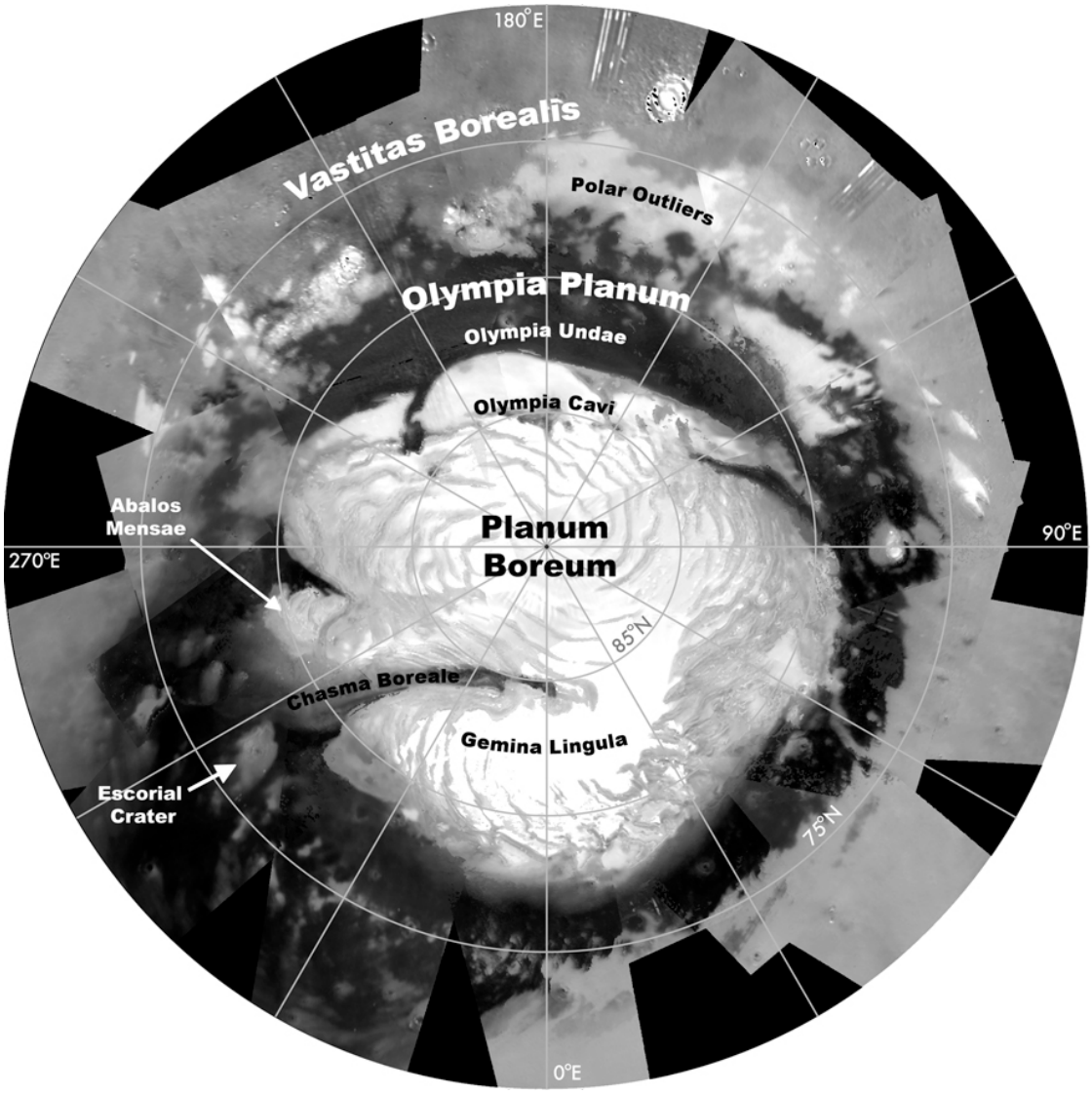

Figure 2.1: OMEGA 0.9-1.1 μm average estimated Lambert albedo mosaic of the 45 early northern summer image cubes used in our study (Table 2.1), stretched between 0.1 and 0.6. Geographic names mentioned in text are indicated.

hydrated calcium sulfates in the Olympia Planum region (Langevin *et al.*, 2005a), possibly implying an important role for surface or near-surface water in the alteration of the dune materials. Langevin *et al.* (2005a) proposed that the observed hydrated calcium sulfates are gypsum ($CaSO_4 \bullet 2H_2O$), based on comparison with spectra taken by OMEGA during ground-calibration. Gypsum can be formed in a variety of environments, but in general, gypsum formation requires a source of sulfur and H_2O (in the liquid or gas phase) interacting with Ca-bearing minerals. Langevin *et al.* (2005a) further suggested that the water necessary to form gypsum was most likely present in or near Olympia Planum due to outflows from the ice cap during a warm climate excursion, but did not propose a source for sulfur-rich material. Fishbaugh *et al.* (2007) reported that although the gypsum deposit is nearly exclusively associated with the dark dunes, there were no apparent correlations between the presence of gypsum and the physical or thermal characteristics of the dune field in the THEMIS data included in their study. Those authors proposed that the water necessary for gypsum formation emanated from the ice cap during a purported Chasma Boreale melting event (Fishbaugh *et al*., 2002) or during an impact melting event in the region near the highest gypsum concentrations. Alternatively, Tanaka (2006) and Tanaka *et al*. (2008) argued that there is no clear geologic evidence for polar outflows during the Amazonian. Instead, they proposed that the Scandia geologic unit may consist of volcanic or hydrothermal deposits, and that the gypsum may be sourced directly from this older (Early Amazonian) unit. Indeed, deposition of large quantities of sulfates since the emplacement of the young (Late Amazonian), transient dune fields does not easily fit within the OMEGA global hypothesis of sulfate deposition during the Hesperian (Bibring *et al*., 2006).

In this study, we examine hydration in the entire north polar region to establish a regional context for the Olympia Planum sulfates, to test the proposed OMEGA

global mineralogic history in the region, and to propose additional or alternate hypotheses to explain the observed mineral distributions and their geologic/stratigraphic context. If the sulfates are limited to Olympia Planum, then they may be intimately related to the dunes and much younger than sulfate deposits elsewhere on Mars; alternately, hydrated minerals associated with older deposits elsewhere in the region may suggest less recent water activity in the region and a possible source for the gypsum from older deposits.

This mapping effort differs from previous OMEGA and Mars Reconnaissance Orbiter Compact Reconnaissance Imaging Spectrometer (MRO/CRISM) mapping efforts (Langevin *et al*., 2005a; Roach *et al*., 2007; Pelkey *et al*., 2007) because we have developed a technique (described in Section 4.2) that allows us to search for hydrated minerals in water ice-rich areas, which previously have not been examined. By using this new technique, we have been able to verify the OMEGA sulfate detection as well as to expand on the OMEGA results with a more detailed search for other hydrated deposits in the region. In addition, our ongoing laboratory studies of potential mineralogies for the hydrated deposits, using newly-available laboratory sulfate mineral spectra (*e.g.,* Cloutis *et al.*, 2006), have allowed us to provide a new assessment of the abundance of hydrated minerals in the region.

In this study, we have employed a range of data sets in addition to the OMEGA spectral data to analyze the distribution of hydrated minerals, including geologic and morphologic maps of the north polar region (Tanaka *et al*., 2008; Tanaka, 2005; Rodriguez *et al*., 2007; Tanaka and Hayward, 2008) high resolution spectral data from CRISM, altimetry data from the Mars Global Surveyor Mars Orbiter Laser Altimeter (MGS/MOLA; Zuber *et al.*, 1992, Smith *et al.*, 2001), and visible-wavelength images from the MRO Context Camera (CTX; Malin *et al*., 2007), the MRO High Resolution Imaging Science Experiment (HiRISE; McEwen, *et al.*

2007), and the Mars Odyssey orbiter's Thermal Emission Imaging System (ODY/THEMIS; Christensen *et al.*, 2004a).

In the next section, we provide an overview of the geologic units and features of the north polar region, with an emphasis on Olympia Planum. In Section 3, we describe the compositional properties of Olympia Planum, provide a background on terrestrial gypsum deposition, and describe previous hypotheses for deposition of the Olympia Planum gypsum. Section 4 details the methods we used to verify the OMEGA sulfate detection and to produce a new map of the distribution of hydrated minerals, and Section 5 presents our spectral maps as well as correlations between our maps and other datasets. Section 6 describes our efforts to model the abundances of gypsum in both CRISM and OMEGA observations using laboratory data, and Section 7 presents our interpretations of our findings in the context of the regional geologic history.

2. Regional Geologic Units

The north polar region of Mars exhibits a complex and dynamic geologic history that extends through the Amazonian. In this section, we provide an overview of previous work on the regional geologic units, with an emphasis on the history and current state of the north polar erg.

2.1 Pre-MGS geologic interpretations

The smoother surfaces and lower crater densities as compared to the southern highlands observed in the northern basin since Mariner 9 has suggested that the northern basin was resurfaced at some point in martian history (*e.g.*, Scott and Carr, 1978), but what processes did the resurfacing and when it happened has only become apparent in more recent mapping efforts.

The availability of higher resolution images and other data sets has steadily decreased the apparent age of the north polar basin materials from the Noachian-Hesperian ages interpreted from Mariner 9 data (Scott and Carr, 1978), to the Hesperian-Amazonian ages interpreted from Viking data, (Dial, 1984; Scott and Tanaka, 1987), and more recently, to the exclusively Amazonian ages interpreted from MGS and ODY data (Tanaka *et al*., 2003, 2008; Tanaka, 2005). The inferred source and nature of the materials has also changed dramatically. During the Viking era, the materials filling the northern basin, or the Vastitas Borealis Formation (VBF), were interpreted as Hesperian volcanic flows with varying degrees of degradation (*e.g.*, Scott and Tanaka, 1987). With higher resolution images from MGS and ODY, the VBF is currently interpreted largely as Late Hesperian outflow sediments that have been extensively reworked by periglacial processes since the Early Amazonian (*e.g.*, Tanaka *et al*., 2005).

2.2 Recent geologic interpretations

According to recent geologic mapping (Tanaka, 2005; Tanaka *et al.*, 2008), the geology of the north polar region can be described by distinct units separated in time and space, as shown in Figure 2.2. In the plains, the Vastitas Borealis interior and Scandia region units have been mapped as having been emplaced during the Early Amazonian by sediments from catastrophic outflows originating at lower latitudes, and reworking of those sediments by phreatic processes such as mud volcanism. The Rupes Tenuis unit is superposed unconformably on top of the plains units, and is interpreted to have most likely formed by redeposition of sediment from the previously much more extensive Scandia unit. The Rupes Tenuis unit makes up the terrace-forming, stratigraphically lowest section of the layers previously classified as the polar basal unit (Edgett *et al*., 2003; Fishbaugh *et al*., 2005), and has a maximum

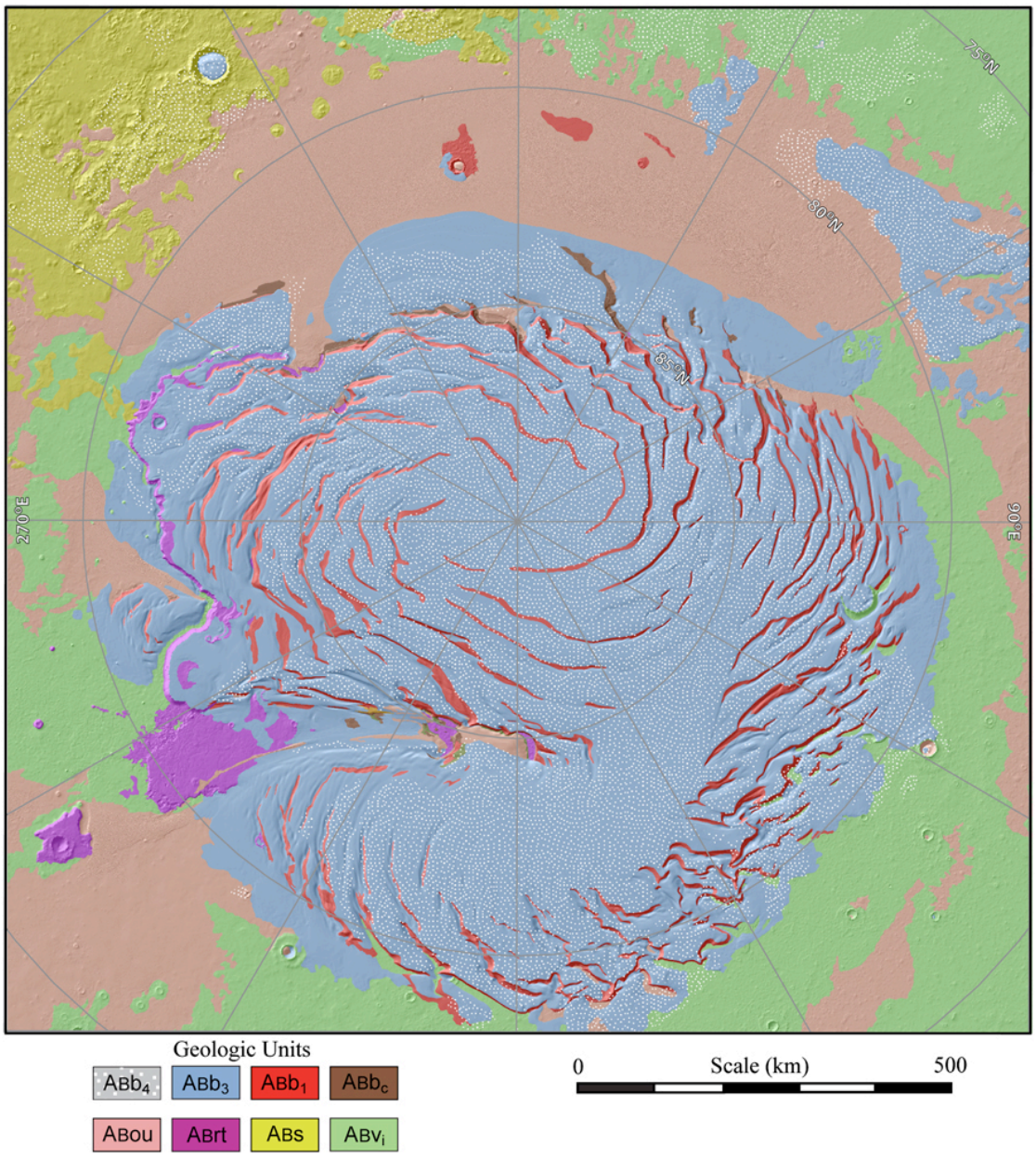

Figure 2.2: Geologic map of the north polar region, after Tanaka *et al*. (2008). Units indicated in legend and in text are the Planum Boreum units 1-4 (ABb_{1-4}), Planum Boreum cavi unit (ABb_c), Olympia Undae unit (ABou), Rupes Tenuis unt (ABrt), Scandia region unit (ABs), and Vastitas Borealis interior unit (ABv_i).

observed thickness of ~1300 m (Tanaka *et al.*, 2008). An extended period of erosion during the Middle Amazonian may have considerably reduced the size of the Rupes Tenuis unit, which, in the plains, may have left behind impact-cemented plateaus such as those exposed at the mouth of Chasma Boreale and in the nearby Escorial pedestal crater plateau (Tanaka *et al.*, 2008).

Tanaka *et al*. (2008) have classified the upper section of the basal unit as the Planum Boreum cavi unit, which formed from many episodes of sand deposition, and has been described as a paleo-erg deposit (Byrne and Murray, 2002; Fishbaugh and Head, 2000, 2001, 2005; Tanaka, 2005). Major geologic evidence for the paleo-erg includes the cross-bedded nature of the Planum Boreum cavi unit and the unit's tendency to be thickest in depressions in the Rupes Tenuis unit (Tanaka *et al.*, 2008). Additionally, the Planum Boreum cavi unit appears to make up the bulk of the topography of Olympia Planum, which suggests that Olympia Planum may have a long history of aeolian activity.

The Planum Boreum 1 unit, which makes up the bulk of the lower polar layered deposits, unconformably overlies the Planum Boreum cavi unit, and exhibits up to ~1500 m of even, fine layering, most likely composed of airfall deposits (Blasius *et al*., 1982; Fishbaugh and Head, 2005; Malin and Edgett, 2001; Milkovich and Head, 2005, 2006; Tanaka, 2005; Tanaka *et al*., 2008). The emplacement of the Planum Boreum 1 unit was followed by another extensive period of erosion, during which katabatic winds may have first carved the spiral troughs that are now being exposed throughout Planum Boreum, potentially by similar processes (Tanaka *et al.*, 2008).

Following the period of erosion, the troughs were subsequently filled in by ~100 m of dark sediments that now comprise the Planum Boreum 2 unit (Rodriguez *et al*., 2007; Tanaka *et al*., 2008). The Planum Boreum 2 unit makes up the lowest portion of the upper layered deposits or "banded terrain" (Howard *et al*., 1982;

Tanaka, 2005), and appears to be comprised of ice-free sand and dust, which is mobilized to form the extensive low-albedo surfaces that mantle much of the periphery of Planum Boreum (Figure 2.1; Rodriguez *et al*., 2007). The low albedo surfaces are thick enough to obscure or partially obscure the spectral signature of the water ice below, but not to obscure the underlying morphology, leading Rodriguez *et al*. (2007) to classify these low albedo deposits as "veneers." The veneers are associated with grooves and striations in the residual cap, implying a highly mobile and abrasive particle component, and exhibit variations in albedo indicative of multiple episodes of formation. The older, lighter toned veneers may be indurated by water ice or hydrated minerals. Rodriguez *et al*. (2007) also speculate that the dark layers within the Planum Boreum 1 and 3 units may be remnants of paleo-veneers.

The uppermost units of Planum Boreum are the shallow, but extensive, Planum Boreum 3 and 4 units. The Planum Boreum 3 unit makes up the bulk of the upper layered deposits mapped by Tanaka (2005), covers all Planum Boreum surfaces except for equatorward trough walls and trough floors, and is also found mantling dunes around the periphery of Planum Boreum. Additionally, HiRISE images have shown the Planum Boreum 3 unit present as bright deposits in interdune areas in Olympia Planum (Roach *et al.*, 2007). The Planum Boreum 4 unit is composed of the young, bright residual ice cap on Planum Boreum and the polar outliers, and exhibits high surface water ice concentrations in OMEGA and initial CRISM studies (Langevin *et al*., 2005b; Seelos *et al*., 2007).

2.3 Olympia Planum and the circum-polar erg

The Olympia Planum erg (Olympia Undae) is the largest aeolian accumulation on Mars, with a surface area of 4.7 x 10^6 km^2 (Lancaster and Greeley, 1990). For scale, this is slightly larger than the state of California, and 150% larger than the Rub

al Khali, Saudi Arabia, the largest active erg on Earth (Tsoar *et al*., 1979). As shown in Figure 2.1, Olympia Undae extends in latitude from 80°N to 85°N, and follows the edge of the residual water ice cap from 140°E to 240°E, with an 800 m topographic high above the adjacent plains near 180°E (Tanaka, 2005; Tanaka *et al.*, 2008). The remainder of the circum-polar erg and associated sand sheets encircle the rest of Planum Boreum (*e.g*, Tanaka and Hayward, 2008), and while the sand sheets exhibit a marked albedo difference compared to the underlying plains (Figure 2.1), they may only be a few grains thick in many areas (Tanaka *et al*., 2008).

Using terrestrial relationships between dune spacing and sediment volume, Lancaster and Greeley (1990) estimated the volume of sediment contained in Olympia Undae at around 900 km^3, compared to approximately 1150 km^3 in the entire circum-polar erg. Using MOLA data, Zuber *et al.* (1998) estimated the volume of sediment in the circum-polar erg to be approximately 10,000 ± 3,000 km^3, although it is unclear what criteria were used to determine dune coverage or individual dune volume in that study. More recently, Hayward *et al*. (2008), in initial mapping of the dune density throughout the north polar region using THEMIS, MOC, and CTX images, have found 835,000 km^2 of terrain with some type of dune coverage. As shown by Tanaka and Hayward (2008), dune density decreases with distance from Olympia Planum and Chasma Boreale.

Previous workers have proposed that the current source of the dark dune material in Olympia Undae is the lower, platy unit of the polar layered deposits or basal unit (Thomas and Weitz, 1989; Byrne and Murray, 2002; Fishbaugh and Head, 2005). In recent geologic mapping, the current source unit has been identified as the Planum Boreum cavi unit, the stratigraphically oldest Planum Boreum unit characterized by alternating layers of cross-bedded, unconsolidated, dark-toned, dune forming materials and light-toned boulder forming materials (Tanaka *et al*., 2008).

Although the dunes appear to be actively sourced from this unit today, the Olympia Undae unit has most likely formed episodically throughout the Amazonian, and may have originally formed as a result of the erosion of the Rupes Tenuis and Scandia region units (Tanaka *et al*., 2008).

Much of the Olympia Undae unit appears to be stabilized, as indicated by mantling of many dune fields by the Planum Boreum 3 unit and the north polar veneers (Section 5.4; Tanaka, 2005; Tanaka *et al*., 2008), as well as by the presence of induration features on dunes, including surface cracks, absence of dry grain flow on avalanche faces, avalanche remnants in interdune areas (Feldman *et al*., 2008), slumps, yardangs, craters, thick dust coverings, and avalanche chutes (Schatz *et al*., 2006). In addition, many of the dunes exhibit muted forms, and have not been observed to move (on the scale of meters) in the 30 years between Viking and MOC observations (Schatz *et al*., 2006). Feldman *et al*. (2008) have suggested, based on modeling of Mars Odyssey Neutron Spectrometer (MONS) data, that the dunes have water ice-rich cores, overlain by a mobile layer on the order of ~10 cm thick. The water ice-rich cores may be similar to terrestrial niveo-aeolian deposits, which are composed of interbedded sand, dust, and water ice or snow, are more resistant to erosion than ice-free dunes, and would account for the overall lack of movement and muted forms. However, it must be noted that even spatially deconvolved MONS data has a 300 km footprint (Feldman *et al*., 2008), so it is unclear how input from Planum Boreum and the surrounding terrains would affect models of the water ice content of Olympia Undae.

Exceptions to the overall stabilized nature of the dune fields include dunes that are associated with dark, down-wind streaks, possibly indicative of recent sand movement (Tanaka *et al*., 2008), and two dunes that have been observed to shrink and disappear over ~3 years of MOC observations (Bourke *et al*., 2008).

3. The composition of Olympia Undae

The dunes of Olympia Undae exhibit the strongest and most areally extensive hydrated sulfate signature yet seen on Mars (*e.g.* Poulet *et al*., 2007). In this section, we review the initial sulfate detection by OMEGA and CRISM, the previously proposed gypsum deposition mechanisms, and proposed mafic mineralogies for the dunes.

3.1 Olympia Undae sulfates

Langevin *et al*. (2005a) first announced the unambiguous detection of hydrated Ca-sulfates in Olympia Undae, by the observation of a strong absorption band at 1.9 μm, indicating hydration, accompanied by several less pronounced bands between 1.0 and 2.5 μm diagnostic of Ca-sulfates, interpreted to be indicative of gypsum. Mapping the band depth of the 1.9 μm feature throughout the north polar region revealed that the signature was largely restricted to the dunes, with the largest band depth located near the eastern margin of Olympia Undae, near 80.2°N, 244.5°E (Langevin *et al*., 2005a). Fishbaugh *et al.* (2007) expanded on the initial OMEGA detection by presenting several regions with putative gypsum signatures outside the main dune field, including a region beyond the eastern dune margin, as well as a localized region on the floor of Chasma Boreale. Fishbaugh *et al*. (2007) also identified a lack of hydrated mineral signatures in the exposed unit between Planum Boreum and Olympia Undae, which they interpreted as indicating that the gypsum is not sourced from the Planum Boreum units.

Fishbaugh *et al*. (2007) modeled the bulk composition of the sulfate-rich dunes as a mixture of gypsum grains and an unknown dark, spectrally featureless (DSF) material. An intimate mixture model of the two components yielded a best fit to the OMEGA data for 55% DSF with a grain size of a few tens of μm mixed with 45%

gypsum with grain sizes between 100 μm and 1 mm. A better fit was found using an intramixture model, where oxide grains are housed as inclusions in larger gypsum grains. The model yielded a best fit with 35% pure gypsum grains with particle sizes of a few tens of μm and 65% mm-sized gypsum grains contaminated with DSF inclusions. Fishbaugh *et al*. (2007) favored the latter model because of the ability of the DSF inclusions to mask the high albedo of the gypsum grains, as well as to mask the large band depth that a nearly pure, coarse-grained gypsum dune would exhibit (*e.g.,* Cloutis *et al.,* 2006). The models did not include any specifically basaltic materials.

The north polar region was a primary target for initial MRO observations after the spacecraft arrived in mid northern summer. In total, 6 targeted CRISM observations were located in Olympa Undae, with the goal of characterizing the distribution of gypsum within the dunes (Roach *et al*., 2007). Initial results indicate that CRISM data appear to confirm the gypsum detection, and show high gypsum band depths along the crests of dunes in the gypsum-rich area (Section 6.1), which, when considered with the apparent aeolian distribution of the gypsum westward in Olympia Undae, suggests a dynamic process controlling the gypsum distribution (Roach *et al*., 2007).

3.2 Gypsum deposition mechanisms and properties

Three principal solid phases occur in the calcium sulfate – water system: $CaSO_4 \bullet 2H_2O$ (gypsum), $CaSO_4 \bullet$ 0.5 H_2O (bassanite), and $CaSO_4$ (anhydrite) (*e.g.,* Deer *et al*, 1992). Of these three, only gypsum and anhydrite are stable phases; however, anhydrite is only dominant in water above 44°C on Earth at standard pressure and neutral pH, although the stability temperature decreases as pressure increases (Deer *et al*, 1992; Holland and Malinin, 1979). With the exception of

environments involving such high temperature waters, anhydrite is generally considered to be a secondary mineral assemblage to gypsum, although re-forming gypsum through hydration of anhydrite is possible (Deer *et al*., 1992).

As a dry solid, gypsum is stable up to temperatures of 70°C at standard pressure, at which point bassanite is generated. Above 200°C, anhydrite is generated (Deer *et al*, 1992; Holland and Malinin, 1979). Gypsum is not stable under burial of more than a few hundred meters, at which point anhydrite is generated, with a volume loss of ~50% (Schreiber and El Tabakh, 2000). Solid gypsum also dehydrates to anhydrite when exposed to high salinity solutions (Deer *et al*., 1992).

Gypsum has been shown to be stable at martian surface pressures for periods of a few months, based on spectral analysis (Cloutis *et al*., 2007). This result can most likely be expanded to much longer timescales, as the structural integrity of gypsum is dependent on the presence of H_2O, and would require either extreme pressure excursions (down to a few Pa) or modest thermal input to dehydrate, as discussed above (Cloutis *et al*., 2007).

On Earth, gypsum is the most common sulfate mineral, and is most often associated with shallow and deep marine precipitate deposits as well as coastal (sabkha or salina) and continental (playa) evaporite deposits (Schreiber and El Tabakh, 2000; Warren, 1982). Typical sea water contains approximately 0.15% dissolved $CaSO_4$, which equals about 1.7 cm precipitated gypsum per 100 m of evaporated seawater (Deer *et al*., 1992; Holland and Malinin, 1979). Gypsum is generally the second mineral to precipitate from evaporating seawater, after calcite (Spencer, 2000; Holland and Malinin, 1979); however, highly acidic conditions that are plausible to have occurred on Mars may have inhibited carbonate deposition (*e.g.*, Catling, 1999; Fishbaugh *et al*., 2007). In shallow marine environments, gypsum is most often deposited as crusts and clusters, while in deep marine environments,

gypsum is most often deposited as fine grained beds, known as alabaster gypsum (Schreiber and El Tabakh, 2000).

In salinas and playas, gypsum is present as (1) gypsite, a fine grained (<60 μm) gypsum crust dissolved and re-deposited by rain, (2) gypsarenite, sand-sized (60μm-1mm) gypsum crystals deposited in unstable or periodic salinity environments, and (3) selenite, large (>2mm) and often twinned gypsum crystals deposited below the water table in a continuously subaqueous environment (*e.g.*, Warren, 1982). Gypsum may also occur as a continental evaporite when it is dissolved in and transported by percolating groundwater, which is pulled to the surface by capillary action, depositing gypsarenite, selenite, and anhydrite crystals as the water evaporates (Deer *et al*., 1992; Langford, 2003).

Gypsum may also be formed without the presence of surface water. Sulfuric acid solutions moving through Ca-rich rocks may result in gypsum and anhydrite deposition. Such waters are often either created by volcanic gases interacting with meteoric water or by weathering of sulfides (Deer *et al*., 1992; Holland and Malinin, 1979). Ferric sulfate formation via weathering of sulfides has been shown to be plausible on Mars, based on mineral assemblages at the Viking landing sites (*e.g.*, Burns, 1987,1988; Burns and Fisher, 1990, 1993). Likewise, gypsum and anhydrite rich mineral assemblages are often produced by the action of sulfurous volcanic vapors on Ca-rich rocks (*e.g*. Golden *et al*., 2005). These assemblages are commonly found in fumarole deposits (*e.g.* Stoiber and Rose, 1974). Finally, gypsum can also be produced by sulfurous fog acting on Ca-rich materials (*e.g.* Eckardt and Schemenauer, 1998; Golden *et al*., 2005).

Gypsum is an especially weak mineral (hardness ~2; Deer *et al*., 1992), and likely would not survive for long as intact grains under the high saltation velocities that are postulated to occur on Mars (*e.g.* Sagan *et al*., 1977). Even under the much

slower saltation velocities of Earth, gypsum sand at the White Sands dune field, NM has been observed to decrease in grain size with distance from the gypsum source (Fryberger, 2002; Ghrefat *et al*., 2007). This may imply that the gypsum source region must be near the highest concentration of gypsum in eastern Olympia Planum (Fishbaugh *et al*., 2007).

3.3 Gypsum deposition hypotheses

Langevin *et al*. (2005a) initially proposed a suite of gypsum deposition mechanisms, including (a) atmospheric weathering of iron sulfides, (b) the interaction of Ca-rich rocks with acidic snow during a period of extensive volcanic activity, (c) sulfate-rich groundwater sourced from basal melting of Planum Boreum, or (d) hypersaline, sulfate-rich surface water sourced from polar outflows.

Fishbaugh *et al*. (2007) evaluated several possible water-related gypsum deposition mechanisms and supported the hypothesis for gypsum deposition via the direct interaction of hypersaline, sulfate-rich surface water from a polar outflow. They proposed that the sulfur-rich outflow emanated from Chasma Boreale and traveled hundreds of kilometers through channels running along the base of Planum Boreum to a putative gypsum source area that today is ringed by dunes with a minor gypsum component. However, the channels identified in MOLA topography have alternately been interpreted as the result of erosion by katabatic winds off of Planum Boreum (Warner and Farmer, 2007). Additionally, outflows from Planum Boreum would most likely be directed into the large basin to the south of Hyperborea Lingula, which in turn would have been dissected by such flood events occurring during the Amazonian, which is not observed (Tanaka, 2006).

Alternatively, Tanaka (2006) proposed that the sulfate deposit is not Late Amazonian in origin, but is rather considerably older than the dunes. In this

hypothesis, the sulfates were originally generated by volcanically-introduced sulfur and hydrothermal alteration of Ca-bearing volcanic rocks in the Scandia region and extending north to Olympia Planitia, due to magmatic intrusions propagating from Alba Patera during the Early Amazonian. The dunes of Olympia Undae would not have been involved in the deposition of the sulfates in this model, but rather would have exposed the sulfates from the substrate via aeolian excavation (Tanaka, 2006; Tanaka *et al*., 2008). This hypothesis is supported by the presence of features suggestive of mud volcanism, pingo-like extrusions, and phreatic or cryo-clastic eruptions in the Scandia unit (Tanaka *et al*., 2003, 2005).

One of the most puzzling aspects of the question of deposition mechanisms for the sulfate deposit is the timing of deposition. Based on OMEGA and Mars Express High Resolution Stereo Camera (HRSC) observations, the most widespread period of sulfate genesis in and around the Valles Marineris region may have been during the early- to mid-Hesperian (Bibring *et al*., 2006). If the Olympia Planitia gypsum was created by the interaction of some form of H_2O with the Olympia Undae dunes, and the dunes are in fact Amazonian in age, then the north polar sulfate deposit does not correlate with the putative ages of sulfate deposits elsewhere. However, if the dunes are not involved in the genesis of the sulfates, and instead the sulfates are sourced from a much older unit, then this aspect of the geologic history of the north polar region may be more consistent with the Bibring *et al.* (2006) interpretation of the geologic history of Mars and the Tanaka (2006) hypothesis for gypsum exhumation.

3.4 Olympia Undae ferrous materials

Aeolian bedforms on Mars are dominantly composed of dark sand grains, which are basaltic in composition based on remote sensing and *in situ* observations (*e.g.,* Bell *et al.,* 2004; Bibring *et al.,* 2005; Christensen *et al.,* 2000, 2004b; Gellert *et*

al., 2004; Morris *et al.,* 2006; Rogers and Aharonson, 2008). Previous workers have classified the Olympia Undae dunes as the lowest albedo and lowest thermal inertia dune field on the planet (Thomas and Weitz, 1989; Herkenhoff and Vasavada, 1999), possibly implying that the erg has undergone unique processes and has a distinct composition as compared to other martian dune fields.

Bell *et al.* (1997) identified a strong 953 nm absorption restricted to the circum-polar dark deposits in near-infrared Hubble Space Telescope (HST) multi-spectral images of the north polar region, implying a strong mafic component to the dunes, most likely a pyroxene. Initial analysis of TES observations by Noe Dobrea and Bell (2001) also suggested a strong pyroxene component to the dunes. OMEGA observations have suggested minor amounts of pyroxene in Olympia Planum (Fishbaugh *et al.*, 2007); however, these detections are largely confined to localized areas outside the main dune field.

Olympia Undae has since been identified as one of the strongest TES surface type 2 (ST2; Wyatt *et al*., 2004) signatures on the planet (Ruff and Christensen, 2007). TES ST2 may be a primary volcanic lithology or an alteration product, possibly in the form of a rind. Wyatt *et al*. (2007) have suggested that the differences between the elemental chemistry implied by deeper-probing Mars Odyssey Gamma Ray Spectrometer data and the TES observations in the northern plains implies that the TES ST2 is a surface coating. Although the exact mineralogy of TES ST2 is still in question, intermediate plagioclase and/or a high silica amorphous phase are strong candidates (Ruff and Christensen, 2007).

4. Methods

4.1 Data Calibration and Reduction

Tools designed by the OMEGA team for basic calibration of OMEGA data are available on the European Space Agency's Planetary Science Archive website (http://www.rssd.esa.int/index.php?project=PSA). We have used the SOFT03 package, released in October 2005. This package contains IDL programs for extracting raw data, calibrated (I/F) data, and associated calibration information (Bellucci *et al*., 2006). We have developed in-house tools for sorting candidate image cubes, removing bad spectels (spectral pixels), removing the solar and atmospheric spectral contributions, creating mapped polar mosaics, and calculating band depth, as discussed below.

A recurrent problem in the majority of these image cubes is the presence of planes of bad pixels 15 pixels wide in the horizontal spatial coordinate, between columns 81 and 96. The bad pixels are either saturated or null, and are confined to alternating pixels in the vertical spatial direction in a fairly consistent pattern ("electronic error," Bellucci *et al*., 2006). For the sake of continuity in our final mosaic, we have removed the bad pixels by replacing each bad pixel with the average of pixels above and below at every wavelength, producing a relatively seamless image without significant spectral errors.

To compensate for atmospheric absorption, we have employed an atmospheric absorption model based on the model created by the OMEGA team (Langevin *et al*., 2005a; Noe Dobrea *et al*., in prep.). In this model, the opacity of the atmosphere between 1.1 and 2.5 μm was empirically derived from the ratio of OMEGA spectra of high and low elevation regions on Olympus Mons (20.9 km and -2.8 km altitude above the ellipsoid), specifically from image ORB0479_5. The atmospheric spectrum for each pixel was then derived by modeling the surface spectrum between 1.954 and

2.010 μm (within the strong CO_2 bands) as a function of the atmospheric opacity and applying the derived model to the rest of the spectrum. Because the 2 μm CO_2 bands vary with atmospheric pressure, the model accounts for elevation changes (Langevin *et al*., 2005a; Noe Dobrea *et al*., in prep.). Unfortunately, atmospheric spectra created using this method do not accurately model the strong upper atmospheric "hot bands" centered at 1.911 μm and 2.177 μm, as the bands are removed in the ratio. Fortunately, these bands are narrow enough that they only strongly affect one spectel, and we remove them by interpolating across each spectel.

We have applied this model to the OMEGA spectra taken with the short wavelength infrared channel (SWIR), which includes our wavelengths of interest between 0.93 and 2.5 μm. We have assumed that atmospheric gas opacity has had little effect on spectra taken with the visible and near-infrared channel (VNIR), which includes wavelengths between 0.38 and 1.05 μm, and have not applied a correction to the spectra in that range. Because the spectra overlap at 1.1 μm, we have combined the two spectral ranges by scaling non-atmospherically corrected VNIR spectra to match the value of the atmospherically corrected SWIR spectra at 1.1 μm.

To correct for viewing angle and obtain an estimate of the surface albedo, we have applied a Lambertian phase function correction to the OMEGA data by dividing the spectra by the cosine of the incidence angle for each pixel. Although a Lambertian correction may not be the most appropriate or rigorous treatment for the surface phase function (*e.g.* Soderblom *et al*., 2006; Bell *et al.,* 2008), it is the simplest solution to implement, given the uncertainties in the derivation of viewing angles for each pixel and our lack of understanding of the photometric properties of the variety of surfaces that we are observing in this region. Our mineralogic interpretations discussed below do not depend critically on the details of this photometric correction.

4.2 Spectral Mapping

The OMEGA image cubes that we have used in this study have resolutions between 1.5 and 5.4 km/pixel, lie north of 70°N, and are limited to L_S between 90° and 115°. We have chosen this time range in order to acquire data after the summer solstice (to minimize the presence of surface CO_2 and H_2O frost), but before the onset of the summer north polar hood (to minimize the presence of water ice clouds). Of these, we have chosen a subset of 45 OMEGA image cubes to map in the north polar region. These 45 were chosen for maximum coverage and quality of data (see Table 2.1 for properties of the image cubes).

To analyze these observations, we first mapped the 45 image cubes in a polar stereographic mosaic with a resolution of 1 km/pixel and a southern extent of 70°N. The resolution of the OMEGA image cubes varies from cube to cube as well as within each cube, so mapping the data to a constant resolution map requires interpolation of the lowest resolution data. As such, the resolution of our final mosaic and the maps produced from it is higher than that of many of the observations, which may be as low as 5 km/pixel (see Table 2.1). The amount of interpolation involved in mapping 5 km/pixel resolution data to a 1km/pixel resolution map could potentially cause artificial mixing of spectra at interfaces between spectrally distinct terrains. To decrease the amount of interpolation that occurs at interfaces between terrains with and without hydration signatures, our mapping method is biased toward images with higher hydration band depths (see Section 4.3), which means that our maps incorporate data with the least amount of mixing at interfaces. Boundaries between spectrally distinct terrains are accurate to within the original resolution of the data, on the order of 2 km in most cases.

Hydrated minerals are primarily identified by the presence of the 1.9 μm molecular H_2O overtone absorption band, and the depth of that band can be used as a

Table 2.1: Properties of images in our OMEGA spectral mosaic.

Image Cube	Center Lat. (°N)	Center Lon. (°E)	Max. Res.[a] (km/pixel)	Min. Res. (km/pixel)	L_s (°)
ORB1054_3	78.7	53.7	1.59	2.49	114.5
ORB1076_3	82.6	46.6	1.60	2.48	117.4
ORB1047_3	77.7	25.7	1.60	2.49	113.6
ORB1072_3	81.9	81.9	1.60	2.49	116.8
ORB1043_3	77.3	62.6	1.60	2.49	113.1
ORB1007_3	71.0	4.0	1.60	2.49	108.5
ORB1069_3	81.5	19.6	1.60	2.49	116.4
ORB1070_3	81.3	276.1	1.60	2.49	116.6
ORB1029_3	74.7	357.4	1.60	2.50	111.3
ORB1081_3	83.3	269.8	1.61	2.50	118.0
ORB1083_3	83.7	72.5	1.61	2.49	118.3
ORB1092_2	84.9	256.0	1.62	2.49	119.4
ORB0915_2	71.6	44.8	2.47	3.73	96.9
ORB0902_2	69.4	242.4	2.47	3.74	95.3
ORB1056_2	82.6	92.3	2.47	3.61	114.8
ORB0912_2	71.0	338.5	2.47	3.73	96.5
ORB0909_2	70.8	286.5	2.47	3.78	96.1
ORB1043_2	84.6	299.3	2.48	3.62	113.1
ORB1065_2	81.1	282.5	2.48	3.62	115.9
ORB1041_2	85.2	134.9	2.48	3.62	112.8
ORB1066_2	81.0	183.9	2.48	3.62	116.1
ORB1032_2	85.8	320.5	2.48	3.62	111.7
ORB0955_2	78.6	67.3	2.48	3.73	101.9
ORB1034_2	85.6	120.1	2.48	3.62	111.9
ORB1030_2	85.9	161.6	2.48	3.62	111.4
ORB0946_2	77.1	233.8	2.48	3.73	100.8
ORB1029_2	85.4	265.1	2.48	3.63	111.3
ORB1040_2	84.9	240.6	2.48	3.62	112.7
ORB0927_2	74.0	306.0	2.48	3.73	98.4
ORB0930_2	74.5	8.8	2.48	3.74	98.8
ORB1037_2	85.5	177.2	2.48	3.62	112.3
ORB0934_2	74.9	332.6	2.48	3.74	99.3
ORB0973_2	81.6	91.5	2.48	3.73	104.2
ORB1001_1	78.9	88.3	3.60	4.79	107.7
ORB1022_1	75.3	180.8	3.60	4.80	110.4
ORB1007_1	77.9	217.2	3.60	4.79	108.5
ORB1015_1	76.7	147.1	3.60	4.79	109.5
ORB1008_1	77.6	121.4	3.61	4.80	108.6
ORB0961_1	84.1	78.9	3.71	4.90	102.6
ORB0965_1	83.6	41.9	3.71	4.90	103.1
ORB0946_1	85.2	124.8	3.71	5.11	100.8
ORB0941_1	85.7	265.4	3.72	5.12	100.1
ORB0888_1	82.6	161.3	3.72	5.33	93.5
ORB0887_1	82.1	255.8	3.72	5.35	93.4
ORB0886_1	80.4	4.9	3.72	4.91	93.3

[a]Maximum Resolution. Resolutions calculated from SWIR telescope resolution (~1.2 mrad; Bibring *et al*., 2004) and slant distance from spacecraft to each pixel.

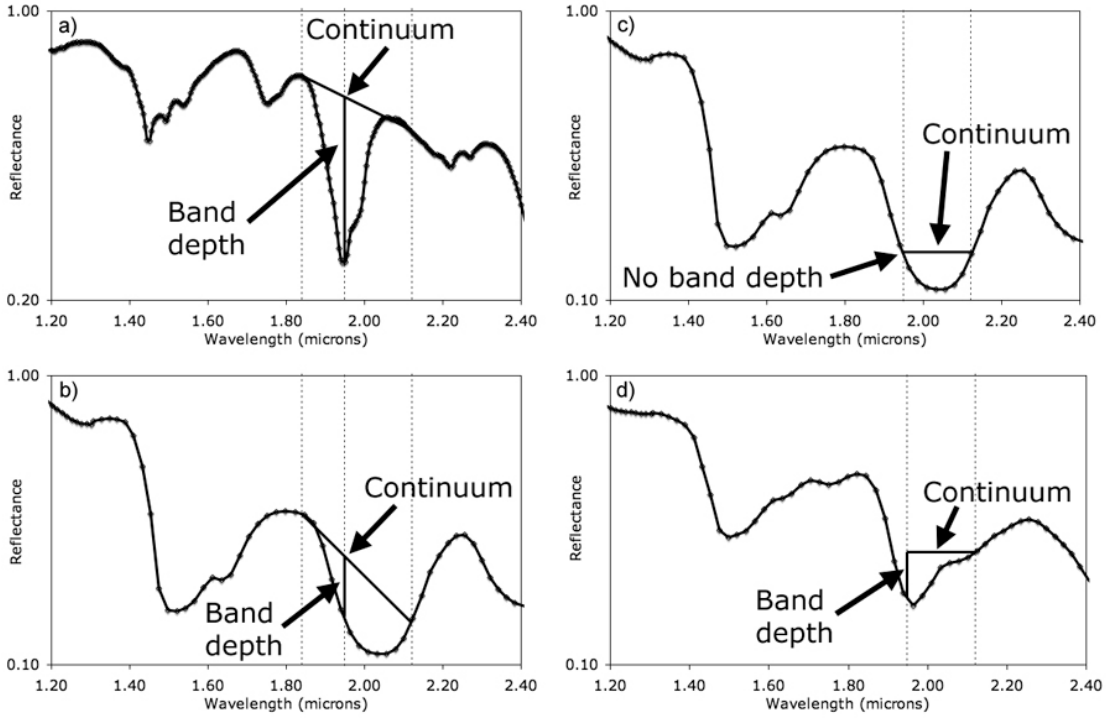

Figure 2.3: (*a* and *b*): Schematic evaluation of the 1.9 μm hydration band depth relative to the continuum value at 1.84 and 2.12 μm for (*a*) gypsum (Cloutis *et al*., 2006), yielding positive detection of the hydration band, and (*b*) water ice (Roush *et al*., 1990), yielding a positive band depth but ultimately a false detection of the hydration band. (*c* and *d*): Schematic evaluation of the 1.9 μm hydration band depth relative to symmetric wavelengths across the 2.03 μm ice band, near 2.1 μm for (*c*) water ice and (*d*) an equal linear mixture of water ice and gypsum.

proxy for mineral abundance (Hunt and Salisbury, 1970; Cloutis *et al*., 2006). The standard approach for evaluating the 1.9 μm hydration band depth is shown in Figure 2.3a, and is expressed by the following equation, where *R(x)* is the reflectance at wavelength *x*:

$$BD(1.934) = 1 - R(1.934) \Big/ \left(\left(\frac{R(2.122) - R(1.842)}{2.122 - 1.842} \right) (1.934 - 1.842) + R(1.842) \right) \qquad (1)$$

By fitting a linear continuum between a spectrum's values at 1.842 and 2.122 μm, the 1.934 μm band depth of that spectrum can be evaluated as the difference

between the spectrum and the continuum at that wavelength, expressed as a percentage (*e.g.*, Clark and Roush, 1984). The precise minimum of the 1.9 μm band is at 1.944 μm (Cloutis *et al*., 2006), so ideally, we should use the 1.941 μm OMEGA spectral channel; however, because atmospheric absorption is much less at 1.927 than at 1.941 (~2% vs. ~10%; Langevin *et al*., 2005a), we are averaging the 1.927 and 1.941 μm channels for a potentially less atmospheric-dependent band depth. This offset from the band center may slightly underestimate the band depth.

This approach yields deceptive results in areas with surface H_2O ice. Water ice has broad absorption bands at 1.5 and 2.0 μm, which vary strongly in depth as a function of water ice grain size (Clark, 1981). Because the 2 μm water ice band overlaps with the 1.9 μm hydration band, using the standard approach to identify the presence of a 1.9 μm hydration band yields a false positive in the presence of water ice, as shown in Figure 2.3b. The solution used in previous mapping efforts with OMEGA and CRISM data has been to exclude icy regions from the maps (Poulet *et al*., 2007; Pelkey *et al*., 2007). An alternate solution that we describe here exploits the symmetry of the 2 μm water ice band to provide a way to include even "water ice-contaminated" surface regions in our analysis.

For spectra that are water ice-rich, we search for the 1.9 μm hydration band by evaluating the percentage depth of the 1.9 μm value below the value of the wavelength on the opposite side of the water ice band, at 2.11 μm, as shown in Figure 2.3c, and as expressed in Equation 2:

$$BD(1.934) = 1 - \frac{CR(1.934)}{CR(2.108)} \qquad (2)$$

To compensate for the negative overall slope (and therefore slight asymmetry in the 2 μm water ice band) of the water ice-rich spectra in the presence of darker

materials (see Figure 2.3d), we use continuum-removed spectra for this step, represented as CR(wavelength) in Equation 2, where the continuum is defined between 1.84 and 2.2 μm (Poulet *et al*., 2007):

$$CR(x) = R(x) \Big/ \left(\left[\frac{R(2.205) - R(1.842)}{2.205 - 1.842} \right] (x - 1.842) + R(1.842) \right) \quad (3)$$

Because the water ice band is fairly symmetric at the spectral resolution of the OMEGA instrument, this gives us a good estimate of the hydration band depth. It must be noted that this method does not work when applied to a pure water ice spectrum, like that shown in Figure 2.3c, as there is no negative slope imposed across the water ice band without the presence of darker material. However, all martian spectra that we have examined have, at minimum, some amount of dust contamination, which imposes a slight asymmetry on the water ice band. Thus, we believe that using continuum removed spectra will indeed yield a more accurate 1.9 μm band depth.

We have parameterized the presence of the water ice spectral features by the band depth of the 1.5 μm water ice overtone absorption band. This band depth is determined by evaluating the depth of a spectrum at 1.5 μm below a continuum established at 1.3 and 1.7 μm, as shown below, where we have averaged all 3 points with neighboring wavelengths (Poulet *et al*., 2007):

$$BD(1.507) = 1 - R(1.507) \Big/ \left(\left(\frac{R(1.707) - R(1.292)}{1.707 - 1.292} \right) (1.507 - 1.292) + R(1.292) \right) \quad (4)$$

Because the standard method for calculating hydration band depth (Equation 1; Clark and Roush, 1984) works well for water ice-free terrains, we have applied the standard method to spectra with 1.5 μm water ice band depths below 2%. Figure 2.4 shows the

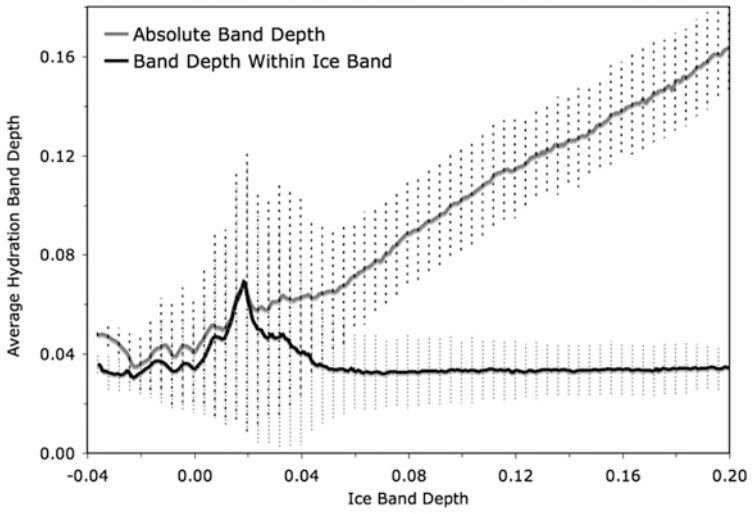

Figure 2.4: Regionally averaged 1.9 μm hydration band depth for varying 1.5 μm ice band depths. 1.9 μm band depths calculated using standard method (grey line) and relative to 2 μm ice band (black line). Error bars are 1 standard deviation. The peak at 0.02 represents the region in Olympia Planum with >15% 1.9 μm band depths (see Figure 2.5), as this region also exhibits 1.5 μm ice band depths between 1-3%, with smaller ice band depths farther from Planum Boreum.

average 1.9 μm hydration band depth for a given 1.5 μm water ice band depth across the north polar region, calculated using both the standard (Equation 1) and new methods (Equations 2 and 3) described above. For the standard method, hydration band depth has a clear correlation with water ice band depth, whereas for hydration band depths found relative to the 2 μm water ice band, the hydration band depth is independent of water ice band depth. Below 2% 1.5 μm water ice band depth, both methods produce similar results, and we can apply the standard method to those spectra; however, it should be noted that the non-standard approach appears to underestimate the 1.9 μm band depth for spectra with 1.5 μm band depths less than 2%, by about 1% (see Figure 2.4). This is caused by the slightly more negative slope of continua taken between 1.84 and 2.12 μm versus those taken between 1.84 and 2.2 μm. Ideally, in water ice-free materials, these slopes should be identical. The

decrease in slope may be due to the presence of the 2 μm water ice band, or the presence of a 2 μm pyroxene band. The major impacts of this discrepancy on our mapping efforts are 1) a discontinuity of <3% in hydration band depth at some contacts between water ice-free and water ice-rich surfaces, and 2) that by imposing the same detection threshold on the hydration band depth calculated using both methods, we may be losing sensitivity to band depths near that detection threshold in water ice-rich terrains.

As a final measure to ensure that we are not detecting anomalous features within the 2 μm water ice band, such as remnant features from poor corrections of the 2 μm CO_2 atmospheric bands, we require that for spectra to have a positive identification of the 1.9 μm hydration band, their minimum between 1.84 and 2.12 μm must be at 1.94 μm or 1.955 μm. This also guarantees that we are not applying this method to pure water ice spectra, which, when the continuum is removed, would yield a negative 1.9 μm band depth.

4.3 Map limitations

The presence of steep scarps and deep troughs in Planum Boreum creates several problems for our mapping effort. On extremely steep slopes, high incidence angles cause Sun-glints off of the specularly-reflecting surfaces, which saturate the pixel and washes out any useful spectral features. As such, we are unable to detect spectral features along the walls of troughs at these unfortunate phase angles. Searching for spectral features within troughs is also problematic because at the incidence angles common in northern summer (~60-70°), either wall of a trough may be in shadow. To correct for the effects of both of these issues in our maps, we have overlaid multiple observations of the same area and searched for the maximum hydration signature in each pixel. This method also allows us to include observations

of the same regions taken throughout the early summer and record the hydration at the minimum amount of frost coverage during that time.

As we are including observations taken during a range of solar longitudes and resolutions, boundaries between images in our maps reflect these variations. Images with better resolutions will tend to exhibit higher band depths, especially in the circum-polar plains, where hydration-signature bearing materials are present in sparse dune fields (Figure 2.5). Additionally, as the fine grained, seasonal water frost deposits continue to retreat poleward into the early summer (~ L_S = 107; Langevin *et al*., 2005b), regions with coverage limited to the very early summer will record the presence of seasonal frost close to Planum Boreum. Examples of seams between images that are apparent due to these effects are present in our maps near 45, 75, and 270°E.

5. Results

5.1 Hydrated mineral distribution

Figure 2.5 shows our 1.9 μm hydration band depth mapped over the north polar region, calculated using the methods described above. The noise uncertainty of the OMEGA data is approximately 2% (Bellucci *et al*., 2006); however, we estimate that our detection threshold in this map is 4.5% band depth. Below this threshold, the hydration signature appears noisy, but above this threshold it begins to show spatially contiguous correlations with geologic features.

The hydration signature is an indicator of the presence of molecular water, either adsorbed onto minerals and/or ice, or bound within the crystal structure of hydrated minerals (*e.g.* Clark, 1981). Because the hydration signature exhibits spatially contiguous correlations with geologic features for 1.9 μm band depths above 4.5%, we propose that we are observing hydrated minerals in this band depth regime.

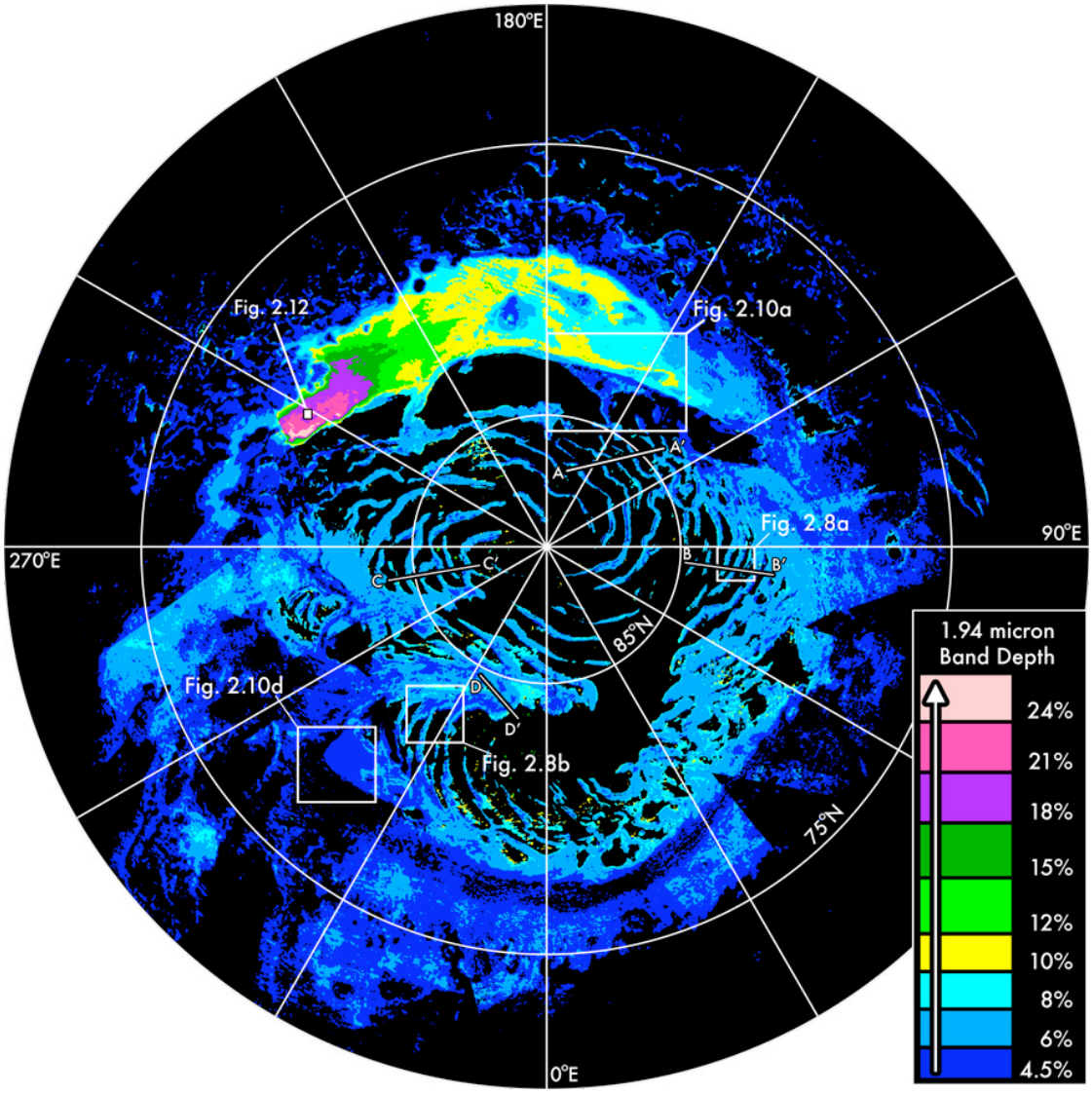

Figure 2.5: Polar stereographic map of the 1.9 μm hydration band depth in the north polar region. Color contour levels have been chosen to illustrate variation in band depth. Contours indicate band depths greater than 4.5, 6, 8, 10, 15, 18, 21, and 24%, respectively. Insets and profiles indicate locations of other figures.

As such, we interpret Figure 2.5 as a map of the distribution of hydrated minerals in the north polar region. It is possible that the noisy signals below 4.5% band depth that we have observed throughout the north polar region may be indicative of the widespread presence of adsorbed water on anhydrous minerals (*e.g.,* Jouglet *et al.,* 2007; Milliken *et al.*, 2007). Adsorbed water, as identified by the 3 μm hydration feature in OMEGA data (Jouglet *et al*., 2007), has been observed to increase with latitude poleward of 50°N, and abundances have been estimated at >8 wt.% during northern summer (Milliken *et al*., 2007). As such, we are unable to differentiate the presence of hydrated minerals from the presence of adsorbed water for 1.9 μm band depths less than ~4.5%.

The maximum hydration band depths that we observe at the resolution of our map (1 km/pixel) are approximately 26%, and are located in the extreme northeastern region of Olympia Planum, near the contact with Planum Boreum. Indeed, the entirety of Olympia Planum exhibits elevated hydration band depths relative to the rest of the region, consistent with the results of Langevin *et al*. (2005a). In addition, many other areas in the north polar region also exhibit hydration band depths above our threshold, including nearly all of the circum-polar dune fields, the cavi of Planum Boreum, Chasma Boreale, and all of the dark veneers on Planum Boreum. The hydration band depths in these areas are generally below 10%, with a few local exceptions.

The apparent dichotomy in the hydration band depths between Olympia Planum and the other hydrated terrains in the north polar region leads us to speculate that we are observing at least two units containing hydrated minerals: (1) deposits with high concentrations of gypsum (Langevin *et al*., 2005a; Fishbaugh *et al*., 2007), restricted geographically to Olympia Planum, and (2) deposits with low concentrations of another hydrated mineral, widely distributed throughout the cavi of Planum Boreum as well as the circum-polar erg. The veneers and circum-polar erg may also each

represent unique deposits containing hydrated minerals, or the hydration in the erg may be related to that in Olympia Planum.

5.2 Variation of water ice band depths in hydrated terrains

The only major spectral characteristics of the polar regions exhibiting hydration signatures that change significantly across the region are the depths of the 1.5 and 2 μm water ice bands. Figure 2.6 shows spectra, created from averages taken across the north polar region, that represent spectral units defined in terms of the presence or lack of the 1.9 μm hydration signature and the depth of the 1.5 μm water ice band. These spectra are samples of a continuum of spectra with water ice band depth ranging from 0 to over 60%.

Figure 2.7 shows these 6 spectral units mapped over the north polar region. Regions bearing hydration signatures in the circum-polar plains are generally water ice-free, and water ice band depth increases with proximity to Planum Boreum. Specifically, we observe water ice-rich hydrated units in the mixed and low albedo regions identified as veneers by Rodriguez *et al*. (2007), on the margins of Planum Boreum, on the margins of the icy outliers, and in the narrower polar troughs and reentrants, many of which have been previously identified as containing dark, water ice-free materials (Tanaka, 2005; Tanaka *et al*., 2008; Rodriguez *et al*., 2007).
Rodriguez *et al*. (2007) proposed, based on OMEGA data, that the mixed and low albedo terrains represent a linear mixing of water ice and the overlying dark veneers. Because we also observe hydrated units with water ice bands at contacts between dark water ice-free and bright water ice-rich terrains, these units are also most likely sub-pixel, spatial mixtures of water ice and dark, hydrated terrain. On the margins of Planum Boreum and at the edges of troughs, the dark materials may be simply abutting water ice-rich surfaces. This conclusion is supported by the preliminary

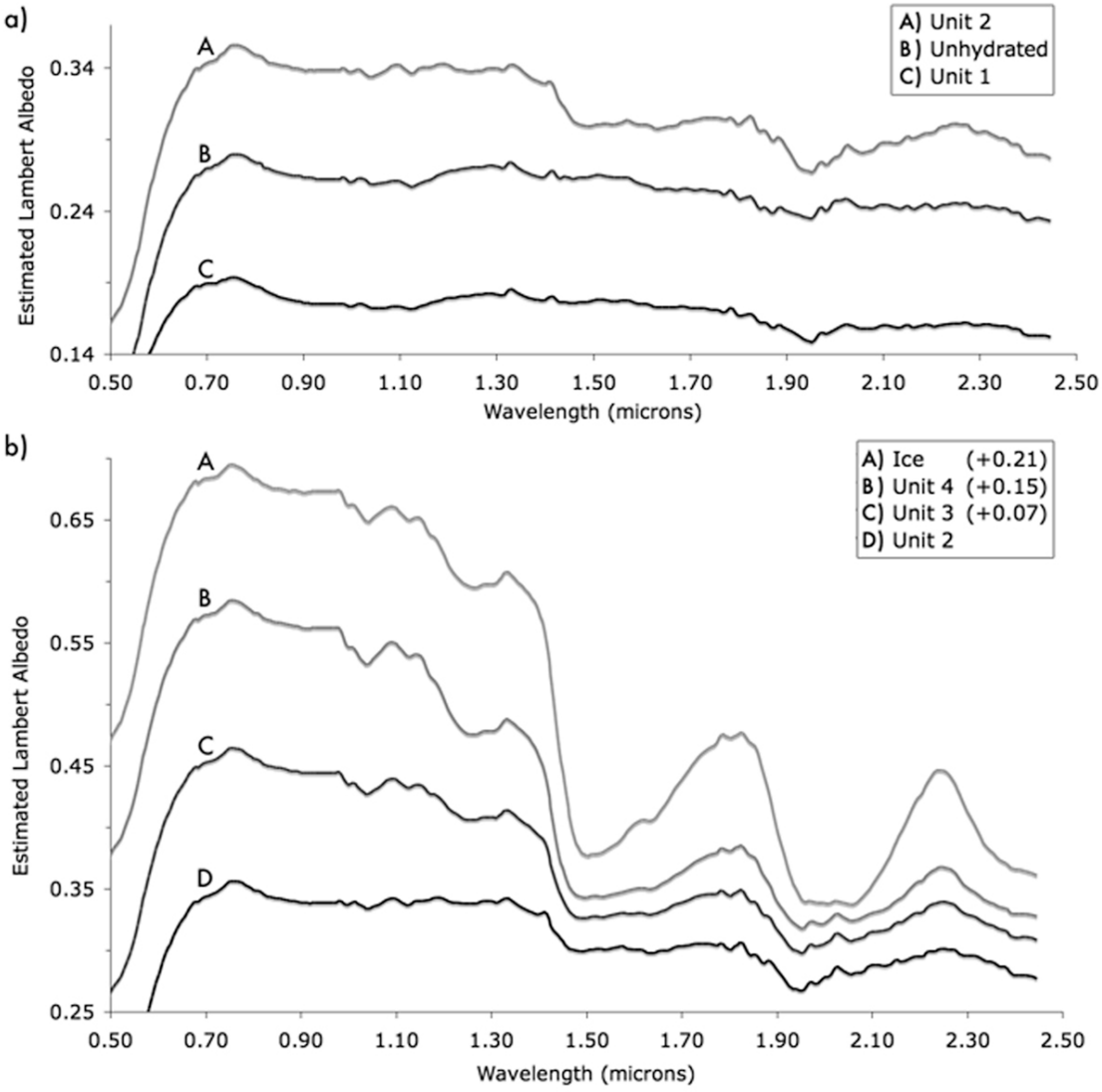

Figure 2.6: OMEGA spectra with > 4.5% 1.9 μm hydration band depth and with increasing 1.5 μm ice band depths, averaged over the north polar region. The 1.9 and 1.5 μm band depth criteria used for determining spectral types are given in Table 2.2. *(a)* Hydrated ice-free, hydrated ice-poor, and unhydrated ice-free units. Unhydrated unit exhibits a minor hydration band due to the inclusion of terrains with 1.9 μm band depths between 0 and 4.5%. *(b)* Ice-rich hydrated and pure ice units. Spectra have been shifted upward in albedo by the amount indicated in the legend for ease of viewing. Unit 2 is shown in both plots for continuity. Together, these spectra represent a continuum of ice band depths throughout the hydrated terrains that we observe in the north polar region.

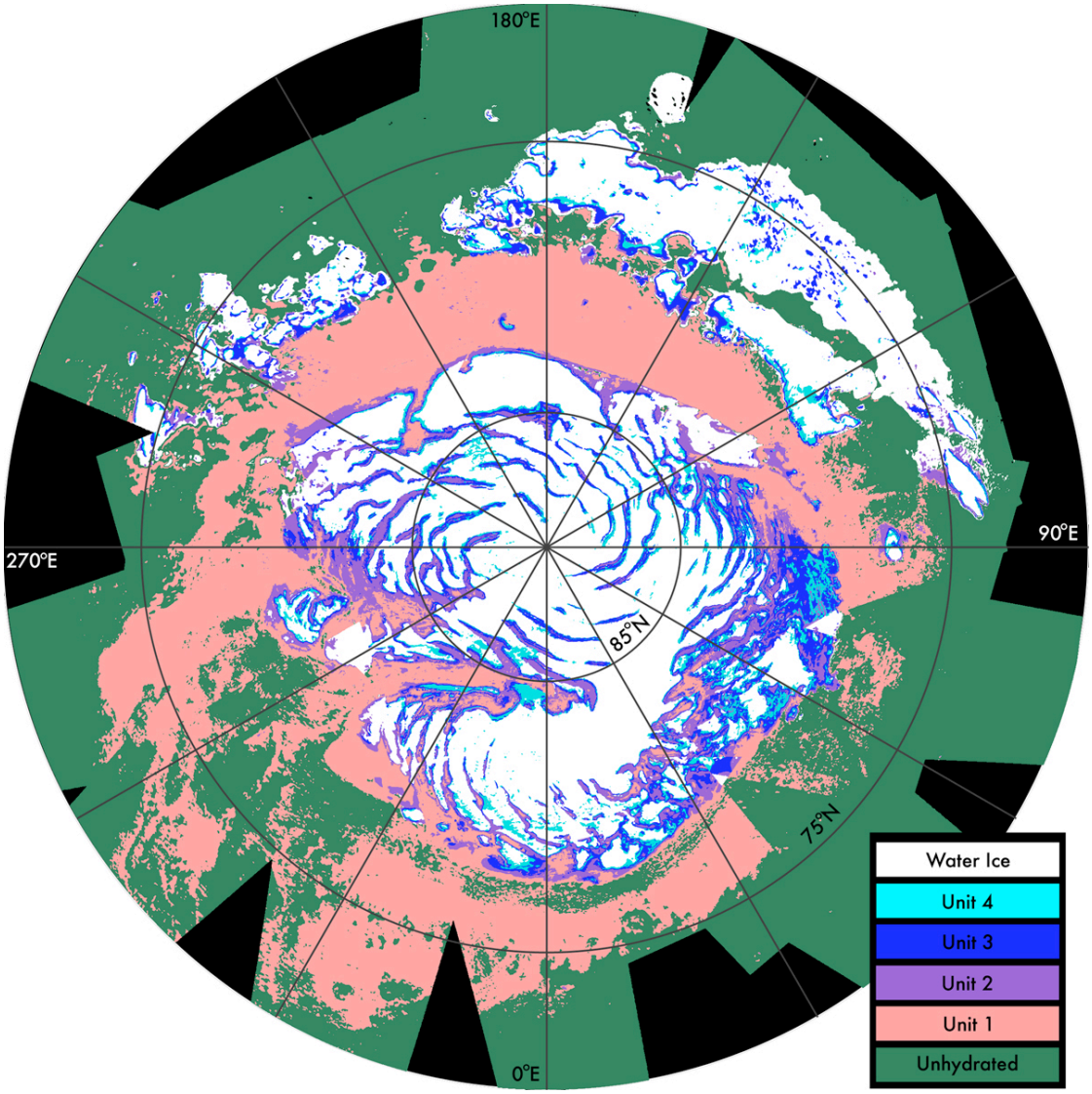

Figure 2.7: Polar stereographic map of the distribution of OMEGA-derived variations in the 1.5 μm ice band depth within hydrated terrains in the north polar region. Spectral types are defined in Table 2.2 and shown in Figure 2.6. Ice band depth increases with proximity to margins of Planum Boreum 3 and 4 units.

Table 2.2: Constraints on and deviation of our defined spectral units.

Spectral Unit	1.9 μm Band Depth	1.5 μm Band Depth	Standard Deviation[a]	
			Average	Median
Unhydrated	< 4.5%	< 3%	0.064	0.071
Unit 1	> 4.5%	< 3%	0.058	0.065
Unit 2	> 4.5%	3 – 10%	0.065	0.067
Unit 3	> 4.5%	10 – 20%	0.046	0.043
Unit 4	> 4.5%	> 20%	0.046	0.040
Ice	< 4.5%	> 3%	0.085	0.089

[a]Standard deviation units: estimated Lambert albedo. Averages and medians were calculated from standard deviations for each wavelength of the average spectral unit spectra shown in Figure 2.6.

results of Langevin *et al*. (2008), which also suggest an areal mixture between icy terrains and the adjacent PLD surfaces in OMEGA data. Simple linear mixtures of the spectra for Unit 1 and Ice (water ice) shown in Figure 2.6 yield approximate fits for Units 2-4 for surface water ice abundances of ~10, ~25, and ~50 wt.%.

With the exception of the variation of the water ice bands, the spectra of the hydrated regions outside Olympia Planum are fairly homogenous. The variations are largely only in albedo, and have a standard deviation of +/- ~0.05 estimated Lambert albedo for the hydrated spectral units, as shown in Table 2.2. The hydration signature is found in dark-toned sand dunes, dark-toned veneers, and dark-toned layered deposits in Planum Boreum, with spectra that are nearly featureless, except for the 1.9 μm hydration band and a broad 1 μm band (see the Unhydrated Unit and Unit 1 in Figure 2.6) that may be due to a ferrous component in the dark material. The spectral homogeneity of the dark, hydrated materials is consistent with the idea that the polar layered deposits and the circum-polar erg have exchanged materials in many episodes, throughout the Amazonian.

5.3 Correlations with geologic units

After a comparison of Figures 2.2 and 2.7, on the regional scale, the hydrated minerals in Planum Boreum appear to be correlated with the Planum Boreum 1 unit of Tanaka *et al*. (2008); however, this may not be accurate under closer inspection. Figures 2.8a and 2.8b show the hydration signatures associated with troughs near 90°E and 270°E, respectively, alongside the THEMIS albedo and the Tanaka *et al*. (2008) geologic map from the same area. The hydration signature does not cover the entire trough where dark layers are visible and the Planum Boreum 1 unit has been mapped, but rather seems to start 1-3 pixels below the top of the layers. Figure 2.9*a-d* show OMEGA hydration, MOLA elevation, THEMIS albedo, and OMEGA water ice band depth profiles taken through many of the troughs on Planum Boreum. The troughs all exhibit hydration signatures on their equator-ward slopes as well as on their floors, and the zone of hydration appears to be sharply defined. On the poleward slope, the sharp drop-off of the hydration signature is accompanied by a sharp increase in the water ice band depth. When compared to similar profiles taken by Tanaka *et al*. (2008) (*e.g.* Figure 4*b* in Tanaka *et al*. (2008)) through the geologic units, it appears that the hydration signature is cut off on the poleward slope by the presence of the Planum Boreum 3 unit.

On the equatorward slope of the troughs shown in Figures 2.9*a-d*, the hydration signature rapidly increases just after the start of the dark layers, as indicated by the decrease of the THEMIS albedo. The hydration signature is consistently greatest at its uppermost extent on the slope, and decreases down slope, possibly indicating a source of hydrated material near the top that is actively eroding and covering/coating lower units. This region of the slopes near the contact of Planum Boreum 1 and 3 units may correspond to the Planum Boreum 2 unit, the thin, dark,

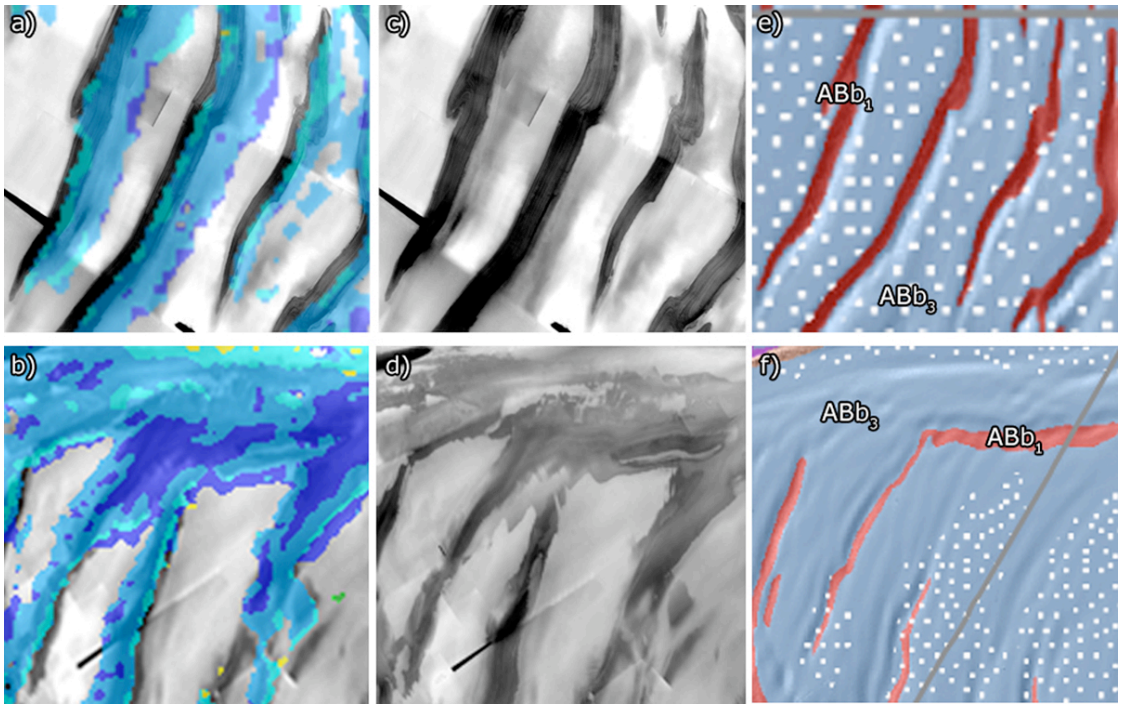

Figure 2.8: 1.94 μm hydration signatures associated with veneers sourced from units within polar troughs (see Figure 2.5 for locations). (*a*) Hydration signatures emanating from troughs near 90°E. (*b*) Hydration signatures emanating from troughs on the eastern wall of Chasma Boreale. The topmost layers exposed in the troughs do not exhibit hydration at the resolution of our map (at best 1.6 km/pix), however, all lower layers do. (*c*, *d*) Visible images of regions shown in (*a*) and (*b*) from 36 m/pixel THEMIS north pole mosaic (N. Gorelick/ASU). The darkest, and presumably youngest, veneers emanating from the troughs also exhibit hydration signatures, while the older, brighter veneers do not. Hydration signatures correlate well with dark veneers, and again, uppermost dark layers exposed in troughs do not exhibit hydration at this scale. (*e*, *f*) Segment of Tanaka *et al*. (2008) geologic map. Hydration signatures are present in troughs below Planum Boreum 1 unit (ABb_1). Planum Boreum 2 unit is not mapped at these scales.

sandy unit intermediate between the upper and lower layered deposits, identified by Rodriguez *et al*. (2007).

As shown in Figures 2.9a-d, we have consistently observed this "gap" in the hydration signature in the Planum Boreum 3 unit below the tops of troughs at all orientations across the polar cap, which leads us to believe that this is a real feature and not an artifact due to misregistration. In addition, the hydration signatures at the edges of these gaps consistently rise sharply to significant band depth values, as would be expected if the source of the hydration is a well-defined layer, such as the veneer forming Planum Boreum 2 unit. If the residual cap was merely obscuring hydration at the top of trough, it is unlikely that we would observe this feature so consistently across the polar cap.

From these observations, we may postulate that the Planum Boreum 3 unit does not contain hydrated minerals, but that the Planum Boreum 2 unit does. If this is the case, then the units stratigraphically below the Planum Boreum 2 unit are likely to be coated in eroded material from this unit, as indicated by the fall-off in hydration band depths within the troughs in Figures 2.9a-d. This debris would obscure any inherent hydration signature the underlying units might have, and as such, we cannot comment on their abundance or lack of hydrated minerals. We have noted, however, that the Rupes Tenuis unit, where it is exposed away from the overlying units, does not exhibit a hydration signature at the resolution of our map.

5.4 Correlations with sedimentary veneers

Comparing Figures 2.1 and 2.7 reveals that the regions on Planum Boreum that exhibit a hydration signature but are not in troughs have a lower albedo than the surrounding water ice. These areas correspond to the north polar veneers identified by Rodriguez *et al*. (2007). Figure 2.8 shows two examples of veneers on Planum

Figure 2.9: Comparison of co-located profiles of OMEGA 1.94 μm hydration band depth, MOLA elevation, THEMIS albedo, and OMEGA 1.5 μm ice band depth. Profile locations shown in Figure 2.5. (*a*) Profiles through troughs near 150°E. (*b*) Profiles taken through troughs near 90°E. (*c*) Profiles taken through troughs near 270°E. (*d*) Profiles taken over the Chasma Boreale head scarp. Grey bands indicated surfaces with hydrated mineral detections. All profiles indicate that hydrated deposits are present throughout the trough cross-sections, and are associated with dark material and low ice band depths. All profiles also consistently show elevated and sharply truncated hydration signatures on the steep, equator-ward scarps of the troughs. This may indicate a source unit for hydrated minerals in the scarps, the erosion of which would spread hydrated minerals at lower abundances throughout the trough cross-section and into or onto the veneers between troughs.

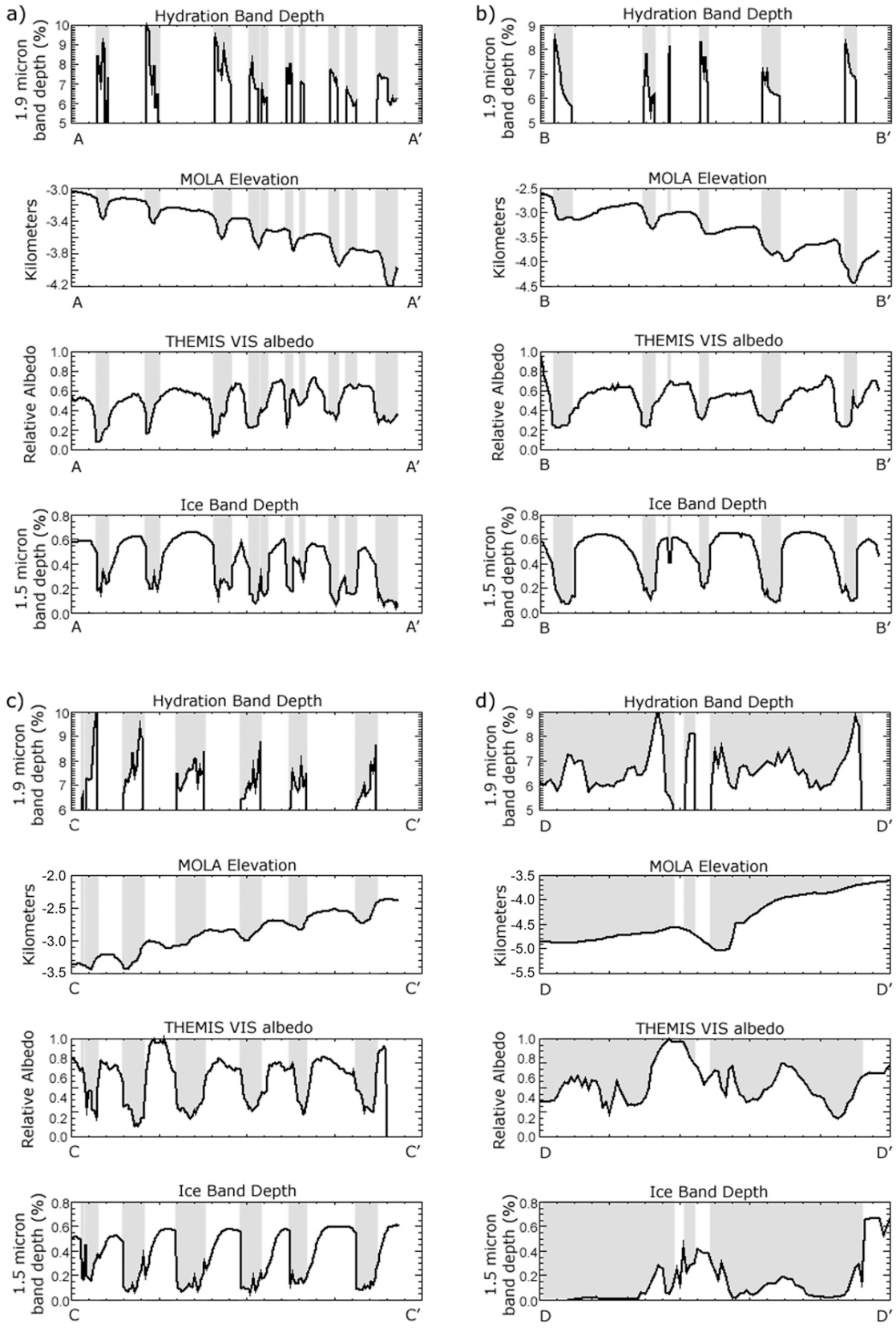
a)
Hydration Band Depth
1.9 micron band depth (%)
A
A′
MOLA Elevation
Kilometers
THEMIS VIS albedo
Relative Albedo
Ice Band Depth
1.5 micron band depth (%)
b)
B
B′
c)
C
C′
d)
D
D′

Boreum emanating from troughs. In Figure 2.8a, the hydration signature extends from the trough down slope to the margin of the darkest veneers shown in Figure 2.8c. In Figure 2.8b, the hydration signature tracks veneers that have spread both up and down slope from the troughs shown in Figure 2.8d. While hydration is not detected in all of the veneers evident in Figures 2.8c and 2.8d, hydration is detected in all of the darkest, stratigraphically youngest veneers.

Rodriguez *et al*. (2007) interpreted the Planum Boreum 2 unit as the source unit for the veneers emanating from troughs. Our observation that these veneers are hydrated provides further support for the idea that the Planum Boreum 2 unit is the source of the hydrated minerals that we have detected in the troughs and on the surface of Planum Boreum.

Where the veneers are transported off of Planum Boreum, they form mantles around the periphery (Rodriguez *et al*., 2007). Several of these mantles embay dune fields, allowing us to observe the contact between these two hydrated sedimentary deposits. Figure 2.10a shows a veneer mantling the periphery of Planum Boreum and the margin of western Olympia Planum. The bright water ice of the Planum Boreum 3 unit covers and embays many fossilized dunes at its margin, as shown in Figures 2.10b and c. Although the ice is covered with the veneer to its margin, it is unclear how far out the veneer extends past the ice and into the dune field, if at all. Moving off of the ice, the hydration signature increases in the plains with sparse dunes, and increases again at the main margin of the dune field. If the veneer does extend past the ice margin, it may be mixing with hydrated material from Olympia Planum to create a hydration band depth between that of the veneer and that of the main dune field. On the other side of Planum Boreum, Figure 2.10d shows the Planum Boreum 3 unit and the veneer covering it at the tip of Gemina Lingula. The ice mantles and embays dunes, as shown in Figure 2.10f (Rodriguez *et al*., 2007). Because the veneer embays

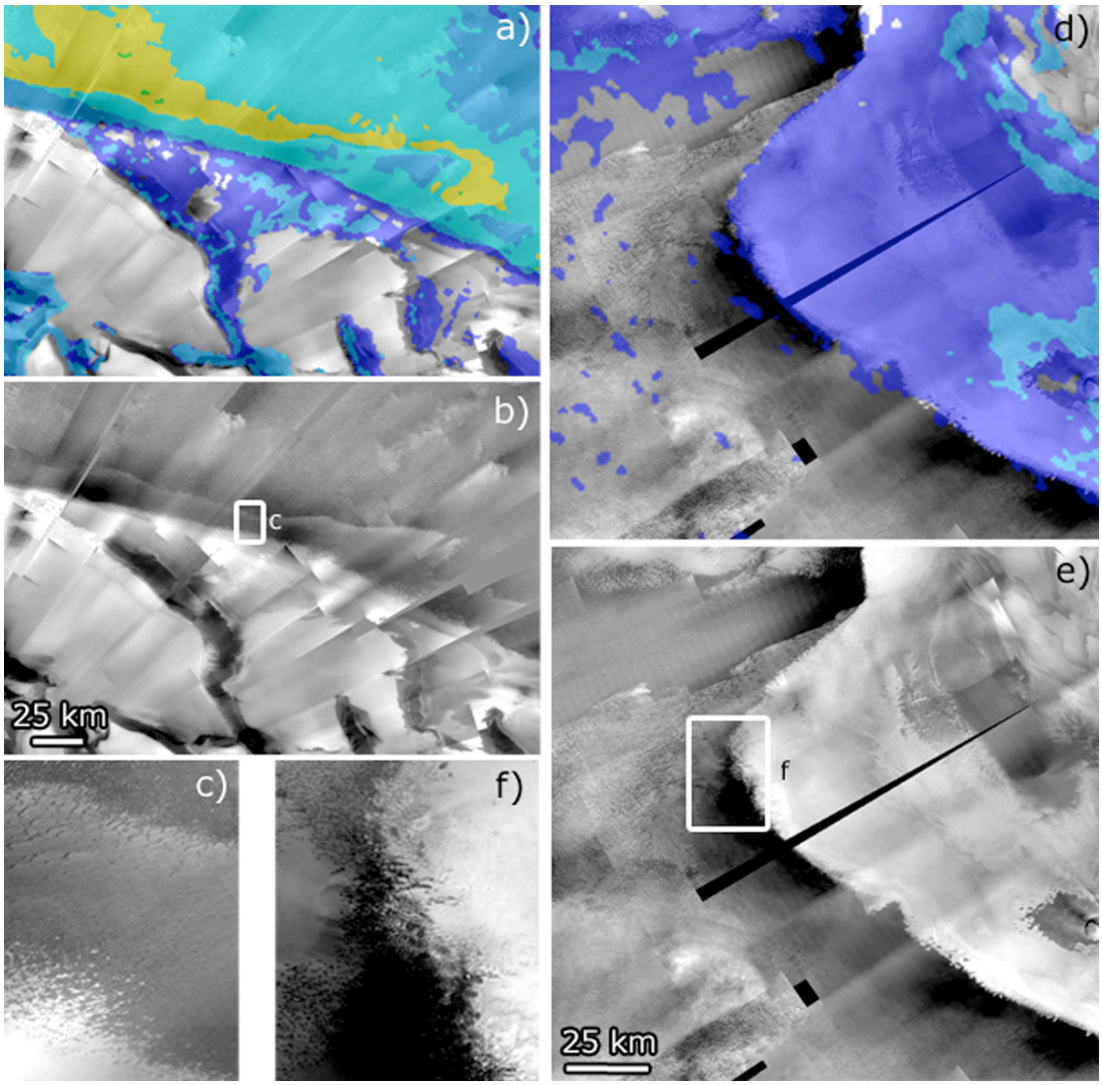

Figure 2.10: Contacts between hydrated veneers and circum-polar dune fields. Visible images from 36 m/pixel THEMIS north pole mosaic (N. Gorelick/ASU; see Figure 2.5 for locations, scale, and 1.9 μm band depth color legend). (*a* and *b*) Hydrated veneers mantle dunes of the Olympia Planum erg. The 1.94 μm hydration signature of gypsum-bearing Olympia Planum dunes is muted by the veneer to a band depth between those exhibited by the veneer and unmantled dunes, implying that spectral mixing is occurring. The mantling also indicates that the veneer has been mobile and dynamic more recently than the dunes. (*c*) Close up of zone of muted dunes, as indicated by inset in (*b*). Because the duneforms, albedos, and hydration signatures are apparent under the mantle, here it must be relatively thin (order several μm). (*d* and *e*) Hydrated veneers mantle dunes near the mouth of Chasma Boreale. Dunes are either unhydrated or hydrated at a level below our detection threshold of 4.5% 1.9 μm band depth. (*f*) Close up of mantled dunes, as indicated by inset in (*e*). Duneforms are indistinct under mantle, indicating much greater thickness (a fraction of the height of the dunes, order meters).

the dunes, this suggests that the veneer has been more recently mobile than the dunes. The veneer exhibits a hydration signature above our threshold, but the dunes do not, which suggests that (1) the veneer does not extend past the ice at this location, and (2) this particular dune field has not been contaminated by hydrated material from Olympia Planum (see next section).

5.4 Correlations with dune fields

In the circum-polar plains, the hydration signatures we observe are largely correlated with the presence of dune fields, as mapped by Tanaka and Hayward (2008). In general, the hydration band depth decreases with a decrease in dune areal density, and both of these parameters decrease with distance from Olympia Planum, in the east and southeast directions (Tanaka and Hayward, 2008; Hayward *et al*., 2008). This suggests that Olympia Planum is the source region for much of the dune material (Tanaka *et al*., 2008), and also that at least some of the hydrated mineral present in all of the circum-polar dunes is gypsum from Olympia Planum.

In comparing the dune density map of Tanaka and Hayward (2008) with Figure 2.5, it appears that, in general, dune areal density correlates with hydration band depth. Because sparser dune fields offer less total exposed area of hydrated minerals for us to detect at the resolution of our maps, this may imply that the dunes exhibit a fairly uniform abundance of hydrated minerals throughout the circum-polar plains. However, there are disparities between dune density and hydration band depth. For example, the region to the southeast of Chasma Boreale is mapped as containing fairly dense dune fields, but exhibits only scattered hydration band depths above our threshold. This may be a resolution issue in the hydration band depth map, or this may indicate a difference between the dunes forming the circum-polar "ring" and the dunes in this region. These dune fields have been proposed to have been sourced from

Chasma Boreale (Tanaka *et al*., 2008; Tanaka and Hayward, 2008), and the lack of widespread hydration signatures may indicate that the source for these dunes contains less hydrated minerals than the dunes sourced from Olympia Planum. It is possible that the mantling of some of the dunes by ice and veneers on the margins of this region (Figure 2.10d) suggests that these dunes are inactive, and that these dunes may be mantled with another deposit so that any hydration signature they would otherwise exhibit is obscured. However, the putative dune source at Abalos Mensae (Tanaka, 2005; Tanaka *et al*., 2008; Tanaka and Hayward, 2008) also exhibits low and sub-threshold hydration band depths, indicating that sources outside of Olympia Planum may, in general, contain a significantly lower abundance of hydrated minerals.

Another disparity in the correlation between dune density and hydration can be found in the region between the margin of Planum Boreum and the mapped dune fields, between -30°E and 60°E. While there are no dunes mapped in this region (Tanaka and Hayward, 2008), and our subsequent searches with CTX images (*e.g.* P02_001651_2567_XN_76N006W) have also not revealed any recognizable bedforms, this region is characterized by a low-albedo mantle that may be sourced from the veneers. The separation of the dunes in this region away from Planum Boreum suggests that strong katabatic winds may be the dominant wind regime here (Tanaka and Hayward, 2008), which would allow transport of the veneers off of Planum Boreum. Indeed, it is quite possible that much of the hydration signature in Chasma Boreale and in other areas adjacent to the polar cap may be due to the presence of the veneers (K. Tanaka, personal communication).

5.5 Spectral relationships

Langevin *et al*. (2005) identified the dominant hydrated mineral present in Olympia Planum as gypsum, based on the presence of spectral features diagnostic of

gypsum at 1.4, 1.75, 1.9, and 2.4 μm. Our results agree with this interpretation in the high 1.9 μm band depth region of Olympia Planum. As shown in Figure 2.11a, when the dark component of the dunes is approximately removed by dividing by the spectrum of a similar albedo area with negligible hydration (< 3% 1.9 μm band depth), the remaining spectrum matches well with a laboratory spectrum of gypsum. Unfortunately, because the reference spectrum does exhibit minor amounts of hydration (albeit below our detection threshold), this method does not produce such clear results in the terrains outside of Olympia Planum, which exhibit < 10% 1.9 μm band depth. Alternatively, visual comparison of the OMEGA spectra from various regions to the spectrum of the gypsum-rich dunes does provide some insight. Figure 2.11b shows a comparison between the spectra of gypsum-rich dunes and dunes 85° east of Olympia Planum. While we cannot make a clear identification of the presence of gypsum in the distant dunes, their spectrum does appear to exhibit a 2.4 μm shoulder and may exhibit a 1.4 μm band, which together, are diagnostic of polyhydrated sulfates (Cloutis *et al*., 2006; Gendrin *et al*., 2005). Figure 2.11c shows spectra of two hydrated Planum Boreum veneers. The top spectrum was selected from veneers directly adjacent to and presumably sourced from a trough near 70°E, and exhibits water ice bands at 1.25, 1.5, and 2.0 μm. The bottom spectrum was selected from veneers near the southwest margin of Gemina Lingula, and appears to be water ice-free. Again, while we cannot make a clear identification of gypsum in these spectra, both top and bottom spectra may exhibit a 1.4 μm band, and while a 2.4 μm shoulder cannot be distinguished from the 2.5 μm water ice band in the top spectrum, a 2.4 μm shoulder may be present in the water ice-free, bottom spectrum. In all of these cases, while we cannot make a clear identification of the hydrated component, the spectra are consistent with a polyhydrated sulfate, and it is certainly plausible that gypsum is the dominant hydrated mineral in these deposits.

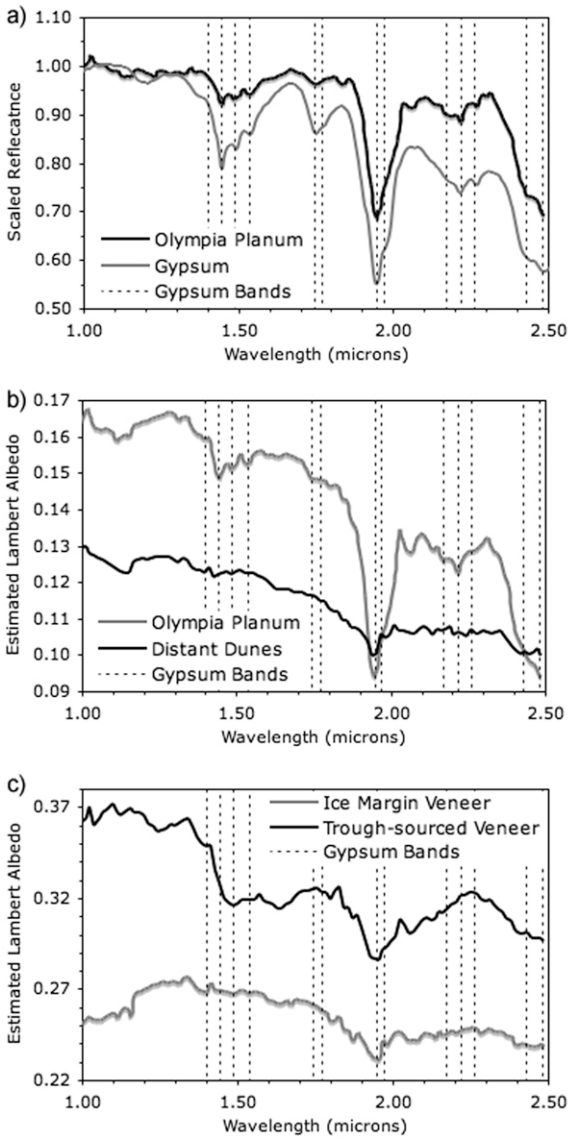

Figure 2.11: OMEGA spectra of selected localities. In all plots, dotted vertical lines indicate gypsum absorption bands (Cloutis *et al*., 2006). (*a*) Black line: ratio of Olympia Planum hydrated mineral-bearing terrain (~10 km^2 average, 80.0°N, 245.2°E) and similar albedo terrain with sub-threshold (~3%) 1.9 μm band depth (~20 km^2 average, 81.1°N, 277.4°E). Gray line: laboratory spectrum of gypsum (< 45 μm grain size; SPT127, Cloutis *et al*., 2006), scaled for similar 1.9 μm band depth. Both spectra have been scaled to 1 at 1.01 μm. (*b*) Spectral comparison of Olympia Planum gypsum-rich dunes (~10 km^2 average, 80.0°N, 245.2°E) and hydrated-mineral bearing dunes 85° longitude distant (~10 km^2 average, 73.6°N, 330.8°E). (*c*) Spectral comparison of veneers sourced from Planum Boreum troughs (~4 km^2 average, 82.4°N, 70.6°E) and veneers at the margin of Planum Boreum (~100 km^2 average, 79.5°N, 316.3 °E).

6. Insights from laboratory data applied to OMEGA and CRISM observations

6.1 CRISM observations

Higher resolution (>18 m) CRISM imagery has provided a greater understanding of how the gypsum is distributed in eastern Olympia Planum, at the scale of individual dunes (Roach *et al*, 2007). As shown in Figure 2.12b, the 1.9 μm band depth, calculated using the method described in section 4.1, has a distinct correlation with dune crests (Roach *et al*, 2007). The crests exhibit band depths, on average, of ~25%, as compared to the bright troughs, which exhibit band depths, on average, of ~12%. While this may be due to an increased abundance of gypsum, this is not the only possible explanation. Because increasing grain size also increases band depths, the higher 1.9 μm band depths at the crests have been suggested to be at least partially due to the greater presence of large gypsum grains, as small grains may have been preferentially removed at the crest by the greater wind exposure (Fishbaugh *et al*., 2007; Roach *et al*., 2007).

Interestingly, the dune crests also exhibit a higher albedo than the flanks of the dunes, as shown in Figure 2.12a. Although the rise in albedo on the illuminated side of the dune is due to photometric effects, the rise in albedo near the crest is most likely not, as it is symmetric across both the illuminated and shadowed sides of the dune. This higher albedo at the dune crests does not support the hypothesis that the greater 1.9 μm band depths observed at the crests are due to larger grains, as increasing grain size tends to decrease albedo, as shown in Figure 2.13a. In addition, in situ terrestrial observations have generally found upslope fining of dune sand, with coarse grains found at the crest only in rare cases due to complications from dune topography and the size distribution of the source (Finkel, 1959; Hastenrath, 1967; Vincent, 1984; Watson, 1986). Based on these observations and the fact that gypsum is a light-toned

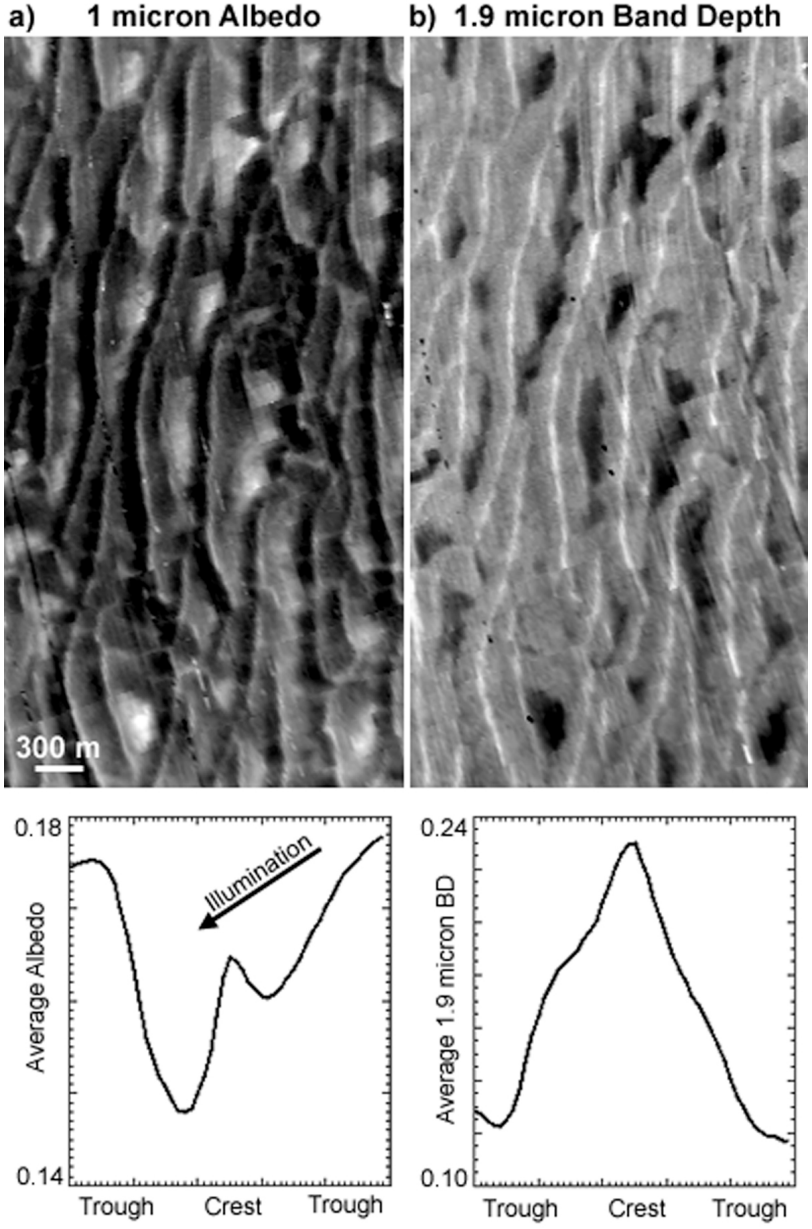

Figure 2.12: CRISM view of eastern Olympia Planum, near 80.1°N, 240.8°E (CRISM observation FRT0000285f_07; adapted from Roach *et al*., 2007). Corresponding plots below show average dune profiles calculated from 12 E-W crest-trough profiles and 12 E-W trough-crest profiles throughout CRISM image. (*a*) 0.95-1.05 μm average CRISM albedo. Dune troughs and crests are both brighter than dune flanks. Asymmetric brightening of right slope in dune profile is due to solar illumination; left slope is in shadow. (*b*) 1.9 μm band depth. Dune crests have greatest hydration signature (~24%), while albedo-bright areas in troughs have lowest (~12%). Brightening of dune crest may be due to gypsum presence.

mineral, we suggest that both the rise in albedo and the rise in the 1.9 μm band depth near the crest may be due to the presence of higher abundances of gypsum.

6.2 Variation of 1.9 μm band depth with grain size

While we hypothesize that the increase in 1.9 μm band depth that we have observed between dune troughs and crests in the CRISM observation presented in Figure 2.12b is due to an increase in gypsum abundance, the possibility that the increase in band depth is due to a change in grain size begs the question: what magnitude of grain size change would be required to increase the 1.9 μm band depth from 12% to 25%? While laboratory studies have been conducted on the optical constants of gypsum (Roush *et al*., 2007), the spectral properties of gypsum (Cloutis *et al*., 2006), and the stability of gypsum under Mars-like conditions (Cloutis *et al*., 2007), empirical models for the changes in the spectral properties with changes in grain size and abundance have not been fully examined. Ghrefat *et al*. (2007) present grain size – band depth relations for sand gathered at White Sands, but only for the 1.75 and 2.15 μm gypsum bands. Clark *et al*. (2008) also present some preliminary findings in this area. To address this deficiency in the literature, here we present our own independent findings on these spectral variations.

Figure 2.13a shows the laboratory spectra of gypsum samples, dry-sieved to various grain size ranges. Reflectance spectra over the 0.35-2.5 μm range were acquired with an Analytical Spectral Devices FieldSpec Pro HR® spectrophotometer. The spectral resolution of the instrument varies between 2 and 7 nm and spectral sampling is done at 1.4 nm intervals. The instrument internally resamples the spectra to 1 nm intervals (Cloutis *et al.*, 2007). The primary change that occurs with increasing grain size is a widening and deepening of the bands. In addition, the 1.75 and 1.9 μm bands appear to saturate. While our study only sampled grain sizes below

Figure 2.13: Laboratory measurements of variation of gypsum spectra with grain size. (*a*) Gypsum laboratory spectra. Samples of naturally occurring gypsum (SPT127; Cloutis *et al*., 2006) were crushed and dry sieved into the following grain size bins: < 45 μm, 45-90 μm, 90-250 μm, 250-500 μm, 0.5-1 mm, 1-2 mm, 2-4 mm, and 4-6 mm. (*b*) The variation in 1.9 μm band depth with grain size, with a logarithmic fit (R^2=0.2189). (*c*) The variation in the shape of 1.9 μm band with grain size, as determined from the ratio of the 1.975 and 1.946 μm band depths, with a logarithmic fit (R^2=0.7284). (*d*) The variation in 1.75 μm band depth with grain size, with a logarithmic fit (R^2=0.9018). Below 500 μm grain size, our data matches well with those of Ghrefat *et al*. (2007).

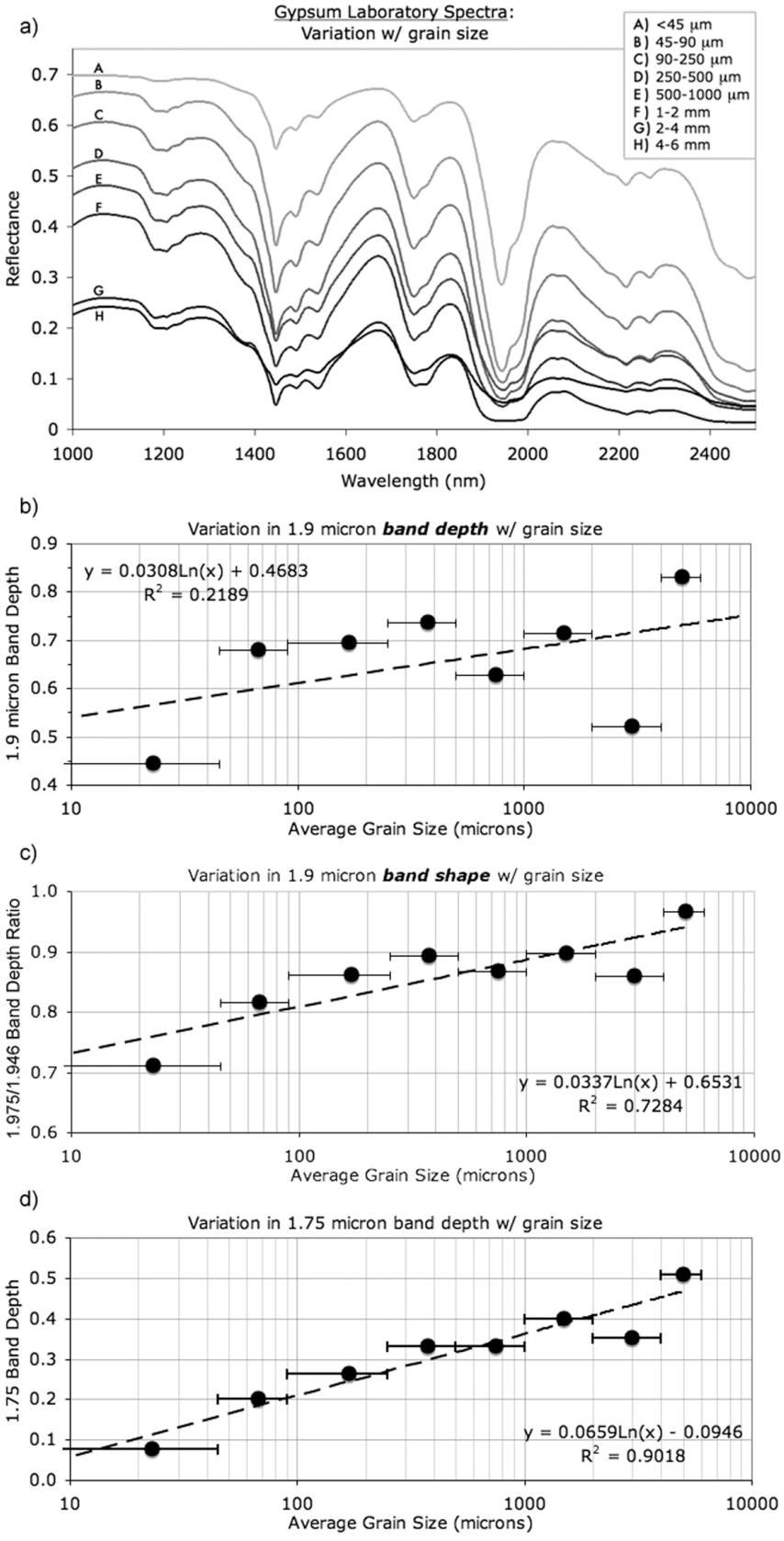
a)
Gypsum Laboratory Spectra:
Variation w/ grain size
A) <45 μm
B) 45-90 μm
C) 90-250 μm
D) 250-500 μm
E) 500-1000 μm
F) 1-2 mm
G) 2-4 mm
H) 4-6 mm
Reflectance
Wavelength (nm)
b)
Variation in 1.9 micron band depth w/ grain size
y = 0.0308Ln(x) + 0.4683
R2 = 0.2189
1.9 micron Band Depth
Average Grain Size (microns)
c)
Variation in 1.9 micron band shape w/ grain size
y = 0.0337Ln(x) + 0.6531
R2 = 0.7284
1.975/1.946 Band Depth Ratio
Average Grain Size (microns)
d)
Variation in 1.75 micron band depth w/ grain size
y = 0.0659Ln(x) - 0.0946
R2 = 0.9018
1.75 Band Depth
Average Grain Size (microns)

45 μm in one bin, Cooper and Mustard (2007) analyzed laboratory samples of montmorillonite for variations in hydration band depths with particle size, and found that small particles (<5 μm) still have detectable (more than several % band depth) 1.9 μm bands.

Figure 2.13b shows the measured change in 1.9 μm band depth with grain size on a logarithmic scale, calculated using Equation 1. While the trendline shown is not a good fit for all the data points – both because we are sampling a range of grain sizes with each spectrum and because of the difficulty in measuring accurate bands near saturation – it illustrates that while this is a complex relationship, there is some dependence on grain size, although poorly defined for this data set. Keeping this in mind, we can extract the general trend from the fit, which is on the order of 5% increase in band depth per order of magnitude change in grain size. If we apply this trend to the CRISM 1.9 μm band depths observed in the gypsum-rich dunes, the grain sizes in the crests would need to be over 100 times greater than those in the troughs for the abundance to remain the same – for example, 1 mm grains in the crests of the dunes would imply ~10 μm grains in the troughs. This scenario is plausible, as extremely fine gypsum grains could be produced by breakdown of larger gypsum grains during saltation.

This change in grain size, if it is real, may be detectable via other spectral analysis methods. A possible method for detecting changes in grain size in gypsum deposits, and possibly other H_2O-bearing mineral deposits, involves analyzing the shape of the spectrum within the 1.9 μm band. The 1.9 μm band is actually a doublet, with centers at 1.94 and 1.97 μm (Cloutis *et al*., 2006). As shown in Figure 2.13a, with an increasing grain size, the minima of the two bands approach the same reflectance value. This is most likely due to the deeper 1.94 μm band saturating first. Figure 2.13c shows how the ratio between the 1.94 and 1.97 μm band depths changes

with grain size: the ratio increases ~18% with an order of magnitude increase in grain size. Ideally, we would like to apply this analysis to CRISM spectra of the gypsum-rich dunes to test for large variations in grain size between the crest and troughs. For the change in grain size required to maintain a constant abundance, the ratio difference between the crests and troughs should be ~40%. Unfortunately, taking the ratio of these band depths enhances what appear to be calibration or low signal-to-noise ratio errors between columns in the CRISM image, obscuring the interpretation of the band depth ratio. Perhaps this method may be applied to CRISM data in the future with an improved calibration routine or with higher signal to noise ratio data.

The 1.75 μm gypsum absorption band may also be used to track grain size changes, as demonstrated by Ghrefat *et al*. (2007) at the White Sands dune field. Figure 2.13d shows the variation of the 1.75 μm band with grain size in our laboratory spectra, calculated using Equation 1, with shoulders at 1.680 and 1.825 μm and a band minimum at 1.750 μm. The 1.75 μm band depth appears to correlate well with grain size, without the fluctuations that are apparent with the 1.9 μm band depth (Figure 2.13a). The 1.75 μm band depth changes ~7% with an order of magnitude change in grain size, and ideally, we should be able to apply this function to the CRISM data. Unfortunately, while the CRISM spectra show 1.75 μm band depths that also are a maximum at the dune crests, the range of 1.75 μm band depths across the dunes is between 0 and 2.5%, which is too small of a change to consider with this method.

While these new methods of constraining grain size have not yielded highly-constrained results in this case study, they could prove quite useful in future efforts with a more precise calibration of the CRISM data. For example, with additional CRISM data over Olympia Undae, a future study could use the grain size discrimination methods we have presented to better classify the distribution of gypsum in the dunes, both within the putative source region and in the rest of Olympia Undae.

Along with observations of how the dune profile albedo changes throughout Olympia Undae, these results could give valuable insight into how the gypsum is transported by and deposited on the dunes.

Such a study would also provide great insight into how the distribution of gypsum grain sizes in the north polar erg differs from what we would expect from terrestrial results. Dune fields on other planets are subject to different environments and different gravitational forces. In particular, the gypsum in the martian north polar erg is a special case because it is a much softer material than the quartz sands that have been studied on Earth. So, when we take into account the vast distances that the gypsum is being transported over in the north polar erg and the order of magnitude higher impact velocities it must experience on Mars than it would on the Earth, it is unclear with how much confidence terrestrial results can be applied to this special case. As such, spectral data on the grain size distribution of the gypsum could provide much needed insight into martian dune dynamics.

6.3 Variation of 1.9 μm band depth with abundance

Laboratory spectral data have also allowed us to empirically explore how the gypsum 1.9 μm band depth varies with abundance. The relationship between band depth and abundance may potentially be quite complicated; however, for the case of the circum-polar erg, the relationship can be slightly simplified. Because the process of saltation only occurs for a specific distribution of grain sizes (*e.g.* Bagnold, 1941), we can make the assumption that we know the typical grain size in the dunes. Observations from the Mars Exploration Rovers (MER) of basalt sand in recently active aeolian bedforms have indicated grain sizes of 100-300 μm (Sullivan *et al*., 2008). For our purposes, we have used a grain size bin with a range of 90-250 μm. To create model mixtures of potential dune components, we created intimate mixtures of

basalt and gypsum, with gypsum abundances of 5, 10, 15, 20, 25, 50, and 75 wt.%. We have chosen to use basalt because the mafic signatures observed by HST (Bell *et al.*, 1997) and OMEGA (Figure 2.6) may indicate a similar composition to the sand observed at the MER landing sites and on the rest of the planet (*e.g.* Bell *et al.,* 2004; Bibring *et al.,* 2005; Christensen *et al.,* 2000, 2004b; Gellert *et al.,* 2004; Morris *et al.,* 2006).

Figure 2.14 shows the change in 1.9 μm band depth with abundance for the basalt-gypsum sand mixtures, with a second-order polynomial trendline (R^2=0.9947). As would be expected, the band depth begins to saturate with high abundances (>70%). We find that sand-sized gypsum should be detectable (above 2-3% band depth) for more than 1-2 wt.%. For comparison, Poulet *et al*. (2007) presented a simulated mixture of gypsum and dust, and found that for 5 and 10 μm grains, the detection level of 2% was reached for >10 wt.% and >5 wt.% abundances, respectively. This indicates that the detection limit decreases with increasing grain size, so our detection limit of 1-2 wt.% for sand-sized particles seems to fit into this model.

Based on this laboratory data set, and the substantial assumptions that the hydrated minerals are all gypsum grains of sand size (100-300 μm; Sullivan *et al*., 2008), that these grains are mixed intimately with materials with spectral properties similar to basalt sand grains, and that the gypsum abundance can be calculated purely from the 1.9 μm band depth, we can make rough estimates for the abundances of hydrated minerals throughout the north polar region. Our threshold 1.9 μm band depth value of 4.5% corresponds to ~7 wt.% gypsum, and the hydration signatures outside of Olympia Planum, between 4.5 and 10% band depth, correspond to between ~7 and 13 wt.%. The maximum OMEGA 1.9 μm band depth values we observe in eastern Olympia Planum are near 26%, which corresponds to ~30 wt.% gypsum.

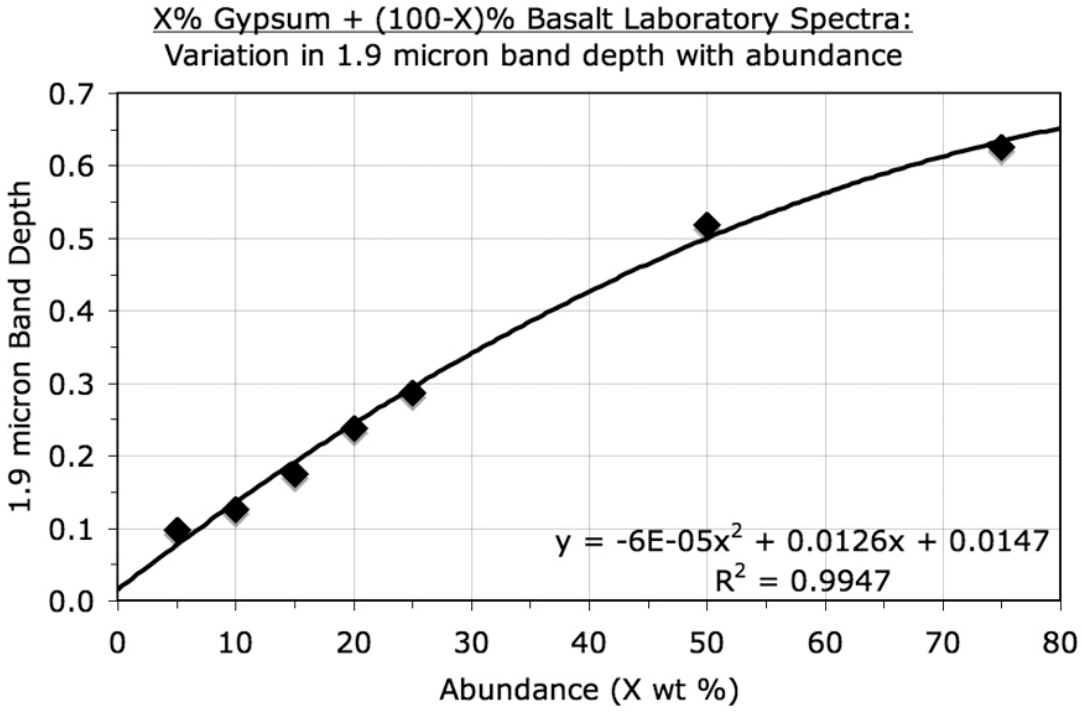

Figure 2.14: Laboratory measurements of variation of 1.9 μm band depth with gypsum abundance for sand-sized (90-250 μm) mixtures of gypsum and basalt. The trendline shown is a second order polynomial fit (R^2=0.9947), and indicates that the band approaches saturation for abundances greater than ~70 wt.%.

Because both the resolution of our map and the original data is at a scale larger than the dune crest separation distance (0.2-1 km; Lancaster and Greeley, 1990), the spectra we have analyzed represent an areal mixture of the dunes and the troughs. 30 wt.% therefore corresponds to the "bulk" value for all surface materials at these locations. The band depths we observe in CRISM spectra, as shown in Figure 2.12b, are typically ~25% at the dune crests, and decreasing down the flanks to ~10% in the bright troughs, which corresponds to a change in abundance from ~30 to ~13 wt.% in our model. The maximum band depths we observe in CRISM spectra are ~40%, which corresponds to ~42 wt.% gypsum in this model.

Our result of ~30 wt.% gypsum determined from OMEGA spectra of the gypsum rich region is somewhat lower than that predicted by the model of Fishbaugh *et al*. (2007), which yielded estimates of 45 wt.% 100 μm – 1 mm gypsum grains for an intimate mixture with a dark, spectrally featureless material with grains <45 μm, and nearly 100 wt.% gypsum of varying grains sizes for a mixture with inclusions of dark oxide grains. While the 45 wt.% gypsum result of Fishbaugh *et al*. (2007) is geologically and spectrally reasonable, the 100 wt.% gypsum result, which implies *in situ* alteration of the dune material, does not seem reasonable in the context of our hypothesis for a sulfate deposit that is older than the dunes.

However, the abundances we have calculated from our model are realistic only if the hydrated phase is indeed gypsum. While we have made the case that it is plausible that the hydrated mineral is gypsum (Section 5.5), these results should also be useful if the hydrated mineral is another polyhydrated sulfate. It seems reasonable to assume that the abundance calculated in our model from a given 1.9 μm band depth inherently depends on the number of water molecules in a hydrated mineral; thus, for a mineral with more water molecules per unit cell, our calculated abundance of that mineral (for a given 1.9 μm band depth) must decrease. As such, our estimated abundance of gypsum (2 water molecules per unit cell) will most likely be greater than any other more hydrated sulfate. Therefore, we believe that our calculations also provide a maximum estimate of the abundance of polyhydrated sulfate in the north polar sand sea.

7. Discussion

The distribution of hydrated minerals that we have mapped in the north polar region and its correlations with geologic features and units has raised many questions about the history of the north polar region, both in terms of aeolian transport and water

activity. In this section, we discuss the implications of our findings on our understanding of these processes.

7.1 Sources and transport of hydrated minerals

One of the most useful ways our map of the distribution of hydrated minerals in the north polar region can be used is to shed light on the sources and transport pathways of aeolian materials. Our results indicate that most of the circum-polar erg is sourced from the gypsum-rich sands of Olympia Planum, but that the lower hydration band depth of many dune fields in the region near Abalos Mensae and Chasma Boreale indicates that they are primarily sourced from outside of Olympia Planum, presumably from Planum Boreum units exposed in these regions. This may imply that the proposed source units for the dunes, primarily the Planum Boreum cavi unit with some contribution from the Rupes Tenuis unit (Tanaka *et al*., 2008; Tanaka and Hayward, 2008), do not contain hydrated minerals.

The hydrated veneers on Planum Boreum appear to be sourced primarily from the Planum Boreum 2 unit, based on the work of Rodriguez *et al*. (2007) and the gap discussed above between the hydrated layers and the top of the layered deposits, but an additional source for hydrated minerals in the Planum Boreum 1 unit cannot be ruled out. Given that these veneers may be highly mobile and more recently active than the dunes, the question of how these deposits have interacted still remains. If the veneers are formed from partly sand-sized material, they may contribute to dune formation and/or hydration, either presently or in the past.

The veneer-forming material may have been sourced from Olympia Planum in the Middle Amazonian. If the gypsum in Olympia Planum is sourced from a unit underlying the eastern dune field, it is possible that the epoch of net erosion that carved the polar troughs before the emplacement of the Planum Boreum 2 unit also

caused excavation, aeolian or otherwise, of the gypsum deposit, and redistribution throughout the region. After deposition onto Planum Boreum, the gypsum-rich material could have been covered and protected by Planum Boreum 3 and 4 units to this day, when it is now being eroded out of the troughs. This situation illustrates what may have been, and still is, a complex relationship between the units of Olympia Planum and the units of Planum Boreum.

If the hydrated component of the veneer-forming material is not sourced from the Olympia Planum gypsum deposit, then formation of the hydrated component is somewhat of a mystery. Materials on the surface of the topographically elevated and icy surface of Planum Boreum could have been altered by water to a hydrated mineral due to acidic snow (*e.g.* Langevin *et al*., 2005a), but otherwise, the hydrated component must have been sourced from some other, unknown region in the north polar basin.

The presence of a mobile layer overlying an icy core in the dunes, as suggested by Neutron Spectrometer modeling (Feldman *et al*., 2008), may have implications for the age and dynamics of the dune fields. In particular, it is possible that the putative indurated, potentially icy interiors or cores of the dunes were formed before the gypsum was exhumed from Olympia Planum. In this case, the cores would be free of hydrated minerals, and just the mobile top layer would be enriched. This may explain why not all dune fields exhibit hydration signatures – many of the mantled or indurated appearing dunes may just be the cores of previously active dunes that are not currently participating in aeolian activity. In this case, the hydration signature may indicate more recent aeolian deposition on these dunes, possibly due to the presence of a "mobile layer," as postulated by Feldman *et al*. (2008). This mobile layer could be partly composed of veneer material.

If the identification of a mobile layer is indeed key to understanding the transport pathways of the north polar region, future work on mapping of induration features throughout the circum-polar erg may help reveal its presence and distribution.

7.2 Interpretations of CRISM and HiRISE data

Our hypothesis of high gypsum concentrations at the crest of dunes in CRISM images raises several questions as to the nature of the gypsum within the dunes. Because gypsum is such a soft mineral, loose gypsum grains may be more likely to be broken down at the crest of dunes, where the wind exposure is greatest. Instead, the presence of gypsum at the crest suggests an indurated layer that is preferentially exposed, possibly by erosion of the indurated dune. Figure 2.15 shows a section of a HiRISE image over the highest gypsum concentration area. The crests of the dune exhibit pits and striations that may be indications of induration (Feldman *et al*., 2008). Note that the flanks of the dunes do not exhibit similar features indicative of induration. This may support the idea of an indurated gypsum layer exposed only at the crest. Interestingly, neither the crests nor troughs exhibit clear water ice spectral signatures (< 3% and < 2% 1.5 μm water ice band depths, respectively), which raises the question of how the putative indurated gypsum layer is related to the putative water ice core suggested by Neutron Spectrometer data.

Figure 2.15 also shows the presence of transverse aeolian ridges (TARs) in the bright troughs. Mars Exploration Rover Sprit observations in Gusev Crater have been used to interpret TARs as coarse grained (several mm) granule ripples (Sullivan *et al*., 2008). This implies that there should not be a great increase in overall grain size from trough to crest, and assuming that the gypsum size distribution follows that of the dune and ripple forming materials, this further suggests that the observed band depth changes from crest to trough may be indicative of abundance changes. Taking a

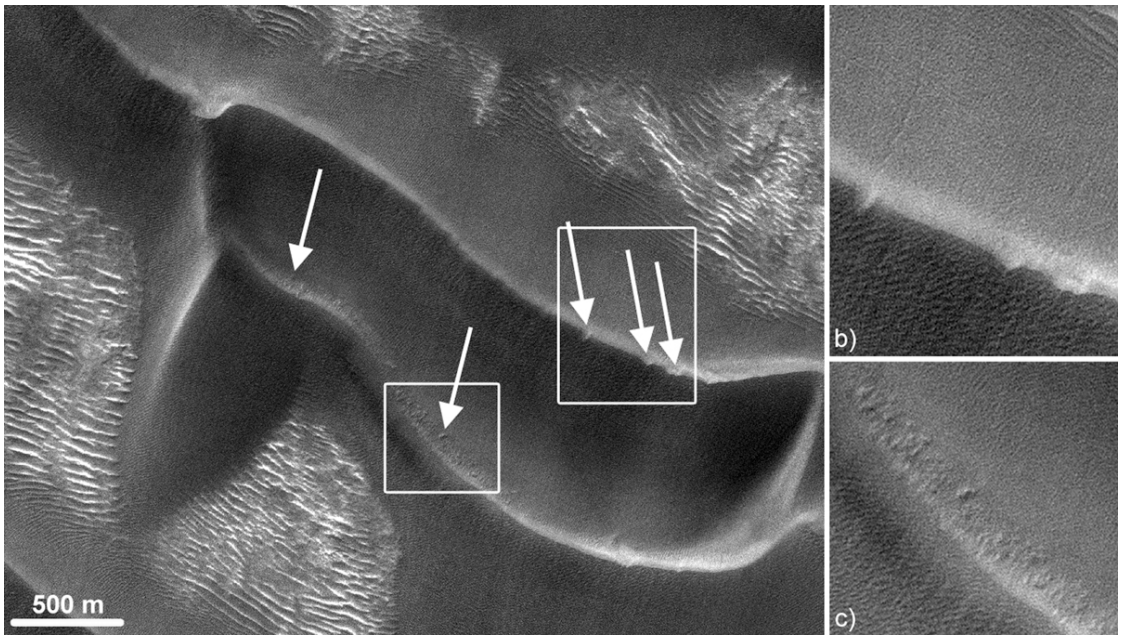

Figure 2.15: (*a*) Portion of HiRISE image PSP_001457_2600, located near 80°N, 246°E. Dune crests show evidence for induration, in the form of pits and striations, as indicated by arrows, and as shown in (*b*) and (*c*). Troughs exhibit transverse aeolian ridges.

potential increase in gypsum abundance into consideration with the problems of preserving loose gypsum at dune crests discussed above, this may support our hypothesis of an indurated layer of gypsum.

7.3 Possible hydrated mineralogies

While it is possible that all of the hydrated minerals we observe in the north polar region are gypsum, the soft nature of gypsum should make it difficult to keep the grains intact when saltating across large distances, and this puts into question the presence of gypsum in the dune fields farthest away from Olympia Planum (*e.g.* near 0°E). While we have suggested that the hydrated mineral is most likely a polyhydrated sulfate (Section 5.5), we cannot discount other possibilities. For example, the hydration signatures we observe in the dune fields outside of Olympia

Planum may be due to another hydrated mineral present at low concentrations in all dune sands sourced from Olympia Planum. This other mineral may be another sulfate – for example, jarosite, which has been identified by the Mars Exploration Rover Opportunity at Meridiani Planum as an aqueous alteration product of mafic materials (*e.g.,* Morris and Klingelhöfer, 2008), or some other hydrated phase like ferrihydrite, a nanophase weathering product of basalt (Deer *et al*., 1992; Bishop *et al.,* 1993; Jambor and Dutrizac, 1998). Future CRISM observations of the hydrated veneers and circum-polar dunes should prove helpful in determining their hydrated mineralogy.

7.4 Implications for proposed deposition mechanisms

If the hydrated minerals in Planum Boreum were indeed sourced from the gypsum deposit in Olympia Planum in the Middle Amazonian or earlier, their existence may not be consistent with the idea that the Olympia Planum gypsum was formed recently due to interactions between polar outflows and the dunes (Fishbaugh *et al*., 2007). However, as Olympia Planum appears to have a long history of dune activity and the underlying materials in Olympia Planum may be the remnants of paleo-ergs (Tanaka *et al*., 2008), formation of gypsum in mafic dunes is certainly a plausible formation mechanism farther in the past. Formation in the subsurface due to interactions with acidic groundwater is also certainly still plausible. An additional mode of formation might be deposition of gypsum elsewhere and fluvial transport to the current location, potentially during a catastrophic outflow from the southern highlands.

The fact that high concentrations of gypsum have been observed within a well-defined region of Olympia Planum suggests that this gypsum is being sourced from a coherent, localized deposit. Such a deposit would be unlikely to accumulate due to aeolian transportation from outside the region, as aeolian transport would most likely

spread such material more uniformly over the north polar region. Therefore, we conclude that this deposit was either formed *in situ*, or was transported by fluvial processes to its current location. Because the units the gypsum is apparently being sourced from have been identified as having an Amazonian crater-retention age and all surrounding units in the region have also been identified as having an Amazonian crater-retention age (*e.g.*, Tanaka *et al*., 2008), we must conclude that the gypsum was either transported to its current location or formed *in situ* during the Amazonian, either of which require significant water activity in the northern basin during the Amazonian. This conclusion does not fit into the current paradigm of a cold, arid Amazonian (*e.g.* Bibring *et al*., 2006). While the putative water event may have been a one-time, outlier event, it has introduced large quantities of otherwise absent minerals into the north polar region. At minimum, this suggests that singular, landscape altering events may have continued to shape the surface of Mars well into the Amazonian and possibly still are today. At the other extreme, if the proposed water activity was not a singular event in the north polar region, and instead the hydrated minerals represent long-term alteration of surface or sub-surface materials, then we must seriously rethink how the current paradigm for the history of water on Mars should be applied to the north polar region.

8. Conclusions

We have generated new maps that enhance our understanding of the distribution of hydrated minerals throughout the north polar region of Mars. These maps provide new constraints on the erosional, transport, and depositional processes that are presently and have previously operated in the north polar region, and they raise new questions regarding the history of water in the region. In this initial mapping

study of the 1.9 μm hydration band depth across the north polar region, we have arrived at the following results and conclusions:

(1) The presence of hydrated minerals in water ice-rich terrains can be detected by exploiting the symmetry of the 2 μm water ice band to estimate the 1.9 μm hydration band depth.

(2) Our results support the Langevin *et al*. (2005a) identification of gypsum in Olympia Planum.

(3) Hydrated minerals are present not just in the dune fields of Olympia Planum, but also in nearly all of the circum-polar erg as well as within Planum Boreum.

(4) The hydrated minerals, and possibly the materials in the circum-polar erg in general, appear to be sourced from Olympia Planum. Thus, the hydration signature in the dune fields outside of Olympia Planum is most likely also due to gypsum. However, other hydrated sulfate-bearing minerals, such as jarosite or ferrihydrite, could also be consistent with some of the observations.

(5) In Planum Boreum, hydrated minerals are present in the dark veneers that emanate from the troughs, and appear to be sourced primarily from the Planum Boreum 2 unit. These materials may have been sourced from the Olympia Planum gypsum deposit in an earlier, more highly erosive epoch.

(6) Our laboratory studies show that variations in the spectrum of gypsum with changes in grain size and abundance can be modeled to estimate the abundance

directly from the observed (or estimated) 1.9 μm band depth. Applying these methods to the highest gypsum concentration area in the north polar region yields a maximum abundance of 30 wt.% at OMEGA resolutions (at best 1.6 km/pixel in this study), and a maximum abundance of 42 wt.% at CRISM resolutions (>18m/pixel).

(7) The presence of hydrated minerals throughout the Amazonian units of the north polar region implies water activity in the north polar basin during the Amazonian, and suggests that we should carefully consider how and whether the current paradigm for the history of water on Mars applies to the north polar region.

CHAPTER 3

ICE INDURATION, SULFATE CEMENTATION, AND DUNE ACTIVITY IN THE NORTH POLAR SAND SEA OF MARS

0. Abstract

High resolution observations of dunes in the north polar sand sea of Mars reveal the presence of five classes of features indicating dune induration: slipface fans, pits/slumps, arcuate ridges, surface cracks, and rounded dunes/grooves. By examining the morphology and distribution of these features and searching for correlations with near-infrared spectral parameters, we show that: (1) indurated dunes on Mars appear to move via dry granular flows with different morphologies than non-indurated dunes that move via classic rectilinear slipface flows, (2) the dunes appear to be indurated by ice, and are undergoing modification consistent with sublimation of that ice, and (3) a strong correlation exists in some regions (*e.g.* Olympia Undae) between the occurrence of tensional cracks and the presence of sulfate spectral signatures, consistent with the dunes in those regions being chemically cemented. There are two major implications that may be drawn from these observations. Firstly, because chemical cementation requires liquid water and the dunes appear to have been active recently based on crater counts and morphologic indicators, this suggests that brines have been present within the dunes recently. Furthermore, evaporation of the brines may be concentrating gypsum near the surface of the dunes, suggesting that previous estimates of volumetric gypsum abundances in the dunes based on spectral models may be inflated, and that the dune substrate should be reconsidered as a potential gypsum source. Secondly, the ice induration and sulfate cementation of dunes that we postulate in the north polar sand sea could be responsible for the lack of observed dune migration in this area during more than 30 years of orbital monitoring. However, our

study also indicates that north polar dunes are still active today, albeit at small spatial scales (meters) and at slow migration rates.

1. Introduction

Cycles of sediment erosion and deposition have shaped much of the martian surface (*e.g.* Malin and Edgett, 2001); however, the processes responsible for sediment transport and lithification are poorly understood. An obvious and potentially active manifestation of these processes is in sand dunes, where saltation must overcome dune stabilization processes to induce dune migration. Many sand dunes on Mars appear dust and crater-free, and exhibit sharp crestlines and well-defined surface ripples (*e.g.* Marchenko and Pronin, 1995; Malin and Edgett, 2001; Fenton and Hayward, 2009). Dunes with these characteristics are most likely active under current climatic conditions, and could serve as a natural laboratory in which to study sediment transport on Mars. However, dune migration has not been observed anywhere on the planet over more than 30 years of orbital imaging, at a variety of spatial and temporal scales (*e.g.* Edgett and Malin, 2000; Zimbelman, 2000; Edgett, 2002; Schatz *et al*., 2006; Bourke, 2008; Fenton and Hayward, 2009). As such, progress in constraining sediment transport rates and influences has been limited to observations of erosion of small dome dunes (Bourke, 2008; Chojnacki *et al*., 2010) and slipface flow features (Fenton, 2006).

The dearth of observed dune movement is probably not due to a lack of wind speeds above the saltation threshold for loose sand, as saltation of individual grains and ripple migration have regularly been observed from the Mars Exploration Rovers during wind events (Sullivan *et al*., 2008), ripple migration and dune erosion have been observed in some orbital images (Bourke, 2008; Chojnacki *et al*., 2010; Silvestro *et al*., 2010), and streaks of dark sand are often observed downwind of dunes (*e.g.*

Tanaka *et al*., 2008). Instead, it has been hypothesized that the lack of migration is due to induration, or stabilization, of the dunes (*e.g.*, Schatz *et al*., 2006). Ultimately, while available *in situ* and orbital observations suggest that induration of sediments is a common process on Mars, it is unknown what mechanisms cause induration, what timescales these mechanisms act over, and how these mechanisms affect dune morphology and migration.

Possible induration mechanisms can be divided into three categories: physical induration, chemical cementation, and ice induration. Physical induration occurs through settling and compaction of sand and/or dust to create a well-packed surface. With burial, compaction can result in lithification of the sediments (*e.g.*, Weller, 1959), although on Earth, this process is usually aided by water.

Chemical cementation occurs when grains are cemented together by minerals precipitated out of a fluid. Specific forms of chemical cements include calcrete/caliche (calcium carbonate cement), silcrete (amorphous silica cement), ferricrete (ferric oxide cement), gypcrete (gypsum cement), and salcrete (salt cement) (*e.g.*, Lamplugh, 1902; Yasso, 1966). Laboratory tests have shown that less than 1 wt.% salt in sand can significantly increase the wind speed necessary to start saltation, and that this speed increases exponentially with salt concentration (Nickling and Ecclestone, 1981; Nickling, 1984). Salts or other cementing agents can be derived from allocthonous materials or from the sediments themselves, as in the gypsum dune fields of White Sands National Monument, where percolating groundwater dissolves and re-precipitates the gypsum in pore spaces (*e.g.,* Schenk and Fryberger, 1988).

Ice induration occurs when a bedform is stabilized by snow or ice (*e.g.,* Cailleux, 1978). On Earth, the most common form of ice induration in dunes results from alternating or concurrent sand and snow deposition. Dunes formed by this process are known as niveo-aeolian bedforms, and are common in terrestrial polar

deserts (*e.g.*, Calkin and Rutford, 1974; Koster and Dijkmans, 1988; Dijkmans, 1990; McKenna-Neuman, 1990). Niveo-aeolian bedforms <<sizes?>> have been shown to exhibit much slower migration rates (on the order of a meter/year) than warm-climate dunes (on the order of tens of meters/year) because of the indurating effect of the ice and snow (*e.g.*, Ahlbrandt and Andrews, 1978; Bourke *et al*., 2009; Bristow *et al*., 2010).

On Mars, all three of these induration processes may be operating. Indurated surface crusts have been observed at all mid and low-latitude landing sites (Arvidson *et al.*, 1989, 2004; Moore *et al*., 1999; Sullivan *et al*., 2008), possibly implying that induration is caused by a widespread process (Sullivan *et al*., 2008). However, similar surface crusts have not been reported at the Phoenix landing site, suggesting that there may be a latitudinal or compositional limit on this unspecified mid- and low-latitude induration process, or that the process is hindered by periglacial/polar processes. Infiltration of dust and dust aggregates into loose particles may provide a mechanism for physical induration; however, it is not clear that this process would result in internal cohesion on the scale of the observed crusts (*e.g.*, Sullivan *et al*., 2008). Cementation by sulfates could be consistent with Viking 1 X-Ray Fluorescence Spectrometer measurements of sulfur enrichment in surface crusts (Clark *et al*., 1977, 1982). Similar sulfate cements could be widespread on Mars if they are derived from interactions between atmospheric water vapor and either *in situ* sulfate-bearing materials or atmospheric dust. However, further attempts at analyzing surface crust compositions at other landing sites were either not possible or were not successful (*e.g.*, Sullivan *et al*., 2008), so this hypothesis has not been confirmed. Cementation of dunes by ice has been proposed for several mid- and high-latitude dune fields on Mars, based on the inferred presence of subsurface ice from Mars Odyssey Neutron Spectrometer (MONS) hydrogen abundance measurements (Feldman *et al*., 2008),

thermal inertia models (Bandfield and Feldman, 2008; Putzig *et al*., 2010), a strong correlation in the southern hemisphere between latitude and apparent dune stabilization based on morphology (Fenton and Hayward, 2009), and the morphology of putative niveo-aeolian features (Bourke, 2005; Feldman *et al*., 2008; Diniega *et al*., 2010; Bourke, in prep). Under current climatic conditions, such ice would most likely be water ice deposited as pore ice during diffusion of water vapor (Bourke, 2005); however, CO_2 ice induration could also play a role during periods of low obliquity (*e.g.*, Kreslavsky and Head, 2010).

The goal of this study is to characterize the relative importance of different potential modes of dune induration by searching for morphologic and spectral evidence of induration within the north polar sand sea, which encircles the north polar plateau (Planum Boreum, see Figure 3.1 for geographic context). By studying and constraining the rates and spatial occurrences of these processes, we also aim to predict how factors like composition and location affect the relative activity level of dunes, in order to help identify potentially active dunes and dune fields for future dune migration detection efforts.

2. Study region: The north polar sand sea

The north polar erg (sand sea) of Mars is one of the largest known sand seas in the solar system. With an estimated area of 10^5-10^6 sq. km, the north polar sand sea is larger than any terrestrial sand sea (Lancaster and Greeley, 1990; Hayward *et al.*, 2010), and is only rivaled in size by the equatorial sand seas of Titan (~10^6-10^7 sq. km; Lorenz and Radebaugh, 2009). The sand is likely currently sourced from within Planum Boreum, the north polar plateau, which is composed of layers of sand, dust, and ice (Tanaka *et al*., 2008). Much of the north polar erg appears relatively young and perhaps recently active, as most dunes in the sand sea appear fresh, with low

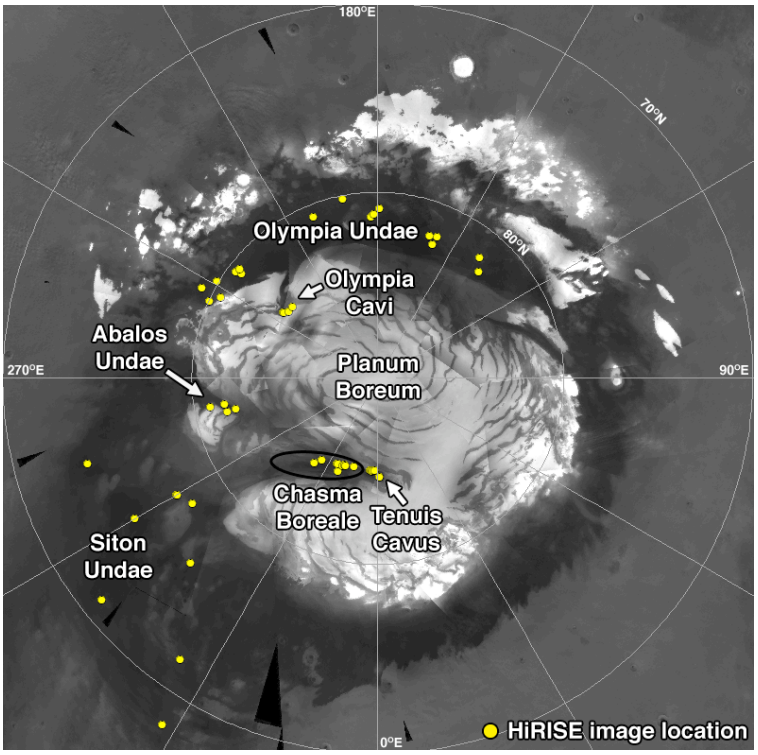

Figure 3.1: Major landmarks in the north polar region and locations of analyzed HiRISE images over MOC-WA.

albedos indicating minimal dust cover, potentially due to recent saltation. Recent searches in HiRISE images across 1640 sq. km in Olympia Undae for impact craters >5 meters in diameter have revealed exactly one crater (Kreslavsky, 2010). Although extracting an absolute crater retention age of the surface from such a small statistic is problematic, estimates place it on the order of 0-1000 years. Regardless, the lack of impact craters >5 meters in diameter implies that Olympia Undae, and possibly the rest of the sand sea, is very young and has been active under current climatic conditions (Kreslavsky, 2010).

The north polar sand sea is an ideal locale to study the relative effects of potential induration processes on martian dunes, as sub-surface ice and possible cementing agents like soluble sulfates are both present in the dunes (*e.g.*, Feldman *et al*., 2008; Langevin *et al*., 2005a).

2.1 Evidence for sulfates

The primary composition of the north polar erg is mafic, but alteration products are present throughout. Near-infrared (NIR) spectra of dunes within Olympia Undae from the Mars Express OMEGA imaging spectrometer (Bibring *et al*., 2005) are consistent with the presence of the hydrated calcium sulfate gypsum (Langevin *et al*., 2005a; Horgan *et al*., 2009). Although the highest gypsum concentrations (inferred to be up to 40 wt.%) are limited in extent (Fishbaugh *et al*., 2007; Horgan *et al.*, 2009), gypsum or another sulfate is likely present at lower levels (less than 10 wt.%) throughout the entire sand sea (Horgan *et al*., 2009). Even a small amount of sulfate present throughout much of the erg could be enough to cause cementation under terrestrial conditions, by analogy with the Nickling and Ecclestone (1981) and Nickling (1984) experiments; however, the limiting factor on Mars is the availability of liquid water in which to dissolve and transport the sulfates. If liquid water is not at least transiently present within the dunes under current or recent climatic conditions, then even the abundant gypsum in parts of Olympia Undae may not be able to cement the dunes.

2.2 Evidence for dune interior ice

Analysis of Neutron Spectrometer and thermal infrared data at a range of scales (100 m – 600 km) indicate that Olympia Undae is best modeled as an ice-cemented layer covered by a layer of non-indurated, ice-free sand, with ice burial depths on the order of 10 cm (Feldman *et al*., 2008; Bandfield and Feldman, 2008; Putzig *et al*., 2010; Titus *et al*., 2010). Based on this model, Feldman *et al.* (2008) proposed that the dune interiors are cemented by pore ice. Morphologic features on the dunes that have been cited in support of this hypothesis include: pits and chains of pits along dune crests, interpreted as collapse features resulting from denivation

(sublimation and/or melting of ice); narrow sinuous depressions, interpreted as tensional surface cracks resulting from change in volatile volume below a coherent surface layer; and high albedo arcuate ridges exposed in interdune areas, interpreted as the permafrost indurated remnants of barchan dune strata (Feldman *et al*., 2008). The pore ice could be sourced from atmospheric water vapor, seasonal water frost, or from ground ice melt and/or vapor mobilizied by the warm overlying dune (*e.g.*, Wood *et al*., 2010).

3. Methods

3.1 Feature mapping

In this study, we have used high-resolution (25-50 cm/pixel) Mars Reconnaissance Orbiter High Resolution Imaging Science Experiment (MRO/HiRISE; McEwen *et al*., 2007) images to identify and map decameter-scale features on sand dunes in the north polar erg. The observation ID's of all HiRISE images used in this study are listed in Table 3.1, and their locations are shown in Figure 3.1. All images were taken during northern summer (solar longitudes or L_S 90-180°) and under illumination conditions such that the majority of both the slipfaces and stoss slopes of the dunes were well lit. For consistency in mapping features, all images were projected into a north polar stereographic projection in ESRI ArcGIS and then examined in 1500x1500 meter quadrangles at a 1:7200 map scale. Only features apparent at this scale were included in the maps. We have divided the observed dune surface features into five classes based on morphology and association: slipface fans, pits/slumps, arcuate ridges, surface cracks, and rounded dunes/grooves.

TABLE 3.1: HiRISE images used in this study.

HiRISE image ID	Latitude	Longitude	Solar Lon.	Region
PSP_010071_2615	81.5°N	139.6°E	129.4°	W Olympia Undae
PSP_009728_2620	82.1	136.6	116.7	W Olympia Undae
PSP_010400_2620	81.7	157.1	141.9	W Olympia Undae
PSP_001460_2625	82.2	157.7	137.1	W Olympia Undae
PSP_009912_2620	81.9	160.0	123.5	W Olympia Undae
PSP_009674_2610	80.9	179.4	114.8	Mid Olympia Undae
PSP_009832_2615	81.2	181.5	120.5	Mid Olympia Undae
PSP_009898_2615	81.3	182.5	122.9	Mid Olympia Undae
PSP_001736_2605	80.2	191.2	147.9	Mid Olympia Undae
PSP_009647_2605	80.6	201.7	113.8	Mid Olympia Undae
PSP_009693_2790	80.7	232.6	115.5	E Olympia Undae
PSP_009904_2795	80.5	231.8	123.2	E Olympia Undae
PSP_010049_2795	80.5	233.2	128.5	E Olympia Undae
PSP_009764_2600	79.9	239.0	118.0	E Olympia Undae
PSP_010120_2605	80.5	242.9	131.2	E Olympia Undae
PSP_001457_2600	80.0	245.4	137.0	E Olympia Undae
PSP_009540_2595	79.4	242.8	110.0	E Olympia Undae
PSP_009882_2640	84.0	230.1	122.4	Olympia Cavi
PSP_009105_2640	84.0	233.3	94.8	Olympia Cavi
PSP_009236_2640	83.8	235.3	99.3	Olympia Cavi
PSP_009052_2640	83.8	235.3	92.9	Olympia Cavi
PSP_010369_2625	82.2	282.2	140.7	Abalos Undae
PSP_009367_2620	81.7	282.6	103.9	Abalos Undae
PSP_010501_2615	81.6	279.6	145.8	Abalos Undae
PSP_010219_2785	81.6	279.9	134.9	Abalos Undae
PSP_009433_2610	80.9	279.8	106.2	Abalos Undae
PSP_001375_2485	68.3	328.0	133.9	Siton Undae
PSP_001468_2515	71.1	308.7	137.4	Siton Undae
PSP_001758_2560	75.9	314.7	148.7	Siton Undae
PSP_009669_2520	71.6	324.9	114.6	Siton Undae
PSP_009195_2550	75.0	300.0	97.9	Siton Undae
PSP_009736_2575	77.5	300.1	117.0	Siton Undae
PSP_009696_2575	77.5	300.1	115.6	Siton Undae
PSP_010422_2540	73.8	286.4	142.8	Siton Undae
TRA_000861_2580	78.0	303.9	114.9	Hyperborea Undae
PSP_010085_2750	85.0	339.6	129.9	Chasma Boreale
PSP_001518_2650	85.0	339.0	139.3	Chasma Boreale
PSP_001374_2650	85.0	338.9	133.8	Chasma Boreale
PSP_009905_2650	85.0	337.5	123.2	Chasma Boreale
PSP_009914_2750	84.9	334.6	123.5	Chasma Boreale
PSP_010682_2650	84.9	334.7	153.1	Chasma Boreale
PSP_009470_2645	84.6	336.6	107.5	Chasma Boreale
PSP_009114_2645	84.7	325.6	95.1	Chasma Boreale

Table 3.1 (Continued)

PSP_009075_2645	84.3	323.1	93.7	Chasma Boreale
PSP_001784_2630	82.7	315.4	149.8	Chasma Boreale
PSP_008968_2650	84.7	0.8	90.0	Tenuis Cavus
PSP_009272_2650	84.7	0.8	100.6	Tenuis Cavus
PSP_009232_2650	85.0	358.2	99.2	Tenuis Cavus
PSP_009416_2650	85.1	356.3	105.6	Tenuis Cavus
PSP_009219_2650	85.1	356.2	98.7	Tenuis Cavus
PSP_009760_2650	85.0	355.4	117.9	Tenuis Cavus
PSP_009166_2650	85.0	355.4	96.9	Tenuis Cavus
PSP_010208_2650	85.1	344.6	134.5	Tenuis Cavus

3.2 Spectral analysis

If sulfates or ice are causing induration of dunes in the north polar sand sea, then we could expect correlations between near-infrared (NIR) spectral indicators of sulfates or water ice and various classes of induration features. However, NIR spectra only sample the upper few μm to tens of μm of the surface, so a broad-scale correlation might only exist if the sulfates and/or ice are cementing the uppermost surface of the dunes. Ice, in particular, is expected to be responsible for bulk volumetric induration of the dunes based on the thermal and neutron models discussed above, but the bulk ice content of the dunes might not be related to the ice content of their surfaces. Instead, it might only be possible to spectrally confirm ice induration of the dunes by locating specific places where the dune interior has been exposed by erosion or collapse of the dune surface.

For analyzing the broad scale spectral properties of the north polar sand sea, we have constructed a north polar mosaic from Mars Express OMEGA observations (Bibring *et al*., 2005). The mosaic was constructed from early summer (L_S=90-135°), atmospherically corrected (Horgan *et al*., 2009; see Chapter 2), moderate phase angle (<60°) OMEGA spectral cubes at wavelengths between 0.95 and 2.5 μm. All observations were converted to Lambert albedo (division by the cosine of the

incidence angle) and projected into a north polar stereographic projection with an average resolution of 1 km/pixel. Spectra for the final mosaic were selected based on minimum spectral contamination by surface and atmospheric dust (lowest albedo at 1.1 μm).

For higher resolution (18-36 m/pixel) spectral analysis of individual dunes, we have used spectral data from the MRO Compact Reconnaissance Imaging Spectrometer for Mars (CRISM; Murchie *et al*., 2009). All CRISM observations used in this study are center-swath images taken during northern summer (L_S=90-180°) that overlap with our mapped HiRISE images. All CRISM images were atmospherically corrected, despiked, and destriped using the CRISM Analysis Tools package for ENVI, converted to Lambert albedo, then mapped into a north polar stereographic projection.

Hydrated sulfates and water ice exhibit strong NIR absorption bands. Hydrated sulfates, like those identified in the north polar sand sea, exhibit narrow absorptions near 1.4 and 1.9 μm due to H_2O in their crystal structure, while water ice exhibits wide, strong absorptions near 1.5 and 2.0 μm (*e.g.* Clark *et al*., 1981). Here we have employed spectral parameters described by Horgan *et al*. (2009) (Chapter 2) for detecting water ice, hydrated minerals, and hydrated minerals in the presence of water ice in OMEGA data, and the BD1500, BD1750, and BD1980 parameters described by Pelkey *et al*. (2007) for searching for spectral signatures from water ice, gypsum, and hydrated minerals, respectively, in CRISM data. All spectral maps were imported into ArcGIS for comparison to HiRISE feature maps, and projected CRISM images were georeferenced to HiRISE images where possible. All possible detections were confirmed by comparing the surface spectra with laboratory spectra (RELAB spectral library; Pieters *et al*., 1995).

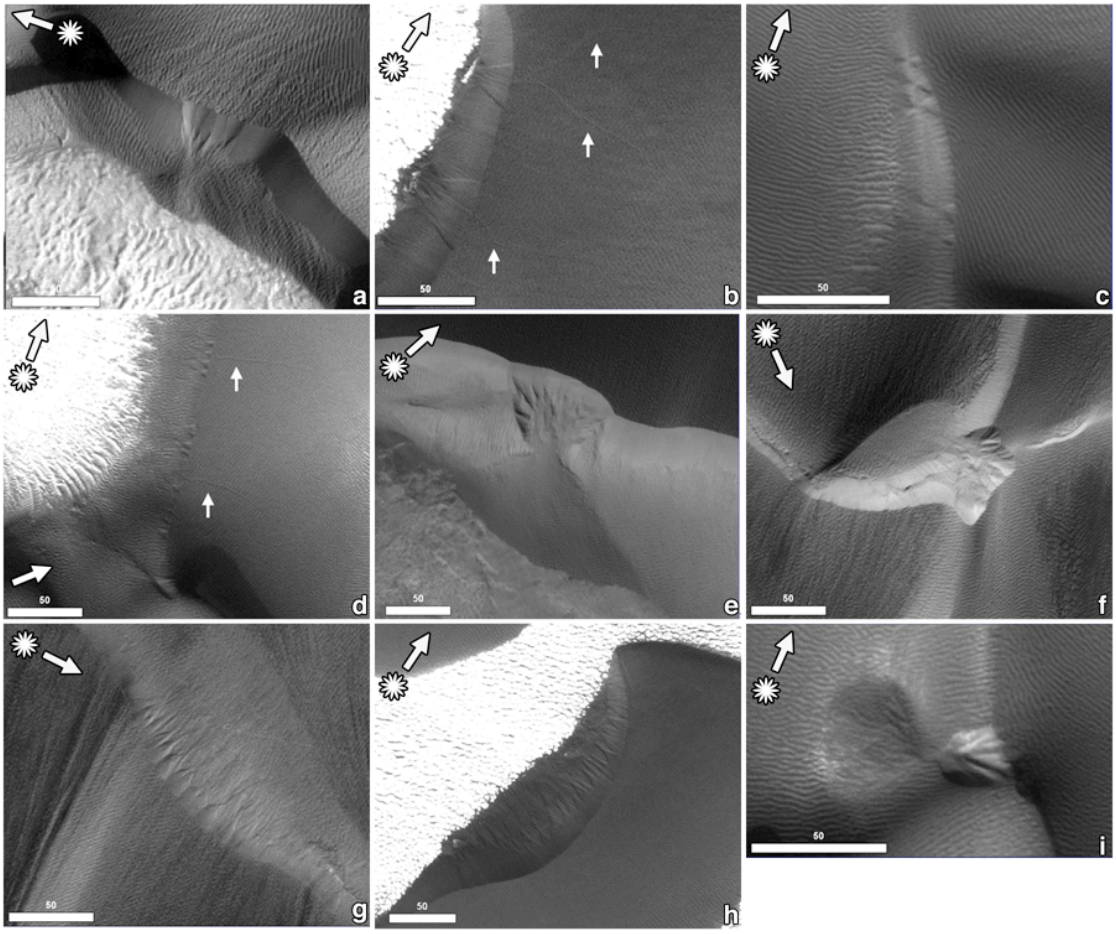

Figure 3.2: Fan morphology examples from HiRISE images. (a) Slipface fan with steep sides (Chasma Boreale: PSP_010682_2650). (b) Simple fans with stoss slope cracks, as indicated by arrows (Tenuis Cavus: PSP_008968_2650). (c-d) Small fans, cracks (arrows), and fan with extensive deposits (Olympia Undae: PSP_009904_2795). (e-f) Large, complex fans (Tenuis Cavus: PSP_9905_2650, Olympia Cavi: PSP_9105_2640). (g-h) Overlapping fans producing a sawtooth pattern (Olympia Cavi: PSP_9252_2640, Tenuis Cavus: PSP_8968_2650). (i) Medium complex fan with fresh, symmetric deposits (Olympia Undae: PSP_9693_2790). All scale bars are 50 meters in length, images have been linearly stretched for contrast, and solar illumination direction is indicated.

4. Observations

4.1 Slipface fans

The most common slipface feature that we have observed in the chasma are wedge-shaped alcoves above fan-shaped deposits (Figure 3.2a-b), hereafter referred to as "fans". The width of the alcoves is typically on the order of 10 m, but ranges up to several hundreds of meters. Small fans (~10 m wide) are usually characterized by a single shallow, symmetric alcove (Figure 3.2b-d), intermediate fans often incorporate several overlapping, shallow alcoves (Figure 3.2a,i), and the much rarer large fans exhibit numerous deep, channeled alcoves (Figure 3.2e-f). Features similar to these largest fans have been identified in the Rabe Crater dune field at 35°E, 44°S (Fenton, 2006; Schatz *et al*., 2006) and in the Kaiser Crater dune field at 19°E, 47°S (Bourke, 2005). Regardless of size, the alcoves are easily identifiable under favorable lighting conditions because of their steep sides. Individual alcoves commonly cluster or overlap on slipfaces, producing a sawtooth morphology (Figure 3.2g-h). Most fan deposits appear to be conical, smooth, and symmetric, without evidence for lobate flow features or multiple flow events (Figure 3.2i), and generally do not extend far beyond the base of the slipface, implying a flow not substantially fluidized by volatiles. Some fan deposits on the long, shallower slopes of transverse dunes in Olympia Undae extend up to 50-100 meters beyond the alcove, sometimes with overlapping, lobate deposits (Figure 3.2d). The length of these deposits appears to be related to the length of the slopes, and as the length decreases, the deposits take on the morphology of the short, symmetric deposits typical of slipfaces. While the shape and magnitude of these slopes are unknown, it is plausible that the upper portion of the slopes where the alcoves have formed is steep, with slopes comparable to those of a normal slipface, while the lower portion of the slope where the deposits run out is

much shallower. Such slope "breaks" have previously been suggested for slipfaces in Olympia Undae (Deniega *et al*., 2010).

Observations indicate that these fans are actively forming under current climatic conditions. For example, comparison of co-located HiRISE images taken during consecutive summers reveals new fans forming between the observations (Figure 3.3a-c), although we have not been able to constrain the formation of the fans to a specific range of L_S. Furthermore, one pair of images taken during the same summer shows a fan undergoing major erosional modification (Figure 3.3d). The apparent total removal of all flow material from the feature in Figure 3.3d appears to be a common process, as fan alcoves often lack associated fan deposits. Additionally, many fan deposits abruptly terminate at the edge of grainfall deposits in the lee of the dunes. These deposits are formed by saltating grains that fall within the wind shadows of dunes, and beyond these deposits, turbulent winds remove loose sand. Together, these observations suggest that fan deposits are largely composed of loose, non-indurated grains.

Fans are generally found on dunes that appear recently active because of their sharp crestlines, both in the polar chasma and in Olympia Undae. Although dune fields are present throughout the chasma, the fans observed to date occur more frequently along the margins of dune fields closest to the large polar scarps than anywhere else in the erg. These steep scarps are hypothesized to be shaped dominantly via undercutting by katabatic winds, which flow down from the cold surface of Planum Boreum onto the warm plains and dunes below, and indicate the flow paths of the strongest winds in the chasma (Howard, 2000; Warner and Farmer, 2008). In Olympia Undae, the observed fans have a strong dependence on slipface direction. For example, in eastern Olympia Undae, fans are found only on east-facing slipfaces (Figure 3.2c-d), while in western Olympia Undae, fans are found only on west-facing slipfaces. In both regions,

Figure 3.3: Active fans in Chasma Boreale. (a-c) Pairs of images showing new fans formed between consecutive summer seasons (L_S=140 and L_S=130). Left images: PSP_001518_2650, right images: PSP_010085_2750. (d) Pair of images showing a fan undergoing erosion between L_S=123 and L_S=153 during one summer season. Left image: PSP_009914_2750, right image: PSP_010682_2650. Scale bars are 50 meters in length, and solar illumination direction is indicated. MY indicates the Mars year of the observation (Clancy *et al.*, 2000; Smith, 2004).

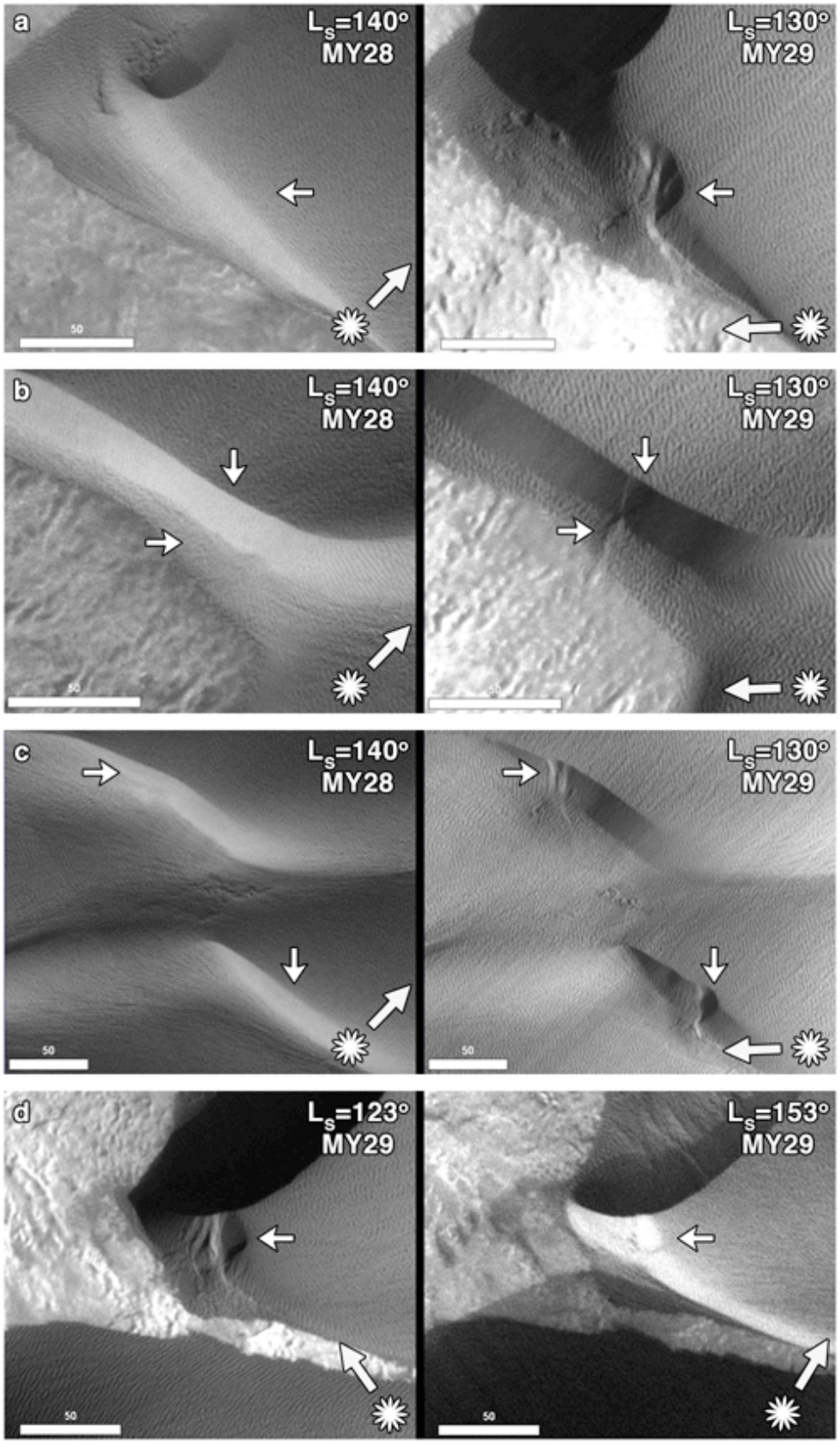
a
L_s=140°
MY28
L_s=130°
MY29
b
L_s=140°
MY28
L_s=130°
MY29
c
L_s=140°
MY28
L_s=130°
MY29
d
L_s=123°
MY29
L_s=153°
MY29

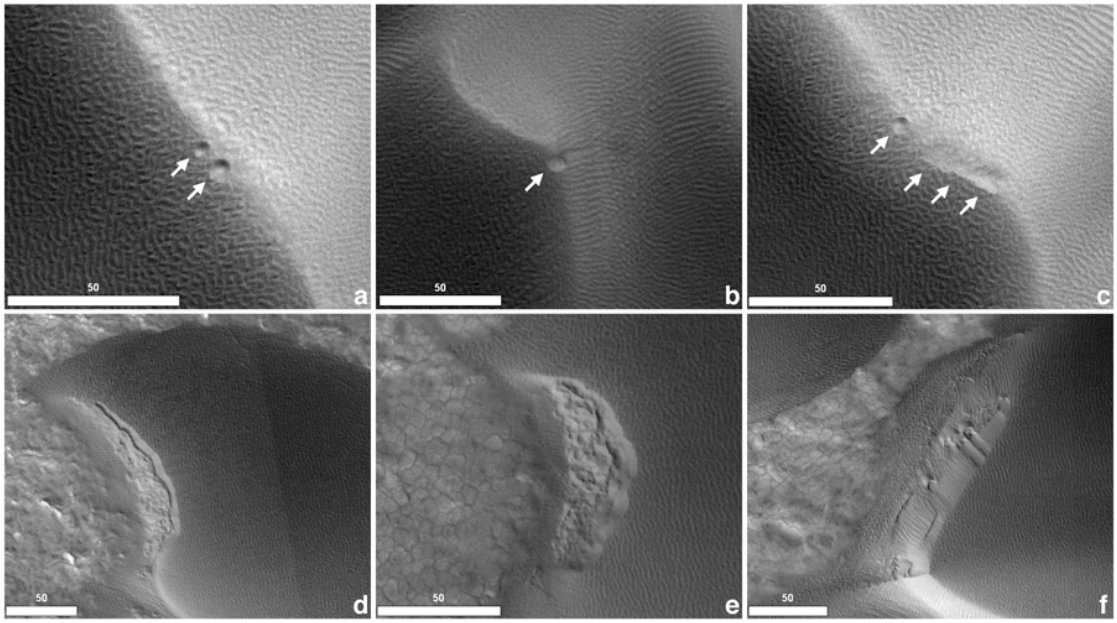

Figure 3.4: Slump and pit morphologies. (a-b) Pits on crestlines (Olympia Undae: PSP_001736_2605, PSP_009647_2645). (c) Pit and coalesced chain of pits on crestline (Olympia Undae: PSP_001736_2605). (d-e) Slumped barchan slipfaces with pitted debris (Chasma Boreale: PSP_009905_2650, PSP_001374_2650). (f) Slumped and pitted slipface with rectilinear collapse features (Chasma Boreale: PSP_009905_2650). All scale bars are 50 meters in length. Solar illumination is from the upper right in (a-c) and from the lower left in (d-f).

fans and sharp crestlines are not observed on bedforms with slipfaces facing any other direction, even where the major bedforms have other orientations. This suggests that solar insolation and other seasonal processes, which would likely create features on northerly or southerly slipfaces, are not a major influence on fan formation in Olympia Undae. Instead, the directionality of the fans could be a manifestation of the direction of the last major wind event or series of wind events, which are commonly easterly or westerly in this region (*e.g.*, Thomas and Gierasch, 1995). Thus, in both Olympia Undae and the chasma dune fields, the distribution and orientation of fans suggest that wind is key in the formation of these features.

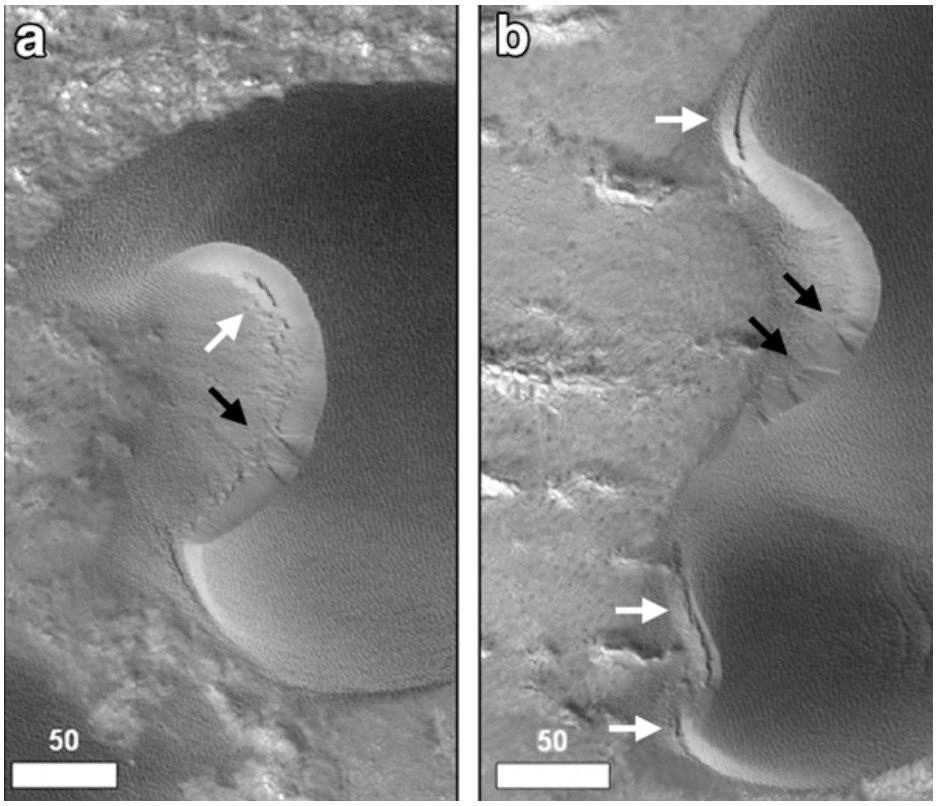

Figure 3.5: Slumps (white arrows) and fans (black arrows) have distinct morphologies that are apparent when they occur on the same dune or even the same slipface (Chasma Boreale: PSP_009905_2650). Solar illumination is from the lower left.

4.2 Pits and slumps

While slipface fans are ubiquitous throughout the north polar sand sea, the dunes also exhibit another class of apparent collapse features, here termed pits and slumps. Pits are circular collapse features that occur as isolated pits, chains of pits, or coalesced chains of pits (Figure 3.4a-c; Feldman, 2008; Bourke, in prep). These features could be confused with small impact craters, but their almost exclusive occurrence on dune crests, often at regular intervals along the crests, suggests that they are instead formed by an endogenic process. Slumps are slipface collapse features with hummocky debris, with the collapse occurring either along a portion of or over the entire length of the slipface (Figure 3.4d-f; Bourke, in prep). We have placed pits and

slumps into the same class of features because they are often difficult to distinguish, as the debris from large slumps are often pitted (Figure 3.4d-e), and small slumps often terminate in pits (Figure 3.4f). Slumps are most common on barchanoid slipfaces, while crestline pits are most common on the symmetric transverse or reversing dunes in central Olympia Undae.

Although both are collapse features, slumps have a distinct morphology from fans, implying that the two classes of collapse features form either under different conditions and/or via different processes. This is most apparent on dunes that exhibit both slump and fan-like collapse features, even on the same slipface (Figure 3.5). Slumps and fans also differ in their distribution: while both occur on dunes with sharp crestlines, slumps also occur on rounded dunes, where fans are rare (see Section 4.5).

Slump deposits are occasionally associated with bright material exposed in the lee of dunes. This bright material may be ice, but we have not observed water ice Spectroscopic signatures associated with slumps or pits above the noise level (~2%) at the resolution of CRISM observations, although this could be because the bright deposits are not large enough to be resolved with CRISM.

4.3 Arcuate ridges

Many dunes exhibit arcuate ridges exposed on or protruding from their stoss (windward) slopes (Figure 3.6a), often with morphologies mimicking that of the slipface and horns of the dunes (Figure 3.6b; Bourke, in prep). In the polar chasma, these ridges are most commonly observed on barchanoid dunes near the margins of dune fields, especially where the margin is near a polar scarp (Figure 3.7a). These features also appear to correlate with dune size, as they are much more common on small barchans and barchanoids than on larger barchans (Figure 3.7b). Arcuate ridges are also occasionally observed occuring as regularly spaced sets behind the stoss

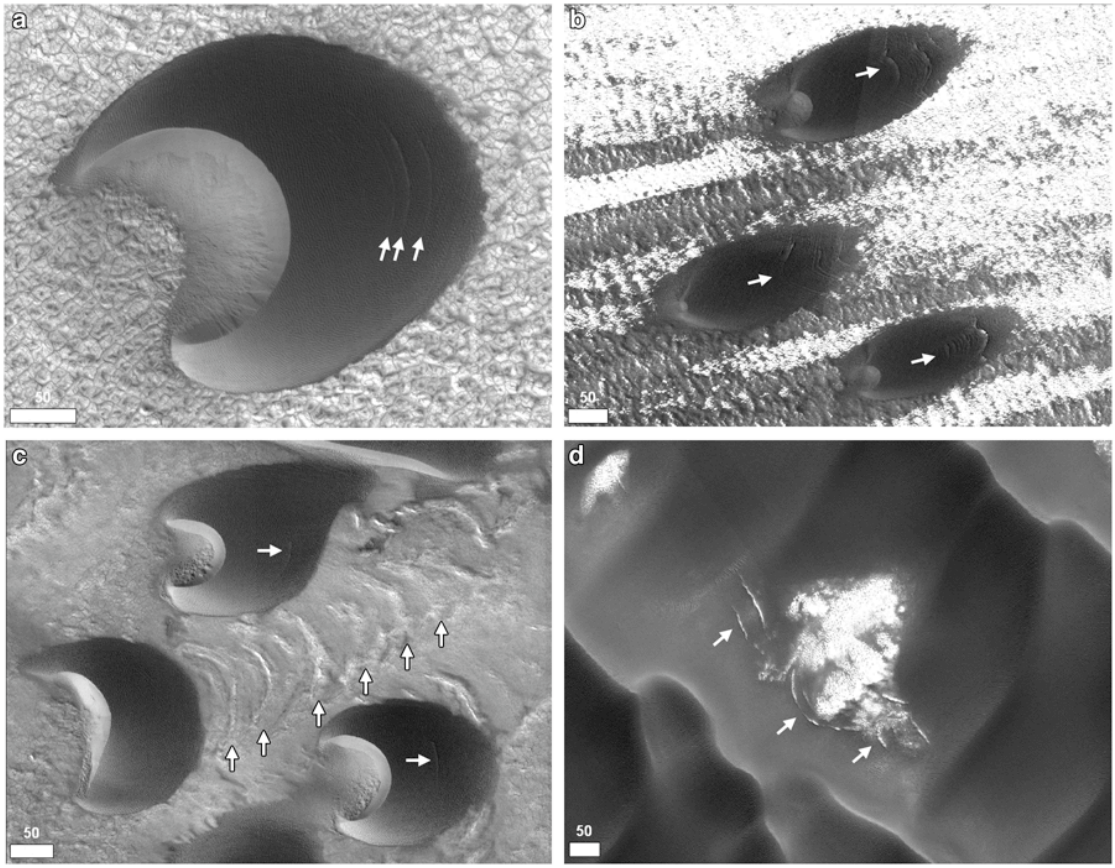

Figure 3.6: (a-b) Ridges, interpreted as indurated slipface strata, exposed on stoss slopes of dunes. Note that ridge shapes match shapes of slipfaces (Chasma Boreale: PSP_009905_2650, PSP_009075_2645). (c) Ridges exposed on stoss slopes and remnant ridges in path of dune (Chasma Boeale: PSP_001374_2650). (d) Remnant ridges exposed in interdune (Olympia Undae: PSP_009647_2605). All scale bars are 50 m in length. Solar illumination is from the lower left in (a-c) and from the upper right in (d).

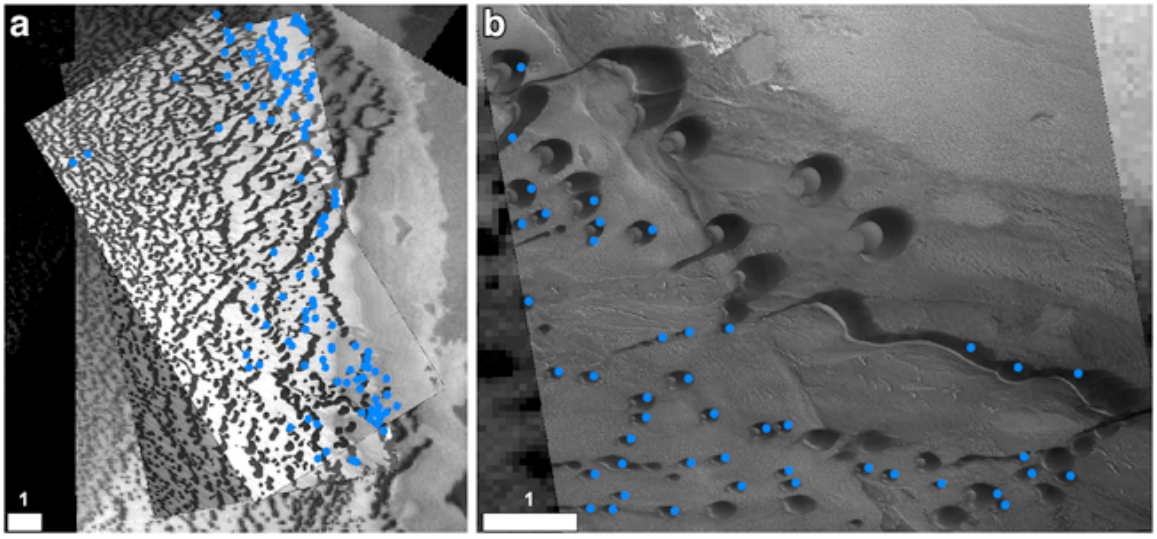

Figure 3.7: Distribution of stoss slope ridges (blue dots) in selected regions of Chasma Boreale. (a) Stoss slope ridges are most often observed on the margins of barchan dune fields (Tenuis Cavus, near the Chasma Boreale head scarp: PSP_008968_2650, PSP_009272_2650 over THEMIS-VIS). (b) Stoss slope ridges are also more common on smaller barchans than on large barchans (Chasma Boreale: PSP_009905_2650). Solar illumination is from lower left in (b).

slopes of dunes, preserved as features on the dune substrate (Figure 3.6c; Bourke, in prep). However, these preserved ridges are rare, even in areas where most dunes exhibit well formed ridges protruding from their stoss slopes (*e.g.*, Figure 3.6b). Stoss slope ridges and these remnant ridges do not appear to be associated with any significant spectral signature at the resolution of CRISM.

In the transverse dunes of Olympia Undae, light-toned arcuate ridges are observed, and occur as either raised ridges exposed on the floor of the interdunes with morphologies that generally do not resemble that of the dunes around them (Figure 3.6d), or as thin, bright arcs on shallow, secondary stoss slopes in the troughs of the primary bedforms (Figure 3.8b). The thin arcs generally occur as regularly spaced sets trending down the interdune troughs, although they are often widely spaced (hundreds of meters).

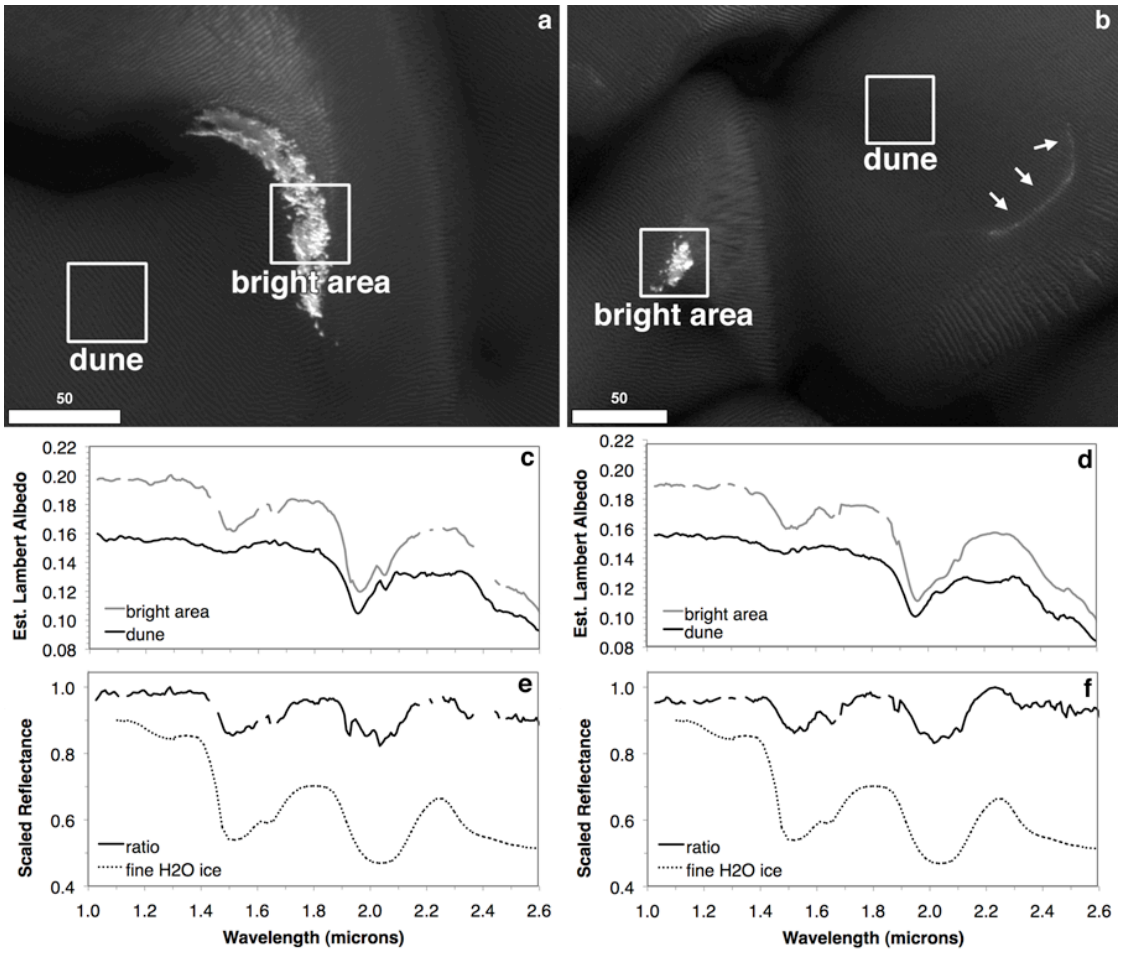

Figure 3.8: Bright ridges exposed at dune margins are spectrally consistent with water ice. (a-b) HiRISE views of bright ridges and bright deposits. Boxes indicate approximate location and areal coverage of CRISM spectra shown in c-f. Arrows indicate location of bright ridge in b. (Olympia Undae: PSP_009693_2790, PSP_009904_2790). Scale bars are 50 meters in length. (c-d) CRISM spectra from regions indicated in a-b. Channels with instrumental spiking effects have been removed. (e-f) When the bright spectra are ratioed with nearby sand spectra, the resulting spectrum is consistent with water ice (90 μm, Roush *et al*., 1990). Spectra have been normalized and shifted for clarity.

There is no apparent correlation between the presence of light-toned ridges and sulfate abundance in Olympia Undae, as arcuate ridges occur irregularly throughout the sand sea. However, in eastern Olympia Undae, we have identified several uniquely bright, polygonally fractured ridges that do exhibit a strong spectral signature in CRISM spectra that is consistent with water ice (Figure 3.8a). Bright patches with ice spectral signatures emerging from under dunes are not uncommon in the available HiRISE images near 230°E in Olympia Undae, although most do not have the characteristic arcuate ridge morphology (Figure 3.8b).

4.4 Surface cracks

A class of dune surface features that are common to all dune fields examined in this study are long, narrow depressions, with linear to sinuous and often branching morphologies, hereafter referred to as surface cracks (Feldman *et al*., 2008; Figure 3.9). The cracks are commonly on the order of 50-100 meters in length and a meter or less in width. Cracks often extend perpendicular to the dune crest on the stoss slope (Figure 3.9d), but also occur in sand-filled troughs (Figure 3.9c). Cracks on the stoss slope are often observed emanating from fan alcoves, possibly indicating a genetic relationship (Fig. 2b,d).

While we have observed surface cracks in all dune fields examined, the distribution of surface cracks is not homogeneous. Throughout much of the erg, we typically observe on the order of one large surface crack per several square kilometers of dune field; however, images within the easternmost region of Olympia Undae show surfaces with ubiquitous cracks or networks of cracks (Figure 3.9). Furthermore, the areal density of surface cracks (cracks identified per image/area of image) continuously decreases into the central and western regions of the sand sea, until the density becomes similar to that observed in the rest of the erg (Figure 3.10). This

Figure 3.9: (a,b) Densely cracked surface in eastern Olympia Undae exhibiting a variety of crack morphologies. *Right:* Cracks outlined for clarity. (c) Example of branching crack in sand-filled trough. (d) Example of long linear crack extending parallel to dune slope. All images from PSP_009764_2600. All images have been linearly stretched for clarity, scale bars are 50 meters in length. Solar illumination is from the upper right in (a), from the lower left in (b), and from the top in (c-d).

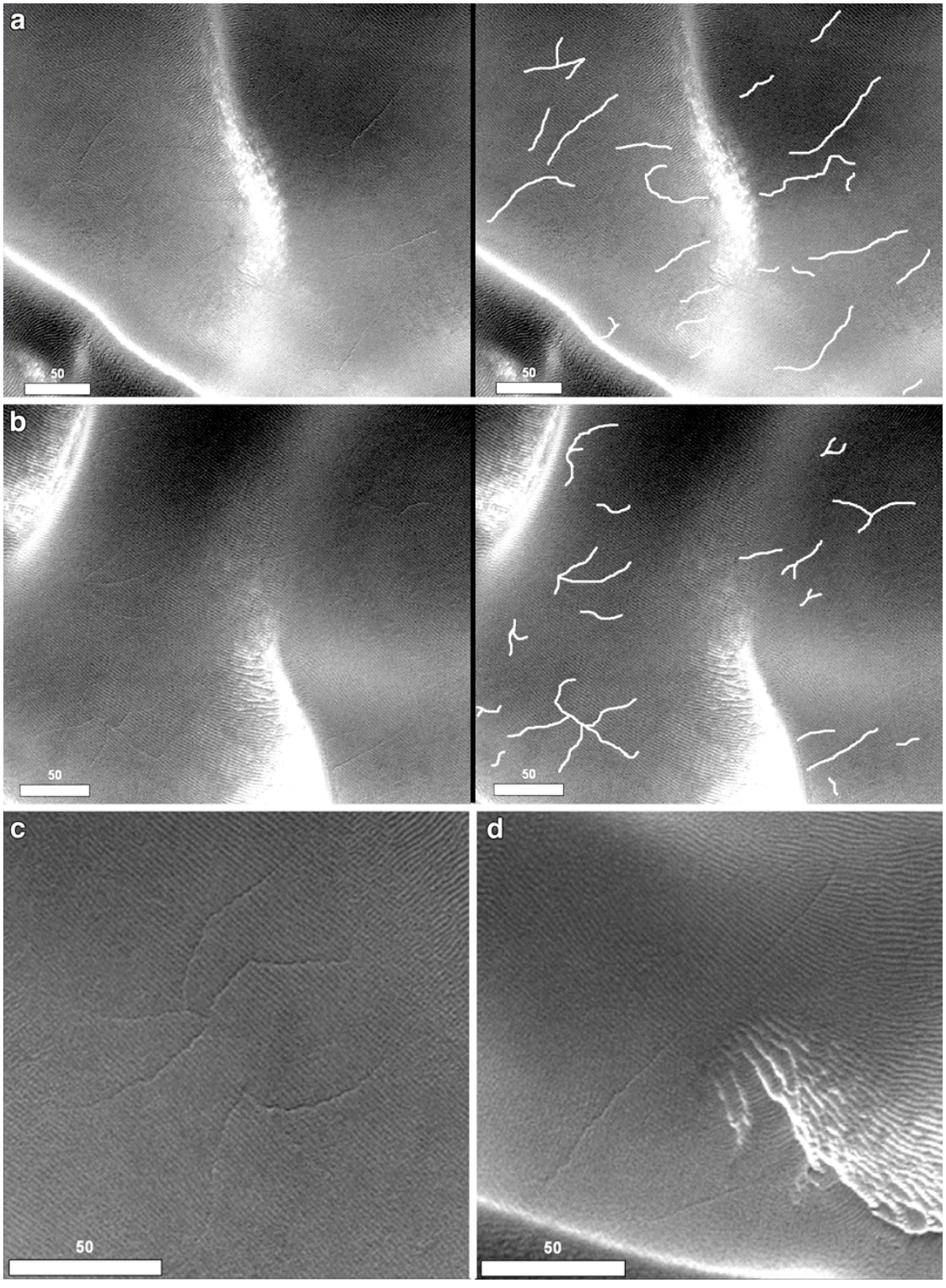
a
50
50
b
50
50
c
50
d
50

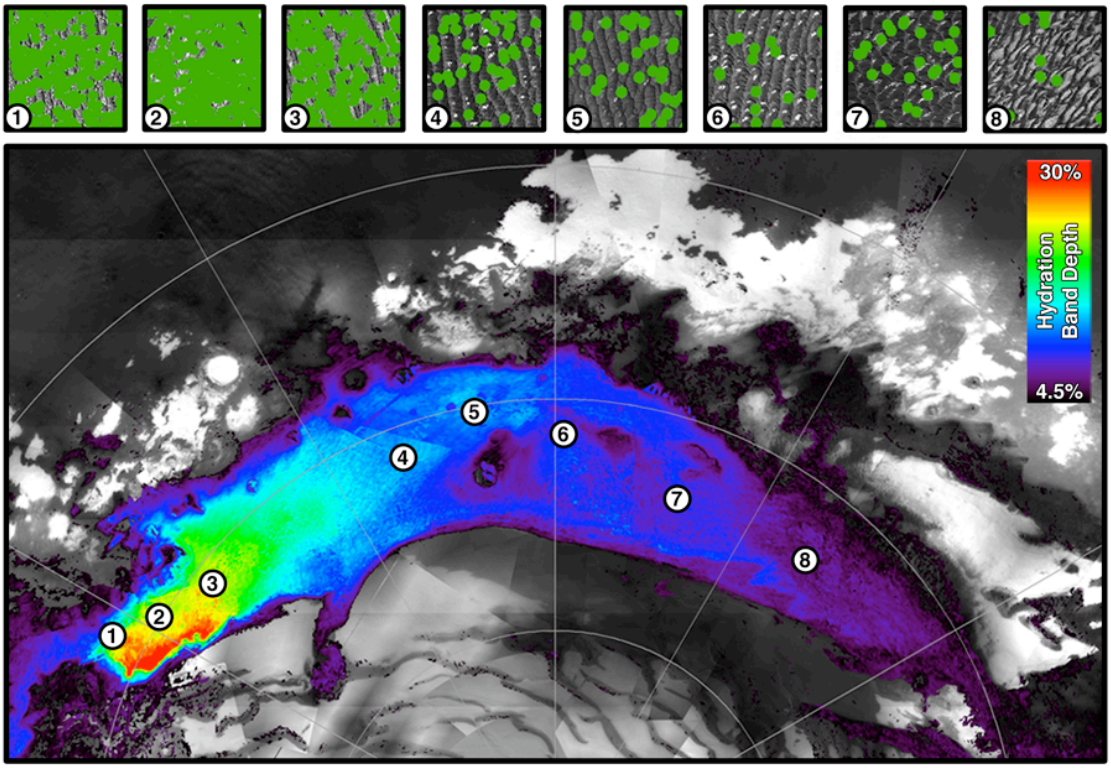

Figure 3.10: Distribution of sulfates in Olympia Undae compared to surface crack density. Top row: subsets of representative HiRISE images (images are 6.5 km squares) from locations indicated on map. Each green dot is one ~50-100m long surface crack or crack network. Map: OMEGA 1.9 μm band depth mapped over MOC wide angle mosaic. This parameter correlates with sulfate abundance (Horgan *et al*., 2009; see Chapter 2), which appears to be highly correlated with surface crack density. Source images, 1-8: PSP_009540_2595, PSP_009764_2600, PSP_009693_2790, PSP_009647_2605, PSP_001736_2605, PSP_009674_2610, PSP_009912_2620, PSP_010071_2615.

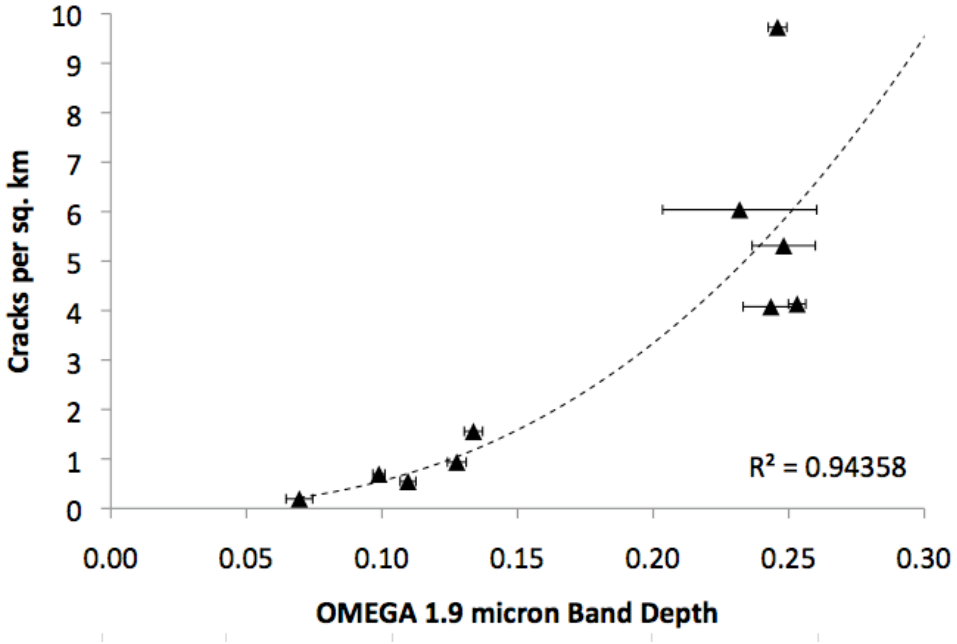

Figure 3.11: Surface crack density versus OMEGA 1.9 μm band depth. Surface crack density was calculated by dividing the total number of cracks identified in each image by the area of the image. Band depth plotted is the mean over the latitude and longitude range of the image, and the error bars are the standard deviation within that range. While we cannot constrain the precise nature of the trend without further data in the 0.15-0.25 band depth region of Olympia Undae, a power law is the best fit to the available data ($R^2 = 0.94$), as shown by the dashed line. An exponential trend is also a good fit ($R^2 = 0.91$) as compared to a linear trend ($R^2 = 0.73$). Regardless, the overall trend is that of increasing surface crack density with 1.9 micron band depth, implying a relationship between gypsum abundance and surface crack formation.

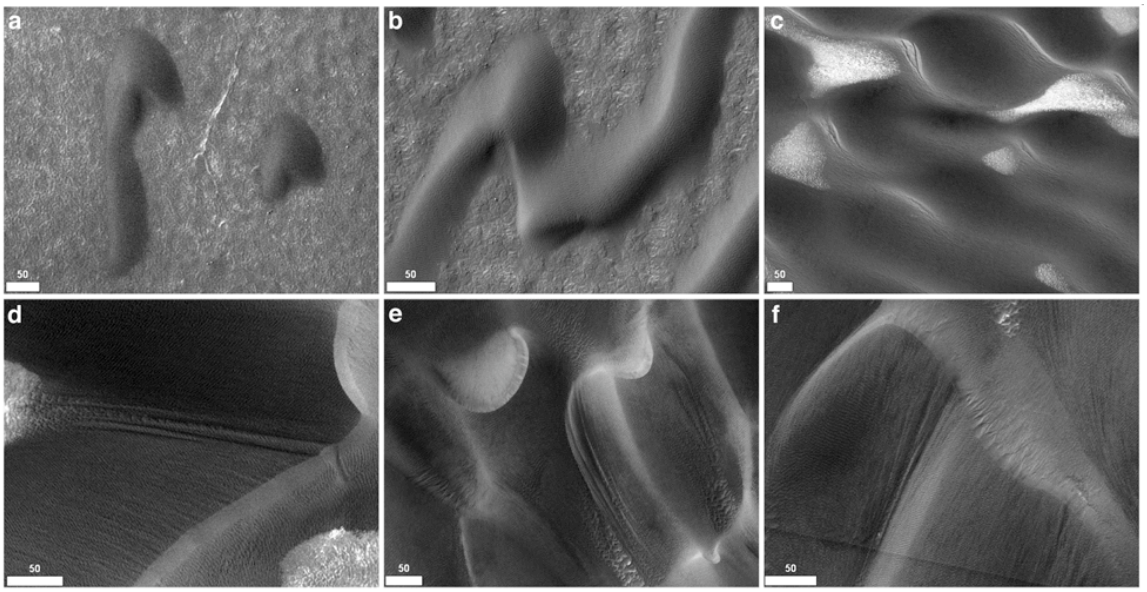

Figure 3.12: Erosional feature morphologies. (a-b) Rounded dunes in the northern plains (Siton Undae: PSP_001468_2515, PSP_010422_2540). (c) Rounded dunes with slumped slipfaces (Tenuis Cavus: PSP_009760_2650). (d-f) Grooved dunes with sharp crestlines and slipface fans (Olympia Undae: PSP_009728_2650, Abalos Undae: PSP_009367_2620, Olympia Cavi: PSP_009052_2640). All scale bars are 50 meters in length. Solar illumination is from upper left in (a-b) and (e-f), from the lower left in (c), and from the upper right in (d).

decrease in surface crack density appears to be highly correlated with the decrease in 1.9 μm hydration band depth westward across Olympia Undae as observed by OMEGA (Figure 3.10, 3.11), possibly indicating a relationship between surface cracks and gypsum or other hydrated mineral abundance.

4.5 Rounded dunes and grooves

Some dunes exhibit shapes or features that we interpret to result from erosion of the dunes. The most extreme examples of this are rounded dunes that lack well-defined slipfaces (Bourke, in prep). These are common in the scattered dune fields in the northern plains (Figure 3.12a-b), where some dunes appear muted and/or heavily rippled. In the polar chasma, rounded dunes often exhibit partially developed slipfaces

with slump-like features (Figure 3.12c). Rounded dunes have also been observed in southern high latitude dune fields (Fenton and Hayward, 2009).

Features apparently resulting from removal of dune material include linear grooves. The grooves that we have observed extend perpendicular to dune slipfaces, usually along the edges of isolated dunes, or through saddle points in transverse dunes. The grooves are on the order of 10 m wide, and can extend up to several hundred meters in length. Perhaps in contrast to their apparent erosional nature, grooves tend to occur on the margins of dunes with sharp crestlines and abundant fans, and even sometimes appear to terminate in fans where they intersect the slipfaces of dunes (Figure 3.12d,f). Grooves occur primarily on dunes near the polar scarps (Figure 3.12e,f), but also occur in regions of Olympia Undae where the dunes appear to have been formed under a strongly unidirectional wind regime (Figure 3.12d), suggesting that consistent winds may be an important factor in the formation of grooves. These features are larger and have a different morphology than the linear features identified on martian dunes at the lower resolution (~11 m/pixel) of the Mars Orbiter Camera (Edgett and Malin, 2000; Schatz *et al*., 2006). Those features were initially interpreted as erosional grooves as well, but have since been alternately interpreted to be secondary bedforms resulting from deposition based on analysis of higher-resolution HiRISE observations (Bridges *et al*., 2007).

5. Interpretations and Discussion

5.1 Slipface fans: Dry grain flow features

The morphology of the fans that we observe on north polar dune slipfaces is not consistent with gullies or other erosional features thought to result from volatile-rich flows. The latter features are variously characterized by narrow, sinuous channels, spur-and-gully alcoves, and extensive, lobate debris aprons (*e.g.*, Costard, *et al*., 2002;

Reiss and Jaumann, 2003; Mangold *et al*., 2003; Miyamoto *et al.*, 2004; Hugenholtz *et al*., 2007; Hansen *et al*., 2010; Diniega *et al*., 2010; Dundas *et al*., 2010). Instead, the morphology of the slipface fans is more consistent with a dry granular flow due to localized collapse of the slipface (*e.g.*,Hunter, 1977). Previous studies have suggested that these fans are niveo-aeolian features, and that the collapse of the slipface is caused by denivation (Bourke, 2005). While we cannot rule out a role for ice sublimation in promoting the collapse of the slipface, the relationship between fans and the polar scarps as well as the E-W directionality of fans in Olympia Undae suggests that wind is the primary trigger for the formation of these features.

These martian fans resemble terrestrial slipface failures caused by scarp recession (Hunter, 1977). As shown in Figure 3.13, this type of failure occurs when a very small flow initiates on the slipface, creating an initial breakaway scarp. As more sand falls away from the scarp, it expands laterally and moves upslope, forming a small alcove at the dune brink (Lindsay, 1973; Hunter, 1977). The sand flowing away from the scarp often forms a bottleneck at the point of greatest slope, which is usually located somewhat downslope from the dune brink (Anderson, 1988). At this point during slipface failure, the morphology of the flow most strongly resembles the martian fans. However, this form is unstable in terrestrial examples, as the sides of the alcove can be above the angle of internal friction. As the sides of the alcoves collapse, the movement, often coupled with additional input of saltating sand, triggers collapses of adjoining areas, and the region of failure and grainflow extends laterally across the slipface (*e.g.*, Cooke *et al*., 1993). Figure 3.13 shows an example of this type of flow morphology from the White Sands dune field and Figure 3.14a shows an example from Namibia (see also Andreotti *et al*. (2002), Sutton *et al*. (2008), and Lancaster (1995)).

Figure 3.13: Formation of alcoves and lateral migration of slipface flows in the White Sands dune field. Illumination is from the left. (a) Overview of active slipface at time of initial observations. Arcs in upper right are saltating sand. Approximate scale is indicated. (b-g) Time series showing changes in alcove and flow structure within area indicated by box in (a). (b) Initial observation of active grain flows. Arrows indicate moving flows. (c) Arrows indicate moving flows and retreating, deepening alcoves. The rightmost arrows in (d-g) indicate an alcove that is retreating but flattening out as it is filled with sand from above. The left arrows in (f-g) indicate where failure of the alcove wall has produced a new alcove and flow. Changes in tone between (c) and (e) are due to changes in viewing angle. Typical alcove depths are a few centimeters (R. Sullivan).

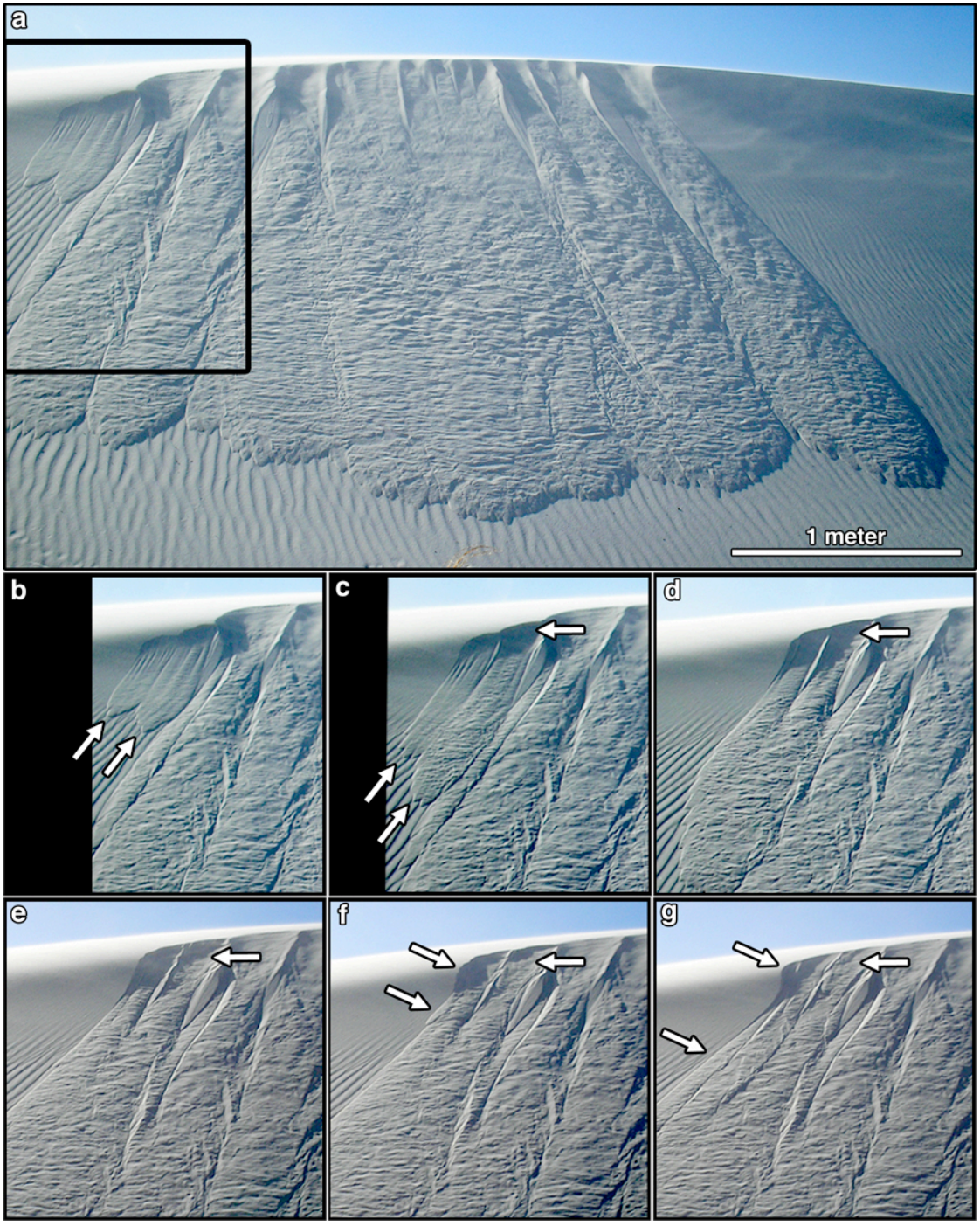
a
1 meter
b
c
d
e
f
g

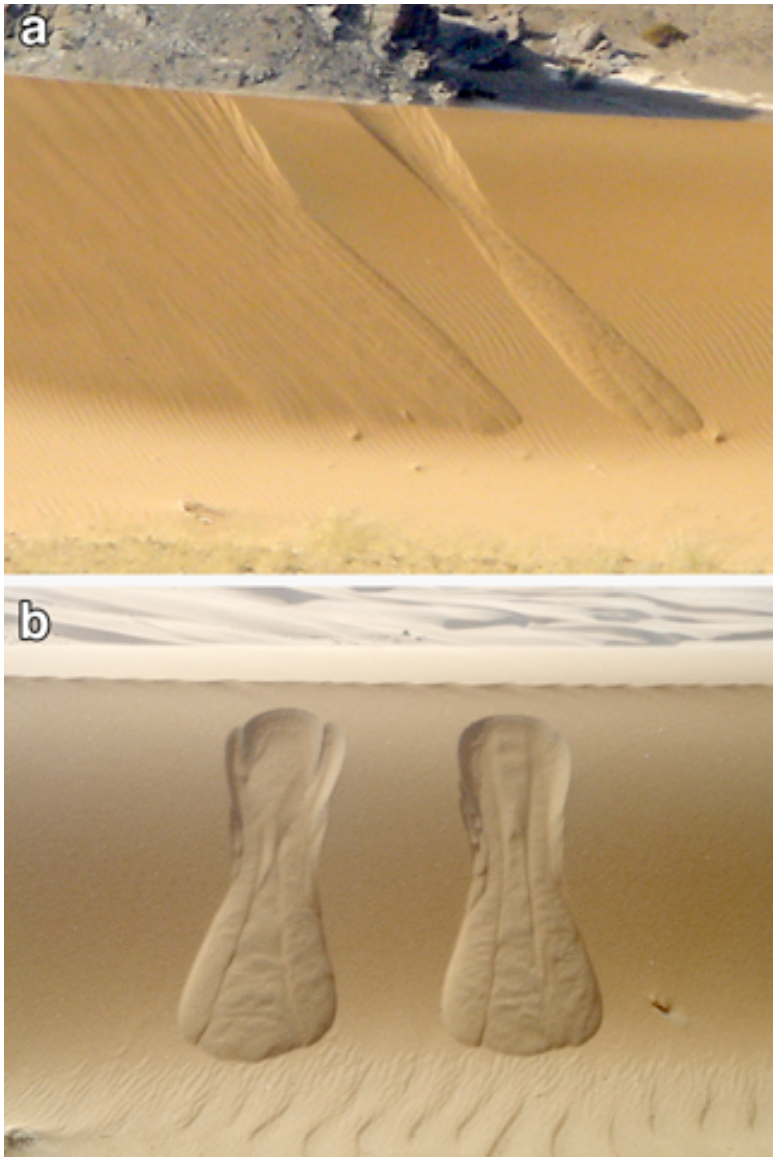

Figure 3.14: Alcoves and fan-shaped grainflows in the Cunene Sand Sea, Namibia. (a) Slipface failure showing both a laterally extended and flattened failure surface and an isolated alcove/fan. (b) Failure on a slope below the angle of repose. Alcove in (a) is approximately 40 cm across at maximum width, and the alcoves in (b) are approximately 35 cm across at maximum width. (M. Bourke).

While some aspects of terrestrial scarp retreat flows resemble martian north polar dune slipface fans, the scales of the two sets of features are quite different. Terrestrial scarp retreat flows are typically ~50 cm wide, with scarps less than a cm and flow lobes on the order of a few cm thick (*e.g.*, Lowe, 1976; Cooke *et al*., 1993). While martian fans could occur on this scale (which is at the limit of HiRISE resolution), most of the fans that we have identified in this study are 10-100's of meters in width with deeper alcoves and relatively more restricted bottlenecks. The difference in size may be caused either by surface or bulk induration of the martian features, which would allow greater over-steepening of the slipface and therefore larger collapses, or enhanced collapse due to denivation.

Another major difference between terrestrial slipface failures and martian fans is their longevity. While alcoves are generally a transient form on terrestrial dune slipfaces, the martian fans are stable over multiple seasons. Also, while the martian fans do occur in groups on some slipfaces, possibly indicating lateral spreading like in terrestrial flows, they also often occur as isolated features. This resistance to collapse may also be due to induration, which would allow steep alcoves to persist (*e.g.*, Bourke, 2005) and prevent lateral extension of the flow. Alternatively, the alcoves may be incised into slopes below the angle of internal friction, and therefore persist simply due to a lack of erosion. Figure 3.14b shows an example of alcoves and fan-shaped deposits on a sub-critical slope of a dune in Namibia, however, to our knowledge, these features have not been documented elsewhere, and the mechanisms of their formation are unclear.

Overall, it appears as though the primary differences in morphology, scale, and persistence between the martian slipface fans and terrestrial dry slipface failures may be accounted for by induration of the martian north polar dunes. While chemical cementation could be responsible, the lack of a correlation between the occurrence of

fans and sulfate or other hydrated mineral spectroscopic signatures suggests that ice induration is more likely. However, the effects of interior ice on the dry grain flow processes of ice-indurated terrestrial dunes have not been well documented.

5.2 Pits and slumps: Denivation features

Pits and slumps strongly resemble denivation features observed on terrestrial niveo-aeolian bedforms. For example, Koster and Dijkmans (1988) observed round sinkholes on the lee slopes of transverse dunes, caused by preferential melting of interbedded snow and ice. The scale of the sinkholes is about 1 meter in width and 50 cm in depth, which appears to be similar to that of the crestline pits we have observed (Figure 3.4a-c),. Dune surfaces with many pits exhibited a hummocky appearance that is reminiscent of the pitted debris of slumps in our observations (Figure 3.4d-e). Further, when pits developed on the upper portion of the lee slope, they were often observed to slide down slope, forming asymmetrical residual sinkholes that resembled small slump blocks. This may be analogous to the smaller, pitted slumps that we have observed on some slipfaces (Figure 3.4f). The larger slumps that we observe exhibit a similar morphology to large slipface slumps observed by Steidtmann (1973), which were caused by melting of sand-covered cornices at dune crests.

While we might expect differences between the morphologies of features of niveo-aeolian bedforms on Earth and Mars because of the occurrence of melting versus sublimation in the two different environments, the morphology of the martian pits and slumps is still generally consistent with terrestrial denivation features. Thus, pits may be caused by localized denivation and the associated volume loss, while slumps may occur when catastrophic or runaway denivation destabilizes an entire slipface layer. This would be consistent with the correlation between the occurrence of pits versus slumps and dune morphology: localized denivation and pitting on steep,

metastable barchanoid crests and slipfaces may trigger slumps, while slumps would not be as likely on the shallower slopes of reversing and/or transverse dunes where we observe crestline pits.

One major difference between terrestrial dune sinkholes and martian dune pits is that terrestrial sinkholes have only been reported to occur on the slopes of dunes (Koster and Dijkmans, 1988), while on martian dunes, we also commonly observe pits occurring on the crests, such as on the transverse dunes of Olympia Undae (*e.g.*, Figure 3.4a-c). Terrestrial sinkholes occur have been reported to occur most commonly on the stoss slopes because that is where snow accumulates (*e.g.*, Koster and Dijkmans, 1988); thus we might expect that the occurrence of pits at dune crests also corresponds to the location of the shallowest pore ice. Dune crests experience the greatest erosion due to wind and saltation impacts, which could strip away surface sand on timescales faster than the pore ice can thermally equilibrate. Ice concentration at the crests could also be due to structural controls on vapor diffusion and ice deposition, but it is not clear how this process would operate.

Alternatively, denivation pits have also been observed to form in association with tensional cracks (*e.g.*, Koster and Dijkmans, 1988). While we have not observed cracks associated with pits on the martian north polar dunes, this may present another way that pits could form at the crest of transverse dunes, especially in Olympia Undae. The density of surface cracks in Olympia Undae suggests that the upper layer of sand is indurated. At the crest of a relatively symmetric transverse dune, down-slope tension pulling away from the crest on either side of the dune could lead to cracking at the crest. This, in turn, would lead to increased exposure of ice-rich materials below to the atmosphere, which may result in denivation and collapse of regions of the crest. An elongated tensional crack along a dune crest could cause the chains of pits that we have observed (*e.g.*, Figure 3.4c). Although we have not observed crestline tensional

cracks, such cracks may have been filled with loose sand, as perhaps indicated by the presence of well-defined ripples on the dune crests.

If slumps and pits are indeed formed via denivation, we expect that the timing of their formation would have a strong seasonal dependence. The diurnal thermal skin depth on Mars is on the order of centimeters, while the seasonal thermal skin depth is on the order of meters (*e.g.*, Putzig and Mellon, 2007). Thus, denivation should occur when warm seasonal temperatures penetrate into the ice-bearing parts of the dunes. It may be possible to constrain the timing of slump formation and add support to this hypothesis by comparing multiple observations of the dunes over the ice-free seasons. Unfortunately, seasonal coverage of these dunes at the required resolution is not yet adequate to perform such an investigation.

5.3 Arcuate ridges: Indurated migration strata

We interpret arcuate ridges as dune migration strata, produced when indurated grainfall and avalanche strata are left behind as the dune moves forward. Both ice indurated and chemically cemented layers can exhibit this behavior in terrestrial dune systems. For example, in the White Sands dune field (New Mexico), the gypsum strata are cemented when ground water levels rise, and many of the interdunes are crossed by sets of remnant strata (*e.g.*, Schenk and Fryberger, 1988). In the Victoria Valley dune field (Antarctica), ice and snow cemented layers have been observed protruding from the stoss slope of the dunes, but do not appear to persist once the dune has moved past them (Bourke *et al*., 2009). In this respect, terrestrial ice indurated dunes may be a better analog than typical terrestrial ice-free dunes for the martian north polar dunes, as remnant strata behind the dunes are rare (Figure 3.6a-b). This would imply that the strata, which commonly protrude from the stoss slopes of the dunes, are removed once they are no longer protected by the dune. The layers would likely be

removed by sublimation, in the case of ice induration. Although chemically cemented layers could also be removed by erosion, because of the spectral evidence for ice induration of strata presented above and the lack of correlation between sulfate spectral signatures and arcuate strata, ice induration seems more likely. The disappearance of ice-rich strata is also consistent with the stability of ice at the martian surface. Sublimation rates for solid (non-particulate) water ice at the surface of Mars vary with pressure and temperature, but are on the order of 10^{-5} kg m^{-2} s^{-1} (*e.g.*, Taylor *et al*., 2006). For typical ice densities (~0.92 g cm^{-3}), this gives surface ice sublimation rates on the order of centimeters per year. Thus, for ice indurated strata on the order of centimeters to tens of centimeters in thickness, we would expect a residence time of years to tens of years. As these dunes have not been observed to move on that timescale (*e.g.*, Schatz *et al*., 2006; Bourke *et al*., 2008), we would not expect to see ice indurated strata persisting behind the dunes at this time.

5.4 Surface cracks: Tensional cracks on an indurated surface

We interpret surface cracks on north polar dunes as tensional cracks in an indurated surface layer, induced by bulk volume change of the dune. Similar cracks have been observed on terrestrial niveo-aeolian bedforms, when volatile loss and volume contraction is followed by down slope sliding and cracking of a wet, cohesive surface layer (*e,g,*, Koster and Dijkmans, 1988). However, these cracks have generally been reported to occur perpendicular to the dune slope, and while cracks with this morphology have been identified on martian dunes (Bourke, in prep), most of the cracks that we have observed are oriented parallel to the dune slope (Figure 3.2b,d, Figure 3.9a,b,d). Volume change could also be caused by thermal expansion and contraction or by dehydration/rehydration of minerals. In particular, changing hydration states from gypsum to anhydrite ($CaSO_4$) can result in a volume change of

up to 50% (*e.g.* Schreiber and El Tabakh, 2000). Polygonal cracks caused by gypsum dehydration after infiltration and evaporation of water from frost or precipitation are commonly observed in the White Sands gypsum dune field (Chavdarian and Sumner, 2006, 2010).

The strong correlation between hydration band depth and surface crack density in Olympia Undae suggests that a hydrated mineral like gypsum is somehow involved in surface crack development. For a surface crack to form, a dune must undergo a volume change and have an indurated or cohesive surface layer. Therefore, the likelihood of a dune to exhibit a surface crack is enhanced if the maximum volume change the dune experiences increases, or if the cohesion of the indurated surface layer is increased. Increasing the gypsum content of a dune could increase either of these, through more expansive dehydration/rehydration of gypsum (case 1), or through greater induration of the surface layer by gypsum cementation (case 2). Furthermore, gypsum dehydration could potentially also lead to cementation of the surface layer. In terrestrial sulfate systems, water released by dehydration of gypsum can dissolve, transport, and reprecipitate surrounding soluble minerals (*e.g.,* Deer *et al*., 1992) (case 3). This process would result in a very strong dependence of surface crack density on gypsum abundance. In cases 2 and 3, gypsum deposition could be concentrated near the surface as brines are drawn upwards by capillary action. Horgan *et al*. (2009) suggested that a gypsum-cemented surface layer resulting from such a process might be exposed at the crests of dunes in eastern Olympia Undae, based on the deep sulfate signatures observed at the crests of these dunes.

Near-surface sulfate cementation in the dunes may support the hypothesis put forward by Calvin *et al*. (2009) that the gypsum may be concentrated at the surface of the dunes by wicking and evaporation of brines. Calvin *et al*. (2009) also suggested that this process may be responsible for the apparent disparity between the lack of any

discernable sulfate signatures from possible gypsum source units within Planum Boreum and the large volumetric gypsum abundances predicted from near-infrared spectra in Olympia Undae (up to 42 wt.%; Fishbaugh *et al*., 2007; Horgan *et al*., 2009). Similarly, these results suggest that the Olympia Undae substrate could potentially also be the source of the gypsum. Previous studies have ruled out the dune substrate as a gypsum source because the substrate only exhibits gypsum signatures that are about half as strong as those observed at the dune crests (Roach *et al*., 2007; Horgan *et al*., 2009). However, capillary wicking of brine sourced from this potentially gypsum-bearing substrate and subsequent precipitation of gypsum near the surface of the dunes could be responsible for the apparent disparity in gypsum abundance.

The three hypotheses presented above for the relationship between gypsum and surface cracks all have major implications for the hydrologic cycle within the dunes. In cases 1 and 3, gypsum dehydration would release liquid water into the dunes, and as spectral observations indicate that not all gypsum in the dunes has been dehydrated to anhydrite, it is possible that water is being supplied to the dunes to rehydrate the gypsum. In case 2, water from another source must be present in the dunes to cause chemical cementation; possible sources of water include melting or sublimation of ground/intradune ice and atmospheric water vapor (*e.g.* Milliken *et al*., 2007). In particular, recent models of the effects of dunes on ground ice stability have suggested that the presence of a warm, low-albedo dune over ground ice could cause sublimation of the ice, which could potentially lead to enhanced water vapor content within the dune and, in the presence of hygroscopic/deliquescent salts, the formation of brines (Wood *et al*., 2010). A process such as this could be responsible for the transport of gypsum from the potentially gypsum-bearing substrate into the dunes, as suggested above.

The apparent young age of the Olympia Undae dunes from morphology and low crater counts implies that at least the sand at the surface of the dunes has been mobile under current climatic conditions. Surface cracks would not persist if the surface layer of sand became mobile, so the cracks that we observe must have formed since the dunes were most recently active. This suggests that crack formation is a recent and possibly ongoing process, and therefore that water has recently been present within the dunes through one of the processes described above. While pure water is not stable under current martian surface conditions, micro-environments within the dunes and the presence of dissolved salts (*e.g.* sulfates) could allow brines to persist long enough to dissolve and re-precipitate gypsum as a cement (*e.g.*, Brass, 1980; Chevrier *et al*., 2009; Zorzano *et al*., 2009; Fairen *et al*., 2009; Kereszturi *et al*., 2010). A possible terrestrial analog for this process is in the ice-cemented soils of Victoria Valley, where ground ice is recharged and chloride salt horizons are formed by brines derived from snow melt (*e.g.*, Hagedorn *et al*., 2010). Indeed, brines may not be unique to the sand seas of the northern plains, as some images taken by the Phoenix lander of blobs adhered to the spacecraft's struts have been interpreted as evidence for stable liquid brines at the surface (Renno *et al*., 2009).

5.5 Rounded dunes and grooves: Erosional features on ice-indurated dunes

We interpret rounded dunes as dunes that have undergone erosion. For a dune to undergo erosion without migration, it must either be indurated or experience wind activity without substantial sediment flux. Many rounded dunes in the northern plains exhibit well-defined ripples, perhaps implying that it is not for lack of winds that the dunes look muted, but more likely a lack of sediments. However, rounded dunes in the polar chasma are likely both sediment starved and indurated by ice, as indicated by the

presence of slump-like features. These dunes also rarely exhibit well-defined ripples, perhaps implying ice induration nearer to the surface than in other dunes.

We interpret grooves as erosional features cut into ice-indurated dunes. The inferred relationship between grooves and strong, unidirectional winds suggests that grooves may be formed when ice-rich sand is eroded from the dune faster than the dune can thermally equilibrate and redistribute the ice. Thus, a subtle channeling effect at a low point in a dune could lead to the development of a groove in this model, which would be consistent with our observations that grooves primarily occur at saddle points within dune fields and around the margins of individual dunes.

6. Conclusions

Dunes in the north polar sand sea of Mars exhibit a variety of features that we interpret to be related to induration by both water ice and sulfate minerals. These features indicate that both liquid water and water ice could have significant effects on the structure and mobility of the dunes. In particular, we interpret the correlation that we observe between gypsum abundance and the presence of tensional surface cracks to indicate that brines have been present in the dunes recently, and most likely must also be present on a seasonal timescale in order to maintain the induration after periods of high wind activity.

Ice and sulfate induration of these dunes could explain the lack of detected dune migration in this area. However, these dunes appear fresh and could indeed be migrating very slowly under current conditions, as indicated by their lack of impact craters, sharp crestlines, and slipface grainflows in the form of fans, which we have shown to be features that are actively forming on Mars today. Continued monitoring of polar dune activity will help us to understand how these features form and evolve, as well as how environmental influences affect the migration rates of polar dunes.

CHAPTER 4

INSIGHTS INTO SEDIMENTARY AND AQUEOUS PROCESSES IN THE NORTH POLAR REGION FROM IRON MINERALOGY

0. ***Abstract***

The north polar region of Mars is dominated by dark toned sediments, and the iron mineralogy of these sediments provides constraints on the sedimentary and aqueous processes that have occurred in this region during the Amazonian. New analysis of ferrous mineralogy in this region from near infrared spectra taken by the Mars Express OMEGA imaging spectrometer has revealed that the sediments in this region are sourced from two compositionally and stratigraphically distinct sources. The stratigraphically older source is the Planum Boreum cavi unit, an indurated paleo-erg near the base of Planum Boreum, with a surface composition that is spectrally consistent with a leached iron-bearing glass. The stratigraphically younger source is the Planum Boreum 2 unit, located between the upper and lower polar layered deposits, with a surface composition that is spectrally consistent with a high calcium pyroxene. Sands in the north polar erg appear to be composed of mixtures of sediments sourced from these two units. The distinct compositions of these two units suggest that they have undergone substantially different processes, and that they have not undergone significant sediment exchange. We interpret the leached, glass-rich deposits to be the end product of widespread and pervasive acidic leaching, likely due to interactions with liquid water derived from surface ice or snow. These extensive deposits represent a new class of alteration byproducts on Mars, and suggest that the northern lowlands of Mars have been both aqueously and chemically active during the Amazonian.

1. Introduction

Low albedo sediments dominate the non-ice geology of the martian north polar region. Dark toned, large, aeolian dune fields and sand sheets (the north polar erg) encircle the north polar cap of Mars in the circumpolar plains above 70-75°N (Tsoar *et al.*, 1979; Thomas and Weitz, 1989; Lancaster and Greeley, 1990), and extend into the deepest part of the northern lowlands and beyond, into Acidalia Planitia. Dark-toned sediments also compose a substantial fraction of the volume of the north polar cap, Planum Boreum (*e.g.,* Malin and Edgett, 2001; Tanaka, 2005; Fishbaugh and Head, 2005; Rodriguez *et al*., 2007; Tanaka *et al*., 2008; Kocurek and Ewing, 2010).

Both *in situ* and remote sensing studies of low albedo regions on Mars have shown that these regions are dominated by mafic (iron- and magnesium-rich) lithologies (*e.g.*, Soderblom, 1992; Bell *et al*., 2004; Mustard *et al.*, 2005; Christensen *et al.*, 2000, 2004a; Bandfield, 2002; Gellert *et al*., 2004; Morris *et al*., 2006; Rogers and Christensen, 2007; Rogers and Aharonson, 2008; Poulet *et al*., 2009). Both ferrous (Fe^{2+}) and ferric (Fe^{3+}) iron in minerals exhibits strong absorptions at visible (0.3-1.0 μm) and near-infrared (NIR; 1-5 μm) wavelengths that can be used to identify trends in iron mineralogy (*e.g.,* Adams, 1968; Adams, 1974; Cloutis and Gaffey, 1991). Because Mars is primarily a mafic planet, these trends can provide a wealth of information on both primary (igneous and impact) and alteration (aqueous and sedimentary) processes.

Previous studies of the north polar region in the NIR have supported a mafic composition for these low albedo deposits. Bell *et al.* (1997) identified a strong 953 nm absorption restricted to the circum-polar dark deposits in visible/NIR Hubble Space Telescope (HST) multi-spectral images of the north polar region, implying a strong mafic component to the dunes, most likely a pyroxene. Observations from the Mars Express OMEGA NIR imaging spectrometer (Bibring *et al*., 2005) have also

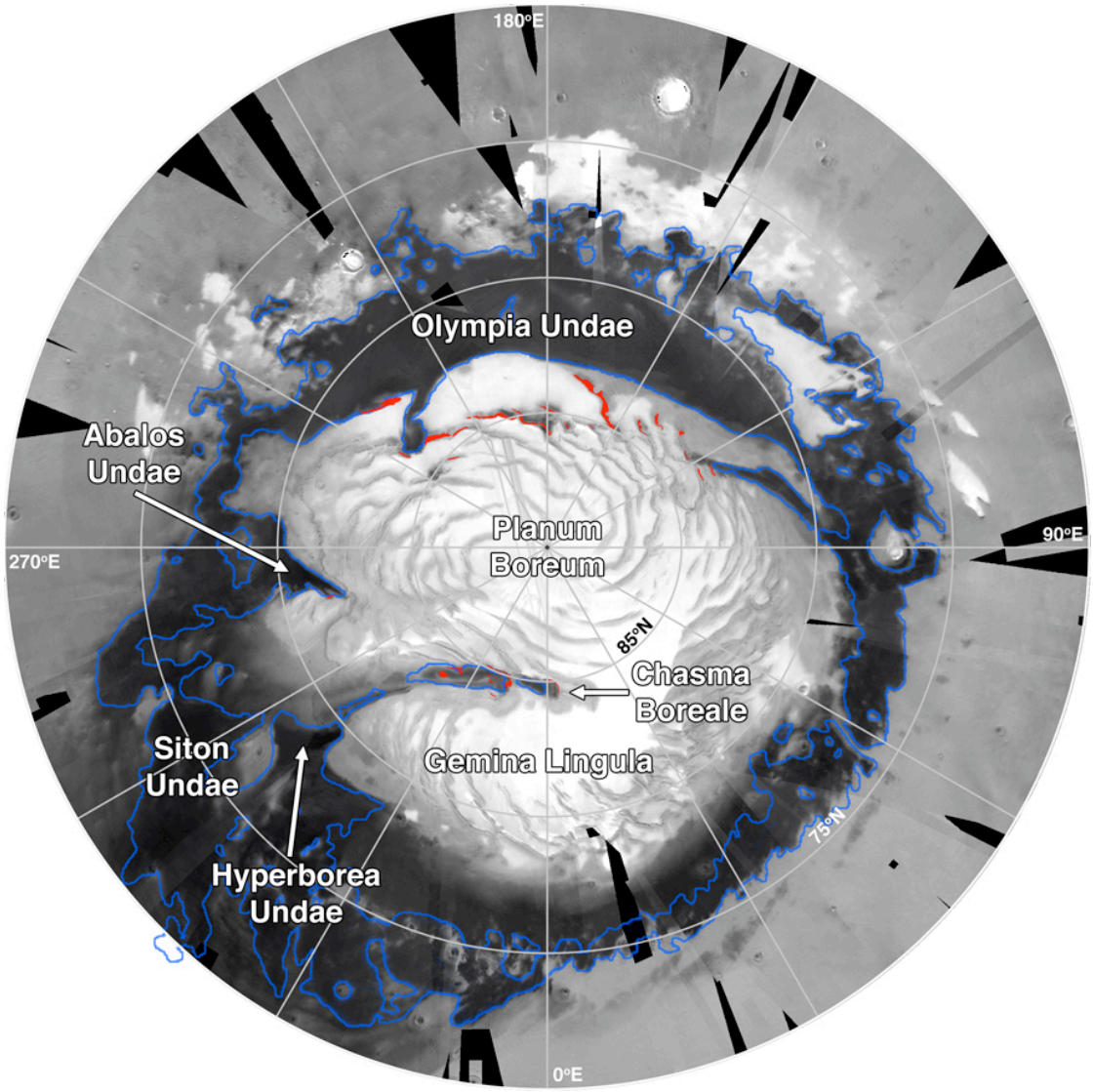

Figure 4.1: OMEGA albedo map (0.75 μm) of the north polar region of Mars. Geographic features from text are indicated. Blue outlines indicate dune fields as mapped by Tanaka and Hayward (2008) and Hayward *et al*. (2010). Red regions indicate major outcrops of the Planum Boreum Cavi unit from Tanaka *et al*. (2008), which is hypothesized to be an indurated paleo-erg and a major modern source of sand for the north polar sand sea (Tanaka *et al*., 2008; Kocurek and Ewing, 2010). The north polar veneers, which are sourced from the Planum Boreum 2 unit within the polar chasma (Rodriguez *et al*., 2007), make up the majority of the dark-toned surfaces on Planum Boreum. On Mars, 1° of latitude is ~60 km.

been interpreted to suggest that pyroxene as well as olivine may be present within the circum-polar dunes (Fishbaugh *et al*., 2007; Poulet *et al*., 2008).

However, other observations indicate that the mineralogy of the north polar sand sea and other north polar sediments may be much more complicated than that of typical martian olivine and pyroxene-bearing sand. Olympia Undae, the largest sand sea within the north polar erg, exhibits the strongest and most areally-extensive hydrated sulfate signature yet seen on Mars (*e.g.,* Poulet *et al*., 2007). The spectral signature of Olympia Undae is consistent with gypsum (Langevin *et al*., 2005a; Fishbaugh *et al*., 2007; Horgan *et al*., 2009; Chapter 2), an evaporite mineral that requires water to form. It has been suggested that the gypsum may have been produced during aqueous alteration of calcium-bearing mafic minerals, however, the calcium-bearing minerals, the associated alteration products, and the water source have not yet been positively identified (Fishbaugh *et al*., 2007; Horgan *et al*., 2009; Chapter 2).

Observations of the north polar sand sea in the mid-infrared (MIR) also suggest an aqueous history. The north polar sand sea and Acidalia Planitia to the south are the type locality for the globally distributed spectral unit known as Surface Type 2 (ST2; Bandfield *et al*., 2000; Wyatt and McSween, 2002; Ruff and Christensen, 2007), previously identified through analysis of MIR spectra from the Mars Global Surveyor Thermal Emission Spectrometer (TES; Christensen *et al*., 2001). Model-derived compositions of ST2 differ from the more widespread olivine-basaltic composition of Surface Type 1 by including an additional amorphous or poorly crystalline high-silica phase (Michalski *et al*., 2005). However, the nature of this phase is not well constrained. Possible high-silica phases include both primary volcanics (*e.g.,* obsidian glass, alkali glass) and secondary alteration products (*e.g.,* zeolites, opal, amorphous silica coatings; Bandfield *et al*., 2000; Wyatt and McSween, 2002; Michalski *et al*., 2005; Rogers *et al*., 2007; Ruff and Christensen, 2007). These possibilities have

significantly different implications for martian history. For example, if ST2 is derived from a more andesitic magma, then it implies substantial compositional evolution from typical martian basaltic magma; if ST2 contains a silica-rich aqueous alteration product, however, then it could instead imply widespread leaching or dissolution of basalt. In either case, none of the above high-silica phases have previously been identified in the NIR in the north polar sand sea or Acidalia Planitia, leading some authors to suggest that spectrally-obscuring coatings or spectrally-featureless glasses might be the main high-silica phase of ST2 (Mustard *et al*., 2005; Poulet *et al*., 2007).

The primary purpose of this study is to identify and map the distribution of iron-bearing minerals and mixtures of these minerals within the north polar region by applying methods developed from laboratory spectral studies to data from the OMEGA NIR imaging spectrometer. This analysis will allow us to place constraints on the sources of sediments for the north polar units and the degree to which the sedimentary units have exchanged material, as well as on the history of aqueous alteration in the region. Results from this study suggest that the primary mafic components of the north polar sediments are spectrally consistent with high calcium pyroxene and iron-bearing glass. The glass exhibits spectral evidence that it has undergone acidic leaching, likely due to interactions with surface ice or snow melt. The glass appears to be sourced from layers within Planum Boreum that have been interpreted as an indurated paleo-erg, and the distribution of glass in the circumpolar plains may indicate the location of outliers of the paleo-erg.

Section 2 reviews current knowledge of the distribution and sources of dark-toned sediments in the north polar region. Section 3 presents the spectral parameters we have developed from laboratory studies to differentiate between various iron-bearing minerals, and Section 4 presents our methods for processing and analyzing OMEGA data. Section 5 presents our observations of spectral parameters in the

region, and Sections 6 and 7 present our interpretations of the minerals and phases responsible for the observed trends. Sections 8 and 9 conclude with our interpretations of the processes that may have lead to the observed mineral distributions.

2. Dark toned units in the north polar region

The dark toned sedimentary units present in the north polar region can be separated into two categories: sediments in units within Planum Boreum and sediments on the circumpolar plains.

There are two known units within the structure of Planum Boreum that contain dark-toned sands: the Planum Boreum cavi unit (Tanaka *et al*., 2008) and the north polar veneers (Rodriguez *et al*., 2007). The cavi unit is located near the base of Planum Boreum and is characterized by alternating dark and light toned layers, often with clear evidence for cross-beds. As such, the cavi unit has been interpreted as a paleo-erg, likely indurated by ice during changing climatic conditions (Fishbaugh and Head, 2005; Herkenhoff *et al*., 2007; Tanaka *et al*., 2008; Kocurek and Ewing, 2010). Based on stratigraphic mapping, the cavi unit is heterogeneously distributed within the main lobe of Planum Boreum, and outcrops primarily between 100-300°E and within Chasma Boreale. No major outcrops have been identified in Gemina Lingula outside of Chasma Boreale. The cavi unit also appears to make up the majority of the material underlying Olympia Undae. The cavi unit is interpreted as a source of sand for the modern dune fields based on the presence of dunes and sand streamers emanating from outcrops (Tanaka *et al*., 2008).

The north polar veneers are the dark toned sediments that cover large portions of the surface of Planum Boreum (Figure 4.1). They appear to be sourced from the Planum Boreum 2 unit, a tens of meters thick unit intermediate between the upper and lower polar layered deposits (Rodriguez *et al*., 2007). The veneers are interpreted to be

composed at least in part of sand sized grains, based on the presence of scour marks on the surfaces of Planum Boreum where the veneers are present.

The majority of sediments on the circumpolar plains are within the north polar sand sea. Dune areal density varies widely within the sand sea (*e.g.,* Hayward *et al*., 2010), such that many of the highest dune density regions can be treated as individual sand seas. These include Olympia Undae, Siton Undae, Hyperborea Undae, and Abalos Undae (Figure 4.1). However, not all dark-toned sediments on the plains are confined within dunes. The best example of this is between 320-30°E, where dark-toned sediments cover a large region to the north of any mapped dunes (Figure 4.1). These sediments are interpreted to result from plains deposition of the north polar veneers, transported down from Planum Boreum by katabatic winds (Rodriguez *et al*., 2007; Tanaka *et al*., 2008).

3. Laboratory spectral analysis and implications

Previous studies of the north polar region using OMEGA data have relied on spectral indices to identify different ferrous minerals (Poulet *et al*., 2008). These spectral indices use combinations of albedos at specific wavelengths to gauge the shape of the spectra, and are useful because they provide a quick method of determining spectral variations over a region (*e.g.*, Poulet *et al*., 2007). However, previously-developed ferrous spectral indices are not optimal for analyzing subtle changes in ferrous mineralogy or differentiating between spectrally similar minerals, and it is not well understood how mineral mixtures affect previously-developed ferrous spectral indices.

In laboratory spectra, ferrous minerals have traditionally been differentiated by analyzing the locations and shapes of their characteristic absorption bands (*e.g*., Adams, 1974; Cloutis and Gaffey, 1991). As shown in Figure 4.2, most ferrous iron-

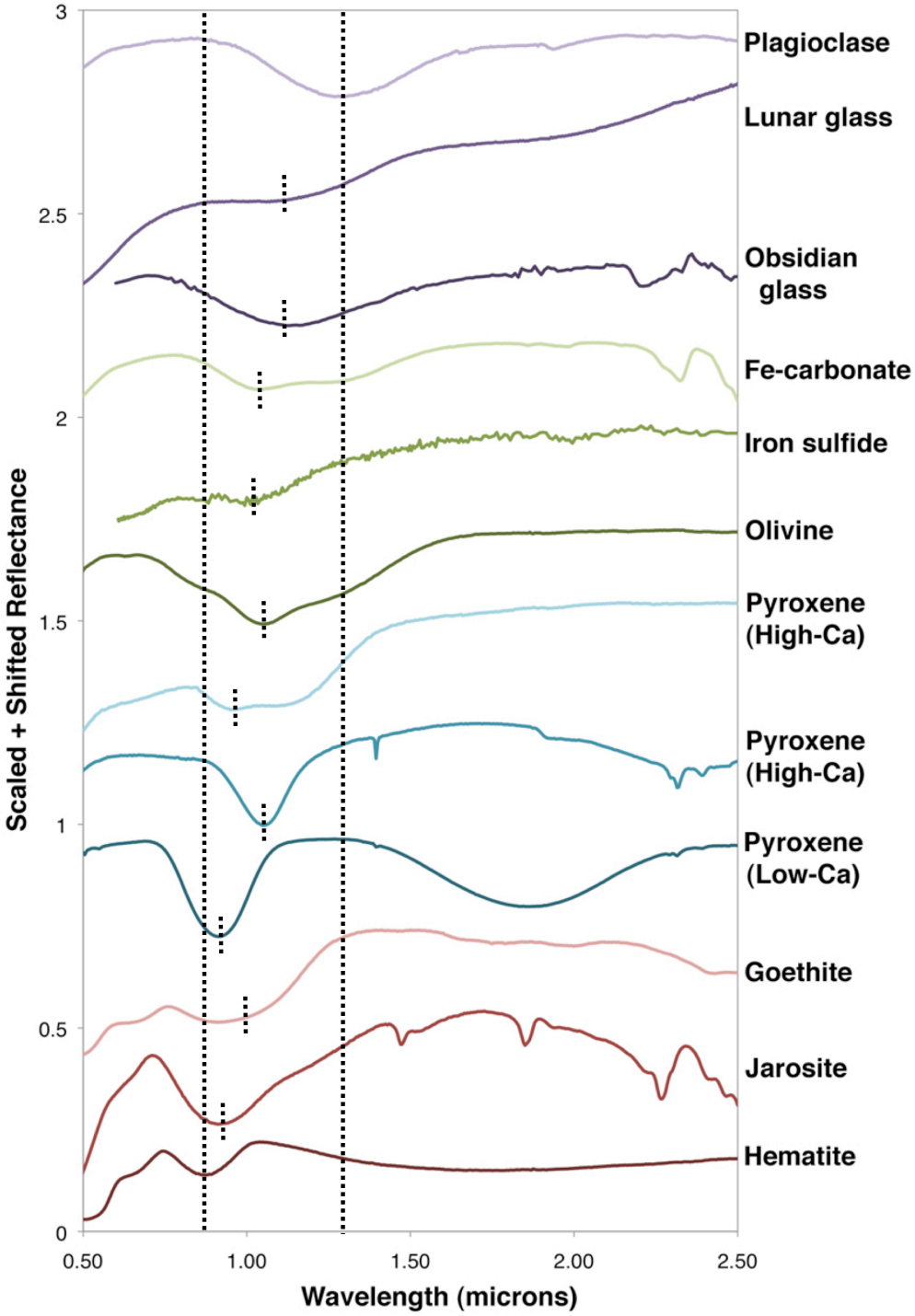

Figure 4.2: Sample spectra of iron-bearing mineral groups used in this study. Note the progression in the minimum of the 1 μm iron band with mineralogy, as indicated by the dashed vertical lines.

bearing minerals exhibit broad absorption bands in the 0.9-2.5 μm region due to crystal field transitions in ferrous iron located in the M2 crystallographic site. These absorptions are most commonly centered around 1 μm, and the exact location of the band is characteristic of the mineral (*e.g.*, Cloutis and Gaffey, 1991). Ferric iron-bearing minerals also exhibit bands in this region, most commonly near 0.9 μm, due to spin forbidden transitions in ferric iron (*e.g.*, Hunt, 1977). The shape of the bands varies with the mineral as well; for example, as shown in Figure 4.2, the 1 μm band of pyroxenes is usually relatively narrow and symmetrical, while the 1 μm band of olivine is actually composed of three separate absorptions, and exhibits a characteristically wide and asymmetric shape (*e.g.,* Sunshine *et al*., 1990).

While characterizing the detailed position and shape of these bands in large spectral data sets can be challenging to automate successfully and may require large amounts of processing time, such an approach yields the detailed analysis that simpler spectral indices alone cannot always provide. As such, for this study, we have chosen to develop spectral parameters based on the position and shape of the 1 μm iron absorption band. To find parameters that produce the most unique mineral identifications, we have applied a variety of parameters to a suite of ferrous and ferric iron-bearing minerals as well as mineral mixtures, as detailed below.

3.1 Acquisition of mineral spectra

When available, spectra of pure minerals were taken from public spectral libraries, including the Brown RELAB spectral catalog[1] (Pieters, 1983), the MRO CRISM spectral library[2] (Murchie *et al*., 2007), the USGS digital spectral library[3]

[1] http://www.planetary.brown.edu/relab/
[2] http://ode.rsl.wustl.edu/MROCRISMSpectralLibrary/
[3] http://speclab.cr.usgs.gov/spectral.lib06/

(Clark *et al*., 2007), and the University of Winnipeg Planetary Spectroscopy Facility (UWPSF) online database[1].

Additional pure mineral spectra and spectra of mineral mixtures were prepared and acquired at the UWPSF. All samples were crushed and dry-sieved to grain size ranges within or near the sand range (tens to hundreds of μm). To test our parameters for sensitivity to grain size, several samples were prepared and spectra were acquired at multiple grain sizes. Mineral mixtures were produced by varying the weight percent of the components. In total, the sample database for this study contains 147 pure mineral samples and 149 mineral mixture samples.

Reflectance spectra over the 0.35-2.5 μm range were acquired with an Analytical Spectral Devices FieldSpec Pro HR® spectrophotometer. The spectral resolution of the instrument varies between 2 and 7 nm and spectral sampling is done at 1.4 nm intervals. The instrument internally resamples the spectra to 1 nm intervals (Cloutis *et al.*, 2006; 2007).

3.2 Continuum removal and smoothing

Mineral absorption bands are superposed on the continuum of the spectrum, and the effects of this continuum must be removed before analysis of the bands can be completed (*e.g.*, McCord *et al*., 1981; Clark and Roush, 1984). The continuum of a laboratory mineral sample is due to a complex combination of influences (*e.g.,* Sunshine *et al*., 1990), so modeling the exact shape of the continuum is difficult at best. Here we have assumed a linear continuum over the 1 μm absorption band, as shown in Figure 4.3 (*e.g.*, Cloutis and Gaffey, 1991). The continuum was initially found by maximizing the band area around the spectral minimum between 0.75 and 1.25 μm; if needed, the fit was manually adjusted. In cases of highly variable or non-

[1] http://psf.uwinnipeg.ca/Sample_Database.html

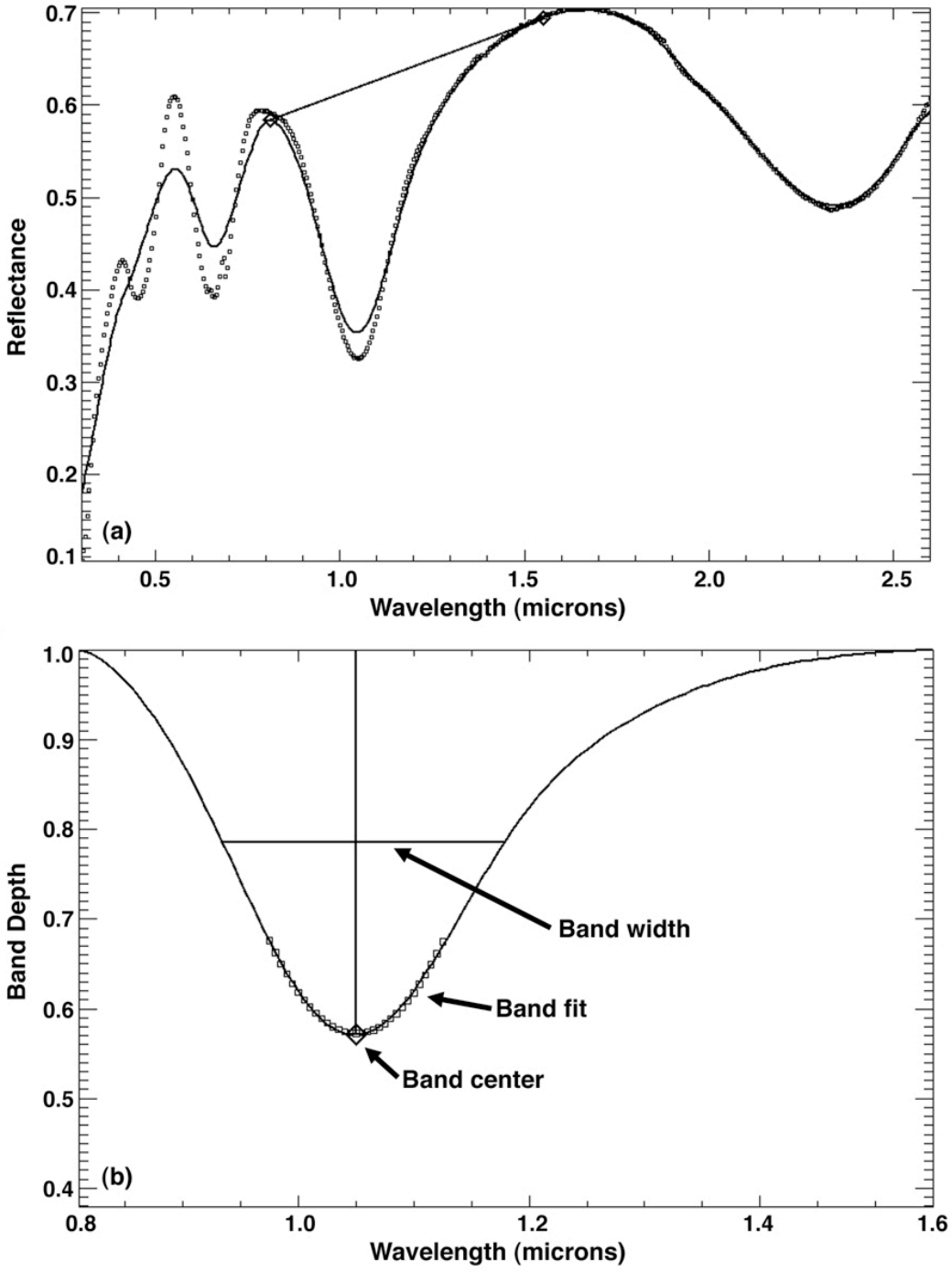

Figure 4.3: Processing of a low calcium pyroxene sample. (a) Original spectrum (squares) compared to smoothed spectrum (solid line) and the continuum fit produced automatically by maximizing the band area. (b) Continuum removed spectrum and derived band parameters. Squares indicate the polynomial fit used to find the band center, which in this case is the same as the band minimum.

linear continua, a horizontal fit was assumed. The small fraction of spectra where a linear continuum could not adequately account for the actual continuum shape were not included in this study. The continuum was removed by dividing it out of the spectrum.

The OMEGA surface spectra used in this study were smoothed using a boxcar smoothing algorithm to minimize the effect of noise, instrumental effects, and narrow absorption bands due to non-ferrous species (see Section 3.5). While most laboratory spectra do not need to be smoothed, smoothing has a tendency to make bands shallower and smoothes out shapes within the bands (*e.g.,* in olivine), as shown in Figure 4.3. So, to be consistent with the processing that we have applied to OMEGA data, we have smoothed the laboratory spectra with the same boxcar width in wavelength space (~0.07 μm) prior to continuum removal (see Figure 4.3), thus allowing a more accurate comparison of the OMEGA data to laboratory data. Especially noisy laboratory spectra (*e.g*., very low albedo glass and oxide spectra) were smoothed with a boxcar average of ~0.25 μm.

3.3 Band analysis

Once the continuum has been removed from the 1 μm absorption band, several band parameters can be derived, as shown in Figure 4.3 (*e.g.*, Clark, 1984; Cloutis and Gaffey, 1991). The *band minimum* is defined as the wavelength position of the spectral minimum between the continuum endpoints. The *band center* is the wavelength position of the minimum of a second order polynomial fit to all channels within 0.075 μm on either side of the band minimum. The band minimum and center only differ in noisy spectra and when the fit has a higher resolution than the spectrum. In smooth spectra, the band minimum and center should be the same or very similar. For the laboratory and OMEGA spectra, the fits have a resolution of 0.005 μm.

The *band depth* of the absorption band is equal to 1 minus the value of the continuum removed spectrum at the band center. The *band width* is the full width of the band at half of the maximum band depth. The *band asymmetry* is defined as the difference between the band width to the left and right of band center as a percent of the total width. A symmetric band has an asymmetry of 0, and bands that have more area to long wavelengths are defined as having a positive asymmetry between 0 and 1.

3.4 Results

Based on our analyses, the parameters that produce the most unique mineral identifications are the band center and band asymmetry. The band center of the 1 μm absorption alone allows broad discrimination of most ferrous minerals (*e.g.*, Adams, 1974; Hunt, 1977; Singer, 1981; Cloutis and Gaffey, 1991). However, the band centers of some minerals do overlap, such as low calcium pyroxene (LCP) and some oxides and sulfates in the 0.9-0.92 μm region, and high-calcium pyroxene (HCP) and olivine in the 1.02-1.08 μm region (*e.g.*, Figure 4.2). As shown in Figure 4.4a, utilizing band center and band asymmetry together reduces most of this overlap in major rock-forming ferrous minerals, although, as shown in Figure 4.4b, there is still some overlap with other ferrous and ferric minerals, such as between HCP and Fe-sulfides and between olivine and Fe-carbonates.

To apply these parameters to planetary data, it is critical to understand how they are affected by mixtures (*e.g.*, Singer, 1981, Cloutis *et al*., 1986; Cloutis *et al*., 1990; Cloutis and Gaffey, 1991; Sunshine *et al*., 1990; Sunshine *et al*., 1993). Figures 4.5 and 4.6 shows spectra and parameter trends for two-component mixtures of LCP, HCP, olivine, and glass. The mixture spectra for olivine and glass compare well with olivine-bearing glass spectra presented by Nicholis *et al*. (2006), suggesting that these results are valid for intimate as well as inter-granular mixtures.

Figure 4.4: Band center vs. band asymmetry for laboratory spectra. (a) Parameters for primary rock-forming ferrous minerals. Regions defined by the distribution of pyroxene (diamonds), olivine (squares), and glass (asterisks) are shown. (b) Parameters for other ferrous and ferric minerals. Regions defined by minerals in (a) are shown for comparison. Note the change in the range of both axes between (a) and (b).

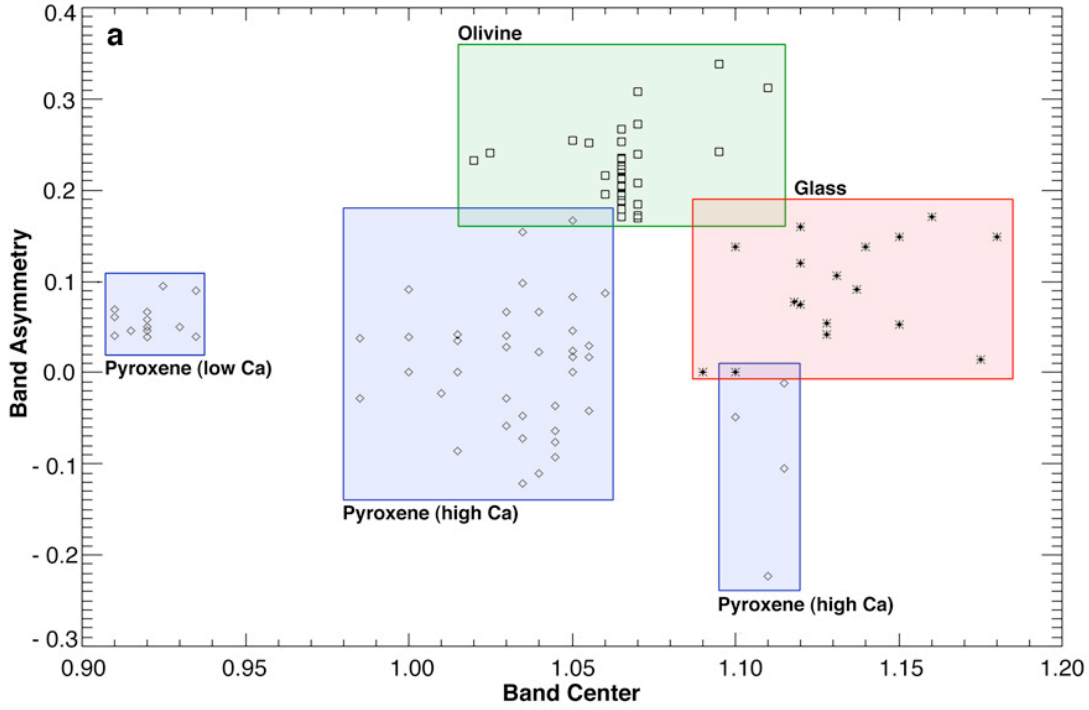
a
Olivine
Glass
Pyroxene (low Ca)
Pyroxene (high Ca)
Pyroxene (high Ca)
Band Asymmetry
Band Center
0.4
0.3
0.2
0.1
0.0
- 0.1
- 0.2
- 0.3
0.90
0.95
1.00
1.05
1.10
1.15
1.20

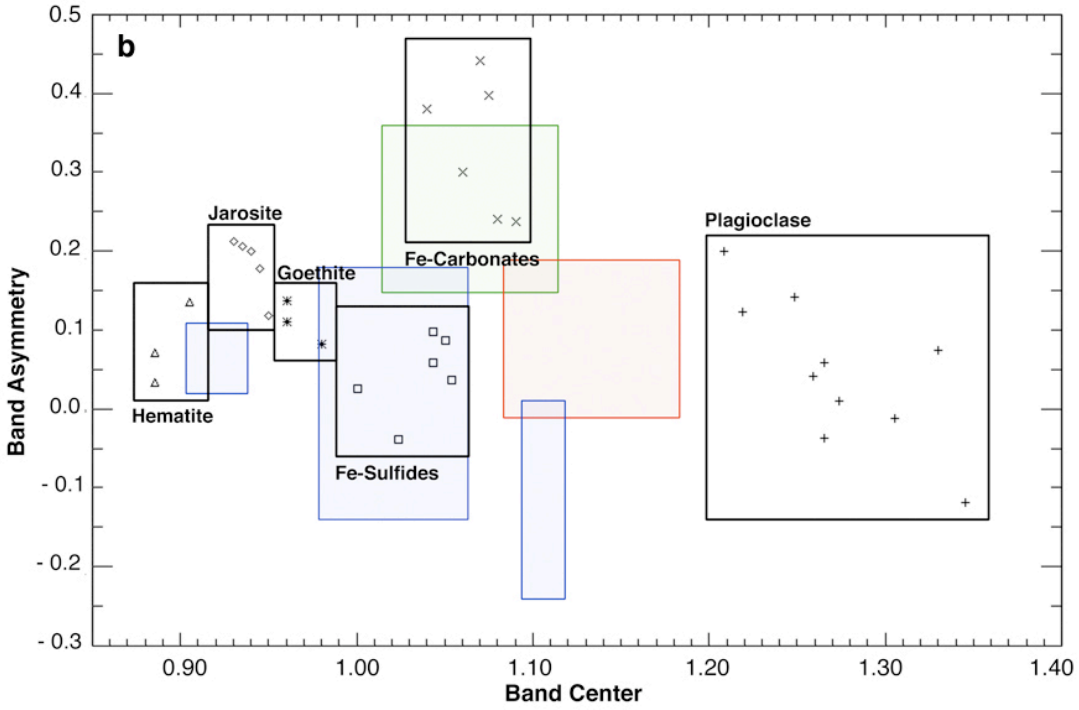
b
Jarosite
Goethite
Fe-Carbonates
Plagioclase
Hematite
Fe-Sulfides
Band Asymmetry
Band Center
0.5
0.4
0.3
0.2
0.1
0.0
- 0.1
- 0.2
- 0.3
0.90
1.00
1.10
1.20
1.30
1.40

From these trends, it is apparent that mixtures can produce spectral parameter values outside the regions for pure minerals, and can produce spectral parameter values within the regions of other pure minerals. This latter possibility could lead to false mineral identifications. For example, Figure 4.5 shows mixtures of LCP, HCP, and olivine with glass. Both the LCP/HCP and glass mixtures trend through the olivine region, and follow a similar trend as the olivine and glass mixture into the glass region. To discriminate between these possible interpretations, the shape of the rest of the spectrum and the presence of other bands can be considered. However, in this particular example, the LCP/HCP/olivine and glass mixtures with similar spectral parameters all appear very similar in spectral shape, as the glass has obscured the 2 μm bands of the pyroxenes. This strongly suggests that olivine is more difficult to uniquely identify in the NIR than just identifying a broad 1 μm band without a strong 2 μm band. Furthermore, this may imply that some previously reported olivine detections in NIR spectra of planetary surfaces could be false identifications.

4. OMEGA mapping and spectral processing

4.1 Data set description

The OMEGA imaging spectrometer acquires spectra with 3 detectors, observing at 352 wavelengths between 0.35 and 5.1 μm (Bibring *et al*., 2005). In this study, we have used all OMEGA visible (0.36-1.07 μm) and NIR (0.93-2.5 μm) north polar surface data taken during the first northern summer of Mars Express observations (2004). While data from later summers are publicly available, the spectra contain artifacts due to damaged spectral channels that severely hamper our ability to apply our atmospheric correction model. The 104 OMEGA image cubes that we have used in this study have resolutions between 0.5 and 5.4 km/pixel, lie north of 70°N, and are limited to solar longitudes (L_S) between 90° and 135°. We have chosen

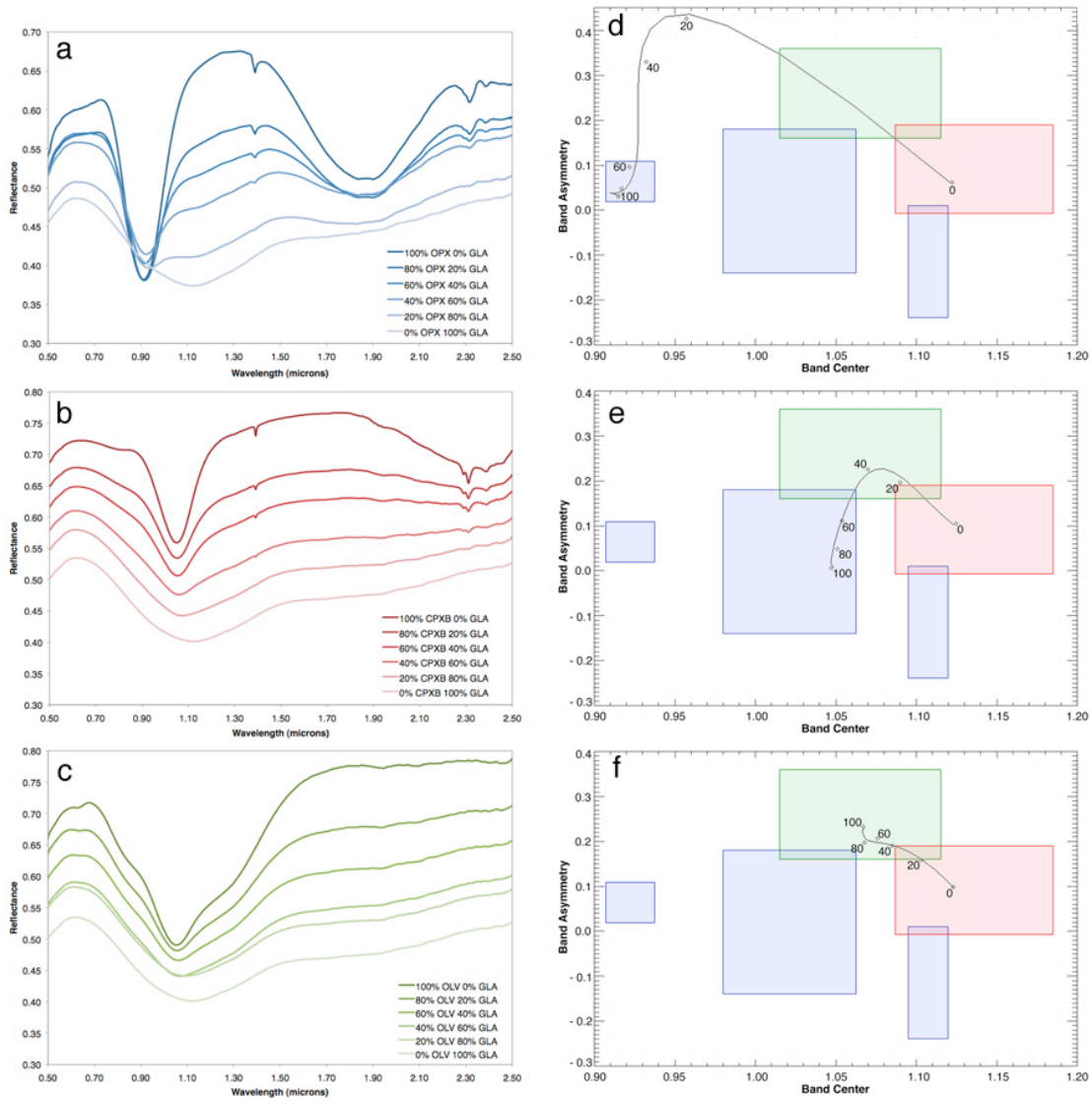

Figure 4.5: Spectra and band parameter plots for mineral mixtures. All mixtures are <45 μm grain size samples at 20 wt.% intervals (a) LCP-glass mixture spectra. (b) HCP-glass mixture spectra. (c) Olivine-glass mixture spectra. (d-f) Band asymmetry vs. band skew for the mixtures in (a-c). Lines indicate parameterized fits in abundance space. As in Figure 4.4, the blue regions are pyroxene, the green region is olivine, and the red region is glass. Note that the parameter trends for all three glass mixtures pass through the olivine region.

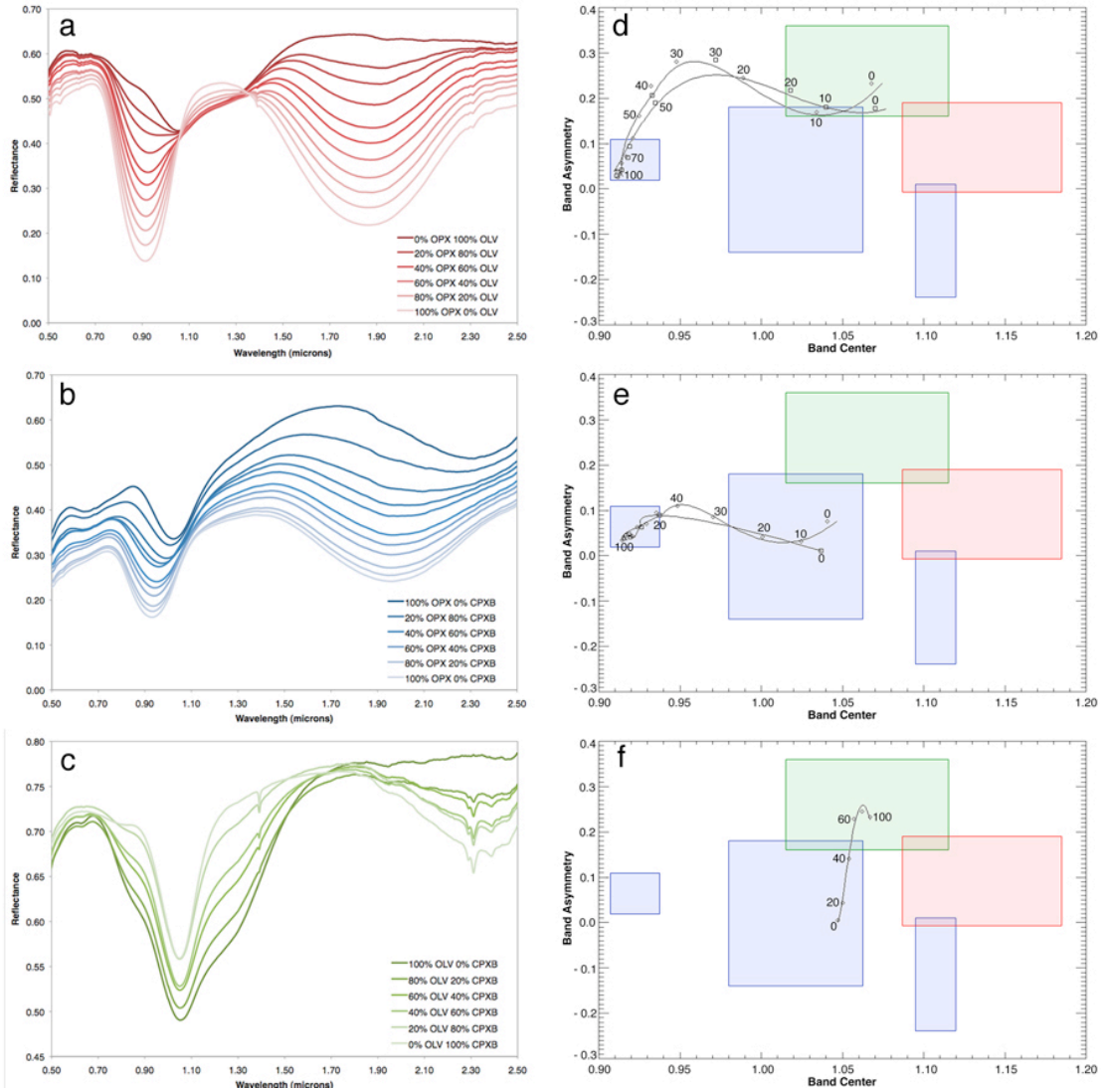

Figure 4.6: Additional spectra and band parameter plots for mineral mixtures. (a) LCP-olivine mixture spectra, < 38 μm grain size samples at 10 wt.% intervals. (b) LCP-HCP mixture spectra, < 45 μm grain size samples at 10 wt.% intervals. (c) Olivine-HCP mixture spectra, <45 μm grain size samples at 20 wt.% intervals. (d-f) Band asymmetry vs. band skew for the mixtures in (a-c). Lines indicate parameterized fits in abundance space. As in Figure 4.4, the blue regions are pyroxene, the green region is olivine, and the red region is glass. (d) also shows parameter trends for 90-125 μm grain size samples, and (e) also shows parameter trends for 90-180 grain size samples. While the parameter values at a given mixture ratio change with grain size, the general shape of the trend does not. Note that as little as 5-25 wt.% LCP can place the parameter values well out of the expected ranges for HCP, olivine, and glass.

this time range in order to acquire data after the summer solstice, to minimize the presence of surface CO_2 and H_2O frost (*e.g.*, Mitrofanov *et al*., 2003; Kelly *et al*., 2007), but well before the onset of the summer north polar hood, to minimize the presence of water ice clouds (*e.g.,* Wang and Ingersoll, 2002). All raw spectra were calibrated to I/F using standard OMEGA calibration routines (Bellucci *et al*., 2006).

4.2 Atmospheric correction

To compensate for atmospheric absorption, we have employed an empirical atmospheric absorption model based on the model created by the OMEGA team (Langevin *et al*., 2005a; Mustard *et al*., 2005) and outlined by Horgan *et al*. (2009) (Chapter 2). We have applied this model to the OMEGA spectra taken with the short wavelength infrared (SWIR), which includes our wavelengths of interest between 0.96 and 2.5 μm. We have assumed that atmospheric gas opacity (primarily from CO_2) has had a negligible effect on spectra taken with the visible and near-infrared (VNIR) channel, which includes wavelengths between 0.38 and 0.96 μm, and so we have not applied a correction to the spectra in that range.

4.3 Phase correction

To correct for viewing angle and to obtain an estimate of the surface albedo, we have applied a Lambertian phase function correction to the OMEGA data by dividing the spectra by the cosine of the incidence angle for each pixel, using separate phase angle information for the SWIR and VNIR channels (which are pointed at slightly different surface locations). Although a Lambertian correction may not be the most appropriate or rigorous treatment for the surface phase function (*e.g.,* Soderblom *et al*., 2006; Bell *et al.,* 2008), it is the simplest solution to implement, given the uncertainties in the derivation of viewing angles for each pixel and our lack of

understanding of the detailed photometric properties of the variety of surfaces that we are observing in this region.

In this study, we have excluded all spectra taken at phase angles greater than 60°. Above this approximate upper cutoff, spectra tend to exhibit characteristics different from spectra of the same location taken at lower phase angles. These effects include higher albedos, higher hydration band depths, and stronger dust features, and may be due to the high-phase angle effects of thin coatings of high-albedo materials over a dark substrate (*e.g.*, Fischer and Pieters, 1993).

4.4 Coregistration and mapping

Visible and atmospherically-corrected NIR spectra were projected into a 1 km/pixel north polar stereographic projection separately, using each spectrometer's individual pointing information, before being joined at 0.96 μm (channel 80/81). Many OMEGA spectra exhibit poor alignment between visible and NIR spectra even after the above corrections, especially bright surfaces and those close to strong albedo boundaries. Because some of our parameters are sensitive to the relative difference between visible and NIR albedos, spectra with poor alignments (greater than 3% difference between the median values of second order polynomial fits to visible channels between 0.77-0.95 μm and NIR channels between 0.98-1.22 μm) were not included in the final mosaic. Spectra with minor offsets (less than 3%) were adjusted to improve alignment by linearly scaling the visible channels to match a value projected at 0.96 μm from adjacent NIR channels. To minimize the amount of atmospheric and surface dust contamination in the spectra, each spectrum included in the north polar mosaic was chosen from the lowest albedo at 0.75 μm out of all available spectra at every location. While this method may be biased toward spectra composed of minerals with overall lower albedos (*e.g.*, glass), we do not believe that

is biases our final mineral maps, as the distribution of surface and atmospheric dust in the region is quite variable (*e.g.* changed more than the composition at the kilometer scale over our period of observation, approximately

4.5 Smoothing and despiking

As we are primarily concerned with analyzing the shape and position of broad ferrous absorption bands that have widths between approximately 0.1 and 0.4 μm, we have implemented a combination of median filters and boxcar average algorithms to minimize the influence of sharp spikes and high-frequency noise in the data. After construction of the mosaics, saturated, null, and known bad channels (1.01, 1.02, 1.32-1.37, 1.80-1.83, 2.23-2.27 μm; Bellucci *et al*., 2006) were replaced with interpolated values, and all spectra were smoothed with a boxcar smoothing algorithm (width ~0.07 μm). As discussed in Section 3.2, smoothing reduces the spectral contrast of narrow bands, like the 1.9 μm hydration band, but improves our ability to characterize broad bands, like those due to ferrous iron in mafic materials. For examples, see Figures 4.7a, 4.8a, and 4.9a.

4.6 Dust removal

A common analysis step in reflectance spectroscopy is to ratio spectra of interest to a nearby "reference" area that shows little or no relevant spectral contrast, such as a dusty plains region. This step can help to remove residual systematic instrumental and/or atmospheric artifacts, enhance otherwise subtle spectral contrasts from region to region, and remove the bulk of atmospheric and surface dust contamination from the spectra. This method is widely used in the analysis of OMEGA spectra *(e.g.*, Bibring *et al*., 2005; Poulet *et al*., 2008). Ideally, ratio spectra should be produced using a reference spectrum from the same observation; however,

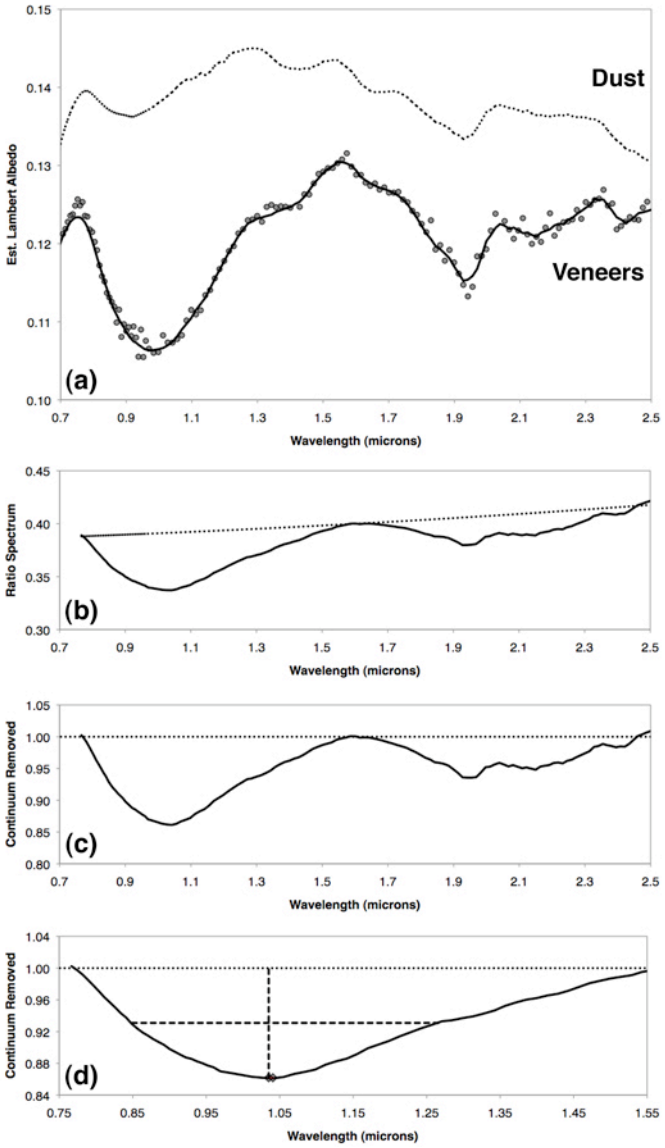

Figure 4.7: OMEGA spectral processing and analysis, shown here for our HCP endmember from 76.2°N, 356.0°E. (a) Spectrum prior to (points) and after (solid line) smoothing and aligning the visible and NIR parts of the spectrum, compared to average ice-free dust spectrum (dotted line). (b) Spectrum after ratioing with dusty spectrum (solid line) and second-order polynomial continuum fit (dotted line). (c) Spectrum after continuum removal. (d) Analysis of the 1 μm band. Diamonds indicate locations of band minimum and center, dashed lines indicate the band depth at the band center and the band width at half the maximum band depth.

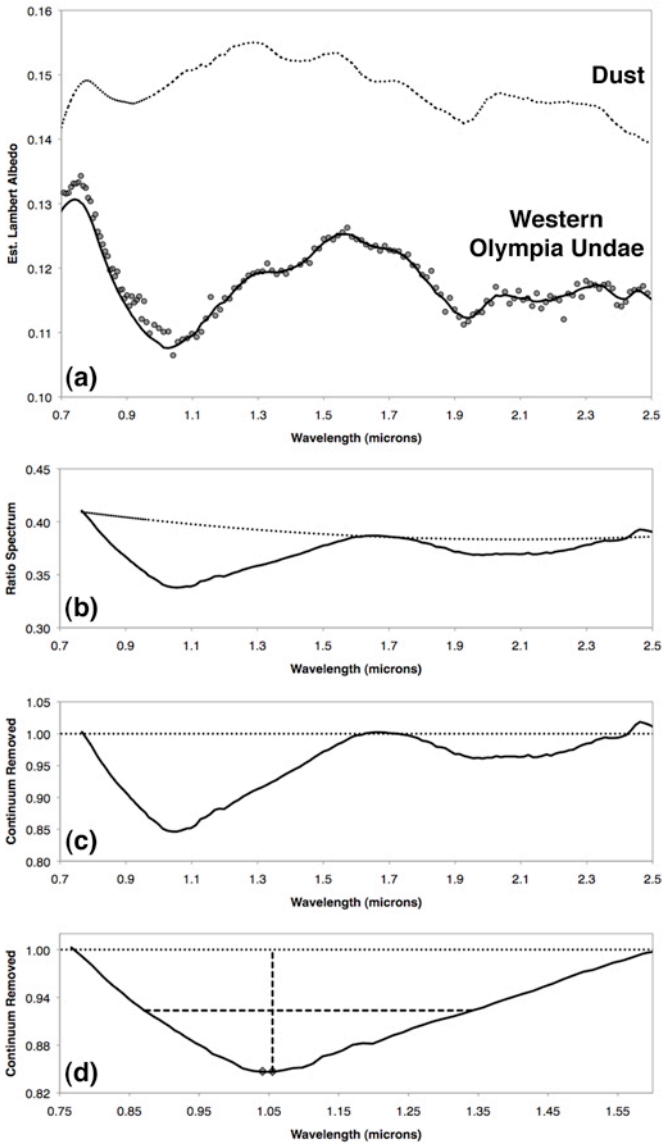

Figure 4.8: OMEGA spectral processing and analysis, shown here for our "olivine" endmember from 77.2°N, 95.4°E. (a) Spectrum prior to (points) and after (solid line) smoothing and aligning the visible and NIR parts of the spectrum, compared to average ice-free dust spectrum (dotted line). (b) Spectrum after ratioing with dusty spectrum (solid line) and second-order polynomial continuum fit (dotted line). (c) Spectrum after continuum removal. (d) Analysis of the 1 μm band. Diamonds indicate locations of band minimum and center, dashed lines indicate the band depth at the band center and the band width at half the maximum band depth.

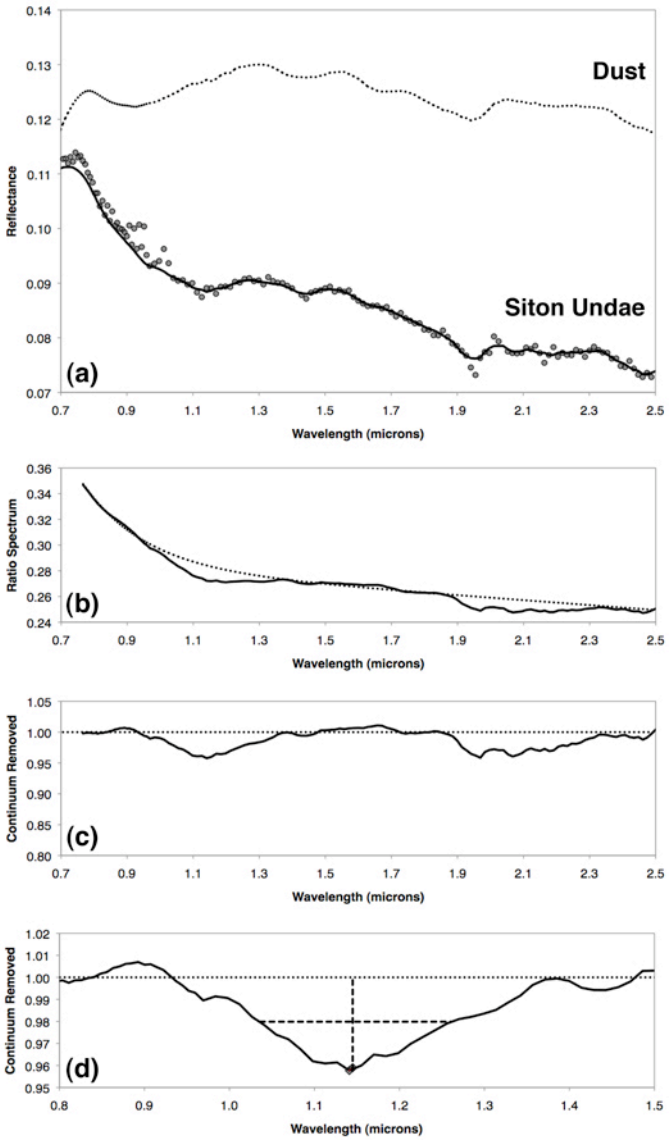

Figure 4.9: OMEGA spectral processing and analysis, shown here for our glass endmember from 75.2°N, 318.0°E. (a) Spectrum prior to (points) and after (solid line) smoothing and aligning the visible and NIR parts of the spectrum, compared to average ice-free dust spectrum (dotted line). (b) Spectrum after ratioing with dusty spectrum (solid line) and exponential continuum fit (dotted line). (c) Spectrum after continuum removal. (d) Analysis of the 1 μm band. Diamonds indicate locations of band minimum and center, dashed lines indicate the band depth at the band center and the band width at half the maximum band depth.

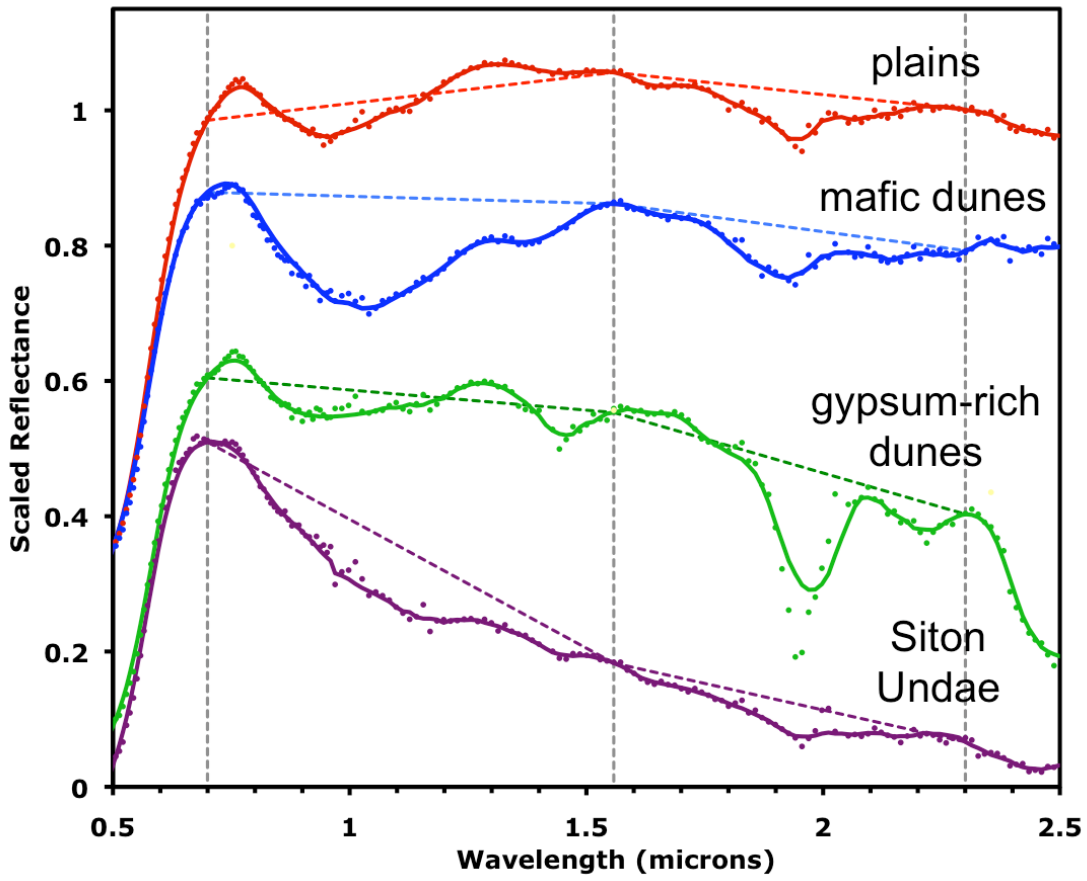

Figure 4.10: Examples of convex (top three spectra) and concave (bottom) spectra, prior to (points) and after smoothing (solid lines). The locations of the channels used in calculating the concavity parameter and short and long wavelength slopes are indicated for comparison (dashed lines).

the large number of observations used in this study precludes this approach. Instead, we have used a reference spectrum that is the average of all high albedo (0.3-0.35), ice-free (1.5 μm band depth less than 1%, see Chapter 2) spectra in our smoothed north polar mosaic (*e.g.*, Figure 4.7a). Because the dust spectrum exhibits strong ferric iron absorptions below the visible reflectance peak at 0.77 μm, our analysis techniques from this point forward only use wavelengths at and above 0.77 μm.

4.7 Continuum modeling and removal

Another common analysis step in reflectance spectroscopy is continuum removal (see Section 2.2), which is necessary if we wish to directly compare the characteristics of the 1 μm ferrous iron absorption band in OMEGA data with laboratory spectra. Most martian spectra exhibit convex shapes, as "red" slopes at shorter wavelengths transition to "blue" slopes at longer wavelengths (Figure 4.10). Red slopes below 1 μm in typical martian spectra are caused by strong ferric iron absorptions, and blue slopes beyond 1 μm are due to either thin coatings of ferric oxides or the wings of the 3 μm H_2O/OH fundamental absorption band (*e.g.*, Fischer and Pieters, 1993; Bell, 1996). For these spectra, we have modeled the continuum as a second order polynomial, fit to three channels at and adjacent to the local maxima between 0.77-0.9, 1.3-1.7, and 2.2-2.5 μm.

While this continuum removal approach works for most spectra in the north polar region, there is a class of spectra that exhibits a strongly concave continuum shape that is not removed well by a standard polynomial fit. The continuum shape of these spectra is concave between about 0.7 and 1.2 μm and transitions into a flat or blue linear slope beyond this point (Figure 4.10). Spectra with this continuum shape can be identified by a parameter based on a difference of ratios, applied to smoothed spectra *before dust removal*:

$$Concavity = A(0.7)/A(1.55) - A(1.55)/A(2.3)$$

where A is the estimated Lambert albedo at the indicated wavelength in μm. We chose 1.55 μm as the reference wavelength because it lies outside the broad ferrous iron bands centered near 1 and 2 μm and H_2O/OH absorptions near 1.4 μm. We have only applied this parameter to smoothed spectra that have not been ratioed. Spectra are considered concave if their concavity parameter is greater than zero, and the highest concavity values that we have observed in the north polar region are near 0.25.

Most concave spectra continuum shapes are consistent with an exponential decrease; however, because some of the concave spectra also exhibit linear blue slopes beyond 1.2 μm, we have modeled the continuum function, *C*, as an exponential function multiplied by a linear function:

$$C = p_0 \exp(-p_1 x) + p_2 \exp(-p_1 x) + p_3 x + p_4$$

To find the exact function for each concave spectrum, $p_{0\text{-}2}$ are constrained to be positive (to create a concave shape), and $p_1 < 4$ (to limit the concavity of the exponential to that of the most concave surface spectra that we observed), and the function is fit to all channels between 0.75-1.0 μm, 1.28 μm, and the three channels at and adjacent to local maxima between 1.2-1.4, 1.5-1.8, and 2.2-2.5 μm. The function above produces a good fit for highly concave spectra that have been ratioed to a dusty reference spectrum (Figure 4.9).

As calculating continuum fits for all 2,853,147 spectra in our north polar mosaic would be time prohibitive, we have only presented results here for low albedo (less than 0.25 estimated Lambert albedo at 0.77 μm) and ice-free (less than 1% 1.5 μm ice band depth; see Chapter 2) spectra, reducing the total number of spectra in our data set to 976,293 spectra. The 1.5 μm band depth is also positive for spectra with strong gypsum components (see Chapter 2), thus we have not analyzed spectra from the eastern most region of Olympia Undae. We have chosen these spectra for removal because spectra with ice and significant hydrated mineral components exhibit strong blue slopes due to the wings of the 3 μm absorption band that distort our continuum fits, and exhibit absorption bands in the 1.4-1.6 μm region that adversely affect our band parameters (see next section).

4.8 Band analysis

Once the continua of the spectra are removed, we can apply the same 1 μm band analysis techniques that we applied to laboratory mineral spectra, as outlined in Section 3.3. Figure 4.7 shows these parameters as applied to OMEGA spectra.

The presence of additional absorptions in the 0.8-1.5 μm region is not something that we had to account for in laboratory spectra, but it is a problem in OMEGA spectra. In particular, the relatively broad 1.4 μm H_2O band due to bound water in hydrated minerals tends to occur at the wavelength location of approximately half the band depth of the 1 μm band, and therefore skews the band asymmetry parameter in the positive direction. Therefore, for the purpose of calculating the band width and band skew, we have interpolated over the 1.37-1.55 μm region of the spectrum in spectra with greater than 1% 1.45 μm band depths, as measured relative to 1.3 and 1.6 μm, in smoothed, dust and continuum removed spectra. As we are not analyzing spectra with very strong hydrated mineral components (see previous section), this minor correction is sufficient.

5. Observations

5.1 Concave continuum

Positive values of our concavity parameter are concentrated in Siton Undae and Hyperborea Undae, but also appear adjacent to Planum Boreum in several locations, as shown in Figure 4.11. With few exceptions, these apparent sources of materials with concave spectra appear to correspond to outcrops of the Planum Boreum cavi unit, as mapped by Tanaka *et al*. (2008) and shown in Figure 4.1, implying that the cavi unit is the source for these materials. The primary exceptions are some apparent sources in the polar outliers, potentially indicating that either the cavi unit or a compositionally similar unit is also present in these locations.

Figure 4.11: Maps of the concavity parameter for all low albedo (less than 0.25 estimated Lambert albedo at 0.77 μm) and ice-free (1.5 μm band depth less than 1%) spectra. (a) shows concavity parameter values -0.15 to 0.15, and (b) shows only positive concavity parameter values. Red arrows in (b) indicate locations where detections of positive concavity are located near scarps, possibly indicating a source within the polar layered deposits. Most of these locations compare favorably with locations of outcrops of the Cavi unit, as shown in Figure 4.1.

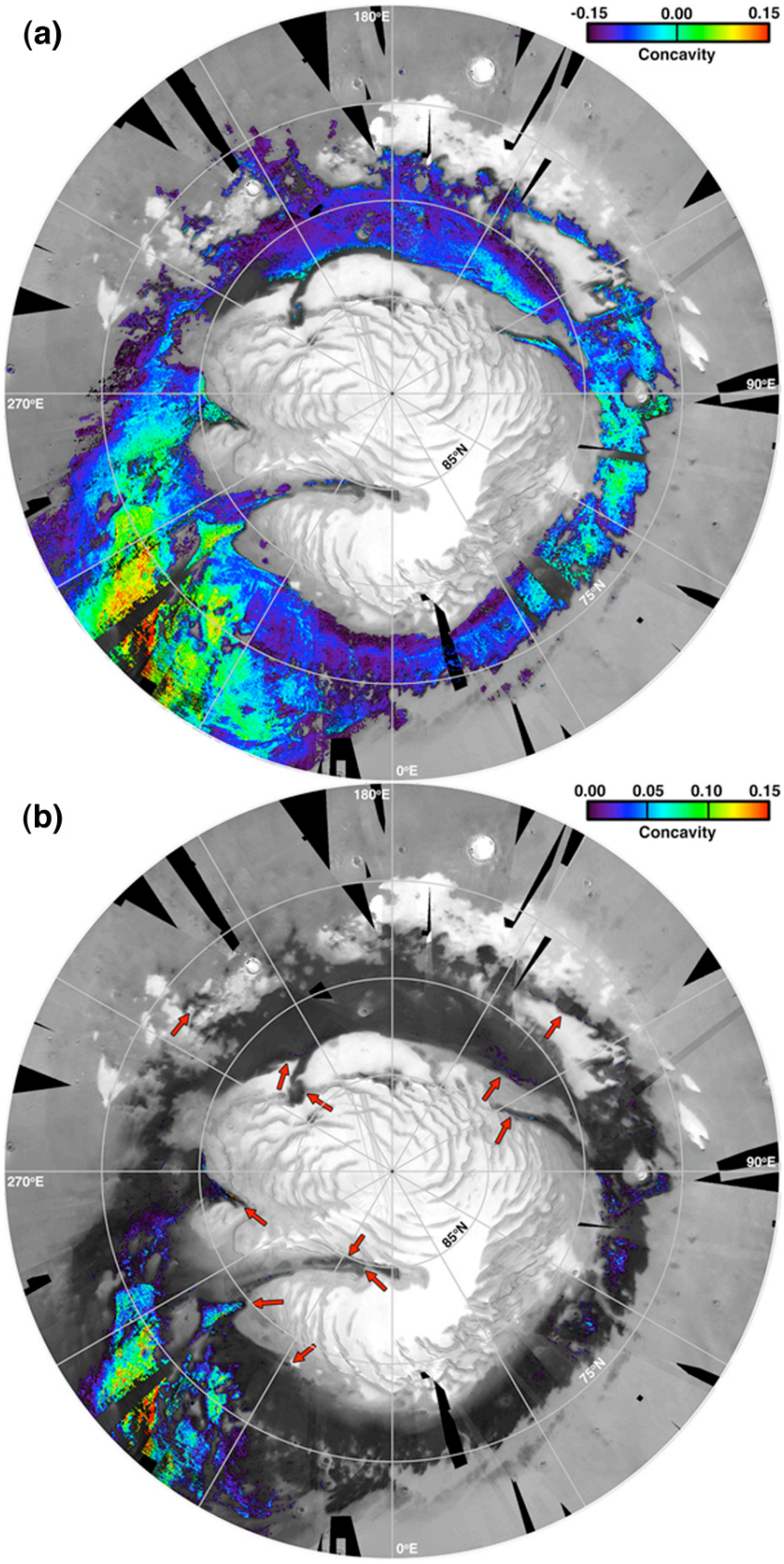
(a)
-0.15
0.00
0.15
Concavity
180°E
90°E
270°E
0°E
85°N
75°N
(b)
0.00
0.05
0.10
0.15
Concavity
180°E
90°E
270°E
0°E
85°N
75°N

5.2 Band parameters

Figure 4.12 shows maps of the 1 μm band center and band asymmetry in the north polar region. Many of the band centers are too long (greater than ~1.1 μm, yellow and red in Figure 4.12a) to be consistent with olivine, but are consistent with iron-bearing glass (Adams, 1974; Gaddis *et al*., 1985; Minitti *et al*., 2002; Moroz *et al*., 2009). These spectra are concentrated within Siton Undae and Hyperborea Undae, but are also observed near exposures of the cavi unit on the margins of Planum Boreum. Overall, the locations of glass-like spectra and spectra with a positive concavity appear to be highly correlated. Indeed, 80% of all concave spectra (concavity greater than 0) and 88% of highly concave spectra (concavity greater than 0.05) have band centers above 1.1 μm, compared to 8% of convex spectra (concavity less than 0). This result confirms the apparent correlation between concave spectra and what we interpret below as glassy spectra, suggesting that that the concave continuum is a property of these putatively glass-bearing materials.

Spectra with band centers consistent with olivine and high-calcium pyroxene are also present in the region. The lowest band centers observed are 1.02-1.03 μm, and largely occur on the southwestern edge of Olympia Undae, near the polar outliers, and in the plains deposits of the north polar veneers between 320°E and 30°E. We do not observe any spectra with band centers below 1.02 μm, suggesting that LCP or mixtures of LCP and other minerals are not primary compositional endmembers in this region. As LCP is primarily associated with ancient Noachian-aged units on Mars (*e.g.*, Mustard *et al*., 2005), this result is not unexpected for the Amazonian-aged terrains of the north polar region.

Geographic trends in the band asymmetry parameter are less apparent, but are discernible. For example, high asymmetry is associated with Olympia Undae, and relatively lower asymmetry is associated with the polar outliers, Siton Undae, and the

Figure 4.12: Maps of the 1 μm (a) band center and (b) band asymmetry parameters for all low albedo (less than 0.25 estimated Lambert albedo at 0.77 μm) and ice-free (1.5 μm band depth less than 1%) spectra with 1 μm band depths greater than 2%. Red arrows in (a) indicate locations where spectra with band centers beyond 1.1 μm are located near scarps. Most of these locations compare favorably those shown in Figures 4.8b and 4.1. Box indicates the location of maps in Figure 4.13b-c.

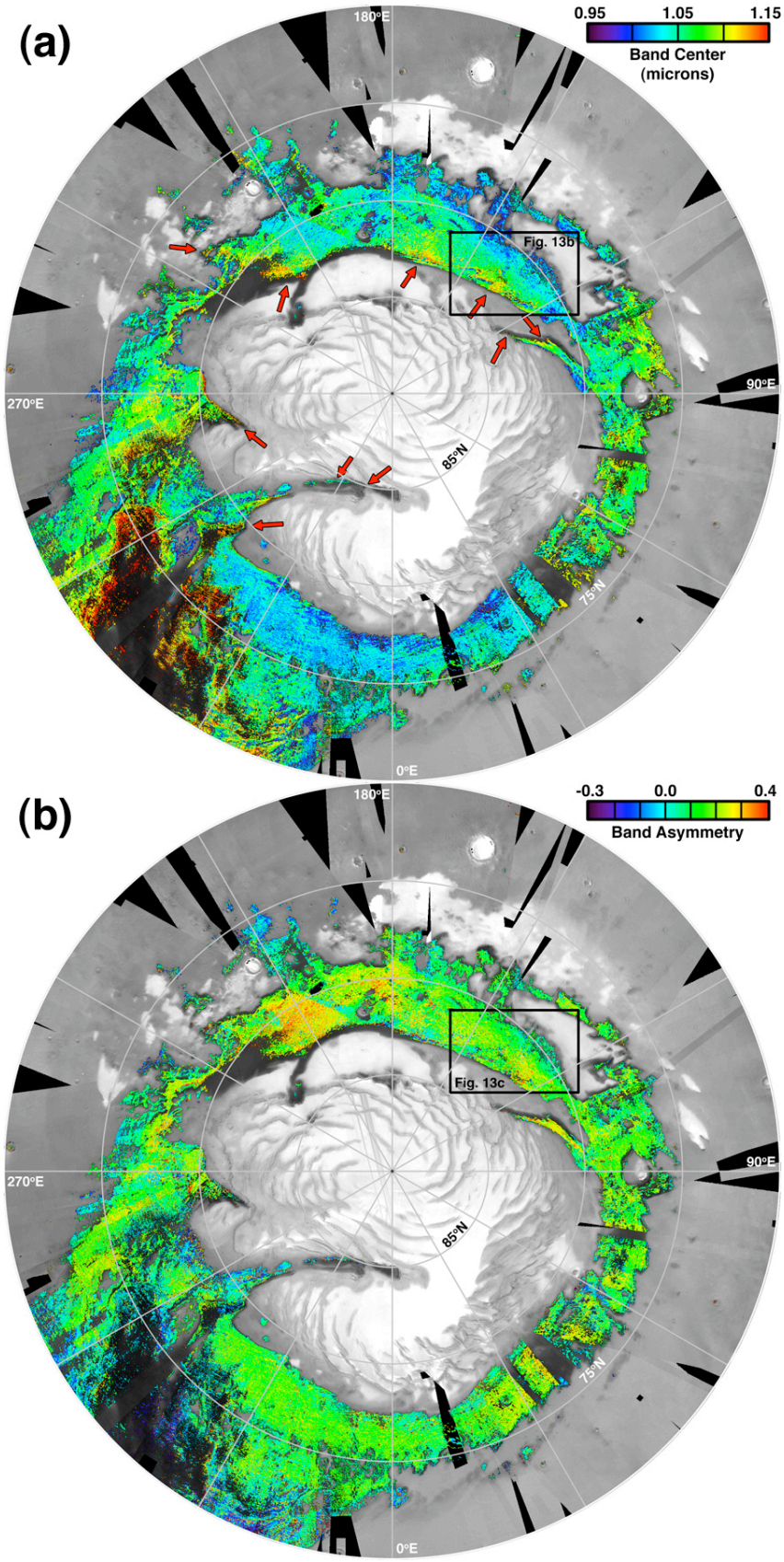
(a)
0.95
1.05
1.15
Band Center
(microns)
Fig. 13b
180°E
90°E
270°E
0°E
85°N
75°N
(b)
-0.3
0.0
0.4
Band Asymmetry
Fig. 13c
180°E
90°E
270°E
0°E
85°N
75°N

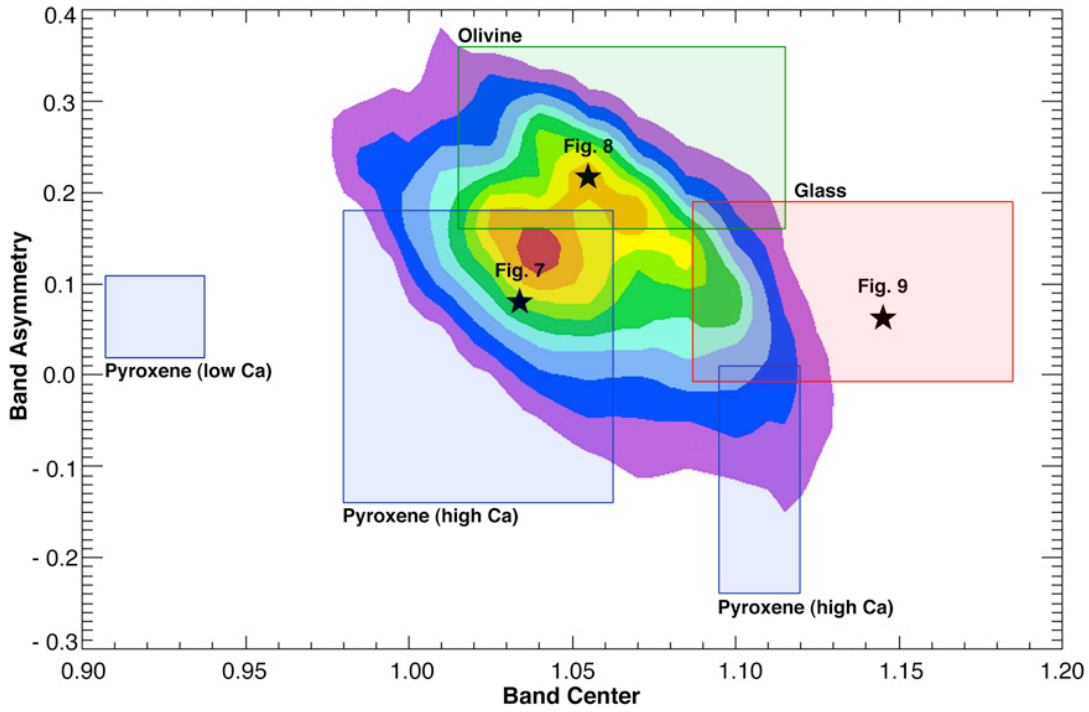

Figure 4.13: Parameter plot for all low-albedo (estimated Lambert albedo less than 0.25 at 0.77 μm) and ice-free (1.5 μm band depths less than 1%) OMEGA spectra with band depths greater than 2% in the north polar region. Contours indicate 10% intervals in the number of total spectra, from 10-90%, such that the outside of the purple contour encloses 90% of all spectra plotted and 10% of all spectra are located inside the red contour. The stars indicate parameter values for our endmember spectra shown in Figures 4.7-4.9.

north polar veneers. The importance of these trends becomes more apparent when considered along with geographic trends in the band center.

Figure 4.13 shows band center and band asymmetry parameter values plotted on the same field as the laboratory data in Figure 4.4a. While there is significant spread in the distribution, this is not statistically unexpected for a data set of nearly 1 million spectra. Within the broad distribution, there is structure that may indicate a trend, extending from the olivine region down into the HCP region on one side, and down into the glass region on the other. The high asymmetry spectra in Olympia Undae fall in the olivine region at the top of this trend, while the low asymmetry

spectra in the veneers and on the edge of Olympia Undae and those in Siton Undae fall into the HCP and glass ends of this trend, respectively. The spectra shown in Figures 4.7-4.9 represent three endmembers of this apparent trend.

6. Interpretation of observed parameter trends

There are several possible reasons for the observed trend in band parameter space. The simplest explanation would be regional HCP-glass mixing, as the shape of the trend in Figure 4.13 closely resembles that of Figure 4.5e. Alternatively, the observed trend could be a composite of more localized HCP-olivine and olivine-glass mixing, as shown in Figures 4.5f and 4.6f. Finally, the trend could be due to statistical spread around three separate and unmixed HCP, olivine, and glass endmembers.

To test these hypotheses, we can examine trends in these parameters at a more local scale. Figure 4.14a-b shows a portion of our band center and band asymmetry maps in the western region of Olympia Undae, where materials with concave, glass-like spectra may be sourced from the cavi unit. Figure 4.14c shows the result of taking a profile through these maps and plotting the corresponding parameter values. The trend in Figure 4.14c closely resembles that of the center of the distribution in Figure 4.13, suggesting that the trend in Figure 4.13 is real, and that it is due to mixing on local scales.

While the above example demonstrates that we are observing mixing of ferrous minerals, it does not necessarily constrain whether that mixing is HCP/glass mixing or a combination of HCP/olivine and olivine/glass mixing. However, we should be able to discriminate between these possibilities by examining the other regions of the spectrum. HCP exhibits a broad ferrous iron absorption band centered between 2-2.4 μm, while glass exhibits a very weak 2 μm band, and olivine has no 2 μm band. While HCP/glass mixtures do not always exhibit this band (*e.g.*, Figure 4.5b), the 2 μm band

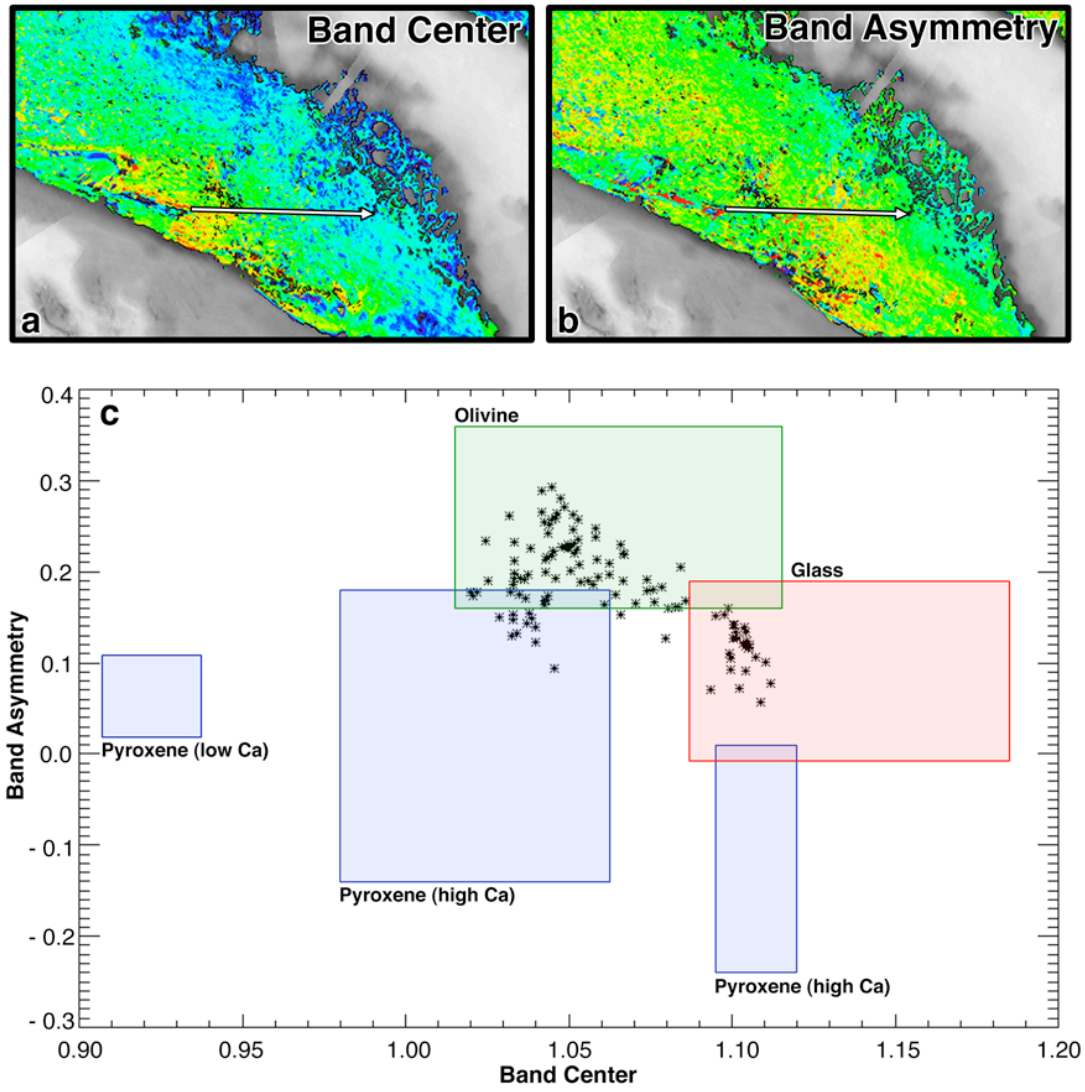

Figure 4.14: Parameter trends in western Olympia Undae, near 135°E. (a-b) Band center and band asymmetry parameter maps in this region. Arrows indicate the location of profiles taken through the maps. (c) Parameter plot for values interpolated along arrows shown in (a-b). Trends were taken through 5 pixels on both sides of the center trendline. As shown in (a-b), higher band centers and lower skews are located near the northern edge of the dune field. The trend from glass to HCP indicated here is also consistent with the overall trend in parameter values for the entire north polar sand sea plotted in Figure 4.13.

in glass is very weak, so olivine/glass mixtures do not exhibit this band except at very high glass contents, when the spectrum has more glass-like parameters (*e.g.*, Figure 4.5c). So, while *not observing* a 2 μm band in spectra that have olivine-like parameters is not necessarily diagnostic of olivine, *observing* a 2 μm band in such a spectrum is diagnostic of a HCP/glass mixture. The endmember from the olivine region shown in Figure 4.8 has a broad band centered near 2.05 μm, making this spectrum consistent with a HCP/glass mixture. The presence of a 2 μm band is typical for most spectra in the region. In fact, 80% of the spectra with 1 μm band depths greater than 2% also exhibit 2.05 μm band depths (as measured from the continuum) greater than 2%.

Thus, we conclude that while some olivine may be present in the north polar sand sea, the dominant ferrous minerals appear to be HCP and iron-bearing glass. Figure 4.15 shows a classification map of which region of the band parameter plot each spectrum in the map falls in, where we have interpreted pixels within the HCP and glass regions as primarily HCP and glass, respectively, and those falling within the olivine region as primarily a mixture of HCP and glass. Our distributions of HCP and HCP-glass mixtures are consistent with previous maps of pyroxene and olivine spectral indices over the north polar region (Poulet *et al*., 2008), except that we interpret the olivine signature as an HCP-glass mixture.

7. Interpretation of concave continua

7.1 Evidence for leached glass rinds

The concave, blue continuum slopes of primarily glass-like spectra in the north polar region are unique, as most martian surface spectra have convex shapes (see Section 4.7). While thin ferric coatings may be responsible for the linear blue slope of these spectra beyond 1.5 μm (*e.g.*, Poulet *et al*., 2007), ferric coating spectra exhibit strong red slopes and absorptions below 1 μm (Singer and Roush, 1983; Fischer and

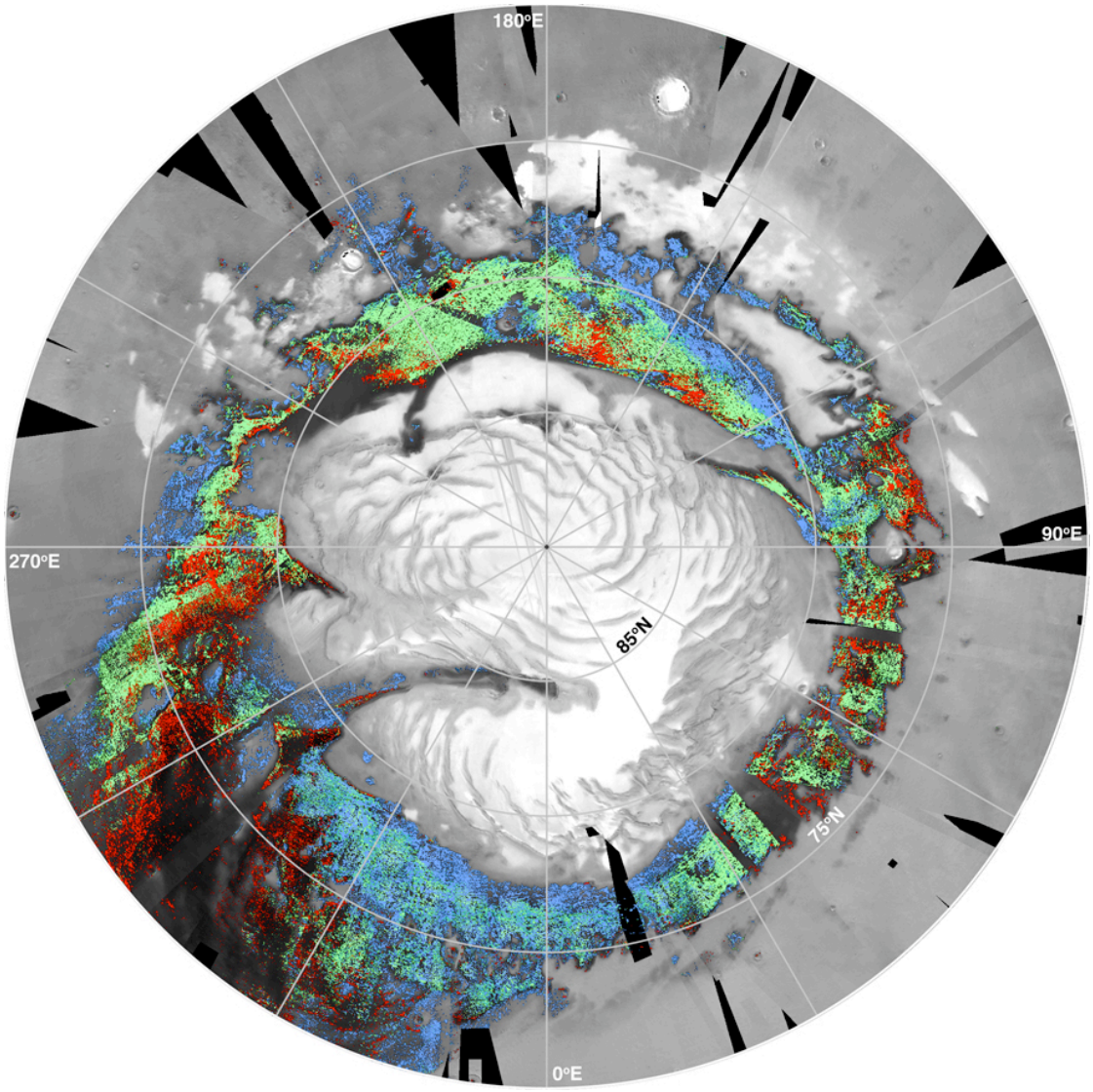

Figure 4.15: Distribution of dominant endmember minerals based on parameter values. Blue, green, and red indicate parameters within the HCP, olivine, and glass regions, respectively. While green regions could be interpreted as olivine based purely on the shape of their 1 μm band, we instead interpret these spectra as a mixture of HCP and glass (see text). HCP appears to be associated with and potentially sourced from the north polar outliers and the north polar veneers, while glass appears to be associated with and potentially sourced from the cavi unit.

Pieters, 1993; Johnson and Grundy, 2001; Morris *et al*., 2001), and thus cannot account for the concave blue slope that we observe between 0.75 and 1.5 μm.

Furthermore, this anomalous continuum slope also cannot be attributed to a specific mineral. If a mineral absorption band was the cause of the concave slope between 0.75-1.2 μm, it would have to be extremely broad and centered beyond 1.2 μm, a rare combination. The best example of such a band is the broad ferrous iron band centered between 1.2-1.5 μm in the spectrum of ilmenite ($FeTiO_3$); however, ilmenite also exhibits a strong red slope below 0.9 μm in the visible, making it a poor match for our concave spectra (*e.g.*, Cloutis and Gaffey, 1991). Alternatively, very steep continuum slopes between 0.7-1.0 μm have also been attributed to bedrock with roughness effects on the scale of tens of μm (Harloff and Arnold, 2002). However, this interpretation is not consistent with the sand-dominated surfaces of our study, and the continuum effects do not extend as far into the NIR.

The concave continuum slope is spectrally consistent with thin (3-10 μm) silica-enriched leached glass rinds on basaltic glass (Figure 4.16), formed during interactions with acidic (pH 3-4) fluids (Minitti *et al*., 2007; Chemtob *et al*., 2010). This would be consistent with the association between the concave continuum and glass-like 1 μm bands. These acidic leached glass rinds are spectrally and physically similar to rinds formed during high-temperature oxidation of glass (Figure 4.16; Minitti *et al*., 2002). During both acidic leaching and oxidation, diffusion into the glass causes preferential migration of lower valence cations (*e.g.,* Na^{+}, Mg^{2+}, Fe^{2+}, Ca^{2+}) out of the glass surface, leaving behind the higher valence cations (*e.g.,* Si^{4+}, Ti^{3+}, Al^{3+}) that form the glass structural network (Cook *et al*., 1990; Cooper *et al*., 1996; Cook and Cooper, 2000; Chemtob *et al*., 2010). Thus, the rind is still structurally similar to the source glass, but is enriched in SiO_2, AlO_2, and TiO_2.

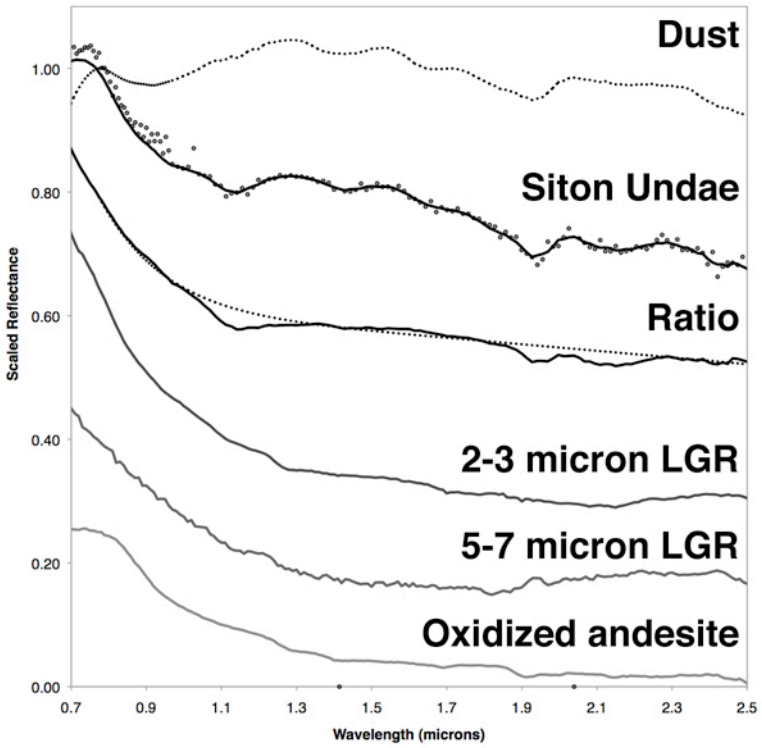

Figure 4.16: Siton Undae spectrum compared to leached glass rinds and oxidized andesite. LGR spectra are MUO and MIY black coating spectra from Minitti *et al.* (2007). Andesite spectrum sourced from the RELAB spectral library (Pieters, 1983).

It is critical to note that these leached glass rinds (LGR) are spectrally and physically unique from depositional silica coatings (DSC), which are formed by aqueous dissolution of silicate minerals and re-precipitation of amorphous or opaline silica out of solution (*e.g.*, Minitti *et al*., 2007). While LGR retain the loosely bound silica tetrahedral structure of the host silicate glass, DSC have an amorphous or opaline structure distinctly different from their substrate (*e.g.*, Chemtob *et al*., 2010). Furthermore, DSC do not exhibit concave spectral signatures in the NIR (Kraft *et al*., 2007), but do exhibit absorption bands at 1.4, 1.9, and 2.21 μm (*e.g.*, Milliken *et al.*, 2008). While we do observe 2.21 μm absorptions in some higher-resolution OMEGA observations of Siton Undae, the detections are not widespread or common.

7.2 Consistency with TES analyses

A silica-enriched LGR on glass could be the high silica phase of TES ST2, as the distribution of LGR and glass that we have detected is spatially consistent with TES mineral deconvolution results. Firstly, the LGR distribution correlates well with the greatest concentrations of ST2 high-silica materials. These materials have been mapped using the TES 465 cm^{-1} index, and the highest index values planet-wide are found in Siton Undae (Ruff and Christensen, 2007). Secondly, our detection of iron-bearing glass in the north polar sand sea is consistent with TES predictions of basaltic glass abundances on the order of 10-20% in the low albedo deposits of the northern lowlands, higher than anywhere else on the planet (Bandfield, 2002). Finally, the TES detection of ST2 at moderate abundances throughout the north polar erg (Ruff and Christensen, 2007) is also consistent with our results, which indicate that the erg is composed of a mixture of HCP and glass. Although concavity values are predominantly negative outside of the region of Siton Undae, the glass endmember of the mixture appears to exhibit positive concavity values consistent with LGR everywhere that we have observed it. This suggests that the glass that is mixed with HCP exhibits LGR as well, but that the spectral signature of the LGR is masked by the mixture.

While LGR appear to be spatially consistent with ST2, more laboratory studies of LGR are needed to confirm that they are also spectrally consistent, as only MIR emissivity spectra of LGR with partial coatings of other alteration products have been published at this time (*e.g.,* MUO and MIY rind spectra in Minitti *et al*. (2007)). However, these spectra of partially coated LGR have been noted to exhibit Si-O stretching features at very similar wavelengths to obsidian (Minitti *et al*., 2007), which has been employed as the high-silica phase in some ST2 deconvolutions (Bandfield *et*

al., 2000; Michalski *et al*., 2005). Thus, we hypothesize that future laboratory studies will reveal that LGR are spectrally consistent with the high-silica features of ST2.

Further investigations of the distribution of ferrous minerals beyond the north polar region have shown that the low albedo deposits of Acidalia Planitia, the large low albedo feature south of Siton Undae, also exhibits concave spectra and 1 μm bands consistent with iron-bearing glass (Horgan and Bell, submitted). This detection strengthens the correlation between LGR and ST2, and places constraints on the formation mechanism for the leached deposits.

8. Implications for north polar history

8.1 Sources and transport history of north polar sediments

The ferrous mineral mixing trend that we have observed in the north polar region is consistent with two separate sources for the two endmember compositions, relatively unaltered HCP-rich sand and leached glass-rich sand.

The glass-rich sands appear to be sourced from the cavi unit, as they are concentrated near exposures of this unit. However, it is not clear if Siton Undae and Hyperborea Undae are also sourced from these exposures. While some dune trains do trend from exposures of the cavi unit into both sand seas, the high concavity values, 1 μm band parameters that plot well into the glass region (*e.g.*, Figures 4.9, 4.13), and the very low albedo of these regions (less than 0.1 estimated Lambert albedo) are consistent with very glass-rich deposits that have undergone little or no mixing. As these sand seas have more glass-like characteristics than any of the potentially freshly exposed sediments, this may suggest that they have a separate origin. Indeed, it is not implausible that Siton Undae and Hyperborea Undae could be remobilized remnants of the cavi unit, emplaced either concurrently with the paleo-erg, or afterward, before major influx of unaltered sediments occurred. Furthermore, while leached glass

appears to be the dominant composition of the cavi unit, it is unclear whether the leaching occurred within Planum Boreum, in the paleo-erg itself, or whether the paleo-erg was formed from previously altered sediments, potentially eroded from elsewhere in the northern basin, such as Acidalia Planitia.

The HCP-rich sands appear to be associated with the north polar veneers, and thus may be sourced from the same unit, the Planum Boreum 2 (PB2) unit. The fact that the mineralogy of this unit appears to be distinct from that of the other major sand-bearing unit, the cavi unit, suggests that the PB2 unit had a separate source from the cavi unit. This also implies that the PB2 unit has not exchanged sediment with this cavi unit. It has been previously suggested that the PB2 unit was sourced from Olympia Undae (Tanaka *et al*., 2008; Horgan *et al*., 2009); however, this is not consistent with the glass-HCP mixture composition that we infer for Olympia Undae. Alternatively, the leaching that occurred in the cavi unit may have occurred after the PB2 units were emplaced. In this case, the leaching of the cavi unit materials must have taken place geologically recently, as the PB2 unit is dated to the Late Amazonian (Tanaka *et al*., 2008).

8.2 Origin of leached glass deposits

On Mars, primary sources of glass-rich deposits include volcanism and impact melts. Impact glass has been hypothesized to exist in the form of melt sheets and dispersed glassy ejecta (*e.g.*, Bouska and Bell, 1993; Schulz and Mustard, 2004). Glass should also be present as a major component of quickly quenched volcanics, such as subaerial pyroclastic flows, or in flows that contacted water or ice (*e.g.*, Bouska and Bell, 1993). A primary source for the glass-enrichment observed in the north polar region is unlikely, however, as the area of the deposits (greater than 10^6 sq. km, including Acidalia Planitia) is much more extensive than expected for any of

these processes, and there is no geomorphic evidence indicating that such processes have taken place in the northern basin (*e.g.*, Tanaka *et al*., 2008).

Alternatively, acidic leaching could have produced both the LGR and the glass enrichment by alteration of common martian glass-bearing mafic sand. Under the acidic conditions necessary for LGR to form, laboratory experiments performed on mafic sand have demonstrated that olivine and pyroxene grains can be preferentially dissolved, while glass and plagioclase remain (Tosca *et al*., 2004; Golden *et al*., 2005). Theoretical calculations predict that fine-grained basaltic glass is unstable during diagenesis (*e.g.*, Pollard *et al*., 2003); however, in sand-sized and larger particles, the glass is preserved by the development of the LGR, which retards further alteration of the glass (Tosca *et al*., 2004; Techer *et al*., 2001; Crovisier *et al*., 2003). The protection afforded by the LGR is greatest under moderately acidic conditions, where the glass solubility curve has a minimum that extends below the solubilities of most pyroxenes and olivines (Minitti *et al*., 2007; Hausrath *et al*., 2008). Thus, it is plausible that widespread acidic leaching was responsible for both the glass-enrichment and the formation of LGR in the north polar region and Acidalia Planitia.

The chemistry of glass leaching places constraints on the processes that may have produced the LGR we observe on Mars. First, to create and preserve the LGR, the leaching solution must be acidic and must maintain that acidity. As basalt alteration tends to alkalize solutions (*e.g.*, Hurowitz *et al*., 2010), the altering fluid must be either constantly renewed, initially very acidic (pH <2-3), or moderately acidic with high (>100) water:rock ratios (Minitti *et al*., 2007). Large quantities of water are unlikely on an arid, Amazonian Mars, although it must be noted that Siton Undae is located at the lowest point of the northern lowlands, and would be the collection basin for long-ranging fluid outflows from the Chryse outflow channels south of Acidalia and for outflows from Planum Boreum. Instead, a more likely

scenario is a low water:rock ratio system with an environmentally-forced acidity. Under current arid martian surface conditions, any dissolved Fe^{2+} in a fluid that is in contact with the atmosphere will oxidize and acidify the fluid, as long as the water:rock ratio is too low to dilute the acid (Hurowitz *et al*., 2010). Possible sources for the water in this scenario could include ground water, ground ice melt, and surface ice or snow melt.

The other major constraint on the leaching process is that it must deposit a suite of secondary alteration products that are spatially and compositionally consistent with the observed mineralogy of the northern lowlands. Acidic leaching of mafic minerals produces a variety of secondary precipitates, including sulfates, oxides, and amorphous silica (Tosca *et al*., 2004; Golden *et al*., 2005). The only confirmed concentrations of possible leaching precipitates in the northern lowlands generally is within the north polar sand sea, where gypsum and possibly other sulfates are present in abundances ranging up to 40 wt.% (Horgan *et al*., 2009; Chapter 2). Because of this general lack of observed precipitates at the surface or incorporated into the glass-rich deposits, any leaching process that produced these materials must have transported secondary alteration products away from the surface before depositing them. If these precipitates are not incorporated into the cavi unit, then this implies that either the sand of the cavi unit was altered before being incorporated into the unit (*i.e.*, that it was sourced from Acidalia Planitia or elsewhere in the northern lowlands), or that the precipitates were deposited at the base of the paleo-erg, implying top-down leaching. This latter process could potentially explain the concentration of gypsum in eastern Olympia Undae. Indeed, although we have not analyzed spectra in the high gypsum concentration region of eastern Olympia Undae, the areas immediately surrounding this region where our analysis has been performed exhibit spectra consistent with glass, suggesting that the gypsum source region may also be a source of glass (Figure

4.15). However, further spectral and stratigraphic analyses are needed to confirm a potential relationship between the gypsum source unit and the cavi unit. If the primary composition of the cavi unit sand was a high calcium pyroxene, like the veneer sands, then gypsum would be one of the most abundant secondary minerals produced during acidic leaching (*e.g.*, Fishbaugh *et al*., 2007).

Based on our observations and the above constraints, we believe that the simplest model for the leaching process that produced the LGR and glass-enrichment in the north polar region and Acidalia Planitia is melting of regional surface ice sheets or snow packs, followed by acidification of the meltwater and downward leaching of mafic materials to form a soil profile with less soluble species (glass and plagioclase) at the surface and more soluble species (sulfates, oxides, amorphous silica) precipitated some distance below. This model is consistent with the glass-rich surface that has been observed in Acidalia Planitia, and could be consistent with alteration of the cavi unit paleo-erg, either before or after the erg was incorporated into Planum Boreum. This model is also consistent with recent analyses of high-resolution spectral observations of impact craters in Acidalia Planitia by Salvatore *et al*. (2010), who showed that mafic signatures are only apparent in layers and associated debris on south-facing slopes, while north-facing slopes are mantled and have no apparent mafic spectral signatures. Mafic signatures in Acidalia also are more rare at higher latitudes, thus Salvatore *et al*. (2010) interpreted this slope-dependent composition as a result of weathering processes. Indeed, spectra presented from the north-facing slopes of craters exhibit concave continuum shapes and shallow 1 μm bands consistent with our leached glass rind spectra.

Furthermore, this model is consistent with observations and models of the past and current distribution of ice on Mars. While ground ice currently exists within meters of the surface to 45°N and may previously have extended much further

(Mustard *et al*., 2001; Byrne *et al*., 2009), models computed at high obliquities indicate that ice also has accumulated at the surface (Mischna *et al*., 2003). These models are supported by new geomorphic analyses of pedestal craters in the northern plains, which have provided evidence that pedestals are the remnants of regional ice sheets, armored by the impact process (Kadish *et al*., 2009). Such ice sheets likely formed and retreated repeatedly during the Amazonian, suggesting the potential for multiple episodes of leaching to produce the homogenous glass-rich deposits that we observe today.

9. Conclusions

The analysis methods presented here have revealed that dark toned sediments in the north polar region appear to be from two compositionally and stratigraphically distinct sources. Sediments sourced from the stratigraphically younger north polar veneers/Planum Boreum 2 unit have spectral characteristics that are consistent with high calcium pyroxene (HCP). These pyroxene-bearing sediments appear to be relatively unaltered compared to the other major sediment type, which is composed of leached iron-bearing glass, and may have formed from pervasive acidic leaching of more typical mafic sand. The glass-rich unit appears to be sourced from the stratigraphically lower cavi unit, which has been interpreted as a paleo-erg indurated by ice and/or snow.

The distinct compositions of these two units implies that they have undergone very little or no sediment exchange, at least since the alteration of the cavi unit occurred. Currently, the timing of this alteration is poorly constrained, as the alteration may have occurred in the northern lowlands before the cavi unit sediments collected in the north polar region, or the alteration may have occurred within Planum Boreum after the sediments were indurated. In the northern lowlands, the lack of secondary

precipitate minerals suggests a top-down leaching process, which we interpret as evidence that the leachate may have been derived from melting of surface ice sheets or snow packs.

These processes may not have been limited to the north polar region during the Amazonian. Ice sheets and/or snow may have covered much of the planet at times, and leaching due to snow has been proposed as one possible explanation of soil profiles observed by the Mars Exploration Rover Spirit (Squyres *et al*., 2004) in Gusev Crater (Arvidson *et al*., 2010). Furthermore, TES ST2 has been identified at both high southern latitudes and at mid latitudes (Bandfield, 2000; Rogers *et al*., 2007; Ruff and Christensen, 2007), although further analysis will be required to investigate whether these other ST2 locations exhibit similar NIR spectral characteristics to the leached glass-rich deposits in the north polar region. If such surface processes have taken place elsewhere on the planet under recent climatic conditions, then they must also be considered as potential alteration processes within ancient terrains as well.

Overall, while it has generally been accepted that the Amazonian has been dominated by physical weathering with little or no aqueous activity, these results suggest that even during the arid Amazonian, liquid water may have had a profound effect on the composition of large regions of the martian surface.

CHAPTER 5

SYNTHESIS AND CONCLUSIONS

This body of work has provided an in depth view of the processes and landforms of the north polar region of Mars, and has revealed new insights into how water and ice have shaped the composition and morphology of sediments in this region. Because the geology of the north polar region has been produced almost entirely in the most recent martian epoch, the Amazonian (*e.g.*, Tanaka *et al*., 2008), these results provide a unique view of what processes may occur under current or similar climatic conditions.

The goal of this final chapter is to review and synthesize the results of the presented studies. Section 1 reviews the new methods that have been developed in this work, Section 2 reviews the major results, Section 3 explores possible future work that could be motivated by these studies, and Section 4 concludes with the broader implications of this work.

1. Development of new spectral techniques

Completing these studies required developing several new techniques for analyzing martian surface spectra, all of which were based on laboratory spectral data. Because the diagnostic 1.9 μm H_2O absorption band in hydrated minerals overlaps with the 2.0 μm water ice absorption band, previous studies did not include any spectra with ice signatures (Langevin *et al*., 2005a; Fishbaugh *et al*., 2007; Seelos *et al*., 2008). While ice can mask the presence of other minerals that it is intimately mixed with at the resolution of OMEGA, there are many pixels where ice is linearly mixed ("checkerboard" mixing) with other surfaces, and the spectral information of the non-ice surface is still retrievable. By developing a simple method of detecting

whether the hydration band is superimposed on the ice band in a spectrum, I was able to show that hydrated minerals are present on the icy terrains of Planum Boreum (Chapter 2). Since my study was published (Horgan *et al.,* 2009), the same parameter was used by Calvin *et al*. (2009) in their investigation of the north polar region using CRISM. That study confirmed many of my results presented in Chapter 2.

Also in Chapter 2, I used laboratory spectra of gypsum samples to derive empirical relationships between the shape and depth of characteristic gypsum absorptions and variables such as grain size and abundance. These relationships had not been previously derived. As previous estimates of gypsum abundance in the north polar sand sea were based on theoretical models (Fishbaugh *et al*., 2007), these experiments provided a basis for discriminating which models were most realistic. These empirical relationships could also potentially be applied to polyhydrated sulfates more generally in other study regions.

While previous studies have noted that iron-bearing glass modifies and widens the absorptions of other ferrous minerals (*e.g.*, Farr *et al*., 1980; Minitti *et al*., 2002; Nicholis *et al*., 2006; Moroz *et al*., 2009), this effect had not previously been quantified. The 1 μm band center vs. band skew parameters and the mixture data sets presented in Chapter 4 provide a method for detecting the presence of glass, even when in a mixture. This development allowed me to confidently identify glass on the martian surface for the first time, and to identify mixtures of that glass with other ferrous minerals. Furthermore, the mixture spectra presented in Chapter 4 also demonstrate the effects of mafic mixtures on diagnostic shapes of spectra. In particular, this data set demonstrates the potential for misidentification of similar ferrous minerals and of pure minerals with mineral mixtures, the best example of which is the likelihood of misidentifying a glass mixture as olivine. Again, while this

effect has been previously documented (*e.g.*, Nicholis *et al*., 2006), a method for discovering when glass is present in a mixture is new from this work.

Finally, my work has led to the development of new parameters to identify and map concave continua in martian polar spectra. While concave continua have been shown in laboratory studies to be consistent with leached rinds on glass, Chapter 4 was the first study to demonstrate that this continuum effect is unique on Mars and that it is potentially diagnostic of surface alteration processes.

2. Synthesis: Major results

The results from these studies suggest that there are at least three distinct compositional and morphological types of dark-toned sediments in the north polar region of Mars. First, the leached glass-rich, but hydrated mineral poor cavi unit; second, the pyroxene-rich and hydrated mineral bearing north polar veneers and their source unit, the Planum Boreum 2 unit; and lastly, the north polar erg, which apparently includes sediments sourced from both of these units and potentially other unidentified units, including the gypsum source unit.

The cavi unit is the cross-bedded unit that makes up part of the lower layer sequence of Planum Boreum. The cavi unit is hypothesized to be the indurated remnants of a once vast sand sea from the Middle Amazonian, and has been observed in exposures up to hundreds of meters thick (Tanaka *et al*., 2008). The shape of the continuum and 1 μm ferrous iron band of materials that appear to be sourced from outcrops of the cavi unit are consistent with an iron bearing glass that has been subjected to acidic leaching (Chapter 4). We hypothesize that the leached and glass-rich nature of the unit is due to pervasive leaching of a more typical mafic sand, during which all phases except the glass were dissolved. Large, low albedo regions of the northern lowlands outside of the polar region exhibit the same spectral characteristics

as the cavi unit. Due to the lack of secondary alteration products at the surface in these regions, we hypothesize that the alteration was caused by oxidized and acidified melt water from regional ice sheets or snow packs. The timing of the alteration of the cavi unit is not well constrained, as the cavi unit material may be the result of erosion and reworking of previously altered material. Alternatively, the alteration may have been a regional effect that altered both the low albedo plains as well as the cavi unit paleo-erg. Finally, it is possible that the alteration of the cavi unit took place after it was indurated and incorporated into Planum Boreum.

The north polar veneers are the low-albedo deposits that cover much of the surface of Planum Boreum and extend into the plains, interior to the circum-polar sand sea. These deposits appear to be sourced from the Planum Boreum 2 unit, a low albedo unit located at the unconformity between the upper and lower polar layered deposits (Rodriguez *et al*., 2007). The origin of the Planum Boreum 2 unit is not well constrained, but it has been hypothesized that the sediments may have been derived from Olympia Undae during an erosive period (Tanaka *et al*., 2008). The presence of hydrated minerals within the north polar veneers supports this hypothesis (Chapter 2; confirmed by Calvin *et al*. (2009) and Masse *et al*. (2010)), as the hydrated minerals have been identified as containing a hydrated mineral that may be spectrally consistent with the gypsum in Olympia Undae (Chapter 2). Further investigation of one CRISM observation of the veneers has confirmed that they have features consistent with gypsum (Masse *et al*., 2010). However, the mafic composition of the north polar veneers and presumably the Planum Boreum 2 unit is primarily that of a high-calcium pyroxene, while Olympia Undae appears to be composed of a mixture of pyroxene and glass, where the glass appears to be sourced from the cavi unit (Chapter 4). Thus, if the Planum Boreum 2 unit was sourced from Olympia Undae, it implies that either the alteration or erosion of the cavi unit is more recent than the Planum Boreum 2 unit.

Alternatively, the Planum Boreum 2 unit may have been sourced from elsewhere in the region or in the northern lowlands.

Olympia Undae and the sand seas that are derived from it appear to be composed of sediments from a variety of sources, including the leached glass of the cavi unit, the pyroxene and hydrated minerals of the Planum Boreum 2 unit and the pyroxene apparently sourced from within the polar outliers, and up to 40 wt.% gypsum, sourced from an as yet unidentified unit (Chapters 2 and 4; Calvin *et al*., 2009; Masse *et al*., 2010). Siton Undae and Hyperborea Undae, however, have a mafic composition that appears to be even more leached-glass-rich than sediments directly sourced from the cavi unit, perhaps suggesting that these sands are remobilized remnants of that unit.

While these new results suggest that the composition of north polar sediments has been significantly affected by the activity of water during the Amazonian, morphologic evidence indicates that both liquid water and ice are actively affecting the morphology of the dunes in the region under current climatic conditions (Chapter 3). A strong correlation between surface cracks on the dunes of Olympia Undae and the OMEGA hydration band depth suggests that these dunes are actively undergoing cementation due to sulfates, which, if true, would require dissolution and reprecipitation of the sulfates by liquid water. While pure liquid water is not stable on the surface of Mars today, this result suggests that brines and/or local environmental conditions can make liquid water stable under current climatic conditions, at least for short periods of times.

The lack of craters and the fresh surfaces of these dunes suggest that they are active today (*e.g.*, Kreslavsky, 2010; Chapter 3), even though no dune migration has been observed in the north polar region or almost anywhere else on Mars to date (*e.g.*, Schatz *et al*., 2006; Bourke *et al*., 2008, Chojnacki *et al*., 2010). Observations

presented in Chapter 3 of active slipface features on dunes provide the first evidence in the northern hemisphere that the dunes are currently active, albeit likely at slow migrations rates. These slow migration rates may be due in part to the presence of ice within the dunes, as inferred from thermal and neutron data sets (*e.g.*, Feldman *et al*., 2008; Putzig *et al*, 2010), and as supported by our interpretations of niveo-aeolian morphologies on the dunes (Chapter 3).

3. Remaining questions and future work

(1) What is the source of the Olympia Undae gypsum and how was it formed?

Neither OMEGA (Fishbaugh *et al*., 2007; Chapter 2) nor CRISM (Calvin *et al*., 2009; Masse *et al*., 2010) investigations have identified a sulfate signature in any of the Planum Boreum units except for the north polar veneers that drape Planum Boreum. This is surprising, as any source unit for the Olympia Undae sulfates should contain at least as much gypsum per unit volume as the dunes (~40 wt.%). There are at least two possible explanations for this lack of detection of gypsum in the Planum Boreum units. First, the gypsum may be masked by dust, oxides, glasses or other highly absorbing phases within the source unit. This situation may be analogous to the widely distributed sulfate-bearing bedrock observed *in situ* at Meridiani Planum by the Mars Exploration Rover Opportunity (*e.g.*, Grotzinger *et al*., 2005), which is not identifiable as sulfate-bearing from orbit (*e.g.*, Calvin *et al*., 2009). Secondly, the gypsum could be concentrated at the surface of the dunes by capillary wicking and surface evaporation of brines, which we have hypothesized may be causing the observed sulfate cementation (Chapter 3), giving a much higher apparent concentration than is actually present volumetrically in the dune (Calvin *et al*., 2009). This suggests that the Olympia Undae substrate could be the source for the gypsum,

even though it was previously ruled out because it exhibits a lower gypsum abundance than the overlying dunes.

It is also possible that the gypsum is sourced from a layer that has not yet been identified. Some new stratigraphic analyses suggest, for example, that the gypsum may be sourced from a unit underlying Planum Boreum (K. Tanaka, personal communication), perhaps implying an older age for the gypsum than previously thought. To some extent, an older age for the gypsum is potentially more exciting, as the diversity of aqueous processes that can plausibly be called into play increases with the age of a surface. A Hesperian-aged gypsum-rich deposit, for example, could more plausibly be explained by evaporation of outflow fluids or other water bodies in the northern basin.

Finally, a potentially critical relationship that is currently unknown is that between the leached glass-rich sands of the cavi unit and the Olympia Undae gypsum. Gypsum would be a major byproduct of leaching of calcium-bearing mafic sand, and thus could have been produced by the leaching of the cavi unit. However, the stratigraphic details of the relationship have not yet been revealed.

(2) What is the source of the north polar veneers and Planum Boreum 2 unit?

The high-calcium pyroxene that has been detected in the north polar veneers has no apparent source within the north polar region, and therefore could be sourced from a unit elsewhere in the northern lowlands. Comparing the location of this unaltered unit with the location of altered terrains (*e.g.*, in Acidalia Planitia) could place some constraints not only on the timing and extent of alteration in the northern plains, but also on the geologic history of the plains more generally.

The source of hydrated minerals, most likely predominantly gypsum, detected in the north polar veneers is also poorly constrained. While the Olympia Undae

gypsum source is the only identified gypsum deposit in the northern plains and could serve as a source for the gypsum in the north polar veneers, this is not consistent with the mafic mineralogy we have observed (Chapter 4).

The Phoenix lander potentially identified a variety of salts on the surface of the northern plains where it landed, including calcium sulfates, perchlorates, and magnesium sulfates (Hecht *et al*., 2009; Kounaves *et al*., 2010). While the origin of these species has not yet been well constrained, they could result from atmospheric exposure or interactions between the atmosphere and surface soils or ice. Thus, similar species could have been produced in the north polar veneers over long term surface exposure. Indeed, Masse *et al*. (2010) detected absorption bands at 2.14 μm in CRISM spectra of the veneers and north polar erg that may be consistent with either a calcium sulfite or a perchlorate; however, the distribution of this spectral feature has not been reported beyond the local extent of the Masse *et al*. (2010) study.

(3) What stratigraphic units are present in the polar outliers?

Material apparently sourced from the polar outliers on the southwestern edge of Olympia Undae has some of the strongest pyroxene signatures in the region; however, I was unable to correlate the source of these materials with a unit in the polar outliers, as the stratigraphy of the outliers has not been as thoroughly studied as Planum Boreum (*e.g.*, Tanaka *et al*., 2008). Further investigation of these structures may provide insight into the source(s) of pyroxene in Olympia Undae as well as in the Planum Boreum 2 unit.

(4) How extensive has surface leaching been on Mars, and when did it occur?

As discussed above, the timing of the apparent leaching of the cavi unit and of the low albedo deposits in Acidalia Planitia is poorly constrained. While the other

major basins in the northern lowlands also contain extensive deposits of low albedo materials, only Acidalia has been identified so far as showing signatures of leaching. Black, sand-sized particles that could exhibit rinds at the limit of resolution were identified at the Phoenix landing site by the Phoenix Lander's Optical Microscope (Goetz *et al*., 2010). If these particles are leached glass, this could suggest that these deposits are widespread across the northern plains. Further investigations of the extent of leaching in the northern lowlands and additional constraints on the ages of the altered surfaces could help to refine the possible sequences of alteration.

Leaching may also be a possibility outside of the northern plains, as TES ST2 has been detected at other latitudes (*e.g.*, Ruff and Christensen, 2007). Preliminary investigation of OMEGA spectra from high southern latitudes with ST2 detections confirms that these spectra have positive concavities, although the character of the 1 μm band has not yet been investigated. A global study of the distribution, age, and NIR spectral characteristics of ST2 surfaces may also aid in establishing the correlation between NIR spectral characteristics consistent with leaching and the high silica phase of ST2.

4. Conclusions

This dissertation has provided abundant new evidence that both water and ice have had major effects on both the composition and morphology of sediments in the north polar region of Mars and, most likely, throughout the northern lowlands. The leached glass alteration assemblage identified herein has not been previously observed on Mars, or even on Earth, at the areal extent and degree of alteration that these results suggest. This work also presents the first thorough treatment of the composition of north polar deposits, and places new constraints on the alteration and transport history

of those deposits. Finally, the new and unique methods developed in this body of work will allow similar analyses to be performed on other planetary surfaces.

Combined, the evidence presented in this dissertation suggests that although the Amazonian has typically been thought of as an arid period dominated by physical weathering, the northern plains have been, and likely continue to be, a dynamic cryo-sedimentary system where both physical and chemical weathering processes have been recently active.

REFERENCES

Adams, J.B. (1968). Lunar and martian surfaces: Petrologic significance of absorption bands in the near-infrared. *Science*, *159*, 1453.

Adams, J.B. (1974). Visible and near-infrared diffuse reflectance spectra of pyroxenes as applied to remote sensing of solid objects in the solar system. *J. Geophys. Res., 79*. 4829.

Ahlbrandt, T.S. and S. Andrews (1978). Distinctive sedimentary features of cold-climate eolian deposits, North Park, Colorado. *Palaeogeo. Palaeocl. Paleoec*., *25*, 327.

Arvidson, R.E., J.L. Gooding, and H.J. Moore (1989). The martian surface as imaged, sampled, and analyzed by the Viking landers. *Rev. Geophys*., *27*, 39.

Arvidson, R.E. *et al*. (2004). Localization and physical properties experiments conducted by Spirit at Gusev Crater. *Science*, *305*, 821.

Arvidson, R.E. *et al*. (2010). Recent scientific results from Spirit's observations of sulfate sands on the side of Scamander Crater, Columbia Hills, Mars. *Lunar Planet. Sci. Conf. 41*, #1247.

Bagnold, R.A. *The Physics of Blown Sand and Desert Dunes,* Methuen Press, London, 1941.

Bandfield, J.L. (2002). Global mineral distributions on Mars. *J. Geophys. Res., 107* 5042.

Bandfield, J.L. and W.C. Feldman (2008). Martian high latitude permafrost depth and surface cover thermal inertia distributions. *J. Geophys. Res.*, *113*, doi:10.1029/2007JE003007.

Bandfield, J.L. *et al.* (2000). A global view of martian surface compositions from MGS-TES. *Science*, *287*, 1626

Bell III, J. F. In *Mineral Spectroscopy: A Tribute to Roger G. Burns,* Geochemical Society Special Publication 5, Dyar, M.D., McCammon, C., Schaefer, M.W., Eds., 359-380 (Geochemical Soc., Washington, 1996).

Bell III, J.F. *et al*. (1997). Mars surface mineralogy from Hubble Space Telescope imaging during 1994-1995: Observations, calibration, and initial results. *J. Geophys. Res*., *102,* 9109.

Bell III, J.F. *et al*. (2004). Pancam multispectral imaging results from the Spirit rover at Gusev crater. *Science, 305,* 800.

Bell III, J.F. *et al*. (2008). Surface albedo observations at Gusev Crater and Meridiani Planum, Mars. *J. Geophys. Res., 113*, E06S18, doi:10.1029/2007JE002976.

Bellucci, G., F. *et al*. (2006). OMEGA/Mars Express: Visual channel performances and data reduction techniques. *Planet. Space Sci.*, *54*, 675.

Bibring, J.-P. *et al*. (2004). OMEGA: Observatoire pour la Minéralogie, l'Eau, les Glaces et l'Activité, In: *Mars Express: the scientific payload*. ESA SP-1240, Noordwijk, Netherlands: ESA Publications Division, 37.

Bibring, J.-P. *et al*. (2005). Mars Surface Diversity as Revealed by the OMEGA/Mars Express Observations. *Science, 307*, 1576.

Bibring, J.-P. *et al*. (2006). Global mineralogical and aqueous Mars history derived from OMEGA/Mars Express data. *Science, 312*, 400.

Bishop, J.L., C.M. Pieters, and R.G. Burns (1993). Reflectance and Mössbauer spectroscopy of ferrihydrite-montmorillonite assemblages as Mars soil analog materials. *Geochim. Cosmochim. Acta*, *57*, 4583.

Blasius, K.R., J.A. Cutts, and A.D. Howard (1982). Topography and stratigraphy of Martian polar layered deposits. *Icarus*, *50*, 140.

Bourke, M.C., in prep.

Bourke, M.C. (2005). Alluvial fans on dunes in Kaiser Crater suggest niveo-aeolian and denivation processes on Mars. Proc. Lunar Sci. Conf. 36, #2373.

Bourke, M.C., K.S. Edgett, and B.A. Cantor (2008). Recent aeolian dune change on Mars. *Geomorphology*, *94*, 247.

Bourke, M.C. *et al*. (2009). Sand dune movement in the Victoria Valley, Antarctica. *Geomorphology, 109*, 148.

Bouska, V. and J.F. Bell III (1993). Assumptions about the presence of natural glasses on Mars. *J. Geophys. Res., 98***,** 18719.

Boynton, W.V. *et al*. (2002). Distribution of hydrogen in the near surface of Mars: Evidence for subsurface ice deposits. *Science*, 297, 81.

Bridges, N.T. *et al*. (2007). Windy Mars: A dynamic planet as seen by the HiRISE camera. *Geophys. Res. Lett., 34*, doi:10.1029/2007GL031445.

Bristow, C.S. *et al*. (2010). Investigation of the age and migration of reversing dunes in Antarctica using GPR and OSL, with implications for GPR on Mars. *Earth Planet. Sci. Lett., 289*, 30.

Breton, C., N. Lancaster, and W.G. Nickling (2008). Magnitude and frequency of grain flows on a desert sand dune. *Geomorphology*, *95*, 518.

Burns, R.G. (1987). Ferric sulfates on Mars. *J. Geophys. Res., 92*, E570.

Burns, R.G. (1988). Gossans on Mars. *Proc. 18th Lunar and Planetary Science Conf*., Cambridge University Press, Lunar and Planetary Institute, 713.

Burns, R.G. and D.S. Fisher (1993). Rates of oxidative weathering on the surface of Mars. *J. Geophys. Res., 98,* 3365.

Burns, R.G. and D.S. Fisher (1990). Iron-sulfur mineralogy of Mars: Magmatic evolution and chemical weathering products. *J. Geophys. Res., 95*, 14415.

Byrne, S. and B. Murray (2002). North polar stratigraphy and the paleo-erg of Mars. *J. Geophys. Res.*, *107*, 5044.

Byrne, S. *et al*. (2009). Distribution of mid-latitude ground ice on Mars from new impact craters. *Science, 325***,** 1674.

Cailleux, A. (1978). Niveo-eolian deposits. *Encyclopedia of Sedimentology*, vol. 6. Academic Press, New York. 501.

Calvin, W.M. *et al.* (2009). Compact Reconnaissance Imaging Spectrometer for Mars observations of northern Martian latitudes in summer *J. Geophys. Res., 114*, doi:10.1029/2009JE003348.

Catling, D. (1999). A chemical model for evaporites on early Mars: Possible sedimentary tracers of the early climate and implications for exploration. *J. Geophys. Res.*, *104*, 16453.

Calkin, P.E. and R.H. Rutford (1974). The sand dunes of Victoria Valley, Antarctica. *Geographical Review*, *64*, 189.

Chavdarian, G.V. and D.Y. Sumner (2006). Cracks and fins in sulfate sand: Evidence for recent mineral-atmospheric water cycling in Meridiani Planum outcrops? *Geol.*, *34*, 229.

Chavdarian, G.V. and D.Y. Sumner (2010). Origin and evolution of polygonal cracks in hydrous sulphate sands, White Sands National Monument, New Mexico. *Sedimentology*, doi:10.1111/j.1365-3091.2010.01169.x.

Chemtob, S.M. *et al*. (2010). Silica coatings in the Ka'u Desert, Hawaii, a Mars analog terrain: A micromorphological, spectral, chemical, and isotopic study. *J. Geophys. Res., 115*, doi:10.1029/2009JE003473.

Chojnacki, M., D.M. Burr, and J. Moersch (2010). Recent dune changes at Endeavour Crater, Meridiani Planum, Mars, from orbital observations. *Lunar Planet. Sci. Conf. 41*, #2326.

Christensen, P.R., J.L. Bandfield, M.D. Smith, V.E. Hamilton, and R.N. Clark (2000a). Identification of a basaltic component on the martian surface from Thermal Emission Spectrometer data. *J. Geophys. Res.*, *105,* 9609.

Christensen, P. R. *et al*. (2001). Mars Global Surveyor Thermal Emission Spectrometer experiment: Investigation description and surface science results. *J. Geophys. Res., 106*, 23823.

Christensen, P.R. *et al*. (2004a). The Thermal Emission Imaging System (THEMIS) for the Mars 2001 Odyssey Mission. *Space Sci. Rev., 110*, 37.

Christensen, P. R. *et al*. (2004b). Mineralogy at Meridiani Planum from the Mini-TES Experiment on the Opportunity Rover. *Science, 306,* 1733.

Clark, B.C. III *et al*. (1977). The Viking X ray fluorescence experiment: Analytical methods and early results. *J. Geophys. Res.*, *82*, 4577.

Clark, B.C. *et al*. (1982). Chemical composition of martian fines. *J. Geophys. Res.*, *87*, 59.

Clark, J.T. *et al*. (2008). Constraining sulfate abundances on Mars using CRISM spectra and laboratory mixtures. *Lunar Planet. Sci. Conf. 39*, #1540.

Clark, R.N. (1981a). The spectral reflectance of water-mineral mixtures at low temperatures. *J Geophys Res., 86*, 3074.

Clark, R.N. (1981b). Water frost and ice: The near-infrared spectral reflectance 0.65-2.5 μm. *J Geophys Res., 86*, 3087.

Clark R.N. and T.L. Roush (1984). Reflectance spectroscopy: Quantitative analysis techniques for remote sensing applications. *J. Geophys. Res., 89,* 6329.

Cloutis, E.A. and M.J. Gaffey (1991). Spectral-compositional variations in the constituent minerals of mafic and ultramafic assemblages and remote sensing implications. *Earth Moon Planets, 53***,** 11.

Cloutis, E.A. *et al.* (1986). Calibrations of phase abundance, composition, and particle size distribution for olivine-orthopyroxene mixtures from reflectance spectra. *J. Geophys. Res.*, *91*, 641.

Cloutis, E.A. *et al*. (1990). Reflectance spectra of glass-bearing mafic silicate mixtures and spectral deconvolution procedures. *Icarus*, *86*, 383.

Cloutis, E.A. *et al.* (2006). Detection and discrimination of sulfate minerals using reflectance spectroscopy. *Icarus*, *184*, 121.

Cloutis, E.A. *et al*. (2007). Stability of hydrated minerals on Mars. *Geophys. Res. Lett.*, *34*, doi:10.1029/2007GL031267.

Cook, G.B. R.F. Cooper, and T. Wu (1990). Chemical diffusion and crystalline nucleation of ferrous iron-bearing magnesium aluminosilicate glass. J. Non-Cryst. Solids (1990) vol. 120 pp. 207-222

Cook, G.B. and R.F. Cooper (2000). Iron concentration and the physical processes of dynamic oxidation in an alkaline earth aluminosilicate glass. *Am. Min.*, *85*, 397.

Cooper, R.F. *et al*. (1996). The mechanism of oxidation of a basaltic glass: Chemical diffusion of network-modifying cations. *Geochim. Cosmo. Acta*, *60,* 3253.

Cooper, C.D. and J.F. Mustard (2007). Effects of very fine particle size on reflectance spectra of smectite and palagonitic soil. *Icarus*, *142*, 557.

Costard, F. *et al*. (2002). Formation of recent Martian debris flows by melting of near-surface ground ice at high obliquity. *Science, 295*, 110.

Crovisier, J.L. *et al*. (2003). Nature and role of natural alteration gels formed on the surface of ancient volcanic glasses (Natural analogs of waste containment glasses). *J. Nucl. Mater., 321*, 91.

Deer, W.A., R.A. Howie, and J. Zussman (1992). *The Rock-Forming Minerals*, Pearson, 612.

Dial, A.L. Jr. (1984). Geologic map of the Mare Boreum area of Mars, scale 1:5,000,000. U.S. Geological Survey Miscellaneous Investigations Series, *Map I-1640*.

Dijkmans, J.W.A., 1990. Niveo-aeolian sedimentation and resulting sedimentary structures; Sondre Stromfjord area, Western Greenland. *Perma. Peri. Process*., 1, 83.

Diniega, S. *et al*. (2010). Present-day martian dune gully activity. *Lunar Planet. Sci. Conf. 41*, 2216.

Diniega, S., S. Byrne, and K. Glasner (2010). Niveo-aeolian process interactions and resultant martian polar dune morphology. *Lunar Planet. Sci. Conf. 41*, 2192.

Dundas, C.M. *et al*. (2010). New and recent gully activity on Mars as seen by HiRISE. *Geophys. Res. Lett.*, *37*, doi:10.1029/2009GL041351.

Eckardt, F. D. and R.S. Schemenauer (1998). Fog water chemistry in the Namib Desert, Namibia. *Atmos. Environ.*, *32*, 2595.

Edgett, K.S. and M.C. Malin (2000). New views of Mars eolian activity, materials, and surface properties: Three vignettes from the Mars Global Surveyor Mars Orbiter Camera. *J. Geophys. Res.*, *105,* 1623.

Edgett, K.S. (2002). Low-albedo surfaces and eolian sediment: Mars Orbiter Camera views of western Arabia Terra craters and wind streaks *J. Geophys. Res*., *107*, 5038.

Edgett, K. *et al*. (2003). Mars landscape evolution: influence of stratigraphy on geomorphology in the north polar region. *Geomorphology, 52*, 289.

Feldman, W. C. *et al*. (2004). Global distribution of near-surface hydrogen on Mars, *J. Geophys. Res*., *109*, E09006, doi:10.1029/2003JE002160.

Feldman, W.C. *et al*. (2008). Hydrogen content of sand dunes within Olympia Undae. *Icarus*, *196*, 422.

Fenton, L.K. (2006). Dune migration and slip face advancement in the Rabe Crater dune field, Mars. *Geophys. Res. Lett.*, *33*, doi:10.1029/2006GL027133.

Finkel, H.J. (1959). The barchans of southern Peru. *J. Geol.*, *67*, 614.

Fischer, E. M. and C.M. Pieters (1993). The Continuum Slope of Mars: Bidirectional Reflectance Investigations and Applications to Olympus Mons. *Icarus, 102***,** 185.

Fishbaugh, K. and J. Head (2000). North polar region of Mars: topography of circumpolar deposits from Mars Orbiter Laser Altimeter (MOLA) data and evidence for asymmetric retreat of the polar cap. *J. Geophys. Res.*, *105*, 22455.

Fishbaugh, K. and J. Head, III (2001). Comparison of the north and south polar caps of Mars: new observations from MOLA data and discussion of some outstanding questions. *Icarus, 154*, 145.

Fishbaugh, K. and J. Head III (2002). Chasma Boreale: Topographic characterization from Mars Orbiter Laser Altimeter data and implications for mechanisms of formation. *J. Geophys. Res.*, *107*, doi:10.1029/2000JE001351.

Fishbaugh, K. and J. Head, III (2005). Origin and characteristics of the Mars north polar basal unit and implications for polar geologic history. *Icarus*, *174*, 444.

Fishbaugh, K.E. *et al*. (2007). On the origin of gypsum in the Mars north polar region. *J. Geophys. Res.*, *112*, doi:10.1029/2006JE002862.

Fryberger, S.G. (2002). Geological overview of White Sands National Monument. Online at http://www.nps.gov/whsa/Geology.

Gaddis, L.R., C.M. Pieters, and B.R. Hawke (1985). Remote sensing of lunar pyroclastic mantling deposits. *Icarus, 61,* 461.

Geissler, P. *et al*. (2008). First in situ investigation of a dark wind streak on Mars. *J. Geophys. Res., 113*, doi:10.1029/2008JE003102.

Gellert, R. *et al*. (2004). Chemistry of Rocks and Soils in Gusev Crater from the Alpha Particle X-ray Spectrometer. *Science, 305,* 829.

Gendrin, A. *et al*. (2005). Sulfates in Martian Layered Terrains: The OMEGA/Mars Express View. *Science, 307,* 1587.

Ghrefat, H.A. *et al*. (2007). Modeling grain size variations of aeolian gypsum deposits at White Sands, New Mexico, using AVIRIS imagery. *Geomorphology*, *88*, 57.

Golden, D.C. *et al*. (2005). Laboratory-simulated acid-sulfate weathering of basaltic materials: Implications for formation of sulfates at Meridiani Planum and Gusev crater, Mars. *J. Geophys. Res.*, *110*, doi:10.1029/2005JE002451.

Gorelick, N.S. *et al*. (2003). JMARS: A multi-mission data fusion application. *Lunar Planet. Sci. Conf. 34*, #2057.

Grotzinger, J.P. *et al*. (2005). Stratigraphy and sedimentology of a dry to wet eolian depositional system, Burns formation, Meridiani Planum, Mars. *Earth Planet. Sci. Lett., 240*, 11.

Hansen, C.J. *et al*. (2010). HiRISE Images of Spring on Mars. *Lunar Planet. Sci. Conf. 41*, #2029.

Harloff, J. and G. Arnold (2002). The near-infrared continuum slope of Martian dark region reflectance spectra. *Earth Moon Planets, 88*, 223.

Hartmann, W.K. and G. Neukum (2001). Cratering chronology and the evolution of Mars. *Space Sci. Rev*., *96*, 165.

Hastenrath, S.L. (1967). The barchans of the Arequipa region, southern Peru. *Zeit. Geomorph.*, *11*, 300.

Hausrath, E. *et al*. (2008). Basalt weathering rates on Earth and the duration of liquid water on the plains of Gusev Crater, Mars. *Geol*., *36*, 67.

Hayward, R.K. *et al*. (2008). Mars global digital dune database: Distribution in north polar region and comparison to equatorial region. *Lunar Planet. Sci. Conf. 39*, #1208.

Hayward, R.K. *et al*. (2010). Mars global digital dune database: Dune volume estimates in the north polar region. *Lunar Planet. Sci. Conf. 41*, #1109.

Herkenhoff, K. and A. Vasavada (1999). Dark material in the polar layered deposits and dunes on Mars. *J. Geophys. Res., 104*, 16487.

Herkenhoff, K.E. *et al*. (2007). Meter-scale morphology of the north polar region of Mars. *Science*, *317*, 1711.

Holland, H.D. and S.D. Malnin (1979). The solubility and occurrence of non-ore minerals. *Geochemistry of Hydrothermal Ore Deposits*. John Wiley & Sons, 461.

Horgan, B.H. and J.F. Bell III. Pervasive Amazonian leaching in the northern lowlands of Mars. Submitted to *Nature Geoscience*.

Horgan, B.H. *et al*. (2009). Distribution of hydrated minerals in the north polar region of Mars. *J. Geophys. Res*., *114*, doi:114, 10.1029/2008JE003187.

Horgan, B.H., J.F. Bell III, and M.C. Bourke (2010). Dry flow, surface cementation, and ice induration features on dunes in the north polar region of Mars. *Lunar Planet. Sci. Conf. 41*, #1325.

Horgan, B.H. *et al*. Sulfate cementation, ice induration, and dune activity in the north polar sand sea of Mars. In prep.

Howard, A.D. (1978). Origin of the stepped topography of the Martian poles. *Icarus, 34*, 581.

Howard, A.D. (2000). The role of eolian processes in forming surface features of the martian polar layered deposits. *Icarus, 144*, 267.

Howard, A., J. Cutts, and K. Blasius (1982). Stratigraphic relationships within martian polar cap deposits. *Icarus*, *50*, 161.

Hugenholtz, C.H., S.A. Wolfe, and B.J. Moorman (2007). Sand–water flows on cold-climate eolian dunes: Environmental analogs for the eolian rock record and martian sand dunes. *J. Sed. Res.*, *77*, 607.

Hunt, G.R. and J.W. Salisbury (1970). Visible and near-infrared spectra of minerals and rocks: I. Silicate minerals. *Mod. Geol.*, *1*, 283.

Hunt, G.R. (1977). Spectral signatures of particulate minerals in the visible and near infrared. *Geophysics, 42*, 501

Hunter, R.E. (1977). Basic types of stratification in small eolian dunes. *Sedimentology*, *24*, 361.

Hurowitz, J.A. *et al*. (2010). Origin of acidic surface waters and the evolution of atmospheric chemistry on early Mars. *Nature Geosci.*, *3*, 323.

Jambor, J.L. and J.E. Dutrizac (1998). Occurrence and constitution of natural and synthetic ferrihydrite, a widespread iron oxyhydroxide. *Chem. Revs., 98*, 2549.

Johnson, J. and W.M. Grundy (2001). Visible/near-infrared spectra and two-layer modeling of palagonite-coated basalts. *Geophys. Res. Lett.*, *28*, 2101.

Jouglet, D. *et al*. (2007). Hydration state of the Martian surface as seen by Mars Express OMEGA: 1. Analysis of the 3 μm hydration feature. *J. Geophys. Res., 112,* E08S06, doi:10.1029/2006JE002846.

Kadish, S. J., N.G. Barlow, and J.W. Head (2009). Latitude dependence of Martian pedestal craters: Evidence for a sublimation-driven formation mechanism. *J. Geophys. Res., 114,* 10.1029/2008JE003318.

Kelley, N.J. *et al.* (2007). Seasonal polar carbon dioxide frost on Mars: CO_2 mass and columnar thickness distribution. *J. Geophys. Res*., *112*, 12.

Kocurek, G. and R.C. Ewing, (2010). Frozen dune dynamics, accumulation and preservation of aeolian cross-stratification in the cavi unit in the north polar region of Mars*. Intl. Conf. Mars Sed. Strat. 1*, #6004.

Koster, E.A. and J.W.A Dijkmans (1988). Niveo-aeolian deposits and denivation forms, with special reference to the Great Kobuk Sand Dunes, northwestern Alaska. *Earth Surface Proc. Land.*, *13*, 153.

Kraft, M.D. *et al*. (2007). A pedogenic weathering model for the formation of silica coatings on high-latitude martian surfaces. *Lunar Planet. Sci. Conf. 38*, #2241.

Kreslavsky, M.A. (2010). Characteristic time scales of dune-related processes in the north polar region of Mars. *Intl. Planet. Dunes Wkshp. 2*, #2033.

Kreslavsky, M.A. *et al*. (2010). North-south symmetry in degradation rates of small impact Craters at high latitudes on Mars: Implications for recent climate change. *Lunar Planet. Sci. Conf. 41*, 2560.

Lamplugh, G.W., 1902. Calcrete. *Geological Magazine*, *9*, 575.

Lancaster, N. and R. Greeley (1990). Sediment volume in the north polar sand seas of Mars. *J. Geophys. Res.*, *95*, 10921.

Langevin, Y. *et al*. (2005a). Sulfates in the north polar region of Mars detected by OMEGA/Mars Express. *Science*, *307*, 1584.

Langevin. Y. *et al*. (2005b). Summer evolution of the north polar cap of Mars as observed by OMEGA/Mars Express. *Science*, *307*, 1581.

Langevin, Y. *et al*. (2008). Weak signatures of water ice at high northern latitudes: Aerosols, frosts and ice outcrops. *Lunar Planet. Sci. Conf. 39,* #2134.

Langford, R.P (2003). The Holocene history of the White Sands dune field and influences on eolian deflation and playa lakes. *Quart. Intl*., *104*, 31.

Lorenz, R.D. and J. Radebaugh (2009). Global pattern of Titan's dunes: Radar survey from the Cassini prime mission. *Geophys. Res. Lett.*, *36,* doi:10.1029/2008GL036850.

Malin, M., and K. Edgett (2001). Mars Global Surveyor Mars Orbiter Camera: Interplanetary cruise through primary mission. *J. Geophys. Res.*, *106*, 23429.

Malin, M.C. *et al*. (2007). The Context Camera investigation onboard the Mars Reconnaissance Orbiter. *J. Geophys. Res.*, *112*, doi:10.1029/2006JE002808.

Mangold, N. and F. Costard (2003). Debris flows over sand dunes on Mars: Evidence for liquid water. *J. Geophys. Res*. *108*, 5027.

Marchenko, A.G. and A.A. Pronin (1995). Study of relations between small impact craters and dunes on Mars. *22nd Russian-American Microsymposium on Planetology*. Vernadsky Institute, Moscow.

McCord, T.B. *et al*. (1981). Moon: Near-infrared spectral reflectance, a first good look. *J. Geophys. Res.*, *86*, 10883.

McEwen, A.S. *et al*. (2007). Mars Reconnaissance Orbiter's High Resolution Imaging Science Experiment. *J. Geophys. Res., 112,* doi:10.1029/2005JE002605.

McKenna Neuman, C. (1990). Role of sublimation in particle supply for aeolian transport in cold environments. *Geografiska Annaler, 72A*, 329.

Mellon, M.T. and B.M. Jakosky (1995). The distribution and behavior of Martian ground ice during past and present epochs. *J. Geophys. Res., 100*, 11781.

Mellon, M.T. *et al*. (2008). Periglacial landforms at the Phoenix landing site and the northern plains of Mars. *J. Geophys. Res.*, *113,* doi:10.1029/2007JE003039.

Michalski, J. R. *et al*. (2005). Mineralogical constraints on the high-silica martian surface component observed by TES. *Icarus, 174***,** 161.

Milliken, R.E. *et al*. (2007). Hydration state of the Martian surface as seen by Mars Express OMEGA: 2. H_2O content of the surface, *J. Geophys. Res., 112*, doi:10.1029/2006JE002853.

Milliken, R.E. *et al*. (2008). Opaline silica in young deposits on Mars. *Geol*., *36***,** 847.

Milkovich, S. and J. Head (2005). North polar cap of Mars: Polar layered deposit characterization and identification of a fundamental climate signal. *J. Geophys. Res.*, *110*, doi:10.1029/2004JE002349.

Milkovich, S. and J. Head III (2006). Surface textures of Mars' north polar layered deposits: A framework for interpretation and future exploration. *Mars*, *2*, 21.

Minitti, M.E., J.F. Mustard, and M.J. Rutherford (2002). Effects of glass content and oxidation on the spectra of SNC-like basalts: Applications to Mars remote sensing. *J. Geophys. Res., 107***,** 5030.

Minitti, M.E. (2007). Morphology, chemistry, and spectral properties of Hawaiian rock coatings and implications for Mars. *J. Geophys. Res., 112***,** 24.

Mischna, M.A. *et al*. (2003). On the orbital forcing of Martian water and CO2 cycles: A general circulation model study with simplified volatile schemes. *J. Geophys. Res., 108,* 5062.

Mitrofanov, I.G. *et al* (2003). Water ice permafrost on Mars: Layering structure and subsurface distribution according to HEND/Odyssey and MOLA/MGS data. *Geophys. Res. Lett., 34*, 5.

Miyamoto, H. *et al*. (2004). Dynamics of unusual debris flows on martian sand dunes. *Geophys. Res. Lett.*, *31*, doi:10.1029/2004GL020313.

Moore, H.J. *et al*. (1999). Soil-like deposits observed by Sojourner, the Pathfinder rover. *J. Geophys. Res.*, *104*, 8729.

Morgan, G.A. *et al*. (2009). Lineated valley fill (LVF) and lobate debris aprons (LDA) in the Deuteronilus Mensae northern dichotomy boundary region, Mars: Constraints on the extent, age and episodicity of Amazonian glacial events. *Icarus, 202*, 22.

Moroz, L.V. *et al*. (2009). Spectral properties of simulated impact glasses produced from martian soil analogue JSC Mars-1. *Icarus, 202*, 336.

Morris, R.V. and G. Klingelhöfer (2008). Iron mineralogy and aqueous alteration on Mars from the MER Mössbauer spectrometers. *The Martian Surface: Composition, Mineralogy, and Physical Properties* (J.F. Bell III, ed.), Cambridge University Press, Cambridge, 339.

Morris, R.V. *et al*. (2001). Effects of palagonitic dust coatings on visible, near-IR, and Mössbauer spectra of rocks and minerals: Implication for mineralogical remote sensing of Mars. *Lunar Planet. Sci. Conf. 32*, 1912.

Morris, R.V. *et al*. (2006). Mössbauer mineralogy of rock, soil, and dust at Gusev crater, Mars: Spirit's journey through weakly altered olivine basalt on the plains and pervasively altered basalt in the Columbia Hills. *J. Geophys. Res*., *111*, doi:10.1029/2005JE002584.

Mustard, J. F., C.D. Cooper, and M.K. Rifkin (2001). Evidence for recent climate change on Mars from the identification of youthful near-surface ground ice. *Nature, 412,* 411.

Mustard, J. F. *et al*. (2005). Olivine and pyroxene diversity in the crust of Mars. *Science,* 307**,** 1594.

Murchie, S. *et al*. (2007). First results from the Compact Reconnaissance Imaging Spectrometer for Mars (CRISM). *Lunar Planet. Sci. Conf. 38*, 1472.

Murchie, S.L. *et al*. (2010). Compact Reconnaissance Imaging Spectrometer for Mars investigation and data set from the Mars Reconnaissance Orbiter's primary science phase. *J. Geophys. Res.*, *114*, doi: 10.1029/2009JE003344.

Nicholis, M. *et al*. (2006). VIS-NIR spectral properties of olivine in a basaltic glass: Implications for olivine-rich terrains on Mars. *Lunar Planet. Sci. Conf. 37*, #2378.

Nickling, W.G. (1984). The stabilizing role of bonding agents on the entrainment of sediment by wind. *Sedimentology, 31*, 111.

Nickling, W.G. and M. Ecclestone (1981). The effects of soluble salts on the threshold shear velocity of fine sand. *Sedimentology*, *28*, 505.

Noe Dobrea, E.Z. and J.F. Belll, III (2001). Composition and mineralogy of the martian north polar dune deposits: Constraints from TES and HST observations. *Lunar Planet Sci. 32*, #2099.

Noe Dobrea, E.Z. *et al*. In prep.

Oehler, D.Z. and C.C. Allen (2010). Evidence for pervasive mud volcanism in Acidalia Planitia, Mars. Icarus, in press, doi:10.1016/j.icarus.2010.03.031.

Paige, D.A., J.E. Bachman, and K.D. Keegan (1994). Thermal and albedo mapping of the polar regions of Mars using Viking thermal mapper observations. *J. Geophys. Res.*, *99*, 25959.

Pelkey, S.M. *et al*. (2007). CRISM multispectral summary products: Parameterizing mineral diversity on Mars from reflectance. *J. Geophys. Res., 112*, doi:10.1029/2006JE002831.

Pieters, C.M. (1983). Strength of mineral absorption features in the transmitted component of near-infrared reflected light: First results from RELAB. *J. Geophys. Res., 88*, 9534.

Pollard, A.M., S.P.E. Blockley, and K.R. Ward (2003). Chemical alteration of tephra in the depositional environment: theoretical stability modeling. *J. Quaternary Sci., 18,* 385.

Poulet, F. *et al*. (2007). Martian surface mineralogy from OMEGA/Mars Express: Global mineral maps. *J. Geophys. Res.*, *112*, doi: 10.1029/2006JE002840.

Poulet, F. *et al*. (2008). Spectral variability of the Martian high latitude surfaces. *Geophys. Res. Lett.*, *35*, doi:10.1016/j.icarus.2008.12.04.

Poulet, F. *et al*. (2009). Quantitative compositional analysis of martian mafic regions using the MEx/OMEGA reflectance data 1. Methodology, uncertainties and examples of application. Icarus, *201*, 69.

Plaut, J.J. *et al*. (2009). Radar evidence for ice in lobate debris aprons in the mid-northern latitudes of Mars. *Geophys. Res. Lett.*, *36*, doi:10.1029/2008GL036379.

Putzig, N.E. *et al*. (2010). Near-surface ice likely cause of thermal anomaly in martian north polar erg. *Lunar and Planet. Sci. Conf. 41*, #2495.

Reiss, D. and R. Jaumann (2003). Recent debris flows on Mars: Seasonal observations of the Russell Crater dune field. *Geophys. Res. Lett., 30*, 54.

Roach, L. *et al*. (2007). CRISM spectral signatures of the north polar gypsum dunes. *Lunar Planet Sci. Conf. 37*, #1970.

Rodriguez, J.A.P. *et al*. (2007). Recent aeolian erosion and deposition in the north polar plateau of Mars. *Mars*, *3*, 29.

Rogers, A. D., J.L. Bandfield, and P.R. Christensen (2007). Surface mineralogy of Martian low-albedo regions from MGS-TES data: Implications for upper crustal evolution and surface alteration. *J. Geophys. Res., 112*, 29.

Rogers, A.D. and O. Aharonson (2008). Mineralogical composition of sands in Meridiani Planum determined from MER data and comparison to orbital measurements. *J. Geophys. Res.*, *113*, doi:10.1029/2007JE002995.

Roush, T.L. *et al*. (1990). Ice and minerals on Callisto: A reassessment of the reflectance spectra. *Icarus*, *86,* 355.

Roush, T.L. *et al*. (2007). Estimated optical constants of gypsum in the regions of weak absorptions: Application of scattering theories and comparisons to independent measurements. *J. Geophys. Res.*, *112*, doi:10.1029/2007JE002920.

Ruff, S. W. and P. R. Christensen (2007). Basaltic andesite, altered basalt, and a TES based search for smectite clay minerals on Mars. *Geophys. Res. Lett.*, *34*, doi:10.1029/2007GL029602.

Sagan, C. *et al*. (1977). Particle motion on Mars inferred from the Viking Lander cameras. *J. Geophys. Res.*, *82*, 4430.

Salvatore, M.R. *et al*. (2010). Definitive evidence of Hesperian basalt in Acidalia and Chryse planitiae. *J. Geophys. Res.*, *115*, doi:10.1029/2009JE003519.

Schatz, V. *et al*. (2006). Evidence for indurated sand dunes in the martian north polar region. *J. Geophys. Res.*, *111*, doi:10.1029/2005JE002514.

Schenk, C.J. and S.G. Fryberger (1988). Early diagenesis of eolian dune and interdune sands at White Sands, New Mexico. *Sedimentary Geology*, *55*, 109.

Schreiber, B.C. and M. El Tabakh (2000). Deposition and early alteration of evaporites. *Sedimentology*, *47*, 215.

Schultz, P.H. and J.F. Mustard (2004). Impact melts and glasses on Mars. *J. Geophys. Res., 109***,** doi:10.1029/2002JE002025.

Scott, D.H. and M.H. Carr (1978). Geologic map of Mars, scale 1:25,000,000. U.S. Geological Survey Miscellaneous Investigations Series, *Map I-1083*.

Scott, D.H. and K.L. Tanaka (1987). Geologic map of the polar regions of Mars, scale 1:15,000,000,000. US. Geological Survey Miscellaneous Investigations Series, *Map I-1802-C*.

Seelos F. *et al*. (2007). CRISM multispectral survey campaign—status and initial mosaics. *Lunar Planet. Sci*. *39*, #2336.

Silvestro, S. *et al*. (2010). Ripple migration on active dunes in Nili Patera (Mars). *Second Intl. Planet. Dunes Wkshp.*, #2010.

Singer, R.B. (1981). Near-infrared spectral reflectance of mineral mixtures: Systematic combinations of pyroxenes, olivine, and iron oxides. *J. Geophys. Res., 86*, 7967.

Singer, R.B. and Roush, T.L. (1983). Spectral reflectance properties of particulate weathered coatings on rocks: Laboratory modeling and applicability to Mars. *Lunar Planet. Sci. Conf. 14*, #708.

Smith, D.E *et al*. (2001). Mars Orbiter Laser Altimeter: Experiment summary after the first year of global mapping of Mars. *J. Geophys. Res.*, *106*, 23689.

Smith, P.H. *et al*. (2009). H2O at the Phoenix Landing Site. *Science*, *325*, 58.

Smith, I.B. and J.W. Holt (2010). Onset and migration of spiral troughs on Mars revealed by orbital radar. *Nature*, *465*, 450.

Soderblom, L.A. (1992). The composition and mineralogy of the martian surface from spectroscopic observations: 0.3 mm to 50 mm. In *Mars*, ed. H. Kieffer *et al.*, pp. 557-593. Tucson: Univ. Arizona Press.

Soderblom, J.M. *et al*. (2006). Martian phase function: Modeling the visible to near-infrared surface photometric function using HST-WFPC2 data. *Icarus*, *184*, 401.

Spencer, R. J. (2000). Sulfate minerals in evaporite deposits. *Reviews in Mineralogy and Geochemistry*, *40*, 173.

Squyres, S.W. *et al*. (2004). The Spirit rover's Athena science investigation at Gusev crater, Mars. *Science*, *305,* 794.

Squyres, S.W. and A.H. Knoll (2005). Sedimentary rocks at Meridiani Planum: Origin, diagenesis, and implications for life on Mars. *Earth Planet. Sci. Lett., 240*, 1.

Steidtmann, J.R. (1973). Ice and snow in eolian sand dunes of southwestern Wyoming. *Science, 179*, 796.

Stoiber, R. E. and W. I. Rose Jr. (1974). Fumarole incrustations at active central American volcanoes. *Geochim. Cosmochim. Acta*, *38*, 495.

Sullivan, R. *et al*. (2008). Wind-driven particle mobility on Mars: Insights from MER observations at "El Dorado" and surroundings at Gusev Crater. *J. Geophys. Res.*, *113*, doi:10.1029/2008JE003101.

Sunshine, J.M. *et al*. (1990). Deconvolution of mineral absorption bands: An improved approach. *J. Geophys. Res.*, *95*, 6955.

Tanaka, K. (1986). The stratigraphy of Mars. *J. Geophys. Res*., *91,* 139.

Tanaka, K. (2005). Geology and insolation-driven climatic history of Amazonian north polar materials on Mars. *Nature*, *437*, 991.

Tanaka, K.L. (2006). North polar gypsum: Possible origin related to Early Amazonian volcanisms at Alba Patera and aeolian mining. *4th Mars Polar Sci. Conf.*, #8024.

Tanaka, K. and D.H. Scott (1987). Geologic map of the polar regions of Mars. USGS Miscellaneous Investigations Series, Map I–1802–C.

Tanaka, K.L. and R.K. Hayward (2008). Mars' north circum-polar dunes: Distribution, sources, and migration history. *Planetary Dunes Workshop*, #1403.

Tanaka, K.L. *et al.* (2003). Resurfacing history of the northern plains of Mars based on geologic mapping of Mars Global Surveyor data. *J. Geophys. Res.*, *108*, doi:10.1029/2002JE001908.

Tanaka, K.L. *et al*. (2008). North polar region of Mars: Advances in stratigraphy, structure, and erosional modification. *Icarus*, *196*, 318.

Techer, I *et al*. (2001). Dissolution kinetics of basaltic glasses: control by solution chemistry and protective effect of the alteration film. *Chemical Geology, 176,* 235.

Thomas, P. and C. Weitz (1989). Sand dune materials and polar layered deposits on Mars. *Icarus*, *81*, 185.

Thomas, P.C. and Gierasch, P.J. (1995). Polar margin dunes and winds on Mars. *J. Geophys. Res.*, *100*, 5397.

Titus, T.N. and G.E. Cushing (2010). Thermal inertia characterization of possible niveo-aeolian formation in Olympia Undae, Mars. *Intl. Planet. Dunes Wkshp. 2*, #2034.

Tosca, N. J. *et al*. (2004). Acid-sulfate weathering of synthetic Martian basalt: The acid fog model revisited. *J. Geophys. Res., 109***,** 29.

Tsoar, H., R. Greeley, and A. Peterfreund (1979). Mars: The North Polar sand sea and related wind patterns. *J. Geophys. Res.*, *84*, 8167.

Vincent, P.J. (1984). Particle size variation over a transverse dune in the Nafud as Sirr, central Saudi Arabia. *J. Arid Environs.*, *7*, 329-336.

Wang, H. and A.P. Ingersoll (2002). Martian clouds observed by Mars Global Surveyor Mars Orbiter Camera. *J. Geophys. Res., 107*, doi:10.1029/2001JE001815.

Warner, N.H. and J.D. Farmer (2008). Importance of aeolian processes in the origin of the north polar chasmata, Mars. *Icarus*, doi: 10.1016/j.icarus.2007.08.043.

Warren, J.K. (1982). The hydrological setting, occurrence and significance of gypsum in late Quaternary salt lakes in South Australia. *Sedimentology*, *29*, 609.

Watson, A. (1986). Grain size variationa on a longitudinal dune and a barchan dune. *Sed. Geol.*, *46*, 49.

Weller, J.M. (1959). Compaction of sediments. *AAPG Bulletin, 43*, 273.

Wood, S.E., S.D. Griffiths, and M.C. Bourke (2010). Subsurface thermal effects of dune migration on Mars: Implications for ground ice stability. *Intl. Planet. Dunes Wkshp 2*., #1552.

Wyatt, M. B. and H.Y. Mcsween Jr. (2002). Spectral evidence for weathered basalt as an alternative to andesite in the northern lowlands of Mars. *Nature, 417*, 263.

Wyatt, M.B. *et al*. (2004). Global geologic context for rock types and surface alteration on Mars. *Geology*, *32,* 645.

Wyatt, M.B. (2007). The chemically altered basaltic northern plains of Mars: TES, OMEGA, and GRS integrated data sets and conclusions. *7th Intl. Conf. Mars*, #3402.

Yasso, W.E., 1966. Heavy mineral concentration and Sastrugi-like Ddeflation furrows in a beach salcrete at Rockaway Point, New York. *J. Sed. Res.*, *36*, 836.

Zimbelman, J.R. (2000). Non-active dunes in the Acheron Fossae region of Mars between the Viking and Mars Global Surveyor eras. *Geophys. Res. Lett.*, *27*, 1069.

Zuber, M.T. *et al*. (1992). The Mars Observer laser altimeter investigation. *J. Geophys. Res. 97*, 7781.

Zuber, M.T. *et al*. (1998). Observations of the north polar region of Mars from the Mars Orbiter Laser Altimeter. *Science*, *282*, 2053.